

**VERY HIGH CYCLE FATIGUE BEHAVIOR OF NICKEL-BASED
SUPERALLOY RENÉ 88 DT**

by

Jiashi Miao

A dissertation submitted in partial fulfillment
of the requirements for the degree of
Doctor of Philosophy
(Materials Science and Engineering)
in The University of Michigan
2010

Doctoral Committee:

Professor J. Wayne Jones, Co-Chair
Professor Tresa M. Pollock, Co-Chair
Professor Michael Atzmon
Assistant Professor Anton Van der Ven

© Jiashi Miao 2010
All Rights Reserved

To my family

Acknowledgements

First, I would like to thank my advisors, Professor Tresa M. Pollock and Professor J. Wayne Jones for their guidance, insight and support throughout this research project. I would also like to thank my thesis committee members, Professor Michael Atzmon and Professor Anton Van der Ven for their helpful review and valuable insights.

I would like to thank my colleagues (past and current) in Pollock and Jones group, Amit Shyam, Aomin Wu, Chris Szccepanski, Fang Cao, Xiaoxia Zhu, Jon Madison, Nick Saddock, Ansih Kumar, Jessica Terbush and Jun Zhu for their assistance and help to this thesis work. Special thanks go to Mr. Christopher Torbet for his talented experimental designs. I would also like to thank Dr. Kai Sun and Dr. Haiping Sun at EMAL for the training and assistance with the operation of electron microscopes used in this thesis.

Last, but not the least, I would like to express my deepest gratitude to my family: my parents Fayun Bai and Chunlun Miao, my wife Hui Zhou and my daughter Margaret Miao, for their love and constant support.

Financial supports provided by AFOSR (F49620-03-1-0069), DARPA and Rackham Pre-doctoral Fellowship Program are gratefully acknowledged.

Table of Contents

Dedication.....	ii
Acknowledgements.....	iii
List of Figures.....	vii
List of Tables.....	xvii
List of Appendices.....	xviii
Chapter 1 Introduction.....	1
1.1 Research background and objectives.....	1
1.2 Scope of this work.....	4
Chapter 2 Literature Review.....	5
2.1 Introduction to nickel-based superalloys.....	5
2.2 Fatigue crack initiation mechanism.....	12
2.2.1 Fundamental theories of fatigue crack initiation.....	12
2.2.2 Cyclic deformation modes in nickel-based superalloys.....	16
2.2.3 Microstructure effects on fatigue crack initiation in polycrystalline nickel-based superalloys.....	21
2.3 Very high cycle fatigue and ultrasonic fatigue.....	30
2.4 Fatigue life prediction for nickel-based superalloys.....	33
2.4.1 The damage-tolerant approach.....	33
2.4.2 Prediction of fatigue crack initiation life.....	36
2.5 Summary of literature review.....	42
Chapter 3 Microstructure Characterization and Ultrasonic Fatigue Testing.....	44
3.1 Microstructure characterization of nickel-based superalloy René 88 DT.....	44
3.2 Ultrasonic fatigue testing.....	54
3.2.1 Principles of ultrasonic fatigue testing and specimen design.....	54
3.2.2 Design of ultrasonic fatigue specimen for nickel-based superalloy René 88 DT.....	58
3.2.3 Ultrasonic fatigue testing instrumentation and experimental setup.....	66
3.2.4 Experimental setup for ultrasonic fatigue testing at room temperature.....	67
3.2.5 Experimental setup for ultrasonic fatigue testing at high temperature.....	71

3.2.6	Detection of fatigue damage using nonlinear acoustics.....	75
3.2.7	Ultrasonic fatigue sample preparation	78
Chapter 4	Quantitative Characterization of Crack Initiation Sites in René 88 DT Fatigued at 593°C.....	80
4.1	Ultrasonic fatigue behavior of nickel-based superalloy René 88DT at 593°C..	80
4.1.1	S-N data of René 88 DT at 593°C	80
4.1.2	General fractographic observations	82
4.2	Quantitative characterization of crystallographic fracture surface	89
4.2.1	Determination of the spatial orientation of crystallographic facets	91
4.2.1.1	Stereo-photogrammetry	92
4.2.1.2	Quantitative tilt fractography.....	100
4.2.2	Determination of crystallographic orientation of crystallographic facets.	102
4.3	Summary	107
Chapter 5	Crystallographic Fatigue Crack Initiation in Nickel-based Superalloy René 88 DT at Elevated Temperature.....	110
5.1	Experimental procedures	110
5.2	Quantitative characterization of crystallographic fatigue crack initiation sites	111
5.2.1	Fractography observations of crystallographic crack initiation sites.....	111
5.2.2	Critical microstructure features associated with subsurface crystallographic fatigue crack initiation	114
5.2.3	Observations of subsurface non-fatal fatigue crack.....	118
5.2.4	Observations of deformation substructures	119
5.2.5	The role of twin boundary in crystallographic fatigue crack initiation	121
5.3	Neighborhood effects on fatigue crack initiation and early small crack growth.....	129
5.4	Environmental effects on ultrasonic fatigue behavior at elevated temperature	134
5.5	Summary	136
Chapter 6	Cyclic Strain Localization and Fatigue Crack Initiation in Nickel-based Superalloy René 88 DT at Room Temperature	137
6.1	Experimental procedures	137
6.2	Experimental results.....	138
6.2.1	S-N data	138
6.2.2	Observations of the fatal fatigue crack at 720 MPa.....	140
6.2.3	Quantitative characterization of microcracks for specimens with machined flats.....	146

6.2.3.1 Microcracks initiated at the region close to $\Sigma 3$ coherent twin boundary...	148
6.2.3.2 Fatigue crack formation along both $\Sigma 3$ and $\Sigma 3s$ ($s > 1$) twin boundary...	153
6.2.3.3 Fatigue crack initiation at $\Sigma 3$ twin boundaries with both coherent and incoherent sections.....	154
6.2.3.4 Effects of favorably oriented neighbor grains on fatigue crack initiation	160
6.2.3.5 Orientation distribution of fatigue crack initiation grains.....	162
6.3 Discussion.....	163
6.3.1 Cyclic strain localization and fatigue crack initiation mechanism at room temperature	163
6.3.2 Fatigue crack initiation process in René 88 DT at room temperature	173
6.4 Summary	175
Chapter 7 Conclusions and Recommendations for Future Work	176
7.1 Conclusions.....	176
7.1.1 Fatigue behavior of René 88 DT at elevated temperature	176
7.1.2 Fatigue behavior of René 88 DT at room temperature	179
7.2 Recommendations for Future Work.....	180
7.2.1 Quantitative characterization of localized plastic strain	180
7.2.2 Deformation substructure at fatigue crack initiation site.....	181
7.2.3 Detection of the evolution of fatigue damage using nonlinear ultrasonic signals.. ..	181
Appendices.....	183
References.....	187

List of Figures

Figure 2. 1	Illustration of Rolls-Royce Trent 800 engine and main structural materials used in the engine (image courtesy of Rolls-Royce)	6
Figure 2. 2	Specific strength versus application temperature for selected structural engineering materials [5].....	6
Figure 2. 3	Primary phases within nickel-based superalloys: (a) Ni-Al binary phase diagram [6] and (b) crystal structure of γ phase and γ' phase	8
Figure 2. 4	Morphology of secondary and tertiary γ' precipitates in IN 100, a typical powder processed polycrystalline nickel-based superalloy IN100 [8]	9
Figure 2. 5	SEM image of blocky MC carbides in a nickel-based superalloy revealed by excessive chemical etching [9]	9
Figure 2. 6	Techniques involved in powder metallurgy processing of superalloys [7].	10
Figure 2. 7	The anomalous flow stress behavior of Ni_3Al as function of temperature and strain rate [12].....	11
Figure 2. 8	The morphology of persistent slip bands in fatigued copper [15].....	14
Figure 2. 9	TEM image of persistent slip band in single crystal nickel-based superalloy CMSX-4 fatigued at 850 °C [26].....	14
Figure 2. 10	Illustration of surface roughening process due to dislocation slip within emerging PSB within a surface grain [28]	15
Figure 2. 11	The formation of surface extrusions and microcrack on the surface of copper single crystal specimen [24]	16
Figure 2. 12	TEM image showing shearing of precipitates in nickel-based superalloy Nimonic PE 16 at room temperature [31]	17
Figure 2. 13	TEM micrographs of cyclic deformation substructures within nickel-based superalloy IN 792-5A at room temperature [32].....	18
Figure 2. 14	TEM micrograph showing dislocation looping in Wasploy with a microstructure of fine γ grain and large γ' precipitates fatigued at room temperature [34]	19
Figure 2. 15	Deformation substructure in nickel-based superalloy Wasploy: (a) fatigued at 500 °C and (b) fatigued at 800 ° C [34]	20
Figure 2. 16	Effects of strain rate on the flow stress of Ni_3Al (Data are cited from the reference [12])	21
Figure 2. 17	AFM images of extrusions on the surface of a Waspaloy specimen fatigued at room temperature [18].....	23

Figure 2. 18	The probability of fatigue crack initiation as a function of orientation in the nickel-based superalloy Waspaloy cycled at room temperature [42]... 24	24
Figure 2. 19	The angle between loading axis and the normal of surface microcracks in the alloy AP1 [45]	25
Figure 2. 20	Two types of extreme configuration for slip system in surface grain subjected to the highest resolved shear stress [45].....	26
Figure 2. 21	Fatigue crack initiation sites in Inconel 718 alloy with two different microstructure: (a) second phase particle cracking in specimen with small grain size and (b) slip band cracking in specimens with large grain size [46].....	27
Figure 2. 22	Surface microcracks in Waspaloy fatigued at room temperature [47]	28
Figure 2. 23	Orientation relationship between neighbor grains at crack initiation region and control region in Waspaloy [47].....	28
Figure 2. 24	Subsurface crystallographic fatigue initiation sites in different superalloys fatigued at elevated temperature: (a) RR1000 [59]; (b) Inconel 718 [58]; (c) Waspaloy [60] and (d) René 88DT [61]	30
Figure 2. 25	(a) Fish-eye topography and (b) Inclusion at the centre of the fish-eye [66]	31
Figure 2. 26	Fatigue crack initiation in copper specimen under loading stress well below the PSB threshold within very high cycle regime: (a) microcracks formed in surface grain and (b) microcracks formed in interior grains [68].....	32
Figure 2. 27	Fatigue crack growth behavior of nickel-based superalloy René 88 DT at 593° C in air and vacuum with a testing frequency of 20Hz and load ratio of 0.05 [61].....	34
Figure 2. 28	Fatigue life prediction using damage tolerant methods as compared with experimental results [61].....	36
Figure 2. 29	Schematic illustration of fatigue crack initiation model used in Chan's fatigue life prediction mode [77].....	37
Figure 2. 30	Comparison between experimental fatigue testing results with predicted fatigue crack initiation life using different crack sizes [76].....	38
Figure 2. 31	The evolution of the product of $I_B \bullet p_{irr}^{cum}$ as a function of the number of loading cycles to fatigue crack initiation in Waspaloy [18]	40
Figure 2. 32	Evolution of macroscopic plastic strain amplitude ε_a as a function of number of cycles to crack initiation N_i [18].....	41
Figure 3. 1	Optic micrograph of the microstructure of René 88 DT	46
Figure 3. 2	SEM images of electropolished microstructure of René 88 DT: (a) SEM image; (b) white particles within the microstructure of Rene 88DT and (c) EDX spectrum of white particles	47

Figure 3. 3	Inverse pole figure map of γ grains and corresponding texture pole figure	48
Figure 3. 4	Grain size distribution analysis: (a) grain map; (b) ellipse fit of grains; (c) grain size distribution (equivalent method) and (d) grain size distribution, (ellipse fit method).....	49
Figure 3. 5	Twin boundaries within the microstructure of René 88 DT	50
Figure 3. 6	Grain boundary character distribution in René 88 DT	50
Figure 3. 7	TEM image showing the morphology of two types of γ' phase	51
Figure 3. 8	EDX mapping showing the distribution of main alloying elements within γ and γ' phases	53
Figure 3. 9	Typical ultrasonic fatigue specimen geometries: (a) specimen with uniform cylinder gage section and (b) specimen with hourglass-shaped gage section	57
Figure 3. 10	The distribution of normalized strain and displacement along the René 88DT specimen at room temperature	60
Figure 3. 11	The variation of resonance length of René 88 DT sample with resonance frequencies.....	60
Figure 3. 12	The distribution of normalized displacement and strain along the René 88 DT specimen at 593°C	62
Figure 3. 13	Distribution of displacement along half of the ultrasonic fatigue specimen at room temperature and elevated temperature under the same loading (R= -1).....	62
Figure 3. 14	Finite element modeling René 88 DT ultrasonic fatigue specimen: (a) 3D FEM Model; (b) distribution of von Mises stress along the specimen and (c) distribution of normalized displacement along the specimen.....	64
Figure 3. 15	Distribution of stress and displacement along the center line of the ultrasonic fatigue specimen: (a) stress and (b) displacement.	65
Figure 3. 16	Determination of resonant frequency spectrum of René 88 DT fatigue specimen at room temperature: (a) experimental setup and (b) resonance frequency spectrum.	65
Figure 3. 17	Ultrasonic fatigue testing system: (a) whole testing system; (b) load train coupling with ultrasonic fatigue sample and (c) strain and displacement distribution along the load train and an ultrasonic fatigue specimen.	67
Figure 3. 18	Experimental setup for calibration of ultrasonic fatigue testing under fully reverse loading: (a) experimental setup and (b) linear relationship between vibration amplitude and strain measurement at the gauge section of the ultrasonic fatigue specimen.	69

Figure 3. 19	Calculated strain and displacement along the specimen and $\frac{1}{4} \lambda$ rod under loading of different amplitudes.	70
Figure 3. 20	Linear relationship between strain at the gage section of ultrasonic fatigue specimen and at the one fourth of lambda rod.	71
Figure 3. 21	Experimental setup for ultrasonic fatigue testing at high temperature under mean load: (a) mean load and (b) induction heating and temperature control.....	72
Figure 3. 22	Experimental measurement of dynamic strain on René 88 DT fatigue specimen at 593°C: (a) the principle of ISDG; (b) laser fringe pattern and (c) dynamic strain versus vibration amplitude at 593°C [86]	74
Figure 3. 23	Frequency spectra of feedback signals collected on René 88 DT specimens vibrated under fully reversed loading at different cyclic stresses [90]......	78
Figure 3. 24	Illustration of the geometry and dimensions of René 88 DT ultrasonic fatigue specimens (All dimensions are in mm.).	79
Figure 4. 1	S-N data of René 88 DT at 593° C for both ultrasonic fatigue and conventional fatigue [61]......	81
Figure 4. 2	Typical subsurface fatigue fracture surface at elevated temperature: (a) SEM image of fracture surface, (b) large crystallographic facets at crack initiation site, (c) and (d) high magnification SEM images of two large facets at the fatigue crack initiation site as indicated in (b). ($\sigma_{\max} = 660$ MPa, $N_f = 3.44 \times 10^6$ cycles, 593°C).....	83
Figure 4. 3	Fatigue crack initiation from subsurface large inclusions ($\sigma_{\max} = 600$ MPa, $N_f = 6.64 \times 10^7$ cycles, 593°C).	84
Figure 4. 4	SEM matching halves of large crystallographic facets at fatigue crack initiation sites. ($\sigma_{\max} = 600$ MPa, $N_f = 3.16 \times 10^6$ cycles, 593°C).....	86
Figure 4. 5	Fatigue failure initiated in the region close to specimen surface (a) fatigue fracture surface, (b) Large crystallographic facet at fatigue crack initiation site. ($\sigma_{\max} = 760$ MPa, $N_f = 6.5 \times 10^5$ cycles, 593°C).	86
Figure 4. 6	The relationship between fatigue life and the distance between fatigue crack initiation sites and specimen surface (The diameter of the gage section is 5 mm).	87
Figure 4. 7	Comparison between fatigue growth life and experimental total fatigue life (Fatigue crack growth data are courtesy of Amit Shyam [91]).....	89
Figure 4. 8	Illustration of the definition of spatial orientation of a crystallographic facet.	92
Figure 4. 9	Flow chart of three-dimensional reconstruction using SEM stereo pairs... ..	93
Figure 4. 10	Illustration of the automated searching method used for finding identical points on SEM stereo pairs.	94

Figure 4. 11	SEM stereo pair of a Vickers hardness indent captured by tilting the sample at +/-7°.	95
Figure 4. 12	3D Reconstruction of the Vickers hardness indent.	96
Figure 4. 13	Cross-section profile of 3D reconstructed indent.	96
Figure 4. 14	3D reconstruction of crystallographic fatigue crack initiation site: (a) SEM stereo image of crystallographic crack initiation site, (b) contour plot of 3D reconstruction fracture surface, (c) 3D view of crystallographic fatigue crack initiation site from different view angles. ($\sigma_{\max} = 660\text{MPa}$, $N_f = 3.51 \times 10^6$ cycles, 593°C).	98
Figure 4. 15	Two type crystallographic facet at fatigue crack initiation site: a) SEM images of two types of facet at fatigue crack initiation site, b) 3D view of two types of crystallographic facet at fatigue crack initiation sites. (testing condition for the specimen in image a): $\sigma_{\max} = 600\text{MPa}$, $N_f = 1.89 \times 10^7$ cycles, testing condition for the specimen in image b): $\sigma_{\max} = 660\text{MPa}$, $N_f = 5.49 \times 10^6$ cycles, 593°C).	99
Figure 4. 16	SEM stereo pair of a standard sample captured at 1000 X magnification. (A, B and C are three different features on the stereo images).	102
Figure 4. 17	Metallographic sectioning of fatigue fracture surface for the determination of the crystallographic orientation of facets.	104
Figure 4. 18	Orientation imaging map collected on a metallographically sectioned plane just beneath the fracture surface.	104
Figure 4. 19	Three Euler angles between specimen coordinate system and crystal coordinate system: (a) specimen coordinates and crystal coordinates, (b) three Euler angles between two coordinate systems.	105
Figure 4. 20	SEM stereo pair of a crystallographic facet.	106
Figure 4. 21	Crystallographic orientation of facets on fatigue fracture surface.	107
Figure 5. 1	Schematic illustration of metallographic sectioning method used in this study.	111
Figure 5. 2	Fracture surface of two failed fatigue specimens: (a) fracture surface, (b) crack initiation site and (c) ellipse fit of the single plane facet at crack initiation site for the first specimen ($\sigma_{\max} = 600\text{MPa}$, $N_f = 3.16 \times 10^6$ cycles); (d) fracture surface, (e) crack initiation site and (f) ellipse fit of the chevron facet at crack initiation site for the second specimen ($\sigma_{\max} = 600\text{MPa}$, $N_f = 1.90 \times 10^7$ cycles, 593°C).	113
Figure 5. 3	Microstructural features of the crack initiation grain: (a) metallographic sectioning through the single plane facet at the crack initiation site; (b) large matching halves of IPF maps (loading direction); (c) IPF map of the crack initiation grain; (d) reconstructed grain boundary map of the crack initiation grain (Blue lines represent random grain boundaries,	

	red lines represent $\Sigma 3$ twin boundaries) and (e) Schmid factors for 12 slip systems within both twin1 and matrix 2 of the crack initiation grain in the first sectioned samples ($\sigma_{\max} = 600\text{MPa}$, $N_f = 3.16 \times 10^6$ cycles, 593°C).	115
Figure 5. 4	Microstructure details of the crack initiation grain in the second sectioned sample: (a) metallographic sectioning through the chevron facet; (b) matching halves of OIM inverse pole figure map (loading direction); (c) matching halves of OIM grain boundary map (red lines represent twin boundaries, blue lines represent random large angle boundaries.) and (d) Schmid factors for 12 slip systems in twin1 and matrix 2 within the crack initiation grain of the second sectioned sample as shown in Figure 5.4 (b). ($\sigma_{\max} = 600\text{MPa}$, $N_f = 1.90 \times 10^7$ cycles, 593°C).	117
Figure 5. 5	Observation of internal non-fatal fatigue crack: (a) the position of internal non-fatal fatigue crack; (b) crystallography of the fatigue crack path; (c) inverse pole figure map (loading direction) and (d) grain boundary map overlapped by image quality map (Blue lines represent random grain boundaries, red lines represent $\Sigma 3$ twin boundaries.) ($\sigma_{\max} = 760\text{ MPa}$, $N_f = 5.9 \times 10^5$ cycles, 593°C)	119
Figure 5. 6	Observation of deformation substructure: (a) cyclic strain localization and slip band formation on twin boundary step in a large grain and (b) formation of dislocations and stacking faults at the region close to a twin intersection ($\sigma_{\max} = 550\text{MPa}$, $N_f = 5.85 \times 10^8$ cycles, 593°C).	120
Figure 5. 7	TEM image of slip bands formed in the region close to a twin boundary ($\sigma_{\max} = 660\text{ MPa}$, $N_f = 3.44 \times 10^6$ cycles, 593°C).	121
Figure 5. 8	Twin/matrix model and twin boundary coordinate for the calculation of internal incompatibility stress at the region close to twin boundary: (a) twin/matrix model, (b) twin boundary coordinate determined by experiment results (superscript 1 represents the twin side, while superscript 2 represents the matrix side).	126
Figure 5. 9	The distribution of normalized internal incompatibility stress and Von Mises equivalent stress at the twin side within the bicrystal model as indicated in Fig. 5.8 (a): (a) $\Delta\sigma_{11}/\sigma_0$, (σ_0 is the uniaxial external loading stress) (b) $\Delta\sigma_{22}/\sigma_0$, (c) $\Delta\sigma_{12}/\sigma_0$, (d) $\Delta\sigma_{eq}/\sigma_0$ (+ indicates the positions of four $\langle 111 \rangle$ directions, and \square indicates the positions of three $\langle 001 \rangle$ directions).	128
Figure 5. 10	Metallographic serial sectioning to collect the crystallographic orientations of neighborhood grains associated with fatigue crack initiation site, (a) Positions of serial sectioning planes, (b) an example	

	of serial sectioning plane ($\sigma_{\max} = 600\text{MPa}$, $N_f = 1.90 \times 10^7$ cycles, 593°C).	130
Figure 5. 11	Inverse pole figure map collected at four serial sectioning positions	131
Figure 5. 12	Crystallographic orientation of neighbor grains at the fatigue crack initiation site: (a) SEM image of fatigue crack initiation site, (b) crystallographic orientation of neighbor grain at crack initiation site and (c) contour plot of Schmid factor and crystallographic orientation of neighbor grains ($\sigma_{\max} = 600\text{MPa}$, $N_f = 1.90 \times 10^7$ cycles, 593°C).	132
Figure 5. 13	Metallographic sectioning through neighbor large grain: (a) top view of fatigue crack initiation site after sectioning and (b) side view of serial sectioning plane ($\sigma_{\max} = 600\text{MPa}$, $N_f = 3.16 \times 10^6$ cycles, 593°C).	133
Figure 5. 14	Crystallographic orientations of fatigue crack initiation grain and the neighbor large grain: (a) inverse pole figure map; (b) grain boundary map and (c) pole figure showing the orientation relationship between crack initiation grain and neighbor large grain, the grid lines are of 15 degrees ($\sigma_{\max} = 600\text{MPa}$, $N_f = 3.16 \times 10^6$ cycles, 593°C).	134
Figure 5. 15	Surface oxidation layer formed on fatigue specimens at elevated temperature ($\sigma_{\max} = 660\text{MPa}$, $N_f = 1.48 \times 10^7$ cycles, 593°C).	135
Figure 6. 1	Geometry and dimensions of cylindrical ultrasonic fatigue specimens with machined flat areas (all dimensions are in mm).	138
Figure 6. 2	S-N data of room-temperature fatigue testing results as compared with elevated temperature testing results.	140
Figure 6. 3	SEM image of the fatal fatigue on the surface of the fatigue specimen tested at $\sigma_{\max} = 720\text{MPa}$	141
Figure 6. 4	Fracture surface of the failed fatigue specimen: (a) top view of fracture surface (low magnification); (b) top view of the fracture surface (high magnification); (c) side view of the fracture of the tilted specimen, (low magnification) and (d) side view of the fracture surface of the tilted specimen (high magnification). ($\sigma_{\max} = 720\text{MPa}$, $N_f = 1.92 \times 10^5$ cycles, 20°C).	142
Figure 6. 5	Detailed features of the fatigue crack initiation site: (a) low magnification SEM image of the crack initiation site; (b) high magnification SEM image of the crack initiation site; (c) striations at the crack initiation site and (d) enlarged view of the dashed square area in Figure 6.5 (c) ($\sigma_{\max} = 720\text{MPa}$, $N_f = 1.92 \times 10^5$ cycles, 20°C).	143
Figure 6. 6	Features of the fatigue crack initiation grain on the specimen surface: (a) and (b) low magnification images of the fatigue crack initiation grain, (c) and (d) high magnification images of microcracks or slip bands formed within the fatigue crack initiation grain ($\sigma_{\max} = 720\text{MPa}$, $N_f = 1.92 \times 10^5$ cycles, 20°C).	144

Figure 6. 7	EBSD characterization of the fatigue crack initiation grain: (a) inverse pole figure map; (b) grain boundary map (red lines - Σ 3 twin boundaries, blue lines - random large angle grain boundary, yellow – other Σ grain boundaries and (c) enlarged view of the highlighted area in Figure 6.7 (b) (σ_{\max} =720MPa, N_f = 1.92×10^5 cycles, 20°C).	145
Figure 6. 8	The positions of selected microcracks subjected to EBSD investigation (σ_{\max} = 640MPa, N_f = 2.97×10^5 cycles).	146
Figure 6. 9	SEM images of microcracks: (a) Microcracks and their neighborhood microstructure; (b),(c) and (d) detailed features of microcrack within the fatigue crack initiation grain (σ_{\max} =640MPa, N_f = 2.97×10^5 cycles, 20°C).	147
Figure 6. 10	Microcrack initiated at the region close to a Σ 3 coherent twin boundary: (a) SEM image of fatigue crack initiation site; (b) SEM image of region close to the microcrack; (c) Inverse pole figure of fatigue crack initiation site; (d) grain boundary map overlaid by SEM image; (e) reconstructed $\{111\}$ twin plane on grain boundary map over-layed with the image quality map (white lines represent reconstructed $\{111\}$ twin boundaries, blue lines represent large angle grain boundaries, including Σ 3 twin boundaries) and (f) Kernel misorientation map overlaid by grain boundary map (σ_{\max} =640MPa, N_f = 2.97×10^5 cycles, 20°C).	150
Figure 6. 11	SEM image of a microcrack: (a) crack initiation site and (b) detail features of the microcrack. (σ_{\max} =640MPa, N_f = 2.97×10^5 cycles, 20°C).	151
Figure 6. 12	EBSD characterization of a microcrack formed at the region close to a Σ 3 twin boundary: (a) inverse pole figure map of the crack initiation site; (b) grain boundary map; (c) reconstructed $60^\circ \langle 111 \rangle$ twin boundary and grain boundary map overlaid by SEM image, (green lines represent reconstructed $\{111\}$ twin boundaries) and (d) detail structure of the Σ 3 Triple junction (σ_{\max} =640MPa, N_f = 2.97×10^5 cycles, 20°C)..	152
Figure 6. 13	Fatigue crack initiated at the region close to Σ 3s twin boundary: (a) inverse pole figure of the crack initiation site; (b) grain boundary map overlaid by image quality map of the crack initiation site; (c) Σ 3 grain boundaries within the fatigue crack initiation grain (Red lines- Σ 3 boundaries, yellow lines - Σ 9 boundaries, blue lines-random grain boundaries) and (d) reconstructed $\{111\}$ twin boundary and grain boundary map overlaid with the image quality map (white line is the reconstructed $\{111\}$ twin boundary). (σ_{\max} =640MPa, N_f = 2.97×10^5 cycles, 20°C).	154

Figure 6. 14	SEM images of small crack: (a) small crack; (b) crack initiation grain of the small fatigue crack and (c) region close to the small pore ($\sigma_{\max} = 680\text{MPa}$, $N_f = 1.85 \times 10^5$ cycles, 20°C).....	157
Figure 6. 15	EBSD characterization of small crack: (a) SEM image of small crack; (b) inverse pole figure map of small crack; (c) grain boundary map over layered by image quality map; and (d) Kernel misorientation map ($\sigma_{\max} = 680\text{MPa}$, $N_f = 1.85 \times 10^5$ cycles, 20°C).	158
Figure 6. 16	Effects of twin boundary step and tips on cyclic strain localization: (a) SEM image of crack initiation grain; (b) SEM images of the microcrack and slip bands within the fatigue crack initiation grain (Different slip bands are abbreviated and marked on the figure); (c) SEM image of the crack initiation grain captured at a tilting angle of 70° degrees (The Schmid factor for different slip system abbreviated as SF was shown in the figure) and (d) grain boundary map overlaid with image quality map of the fatigue crack initiation grain (red lines - $\Sigma 3$ twin boundaries, blue lines- random grain boundaries, black arrows indicate the positions of twin boundary step) ($\sigma_{\max} = 680\text{MPa}$, $N_f = 1.85 \times 10^5$ cycles, 20°C).	159
Figure 6. 17	The analysis of coherence of $\Sigma 3$ twin boundaries.(red lines - $\Sigma 3$ twin boundaries, blue lines - the reconstructed $60^\circ \langle 111 \rangle$ twin boundaries, the incoherent part on the $\Sigma 3$ twin boundary was pointed out by black arrows). ($\sigma_{\max} = 680\text{MPa}$, $N_f = 1.85 \times 10^5$ cycles, 20°C).	160
Figure 6. 18	SEM image of a microcrack: (a) low magnification and (b) high magnification ($\sigma_{\max} = 680\text{MPa}$, $N_f = 1.85 \times 10^5$ cycles, 20°C).	161
Figure 6. 19	Neighborhood effects on fatigue crack initiation and small crack growth: (a) inverse pole figure map of the fatigue crack initiation site and (b) grain boundary map, (blue lines - random large angle grain boundaries, red lines - $\Sigma 3$ twin boundaries, green lines - small angle grain boundaries whose misorientation angles are smaller than 15 degrees.). ($\sigma_{\max} = 680\text{MPa}$, $N_f = 1.85 \times 10^5$ cycles, 20°C).....	162
Figure 6. 20	Orientation distribution of microcrack initiation grains: (a) orientation distribution and (b) Schmid factor contour plot.	163
Figure 6. 21	Geometry of the slip plane parallel to a $\Sigma 3$ twin boundary: (a) illustration of geometry of slip plane and slip direction with respect to specimen surface and (b) two types of shearing deformation in case for the angle relationship between slip direction and the twin boundary trace.	165
Figure 6. 22	The angle between the slip direction (with highest resolved shear stress on the slip plane parallel to twin boundary) and the twin boundary trace.	167

Figure 6. 23	Illustration of twin-matrix model used for calculation additional resolved shear stress on slip plane parallel to twin boundary.	169
Figure 6. 24	Schmid factor on slip systems in twin and matrix within a fatigue crack initiation grain: (a) inverse pole figure map of the crack initiation grain; (b) Schmid factor on 12 slip system in the matrix and (c) Schmid factor of the 12 slip systems in the twin side.	171
Figure 6. 25	The effects of twin boundary on the resolved shear on slip system with the highest Schmid factor on the slip plane parallel to the twin boundary.	172
Figure 6. 26	Illustration of fatigue crack initiation process at room temperature.....	173
Figure 7. 1	The change of nonlinear parameter with fatigue loading cycle in René 88DT tested at room temperature under fully reversed loading. (Image is courtesy of Dr Anish Kumar).	182

List of Tables

Table 3. 1	Nominal composition of nickel-based superalloy René 88 DT (wt%).	45
Table 3. 2	Comparison between experimental measurement and analytical calculation.	71
Table 4. 1	Comparison of experimental measurement of spatial orientation of flat facet using SEM stereo images of different magnifications.	101
Table 5. 1	Notation for 12 FCC slip systems [106].	116
Table 5. 2	Twin boundary incompatibility stresses on the side 2 near twin boundaries in crack initiation grains.	127
Table 6. 1	Stress-fatigue life of samples tested at room temperature (R = -1).	139
Table 6. 2	Effects of twin boundary incompatibility stresses on the resolved shear stress on slip system parallel to twin boundary.	172

List of Appendices

Appendix 1	René 88 DT Ultrasonic Fatigue Specimen Drawing.....	184
Appendix 2	S-N Data of René 88 DT at 593°C	185

Chapter 1

Introduction

1.1 Research background and objectives

Nickel-based superalloys have been widely used in the aerospace and power-generation industries for over 50 years, owing to their excellent combination of mechanical and chemical properties at elevated temperature [1]. The increasing demand for more efficient and powerful turbine engines constantly drives the need for modifying or developing new generations of nickel-based superalloys. More recent development of physically-based materials behavior models has become a priority. Predictive models could not only reduce the time needed to develop new alloys but also could extend the service life of superalloy components in current applications.

Among all the properties of polycrystalline nickel-base superalloys, fatigue is one of the most important, often limiting the overall service life. Fatigue behavior of nickel-based superalloys depends on both intrinsic microstructure heterogeneities and extrinsic service conditions. Examples of intrinsic microstructural heterogeneities include: inclusions such as carbides, pores, grain orientation, grain size inhomogeneity and special grain boundaries. Service conditions include: temperature, load ratio, maximum loading stress, testing frequency and environment.

The total fatigue life of metals and alloys is composed of three parts: an initiation life required to develop crack precursors and to nucleate a small crack, a small crack propagation life, and a large crack propagation life [2]. In general, low cycle fatigue is associated with high loading stress and relatively few testing cycles ($< 10^5$), whereas very high cycle fatigue (VHCF) is associated with very low loading stress and fatigue loading cycle beyond 10^7 cycles. The conventional fatigue limit assumes a constant minimum fatigue strength which normally is equal to the fatigue strength at 10^6 or 10^7 cycles. Below this fatigue limit, a material is thought to have an infinite life. Based on the observations that an endurance limit does not exist for most engineering materials, the Air Force manual, Engine Structural Integrity (ENSIP) handbook [3], requires that all engine parts should have a minimum HCF life of 10^9 cycles.

Most previous VHCF research has focused on the fatigue behavior of materials with a relatively high density of defects, such as inclusions or solidification induced porosity. Until recently, little research has been dedicated to understanding the VHCF behavior of engineering alloys with a minimal content of defects, such as nickel-based superalloys. Microstructure heterogeneities in this group of materials are expected to be the main factors controlling VHCF behavior.

Damage-tolerant design methodology has achieved great success in predicting and preventing fatigue failure by crack propagation. This method basically assumes that a crack exists in the component from the beginning of service life. The lifetime of the component is estimated by integrating the fatigue crack propagation behavior over the cyclic loading history. However, in the very high cycle regime, most of the fatigue life of the component is spent in fatigue crack initiation [4]. Conventional fatigue life

methodologies are, therefore, not effective in accurately predicting very high cycle fatigue life. Additionally, the uncertainty of life prediction increases as the fatigue life shifts from low cycle regime to very high cycle regime.

Due to high costs and very long times consumed, it is impractical to use conventional fatigue test methods to study the fatigue behavior of materials in very high cycle regime. In recent years, there has been world-wide interest in the study and development of ultrasonic fatigue test instrumentation and methods. With ultrasonic fatigue testing equipment operating at 20 KHz, a large number of very high cycle fatigue datasets can be generated in a very short time. With the development of this technique, very high cycle fatigue crack initiation mechanisms and microstructural small crack growth behavior can be studied in a reasonable time period. Ultrasonic fatigue also provides a method to assess potential frequency effects on turbine engine components subjected to vibratory loading in the kilohertz frequency regime.

Therefore, studying very high cycle fatigue behavior of nickel-base superalloys using ultrasonic fatigue instruments is of significant theoretical and practical interest. A thorough understanding of fatigue crack initiation and the role of microstructure heterogeneities in fatigue crack initiation is therefore crucial for building a physically-based life prediction models for very high cycle fatigue lifetime. A sound coupling of microstructure variation with fatigue life variability is required in order to reduce the uncertainty of fatigue life prediction.

In this research, a polycrystalline nickel-based superalloy René 88 DT was selected as the model material to study VHCF behavior using ultrasonic fatigue techniques. The primary objectives of this research are as follows:

To examine the fatigue behavior of René 88 DT at elevated temperature and room temperature in high cycle and very high cycle regime using ultrasonic fatigue techniques.

To quantitatively characterize critical microstructure features that control cyclic strain localization and fatigue crack initiation in this alloy at both elevated temperature and room temperature.

To identify the role of critical microstructure features in fatigue crack initiation.

1.2 Scope of this work

In Chapter 2, relevant literature addressing fatigue behavior of nickel-based superalloys is reviewed. Chapter 3 presents general microstructure features of René 88 DT and experimental techniques used in this study. Chapter 4 presents fatigue behavior of René 88 DT at elevated temperature and quantitative characterization of the crystallographic fatigue crack initiation sites. In Chapter 5, critical microstructure features associated with fatigue crack initiation and early small crack growth at elevated temperature are analyzed. Chapter 6 presents fatigue behavior of René 88 DT at room temperature. Microcrack initiation sites at room temperature were quantitatively characterized. Finally, in Chapter 7, the major conclusions obtained in this work are given, along with recommendations for future research.

Chapter 2

Literature Review

2.1 Introduction to nickel-based superalloys

Nickel-based superalloys are an important class of high temperature materials based on the Ni-Al system, with an array of higher order alloying additions. These alloys have been widely used to fabricate the hottest sections in turbine engines in aircraft industries and land-based power generation industries due to their excellent combination of mechanical and chemical properties at high temperatures [1]. Nickel-based superalloys can be grouped into two types: cast superalloys including cast polycrystalline and single crystal alloys and wrought polycrystalline nickel-based superalloys. Single crystal superalloys with excellent creep resistance are mainly used in blades in turbine engines, while polycrystalline nickel-based superalloys with good fatigue resistance are mainly used to manufacture turbine disks. Figure 2.1 illustrates the structure of a Rolls-Royce Trent 800 engine and nickel-based superalloy engine components are highlighted in red. Figure 2.2 shows the relationship of specific strength versus application temperature for nickel-based superalloys as compared with other structural materials.

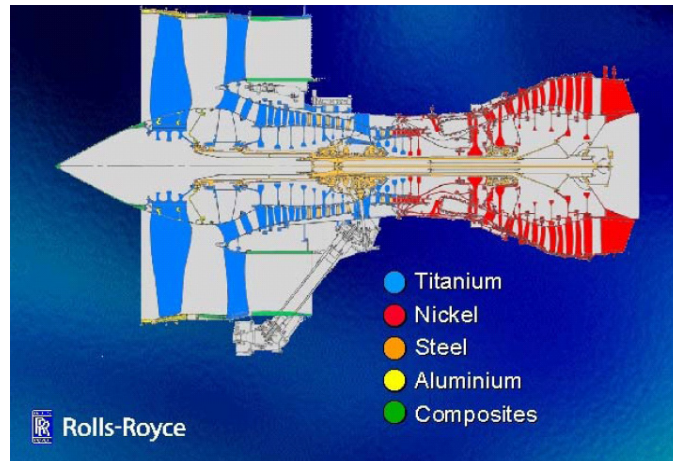


Figure 2.1 Illustration of Rolls-Royce Trent 800 engine and main structural materials used in the engine (image courtesy of Rolls-Royce).

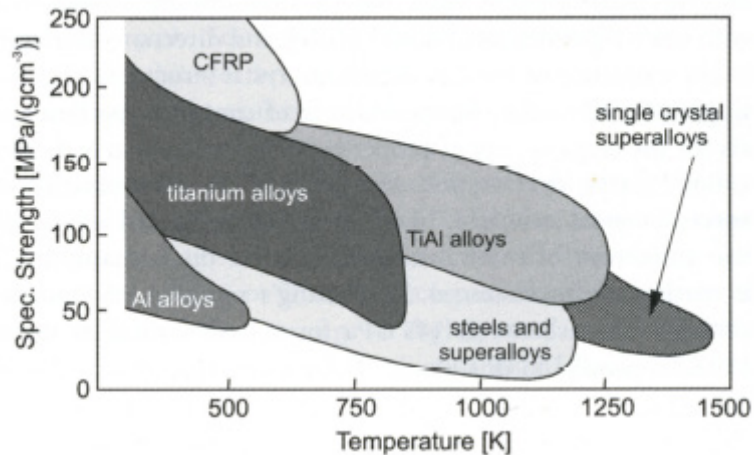


Figure 2.2 Specific strength versus application temperature for selected structural engineering materials [5].

Figure 2.3 (a) shows the Ni-Al binary phase diagram [6]. With the addition of Al, precipitation of the γ' phase (Ni_3Al) occurs. This L_{12} intermetallic is the primary strengthening phase in nickel-based superalloys. As shown in the phase diagram, the γ' phase is formed at about 1383°C through a peritectic reaction between the disordered nickel rich solid solution and the liquid. Strengthening is achieved by the precipitation of a high volume fraction, coherent, ordered intermetallic γ' phase with L_{12} crystal in the

disordered FCC matrix. Figure 2.3 (b) shows the crystal structure of these two phases. The γ' phase and γ matrix have a cubic-cubic relationship [7]:

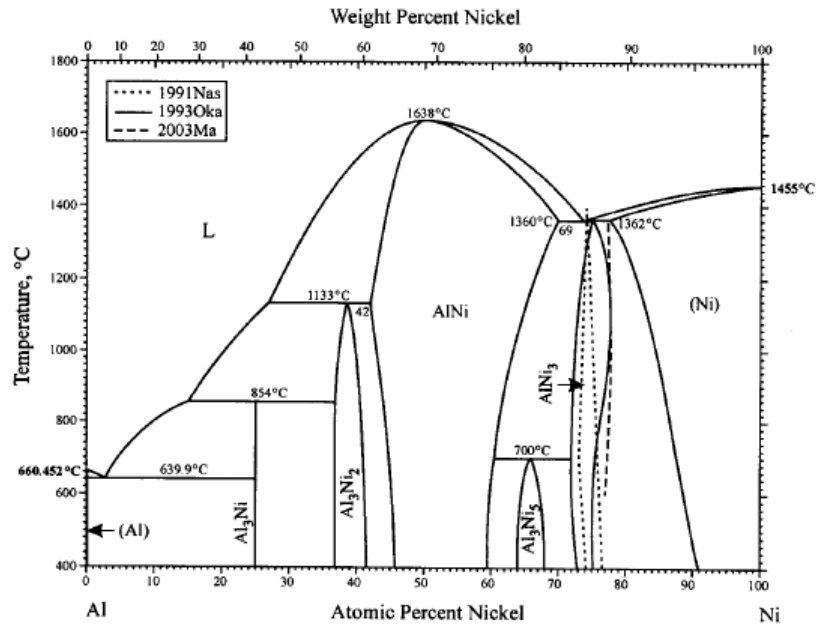
$$(001)_{\gamma} // (001)_{\gamma'}$$

$$\langle 010 \rangle_{\gamma} // \langle 010 \rangle_{\gamma'}$$

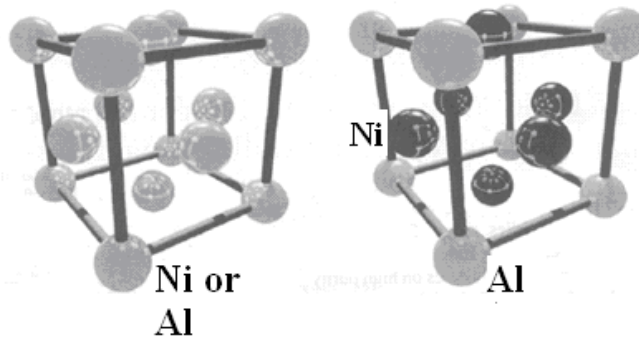
Figure 2.4 shows the morphology of the γ' phase for the polycrystalline nickel-based superalloy IN100 [8].

Minor phases including carbides and borides are also present in nickel-based superalloys. Figure 2.5 shows blocky MC carbides within the microstructure a single crystal nickel-based superalloy [9].

Polycrystalline nickel-based superalloys can be produced by casting/wrought processes or by powder metallurgy processes. For cast-wrought superalloys, the metallurgical processing mainly uses the conventional ingot metallurgy techniques, normally involving vacuum induction melting and electro-slag remelting or vacuum arc remelting, followed by extrusion and/or forging [7,10]. The main disadvantage of the ingot approach is the high degree of segregation of alloying elements in the microstructure, which is deleterious to the properties. Normally, an annealing process is required for cast ingots to homogenize the composition. Cast-wrought processing is mainly used to produce nickel-based superalloys with relatively low content of alloying elements. For polycrystalline nickel-based superalloys containing high fraction of alloying elements such as René 95 and René 88 DT, powder metallurgy methods are needed.



(a)



(b)

Figure 2.3 Primary phases within nickel-based superalloys: (a) Ni-Al binary phase diagram [6] and (b) crystal structure of γ phase and γ' phase.

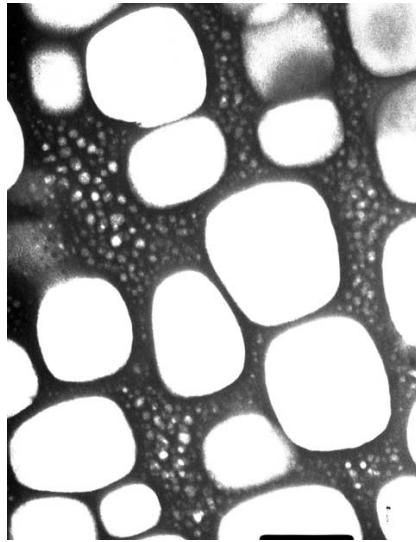


Figure 2.4 Morphology of secondary and tertiary γ' precipitates in IN100, a typical powder processed polycrystalline nickel-based superalloy IN100 [8].

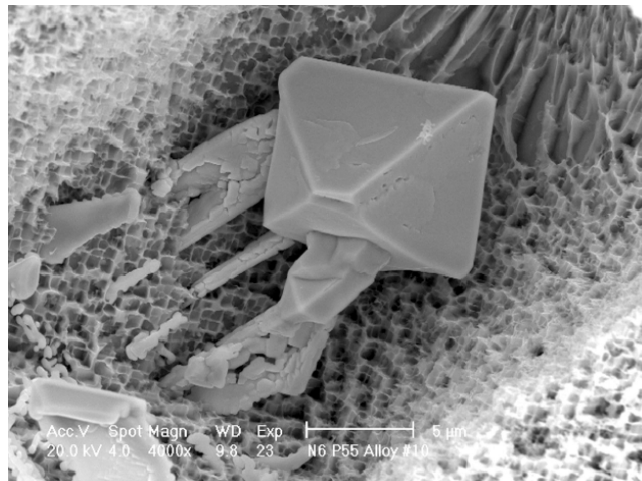


Figure 2.5 SEM image of blocky MC carbides in a nickel-based superalloy revealed by excessive chemical etching [9].

The general steps involved in powder metallurgy processing of superalloys are illustrated in Figure 2.6 [7]. Similar to conventional cast-wrought processing, vacuum induction melting is used to produce superalloy ingots. These ingots are re-melted and the melting superalloys are then atomized to produce superalloy powders which are screened

to remove large powder particles and nonmetallic inclusions. Then the sieved powders are canned, degassed and sealed into stainless cans. The canned superalloy powders are subsequently subjected to hot isostatic pressing, followed by general thermal mechanical processing such as extrusion and forging as shown in Figure 2.6. Powder metallurgy processing techniques can significantly reduce both the segregation of alloying elements and the size and amount of metallurgical defects.

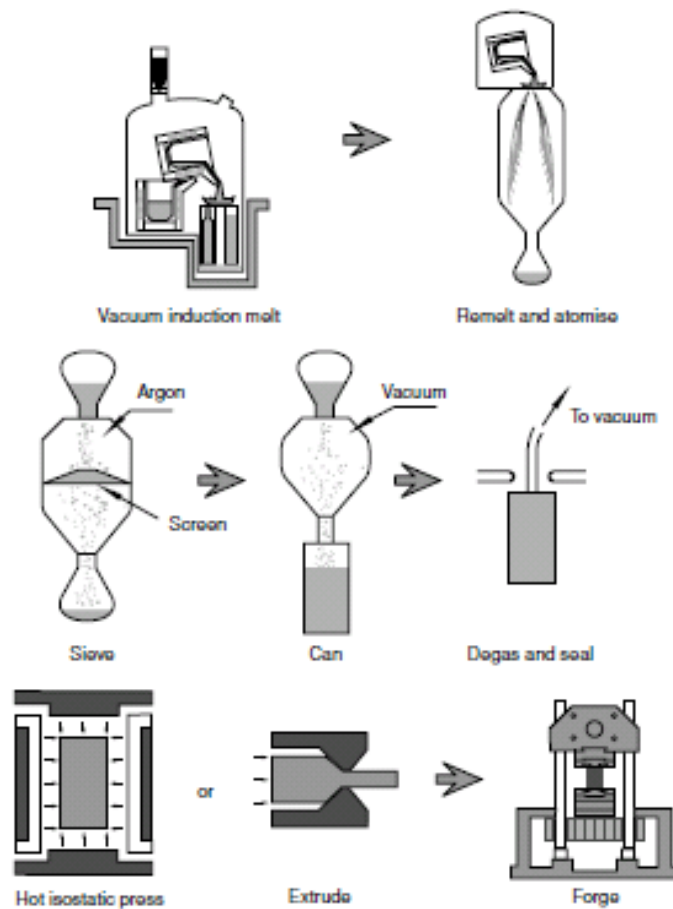


Figure 2.6 Techniques involved in powder metallurgy processing of superalloys [7].

Strengthening of polycrystalline nickel-based superalloys can be achieved by solid-solution strengthening, precipitation strengthening and grain boundary

strengthening or grain size strengthening [8], among which precipitation strengthening is the most important. The magnitude of precipitation strengthening depends on the size, morphology, and volume fraction of the Ni_3Al phase, as well as the degree of interface misfit between the coherent γ' precipitates and the matrix. Fundamentally, the strengthening of the γ' phase is associated with the anomalous flow stress behavior of Ni_3Al [11-13]. As shown in Figure 2.7, the flow stress of Ni_3Al increases with increasing temperature and is sensitive to deformation strain rate. This flow behavior is different from other engineering materials where flow stress decreases with increasing temperature. The anomalous flow behavior is thought to be due to the immobilization of thermally activated cross-slip of dislocations via a Kear-Wilsdorf locking mechanism [14].

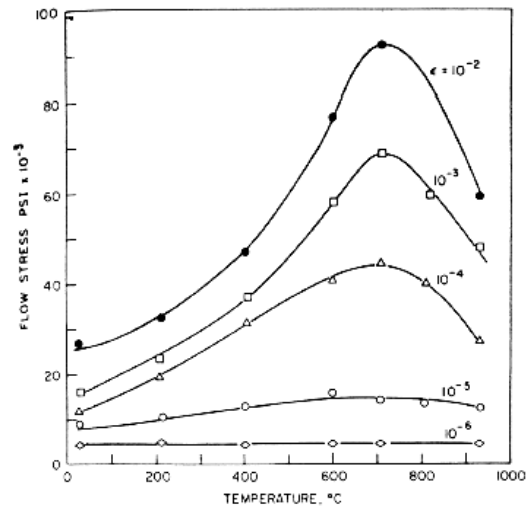


Figure 2.7 The anomalous flow stress behavior of Ni_3Al as function of temperature and strain rate [12].

2.2 Fatigue crack initiation mechanism

2.2.1 Fundamental theories of fatigue crack initiation

In service, superalloy components are subjected to cyclic loading and fatigue performance is one of the key properties that limit service life. Cyclic strain localization and fatigue crack initiation are closely related to the irreversible slip of dislocations under cyclic loading. This irreversible slip comes from the fact that the displacement imparted by the motion of dislocations in the forward loading cycle is not completely recovered in the reverse loading cycle [15]. A parameter of slip irreversibility can be used to quantify the irreversible dislocation slip. The value of slip irreversibility is in the range of 0 to 1. There are many factors that can influence dislocation slip, thus influencing slip irreversibility. In general such factors can be grouped into two types. The first type of factors is related to the microstructure features, such as grain boundaries and the morphology, size and distribution of precipitates. These factors can be labeled as intrinsic or internal variables. The second type includes applied fatigue testing conditions such as stress amplitude, temperature, cyclic frequency and environmental effects. These factors can be labeled as external variables. Therefore, slip irreversibility is a function of these external and internal or extrinsic variables. Apparently, it is difficult to include all variables into a quantitative characterization of slip irreversibility. In practice, most current definitions of slip irreversibility are based on the shear strain carried by the irreversible slip of dislocations [15-19]. Mughrabi [15] defines slip irreversibility as the ratio of irreversible plastic shear strain to the cumulative total plastic shear strain due to the irreversible slip of dislocations under cyclic loading.

The irreversible slip of dislocations will cause the development of an inhomogeneous distribution of plastic deformation (or cyclic strain localization) and the resulting local microstructure changes, leading to permanent fatigue damage. Among all microstructure changes, persistent slip band formation is the most important one and has been the subject of extensive studies [20-26]. Persistent slip bands can be defined as a local deformation zone that fulfills the following three conditions [26]: 1) there is a cyclic strain localization in the zone, 2) its dislocation structure differs from that in the surrounding matrix, 3) in single crystal and surface grains (if in polycrystals) the zone ends on the specimen surface in intrusions and extrusions. Extrusions are thin ribbons of metal extruded at the specimen surface from persistent slip bands under cyclic loading [27]. Figure 2.8 shows the morphology of persistent slip bands formed within a fatigued copper specimen. The dislocation density within persistent slip bands is very high compared to that of the surrounding matrix, indicating the inhomogeneity of cyclic deformation or cyclic strain localization. It can be seen that these persistent slip bands have a ladder dislocation structure. However, the specific morphology of persistent slip bands may depend on specific alloys and the associated testing conditions. Therefore, the ladder structure frequently observed in pure copper is not always observed in other alloys [15, 26]. Figure 2.9 shows the persistent slip band in single crystal nickel-based superalloy CMSX-4. The dislocation density within the persistent slip band is very high, while the dislocation density in the surrounding area is very low, indicating severe strain localization within the persistent slip band. It can be seen that the persistent slip band in this alloy does not have the typical ladder structure of PSB in copper as shown in Figure 2.8.

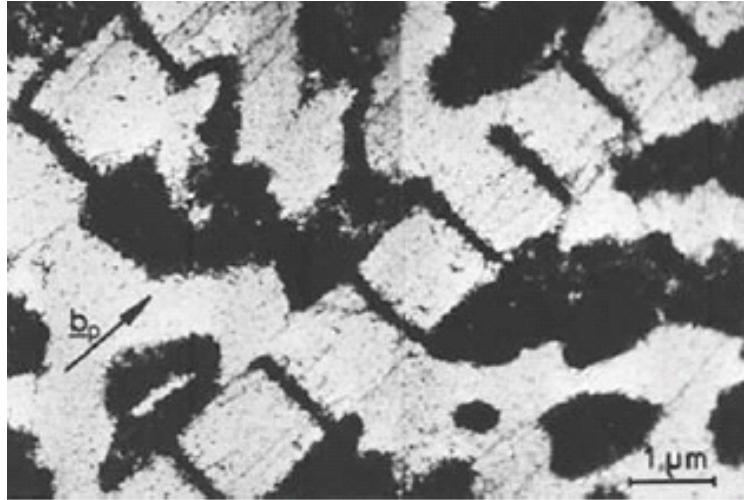


Figure 2.8 The morphology of persistent slip bands in fatigued copper [15].

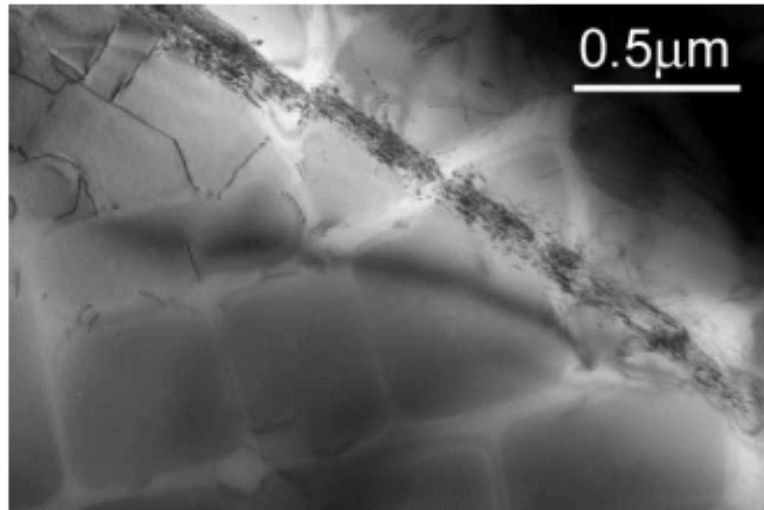


Figure 2.9 TEM image of persistent slip band in single crystal nickel-based superalloy CMSX-4 fatigued at 850 °C [26].

When persistent slip bands intersect specimen surfaces, dislocation slip within the persistent slip band can gradually roughen the specimen surface. This surface roughening process under cyclic loading, which is based on the Essmann-Gosele-Mughrabi model [22], is schematically illustrated in Figure 2.10. Figure 2.10 (a) shows the accumulation of dislocations at the interface between PSB and the matrix. Surface extrusions can be rapidly formed by emergence of the slip of these interfacial dislocations, as indicated in

Figure 2.10 (b). This rapidly formed surface extrusion is referred as a “static extrusion” whose formation process is purely mechanical and thus can occur at low temperatures. Figure 2.10 (c) shows the gradual surface roughening process due to random dislocation slip within the PSB. These surface extrusions can act as sources for microcrack initiation. Figure 2.11 shows the formation of extrusions on the surface of copper single crystal specimen. A microcrack was formed near the surface extrusions as shown in Figure 2.11.

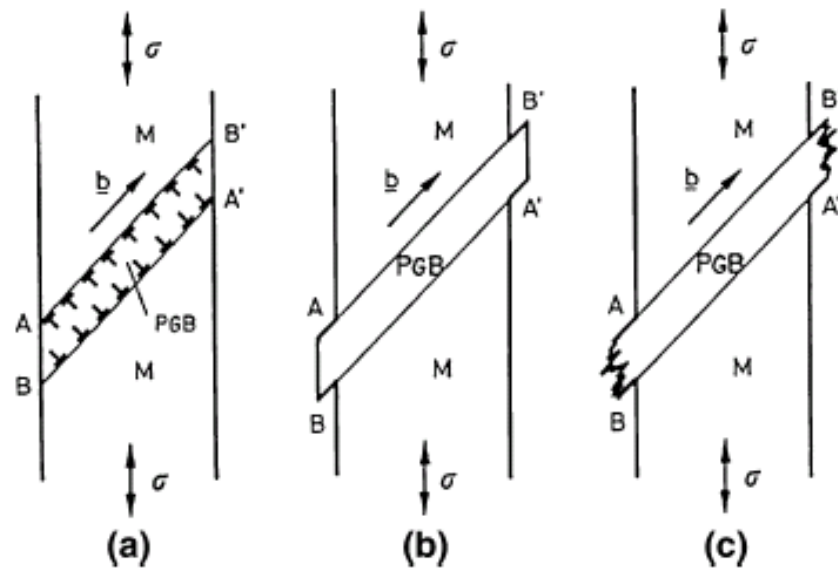


Figure 2.10 Illustration of surface roughening process due to dislocation slip within emerging PSB within a surface grain [28].

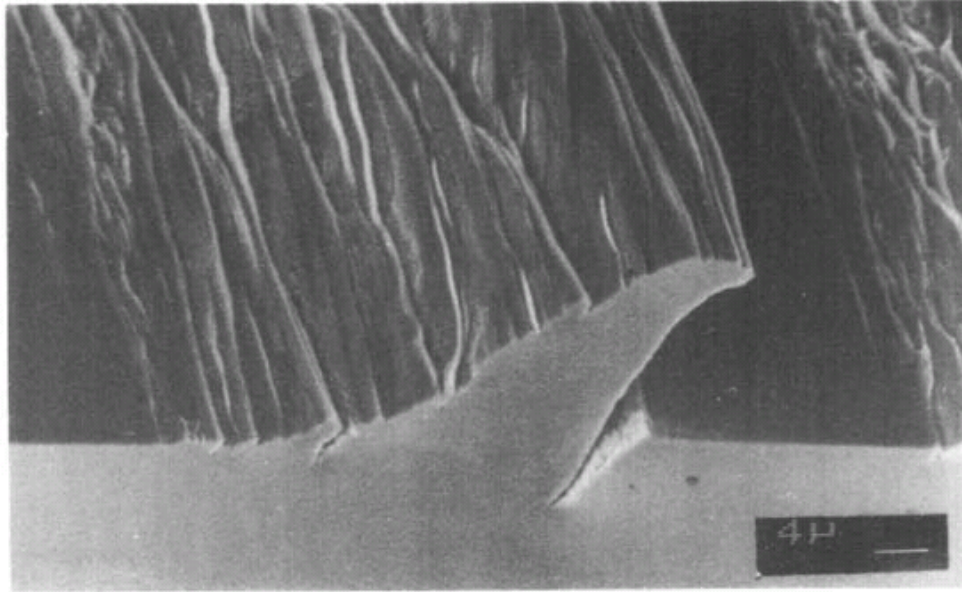


Figure 2.11 The formation of surface extrusions and microcrack on the surface of copper single crystal specimen [24].

2.2.2 Cyclic deformation modes in nickel-based superalloys

Cyclic deformation and the accumulation of fatigue damage in nickel-based superalloys are closely related to the operative deformation modes under testing conditions [29, 30].

At low temperature, precipitate shearing is the dominant deformation mode in nickel-based superalloy since thermally activated dislocation behavior such as cross slip is inhibited at low temperature. Dislocations are restricted to $\{111\}$ slip planes. Planar slip bands with a high density of dislocations and inhomogeneous cyclic deformation have been frequently observed in nickel-based superalloys [31-34]. Figure 2.12 shows the deformation substructure of a polycrystalline nickel-based superalloy Nimonic PE16 fatigued at room temperature [31]. The γ' precipitates have been heavily sheared by dislocations within the slip bands, resulting in offsets that are similar in magnitude to the

precipitate diameter. Similar results were found in nickel-based superalloy Inconel 792-5A cycled at room temperature [32]. The microstructure of Inconel 792-5A contains duplex γ' precipitates with average sizes of 0.2 μm and 0.6 μm . As shown in Figure 2.13, planar slip bands are parallel to $\{111\}$ slip planes and have high density of dislocations and cut through both γ matrix and γ' precipitates. The slip bands are separated by regions with low dislocation density, forming a highly inhomogeneous deformation substructure.

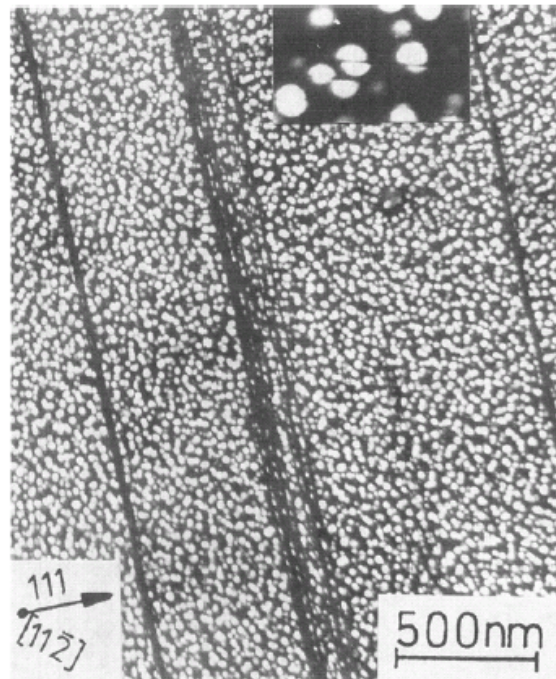


Figure 2.12 TEM image showing shearing of precipitates in nickel-based superalloy Nimonic PE 16 at room temperature [31].

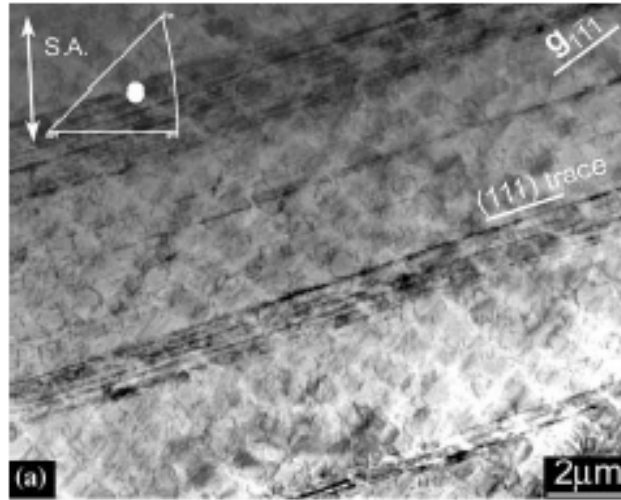


Figure 2.13 TEM micrographs of cyclic deformation substructures within nickel-based superalloy IN 792-5A at room temperature [32].

In studying the effects of microstructure on fatigue deformation behavior of nickel-based superalloy Wasploy [34], two kinds of microstructure were obtained using different heat treatment processes: microstructure with coarse γ grains (125 μm) and fine γ' precipitates (50-80nm) and microstructure with fine γ grains (16 μm) and coarse γ' precipitates (300nm-90nm). It was found that for microstructure with coarse γ grains and small γ' precipitates, the dominant deformation mode is precipitate shearing and cyclic deformation is localized within planar slip bands, while in the microstructure with fine γ grains and large γ' precipitates, the main deformation mode was attributed to Orowan looping, as indicated in Figure 2.14.

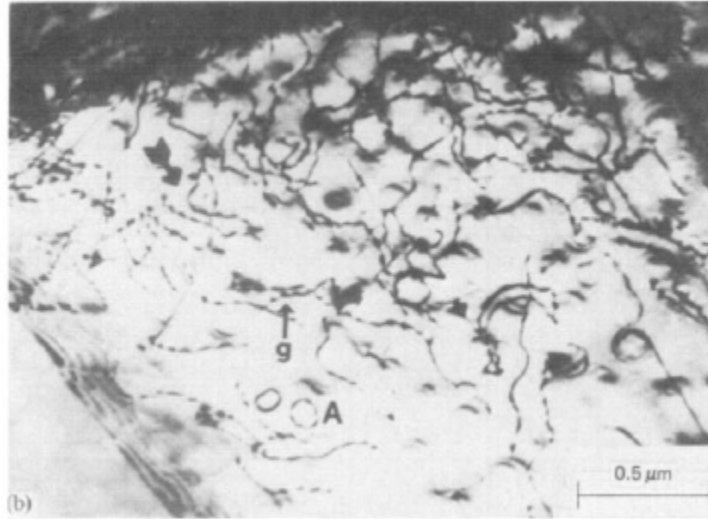
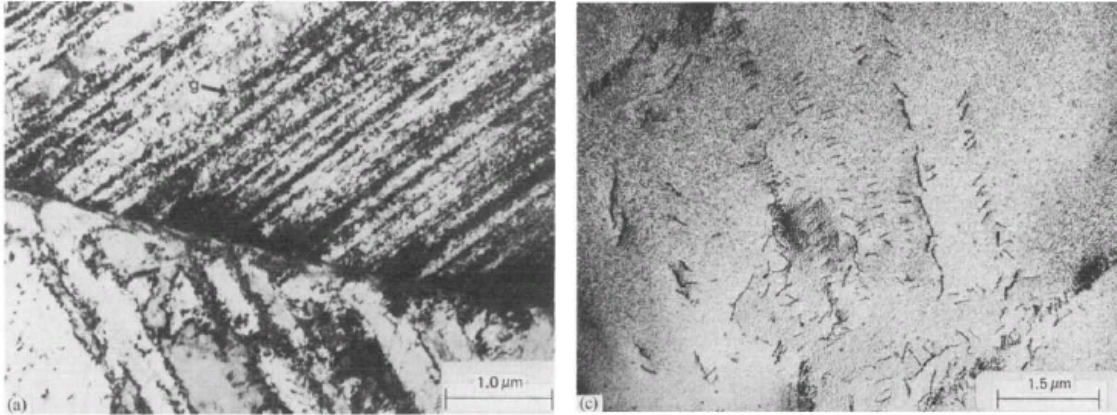


Figure 2.14 TEM micrograph showing dislocation looping in Waspalloy with a microstructure of fine γ grain and large γ' precipitates fatigued at room temperature [34].

At higher temperatures, thermally activated dislocation processes such as cross-slip can operate. It can be expected that at high temperature dislocations became more mobile and cyclic deformation becomes more homogenous as compared to the behavior at lower temperature. Figure 2.15 shows the deformation substructures of Waspalloy cycled at different temperatures [34]. It can be seen that although planar slip bands and precipitate shearing are observed at both 500°C and 800°C, the densities of planar slip bands and dislocations within these slip bands at 800°C are much lower than at 500°C.



(a)

(b)

Figure 2.15 Deformation substructure in nickel-based superalloy Wasploy: (a) fatigued at 500 °C and (b) fatigued at 800 ° C [34].

Cyclic frequency has a large effect on the cyclic deformation behavior and fatigue life of nickel-based superalloys. In studying fatigue behavior of the nickel-based superalloy Udimet 700 at 760°C [35], it was found that fatigue life was increase 100 times when the testing frequency was increased from 0.033 Hz to 10 Hz. It was reasoned that the increase in cyclic frequency can reduce the creep damage accumulation at high temperatures, thus contributing to the increase of fatigue life. However, with the further increase of testing frequency to 1000 Hz, fatigue life was significantly reduced. It was thought that the increase of testing frequency has a similar effect as decreasing testing temperature, which favors inhomogenous cyclic deformation and cyclic strain localization [35]. Deformation strain rate increase with the increasing test frequency. The frequency effects on cyclic deformation in nickel-based superalloy can be explained in terms of the anomalous flow behavior of γ' precipitates. As shown in Figure 2.7, with the increase of strain rate, the flow stress of γ' Ni₃Al phase increases. Thus the obstacles to shearing deformation of γ' precipitates in nickel-based superalloys increase, leading to

more inhomogeneous cyclic deformation and strain localization. This strain rate dependent flow behavior of Ni_3Al is affected by temperature. The influences of strain rate on flow stress at different temperatures are shown in Figure 2.16. At lower temperature, the flow stress of Ni_3Al phase is less sensitive to strain rate, while at elevated temperature, the flow stress is more sensitive to deformation strain rate. Therefore, it can be expected that test frequency has less effect on cyclic deformation behavior of nickel-based superalloys at lower temperature such as room temperature than at elevated temperature.

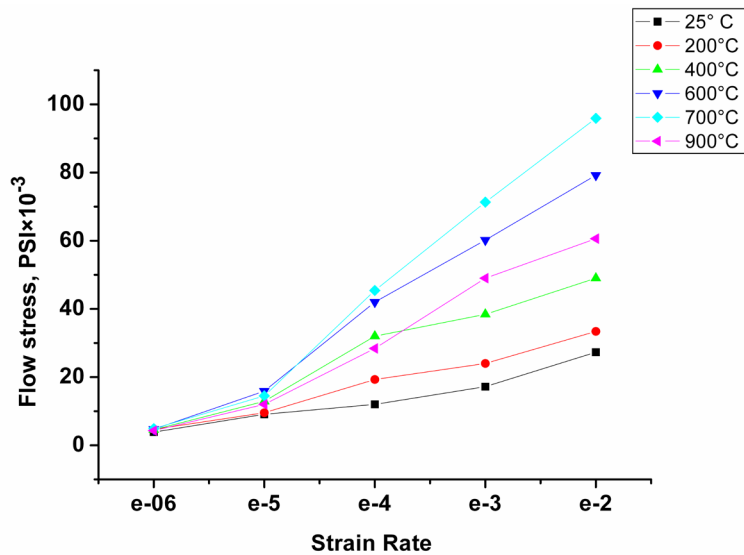


Figure 2.16 Effects of strain rate on the flow stress of Ni_3Al (Data are cited from the reference [12]).

2.2.3 Microstructure effects on fatigue crack initiation in polycrystalline nickel-based superalloys

In nickel-based superalloys, fatigue cracks not only can initiate from metallurgical defects such as pores and inclusions [36-38], but also can initiate from microstructure via cyclic strain localization. Due to the limitations of materials processing techniques, it is very difficult to obtain a completely uniform microstructure. Therefore, the

microstructure of most engineering alloys may contain microstructure inhomogeneities such as grain size, microtexture and grain boundary character. These microstructural inhomogeneities can cause local stress concentrations that contribute to cyclic strain localization. In the regime of low cycle fatigue, under high loading stresses, the majority of grains can be plastically deformed. The effect of such microstructure heterogeneities would, therefore, be expected to be very small. However, in the very high cycle regime, under very low loading stresses, only a small fraction of grains is actively involved in the fatigue deformation process. The deformation then becomes much more localized [39]. This effect of microstructure heterogeneity on fatigue crack initiation and fatigue life is expected to be more prominent in the regime of very high cycle fatigue where deformation is primarily elastic over most of the material volume.

At room temperature, in nickel-base superalloys, dislocations are restricted to $\{111\}$ planes because cross-slip is difficult. Consequently, the initiation of fatigue cracks along slip bands has been frequently observed in superalloys at room temperature [40-45]. Shear stresses provide a driving force for motion of dislocations within the slip bands and produce cracking along such planes. This type of cracking along slip bands is termed as “stage I” cracking. These cracks are often associated with planes oriented approximately 45° to the load axis, which would have the maximum resolved shear component under uniaxial loading conditions.

Hornbogen and Verpoort [40] observed that planar dislocation slip caused slip steps at specimen surface in nickel-based superalloy Nimonic 80A. Such steps acted as stress concentrators and initiated cracking. They found that for a certain load, a defined critical slip step height was necessary to initiate a crack. In order to correlate the

likelihood of fatigue crack initiation with extrusion height, Risbet et al [18,41,42] quantitatively examined, using atomic force microscopy, the height of surface extrusions produced by cyclic strain localization in the nickel-based superalloy Waspaloy. Figure 2.17 shows AFM images of extrusions on Waspaloy specimen surface. No direct relationship between the maximum extrusion height and the likelihood of fatigue crack initiation was observed. However, extrusion height exceeds 50 nm within most fatigue crack-initiating grains [42]. The orientations of grains in which fatigue cracks initiated were determined using electron backscatter diffraction techniques. The grain with orientation close to $\langle 001 \rangle$ orientation were found be more susceptible to fatigue damage and fatigue crack initiation, as shown in Figure 2.18.

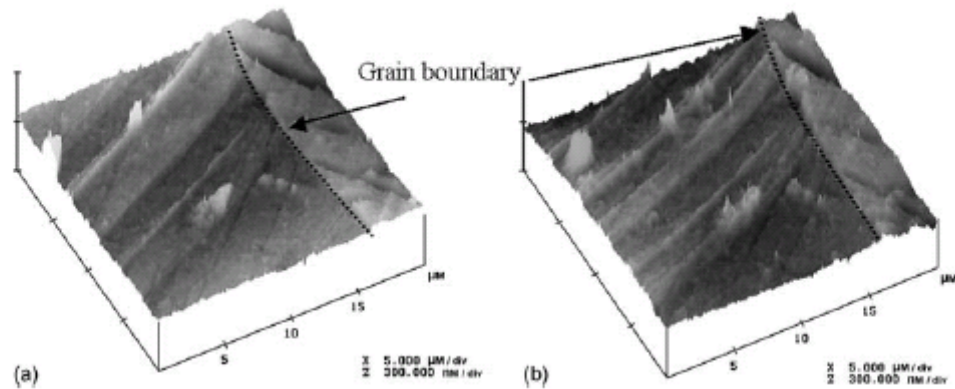


Figure 2.17 AFM images of extrusions on the surface of a Waspaloy specimen fatigued at room temperature [18].

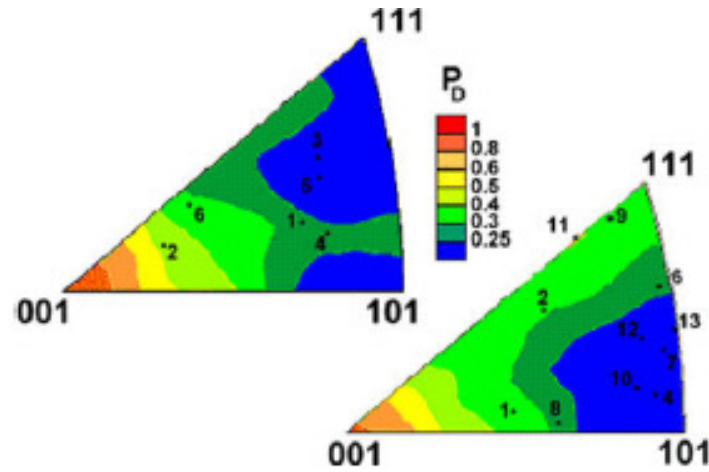


Figure 2.18 The probability of fatigue crack initiation as a function of orientation in the nickel-based superalloy Waspaloy cycled at room temperature [42].

Grain size plays an important role in fatigue behavior of polycrystalline nickel-based superalloys. Healy et al. [43, 44] found that at room temperature in Waspaloy, for $R = 0.1$ and $R = -1$ ($R = \sigma_{\max}/\sigma_{\min}$), fatigue crack nucleation in shallow notched specimens occurred predominantly at the specimen surface in large grains where slip bands were inclined between 30 and 60 degrees to the principal stress axis. Lee and King [45] in studying the fatigue behavior of the nickel-base superalloy, AP1, at room temperature, also found that fatigue cracks initiated from large surface grains. Using metallographic sectioning, the angles between loading direction and the normal of surface microcrack planes were determined and are shown in Figure 2.19. It can be seen the average angle is 45 degrees with 6.5 degrees standard deviation. Based on experimental observations, two extreme conditions for surface grain deformation were proposed as shown in Figure 2.20. In one configuration, the slip plane is inclined 45° with respect to loading axis and normal to the specimen surface. The slip direction is also oriented at 45° to the loading axis and parallel to specimen surface. In this configuration, the

deformation is restricted within the specimen surface and thus no surface step can be generated. In another configuration, the slip plane is oriented 45° with respect to specimen surface and the slip direction is not parallel to specimen surface. The dislocation slip in this configuration will cause formation of surface extrusions. The first kind of configuration was thought to be responsible for surface crack initiation in this alloy [45].

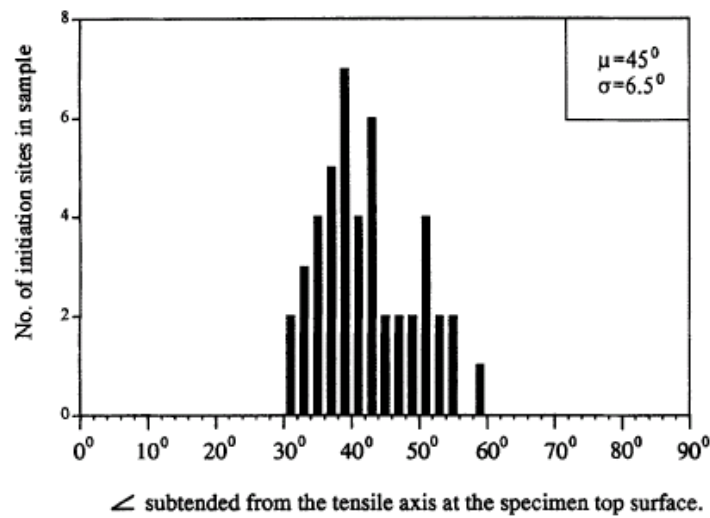


Figure 2.19 The angle between loading axis and the normal of surface microcracks in the alloy AP1 [45].

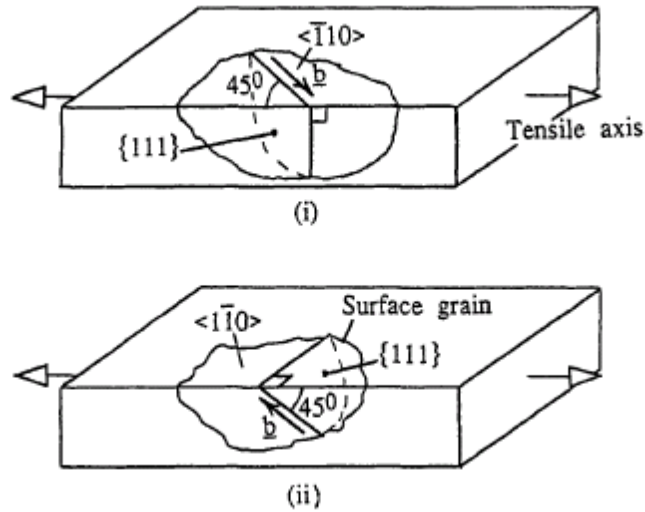


Figure 2.20 Two types of extreme configuration for slip system in surface grain subjected to the highest resolved shear stress [45].

Alexandre et al. [46] studied how grain size affects crack initiation mechanisms in the nickel-based superalloy Inconel 718 with different microstructure. The average grain size in testing materials ranged from 5 to 150 μm , and the fatigue testing were conducted at 600°C with applied strain ranges between 0.7% and 1.7%. In specimens with small grain size, the initiation sites were consistently associated with second phase particles, however, in specimens with the larger grain size, crack initiation was purely from slip bands as shown in Figure 2.21.

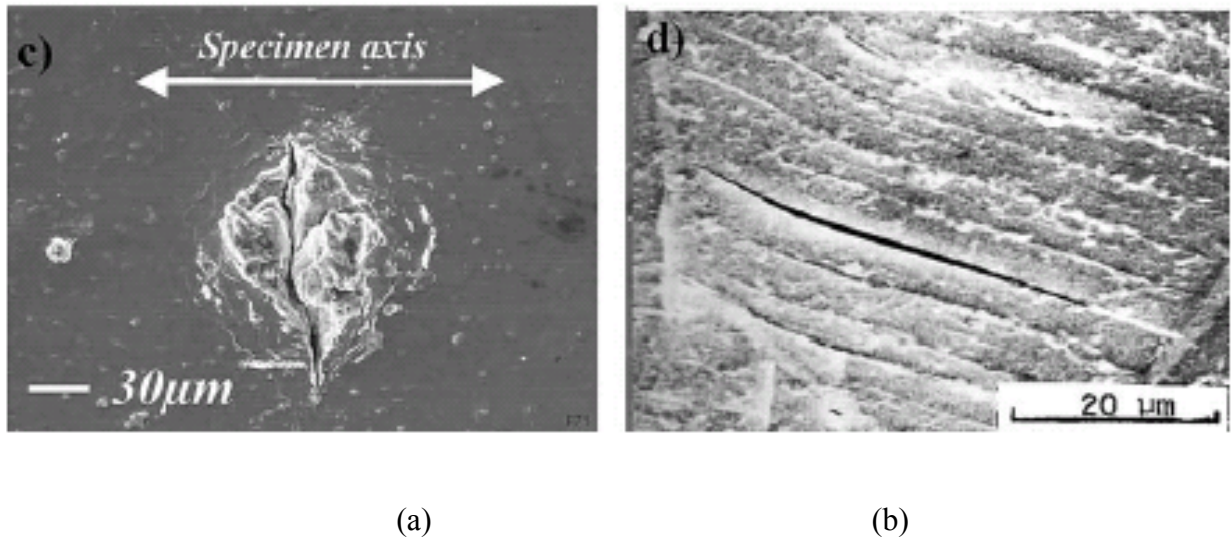


Figure 2.21 Fatigue crack initiation sites in Inconel 718 alloy with two different microstructures: (a) second phase particle cracking in specimen with small grain size and (b) slip band cracking in specimens with large grain size [46].

Favorably oriented neighbor grains can promote fatigue crack initiation and early small crack growth. Davidson et al.[47] found that “supergrains” play an important role in fatigue crack initiation in Waspaloy fatigued at room temperature. A “supergrain” is defined as a cluster of grains having misorientation close to “ideal orientation” [47]. The ideal misorientations align the slip planes or slip directions of two grains, facilitating the slip transmission between grain and its neighbors. The alignment of $\{111\}$ slip planes occurs for the following angle/axis combinations: $0^\circ/\langle 100 \rangle$, $90^\circ/\langle 100 \rangle$, $180^\circ/\langle 100 \rangle$, $270^\circ/\langle 100 \rangle$, $70.5^\circ/\langle 110 \rangle$, $109.5^\circ/\langle 110 \rangle$. The alignment of $\langle 110 \rangle$ slip directions on $\{111\}$ slip planes happens when the angle/axis combinations are $60^\circ/\langle 111 \rangle$, and $120^\circ/\langle 111 \rangle$ [47]. Figure 2.22 shows a surface fatigue crack. The misorientation between the large fatigue crack initiation grain and surrounding neighbors was calculated and plotted in Figure 2.23. As shown in Figure 2.23, as compared with control area which is close to fatigue crack initiation site and in which fatigue crack initiation did not occur,

most misorientations between the fatigue crack initiation grains and their neighbor grains are close to ideal.

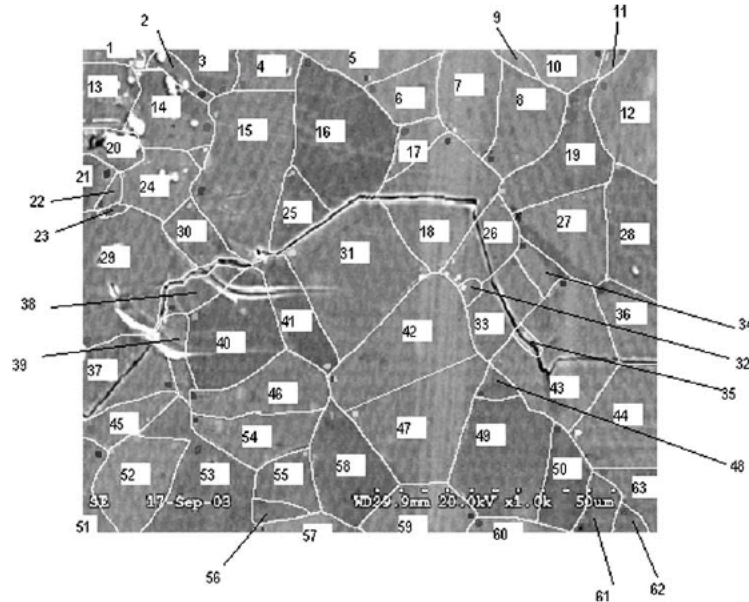


Figure 2.22 Surface microcracks in Waspaloy fatigued at room temperature [47].

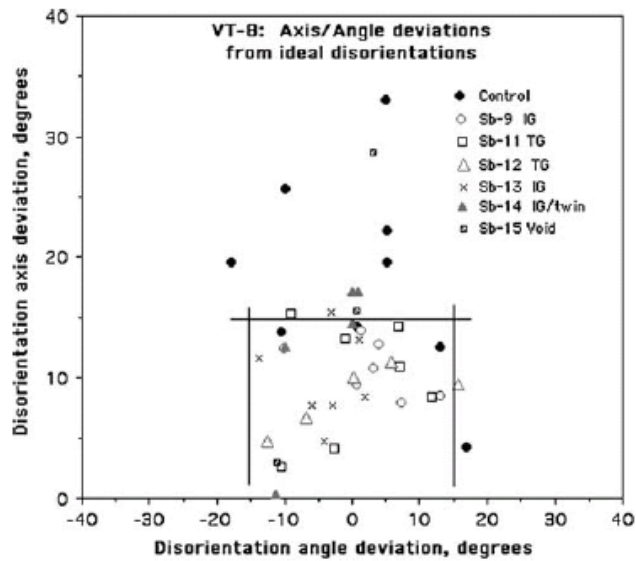


Figure 2.23 Orientation relationship between neighbor grains at the crack initiation region and control region in Waspaloy [47].

Annealing twin boundaries have much lower energy than other types of high angle grain boundaries. However, twin boundaries have been frequently observed as fatigue crack initiation sites in nickel-based superalloys [45, 48, 49]. Annealing twin boundaries also have been observed to be preferred sites for crack nucleation in other FCC materials fatigued in high cycle regime [50-56]. Heinz and Neumann [52] showed that the elastic incompatibility of twin pairs can yield additional shear stresses at the surface. Such additional shear stresses can trigger local plastic deformation in the area near annealing twin boundaries. In low cycle fatigue, cyclic stresses are high enough to initiate cracks at sites other than twin boundaries, whereas in high cycle fatigue, where cyclic stresses are low, the relative frequency of cracks initiating at twin boundaries increases [52]. Until now, no research has been devoted to understanding the role of twin boundaries in cyclic deformation in nickel-based superalloys and the mechanisms of fatigue crack initiation at twin boundaries in nickel-based superalloys remains unknown.

At room temperature, fatigue cracks generally initiate from the specimen surface. However, at elevated temperature, fatigue cracks have been observed to initiate from microstructure features located in subsurface regions within polycrystalline nickel-based superalloy specimens [57-62]. Crystallographic facets are frequently observed at these subsurface fatigue crack initiation sites. Figure 2.24 shows crystallographic fatigue crack initiation sites for several polycrystalline nickel-based superalloys fatigued at elevated temperatures. Thus far, the microstructure feature and mechanisms associated with these subsurface crystallographic fatigue crack initiations have not been investigated in detail.

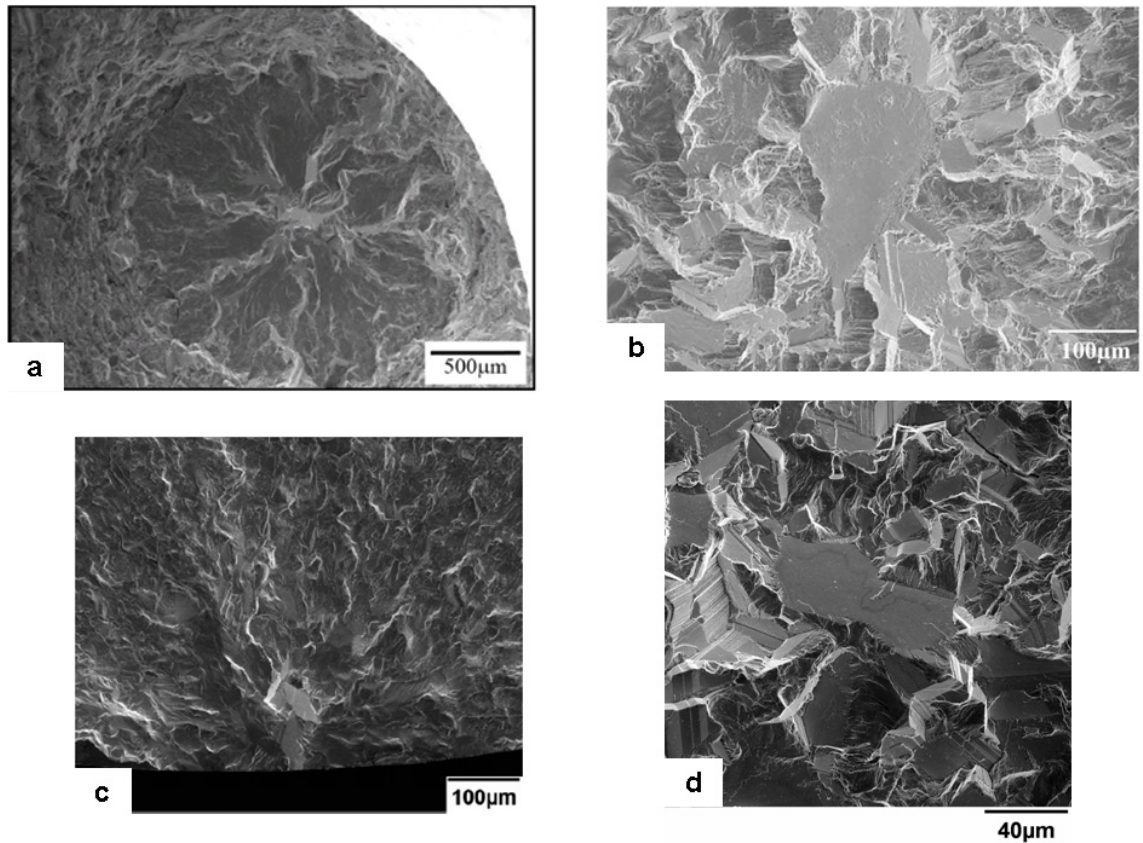


Figure 2.24 Subsurface crystallographic fatigue initiation sites in different superalloys fatigued at elevated temperature: (a) RR1000 [59]; (b) Inconel 718 [58]; (c) Waspaloy [60] and (d) René 88 DT [61].

2.3 Very high cycle fatigue and ultrasonic fatigue

Recent research [62-68] has shown that fatigue failures can occur at stresses well below the conventional endurance limit and at lifetimes well beyond 10^7 cycles within the very high cycle fatigue (VHCF) regime. For materials with a high density of defects such as cast steels, fatigue cracks normally initiate from subsurface regions in the very high cycle regime, giving rise to so-called “fisheye” initiation sites first observed in steels [66]. As shown in Figure 2.25, such a crack initiation site has radial appearance with a small bright spot at the center. The inclusion is usually at the center of the bright spot.

The fish-eye area is also called the optically dark area (ODA) because of its visual character under a microscope.

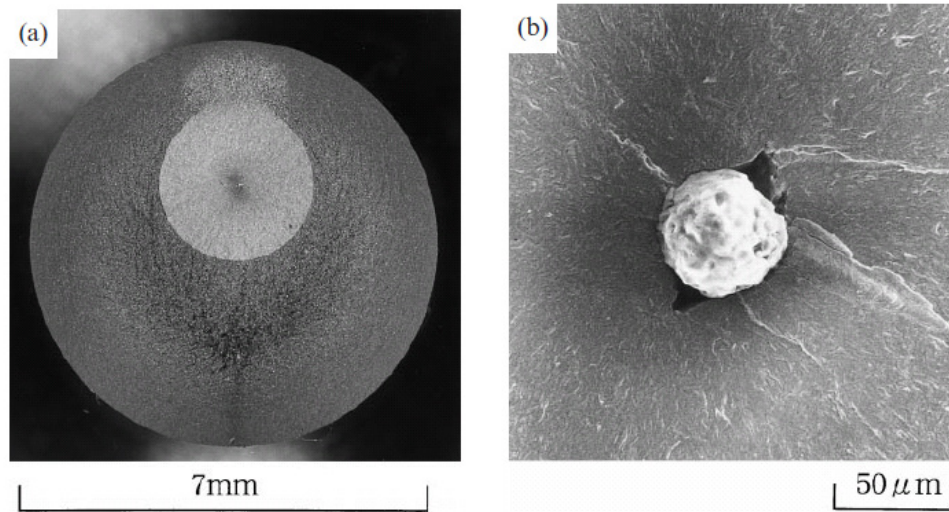
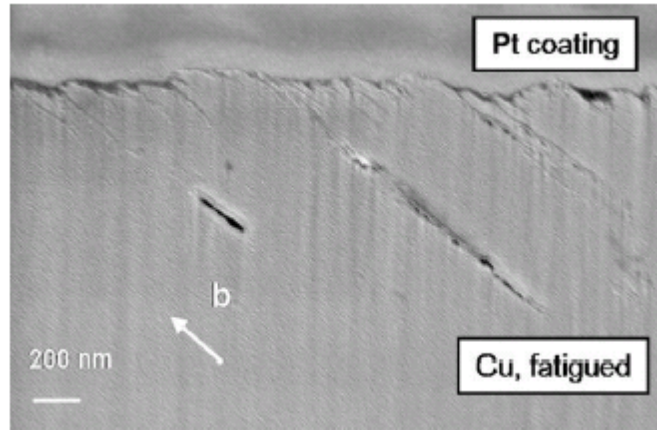
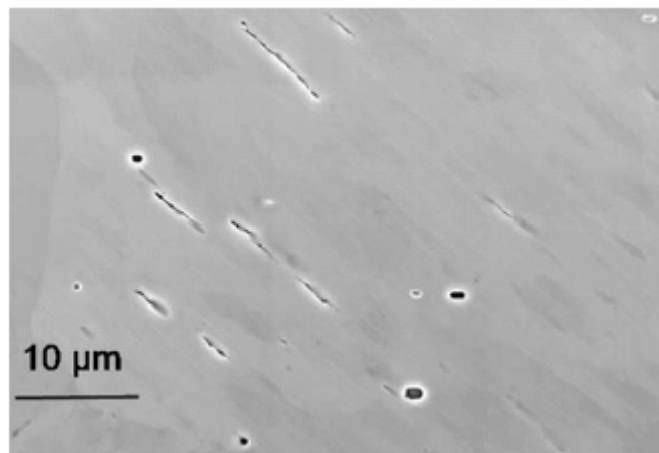


Figure 2.25 (a) Fish-eye topography and (b) Inclusion at the centre of the fish-eye [66].

However, for materials with a very limited number of metallurgical defects, as is the case in nickel-base superalloys, fatigue damage still can accumulate via cyclic strain localization in the very long life regime. Recent research on very high cycle fatigue behavior of copper at stress level below the threshold stress of PSB formation using ultrasonic fatigue technique found that though the slip irreversibility is very small under very low loading amplitudes, fatigue damage still can be gradually accumulated in very high loading cycles [68]. Figure 2.26 (a) shows surface roughness and stage I microcrack formation in copper fatigued at stress level well below PSB formation threshold within very high cycle regime. One interesting finding of this study is that a stage I microcrack not only can be found in surface grains, but are also located in the interior grains. Figure 2.26 (b) shows the microcracks formed within an interior grain.



(a)



(b)

Figure 2.26 Fatigue crack initiation in copper specimen under loading stress well below the PSB threshold within very high cycle regime: (a) microcracks formed in surface grain and (b) microcracks formed in interior grains [68].

In the very high cycle regime, fatigue crack initiation rather than fatigue crack propagation is the dominant part of the total fatigue life [4,69,70]. The cyclic stresses are much lower than the yield stresses of test materials in the very high cycle fatigue testing and whole specimens are fatigued in the nominally elastic range. Cyclic strain localization and fatigue crack initiation only can occur at the most critical microstructure configuration or microstructure heterogeneities [26]. Therefore, quantitative characterization of these critical microstructure features associated with fatigue crack

initiation and development of a better understanding of their roles in fatigue crack initiation will be crucial to develop physically-based fatigue crack initiation model and examine the large variability in fatigue life in the very high cycle regime. However, use of conventional fatigue instruments requires a very long time to collect very high cycle data, which greatly limits the study of very high cycle fatigue behavior of engineering materials.

Fatigue testing at ultrasonic frequencies was developed in the 1950s [71], and recent developments in ultrasonic fatigue techniques provides a powerful and promising methodology for the investigation of cyclic damage accumulation in the very high cycle regime [72, 73]. Ultrasonic fatigue has therefore been used to studied fatigue behavior of a wide range of engineering alloys [62-74]. The principle of ultrasonic fatigue testing and details of the experiment setup are given in Chapter 3.

2.4 Fatigue life prediction for nickel-based superalloys

2.4.1 The damage-tolerant approach

Fatigue life includes both fatigue crack initiation and fatigue crack propagation, consisting of small crack growth and long crack growth. Generally, two methods are used to experimentally determine fatigue life: stress (strain) /life and damage-tolerant method. Damage tolerance fatigue life prediction is based on fatigue crack growth. Assuming that there is a small crack that exists within the test specimen, the fatigue crack growth rate can be described using the Paris's law [75] as:

$$\frac{da}{dN} = C(\Delta K)^m \quad (2.1)$$

Where da/dN is the crack length increment per cycle, C and m are scaling constants which depend on materials and fatigue parameters such as temperature and load-ratio, ΔK is the stress intensity factor range defined as:

$$\Delta K = K_{\max} - K_{\min} \quad (2.2)$$

where stress intensity corresponds to maximum and minimum loads. For a circular crack, K can be written as:

$$K = Q(\pi a)^{1/2} \quad (2.3)$$

Where a is the crack size and Q is a geometry factor.

Figure 2.27 shows an example of fatigue crack growth data of nickel-based superalloy René 88 DT at 593°C within different environment [61].

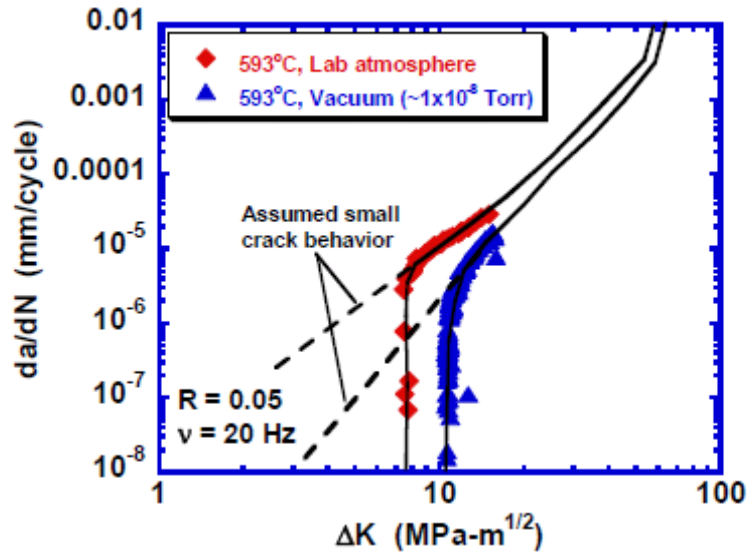


Figure 2.27 Fatigue crack growth behavior of nickel-based superalloy René 88 DT at 593° C in air and vacuum with a testing frequency of 20Hz and load ratio of 0.05 [61].

Fatigue life, N , based on the damage-tolerant method can be obtained by integrating Eq.2.1:

$$N = \int_{a_0}^{a_f} \frac{da}{C(\Delta K)^m} \quad (2.4)$$

where a_0 is the initial crack length and a_f is the final crack length.

The fatigue life predicted using damage-tolerant methods dose not consider fatigue crack initiation life, but assume the existence of a propagating crack. This method is valid when fatigue crack growth life is the dominant portion of the total fatigue life. However, in the high cycle regime or the very high cycle regime, fatigue crack initiation life is the dominant part of the total fatigue life. Thus the fatigue life prediction based on damage tolerant methodology will not be effective. Figure 2.28 shows the S-N data of nickel-based superalloys at 593°C in the high cycle regime. Two types of fatigue crack initiation sites were observed: inclusions and crystallographic facets. It can be seen there is large variation in fatigue life at low loading stresses. Using fatigue growth data, the fatigue propagation life for this alloy was calculated and plotted in Figure 2.28. As shown in Figure 2.28, the predicted fatigue crack growth life is much shorter than the total fatigue lives especially at the lowest cyclic stresses. The variability of predicated fatigue life based only on fatigue crack propagation, is also much smaller than the observed variability of total fatigue life, which the authors attribute to the variability in fatigue crack initiation lifetime caused by the operation of two distinct fatigue crack initiation mechanisms [61]. Therefore, the fatigue crack initiation life should be taken into account in order to obtain accurate prediction of fatigue life and the variability of fatigue life.

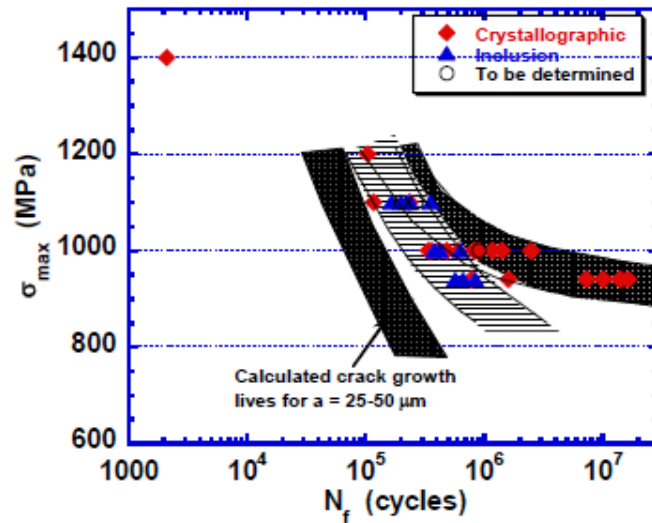


Figure 2.28 Fatigue life prediction using damage tolerant methods as compared with experimental results [61].

2.4.2 Prediction of fatigue crack initiation life

A microstructure-based fatigue crack initiation life model for nickel-based superalloys was proposed by Chan [76-78]. This model is based on Mura's fatigue crack initiation model [79-80] and incorporates some critical microstructure parameters associated with fatigue crack initiation such as crack size, grain size and grain orientation effects. Figure 2.29 illustrates Chan's fatigue crack initiation model. During cyclic loading, irreversible slip of dislocations on parallel slip planes 1 and 2 occurs in a favorably oriented surface grain and generates dislocation dipoles at the ends of double pileups. Fatigue crack initiation results from the coalescence of dislocation dipoles. The fatigue crack initiation life is equal to the number of loading cycles within which the stored energy within dislocation dipoles is equal to the specific fracture energy of test material.

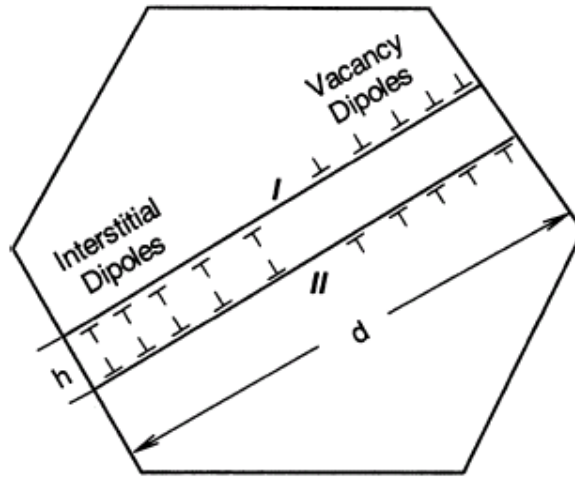


Figure 2.29 Schematic illustration of fatigue crack initiation model used in Chan's fatigue life prediction model [77].

Based on this model, the fatigue crack initiation life can be given as [76-78]:

$$(\Delta\sigma - 2Mk)N_i^a = \left[\frac{8M\mu^2}{\lambda\pi(1-\nu)} \right]^{1/2} \left(\frac{h}{D} \right) \left(\frac{c}{D} \right)^{1/2} \quad (2.5)$$

Where $\Delta\sigma$ is the loading stress range, M is the Taylor factor, k is the friction stress, N_i is the fatigue crack initiation life, μ is the shear modulus, ν is the Poisson's ratio, λ is a universal constant, D is the slip band width which is equal to grain size, h is the dislocation pileup length or crack depth and parameter a ($0 < a < 1$) is a generalized exponent of fatigue life N_i , which depends on slip irreversibility and stacking fault energy of testing materials [78]. It can be seen this fatigue life prediction model includes some critical microstructure parameters including grain size and the effect of favorable orientation and slip irreversibility.

Figure 2.30 shows the fatigue life prediction using Chan’s model as compared to experimental fatigue data. In the low cycle regime and under high loading stresses, there is a large difference between predicted fatigue initiation life and experimental fatigue life. This is reasonable because fatigue crack propagation life rather than fatigue initiation life is dominant. In the high cycle regime, the predicted fatigue crack initiation life fits the total fatigue life well. The effects of different critical microstructure parameters on fatigue life viability can also be evaluated using this model and the effect of crack size on fatigue crack initiation life is shown in Figure 2.30.

One limitation of Chan’s fatigue crack initiation life model is that the value of slip irreversibility is arbitrarily selected and without experimental verification. Robist et al. [18,41,42] quantitatively studied the slip irreversibility in Waspaloy using atomic force microscopy.

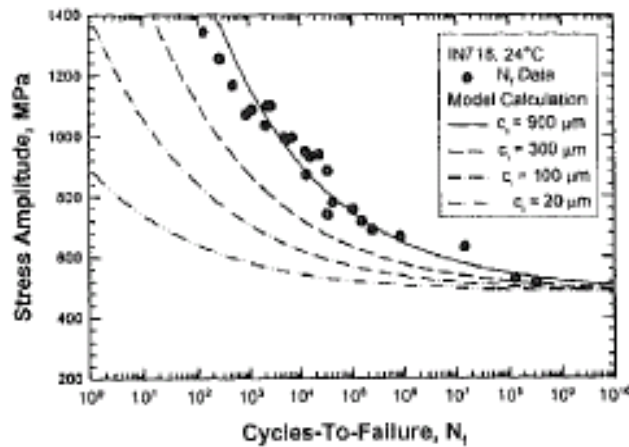


Figure 2.30 Comparison between experimental fatigue testing results with predicted fatigue crack initiation life using different crack sizes [76].

Irreversible plastic strain accumulated in the extrusion $\gamma_{irr,pl,loc}^{cum}$ is given as [18]

$$\gamma_{irr,pl,loc}^{cum} = \frac{h}{D} \quad (2.6)$$

Where h is extrusion height and D is average dimension of a grain.

The local plastic strain $\gamma_{pl,loc}^{cum}$ can be expressed as [18]

$$\gamma_{pl,loc}^{cum} = \sum_{i=1}^N \gamma_{pl,loc} = \left(\sum_{i=1}^{N_i} I_B(N, \varepsilon_a) \right) \cdot \frac{4\varepsilon_a \cdot M}{D \cdot f_1} = \gamma_{pl,loc}^{cum}(N, \varepsilon_a) \quad (2.7)$$

Where ε_a is plastic strain amplitude, M is Taylor factor, I_B is the slip bands spacing and f_1 is volume fraction of one slip band.

Plastic strain irreversibility p_{irr}^{cum} is defined as [18]

$$p_{irr}^{cum} = \frac{\gamma_{irr,pl,loc}^{cum}}{\gamma_{pl,loc}^{cum}} \quad (2.8)$$

By combining above three equations, p_{irr}^{cum} can be rewritten as [18]

$$p_{irr}^{cum} = \frac{h \cdot f_1}{N \cdot I_B(N_i, \varepsilon_a) \cdot \varepsilon_a \cdot 4M} = P_{irr}^{cum}(N, \varepsilon_a) \quad (2.9)$$

Assuming the surface damage initiation following the Manson–Coffin-type law,

Then it results that [18]

$$P_{irr}^{cum}(N_i) \cdot I_B(N_i) \cdot N_i^{c+1} = \frac{h(N_i) \cdot f_1}{2M \cdot \varepsilon_f' \cdot 2^{c+1}} = \text{constant} \quad (2.10)$$

I_B and $h(N_i)$ can determined experimentally from AFM measurements. Figure

2.31 shows the evolution of the product of $I_B \cdot p_{irr}^{cum}$ as a function of N_i .

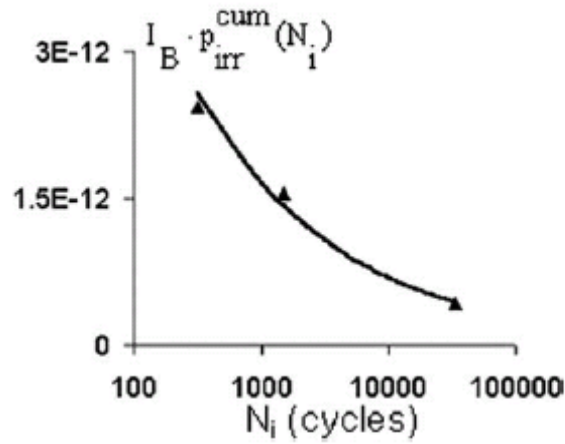


Figure 2.31 The evolution of the product of $I_B \cdot p_{irr}^{cum}$ as a function of the number of loading cycles to fatigue crack initiation in Waspaloy [18].

The value of ε'_f can be given as [18]

$$\varepsilon'_f = \frac{h(N_i) \cdot f_1}{2M \cdot 2^{C+1} \cdot 2 \times 10^{-11}} \quad (2.11)$$

Based on experiment measurements, for a Taylor factor $M=3$, ε'_f is determined to be 0.54, and for $M=2$, ε'_f is equal to 0.41. The Manson–Coffin law was determined for this material is given as [18]:

$$\varepsilon'_a = -0.45(2N_i)^{-0.61} \quad (2.12)$$

The predicted results are shown in Figure 2.32 and compared with experimental results. It can be seen that good agreement is reached between experimental fatigue life and prediction fatigue life.

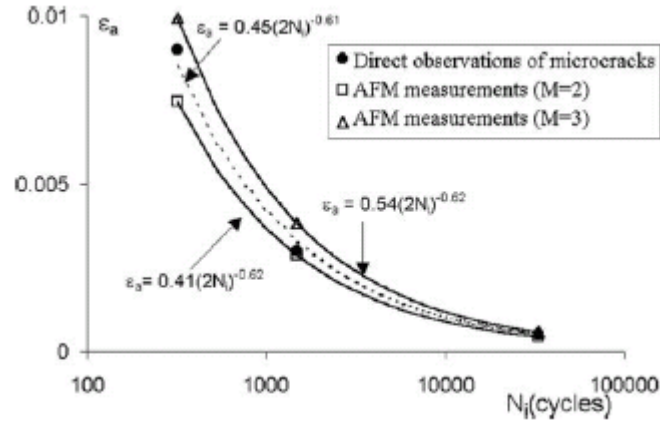


Figure 2.32 Evolution of macroscopic plastic strain amplitude ε_a as a function of number of cycles to crack initiation N_i [18].

Both Chan's and Robist's fatigue-crack-initiation-life prediction model take into account the effect of some microstructure features such as grain size and orientation on fatigue crack initiation. However, as shown above, Chan's model was based on Mura's fatigue crack initiation model. The validity of Mura's fatigue crack initiation model in nickel-based superalloys lacks experimental confirmation. In view of the complex microstructure of nickel-based superalloys, fatigue crack initiation in superalloys may be quite different from pure metals, which have been subjected to extensive studies for developing fatigue crack initiation models. Moreover, the role of these microstructure features in fatigue crack initiation is unclear because of a lack of direct experiment studies. It is thus difficult to evaluate the effects of microstructure variations on fatigue life variability. Robist's model is based on direct experimental observations. However, all experimental results came from fatigue tests in the low cycle fatigue regime. As shown in Figure 2.17, multiple slip systems are activated and grains deform uniformly in test specimens. Orientation effects on cyclic plastic deformation are evaluated in the

fatigue crack initiation model using Taylor factor. In high cycle or very high cycle regime, cyclic stresses are much lower than the yield stress of test materials. Cyclic plastic deformation can be localized within critical microstructure configurations and such uniform plastic deformation as observed in high cyclic stresses will not occur. For high cycle or very high cycle fatigue, different parameter need to be used in fatigue crack initiation models to evaluate microstructure effects on fatigue crack initiation and fatigue life. Therefore quantitative characterization of the critical microstructure features associated with fatigue crack initiation are necessary in order to identify fatigue crack initiation mechanisms and develop physically-based fatigue crack initiation life prediction models in the very high cycle regime.

2.5 Summary of literature review

In this chapter fundamental aspects of nickel-based superalloys and previous relevant work on fatigue behavior of polycrystalline nickel-based superalloys have been reviewed. The most important points can be summarized as follows:

Nickel-based superalloys have a complex microstructure and the nature of cyclic plastic deformation and fatigue crack initiation depends sensitively on microstructure. Microstructure heterogeneities are important sources for cyclic strain localization and therefore influence fatigue crack initiation lifetime in nickel-based superalloys.

In the high cycle and very high cycle fatigue regimes, fatigue crack initiation rather than fatigue propagation is the life-determining process. Conventional damage tolerant methods may not provide valid fatigue life prediction for nickel-based superalloys in the high cycle or very high cycle regimes. Fatigue crack initiation life should be considered in this life prediction process.

Physically-based models for the prediction of fatigue crack initiation life must include the critical microstructure parameters controlling fatigue crack initiation. Quantitative characterization of such critical microstructure and detailed understanding of the mechanisms of cyclic strain localization processes at these critical microstructure features is crucial to the development of accurate fatigue life prediction models and to assess the role of microstructure variation on the variability of fatigue life in high cycle and very high cycle regime.

In the following chapters, the fatigue behavior of a polycrystalline nickel-based superalloy René 88 DT will be presented. The critical microstructure features associated with cyclic strain localization and fatigue crack initiation are quantitatively characterized and the effects of these critical microstructure features on the fatigue behavior of this alloy are discussed.

Chapter 3

Microstructure Characterization and Ultrasonic Fatigue Testing

This chapter addresses microstructure characterization of the nickel-based superalloy René 88 DT and ultrasonic fatigue testing. In the first section, the characterization of the microstructure of René 88 DT is described. In the second section, the principles of ultrasonic fatigue testing and methods used in designing ultrasonic fatigue specimens for both room temperature and high temperature testing are presented. Experimental set-up and calibration for ultrasonic fatigue testing at room temperature and high temperature are described. Selected techniques associated with fatigue testing, such as fatigue damage detection using nonlinear ultrasonic signals and the preparation of ultrasonic fatigue specimen, are also briefly introduced.

3.1 Microstructure characterization of nickel-based superalloy René 88 DT

The material used in this study is a polycrystalline nickel-based superalloy, René 88 DT. This alloy is used for turbine disks in aircraft engines. It was developed by General Electric Aircraft Engines in order to achieve better fatigue damage resistance, creep and tensile strength as compared with the previous generation superalloy René 95 [81]. The nominal chemical composition of this alloy is shown in the Table 3.1.

Table 3.1 Nominal composition of nickel-based superalloy René 88 DT (wt%).

Cr	Co	Mo	W	Ti	Al	Nb	Zr	C	B	Ni
16	13	4	4	3.7	2.1	0.7	0.03	0.03	0.015	Balance

Advanced powder metallurgy techniques are used to minimize defects in this alloy. The typical heat treatment includes a supersolvus solutionizing process in the γ phase region, a delayed oil quench and a subsequent aging procedure [82]. The microstructure of the alloy consists of a disordered FCC γ matrix and two populations of gamma prime (γ') precipitates: secondary γ' that forms during cooling from the supersolvus temperature and tertiary γ' that forms during aging period [82].

Metallographic samples for optical microscope observations were prepared following general mechanical grinding and polishing procedures. Samples were mechanical ground successively from coarse 120 grit SiC grinding paper to fine 1200 grit SiC grinding paper. Subsequently, the samples were mechanically polished using 6 μ m and then 1 μ m diamond suspensions. Finally, the metallographic samples were etched using waterless Kalling's reagent (5g CuCl₂, 100ml ethanol and 100ml HCl). An Olympus PME3 optical microscope was used to examine the etched samples. Figure 3.1 is an optical micrograph showing the morphology of the γ grains.

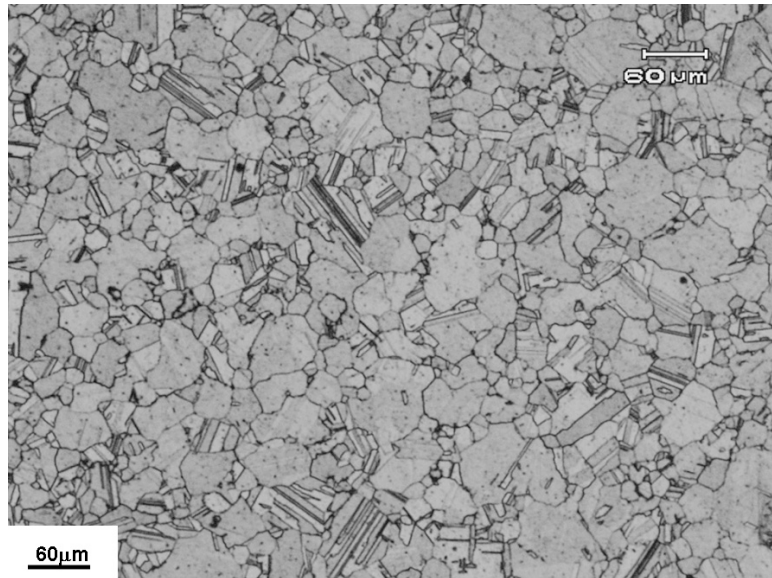
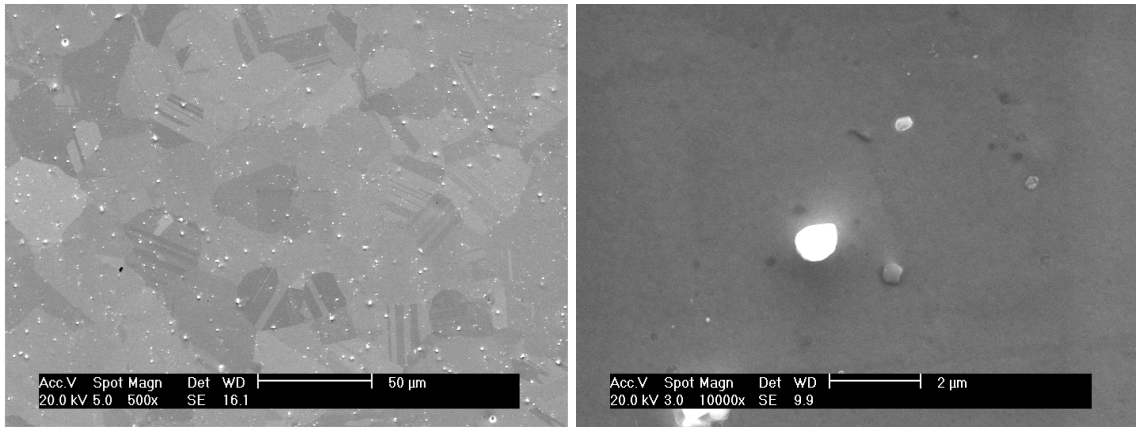


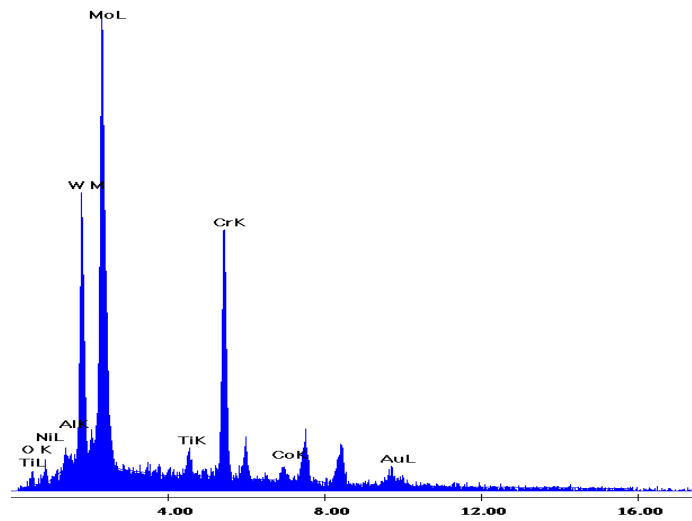
Figure 3.1 Optic micrograph of the microstructure of René 88 DT.

Electropolished samples were used for SEM observations. Electropolishing was conducted using an electrolyte of 55% ethanol with 35% butyl cellulose and 10% perchloric acid at 40 V and -30°C . All SEM investigation were conducted using a FEG XL-30 SEM equipped with a TSL EDAX detector. Figure 3.2 (a) is a SEM image of electropolished microstructure, showing a high density of twin boundaries within the microstructure. There are some isolated white particles within the microstructure as shown in Figure 3.2 (b), ranging from 1 μm to 5 μm in diameter. EDX analysis in Figure 3.2 (c) shows this phase contains Mo, Cr and W, which belongs to one of the M_5B_3 phases [82]. MC carbides having similar microscopic appearance like M_5B_3 boride also exists in the microstructure of René 88 DT [82].



(a)

(b)



(c)

Figure 3.2 SEM images of electropolished microstructure of René 88 DT: (a) SEM image; (b) white particles within the microstructure of René 88 DT and (c) EDX spectrum of white particles.

Electron backscatter diffraction was used to quantitatively characterized γ grain size and grain orientation and the nature of grain boundaries. The EBSD data was collected and analyzed using TSL OIM software (version 4.5) installed on a FEG XL-30 SEM. Figure 3.3 is an inverse pole figure map based on a large area OIM scan which is about 1mm \times 0.8mm. The orientation distribution function was calculated using the

harmonic method and the resulting pole figures are shown in Figure 3.3. No significant texture was observed in the microstructure.

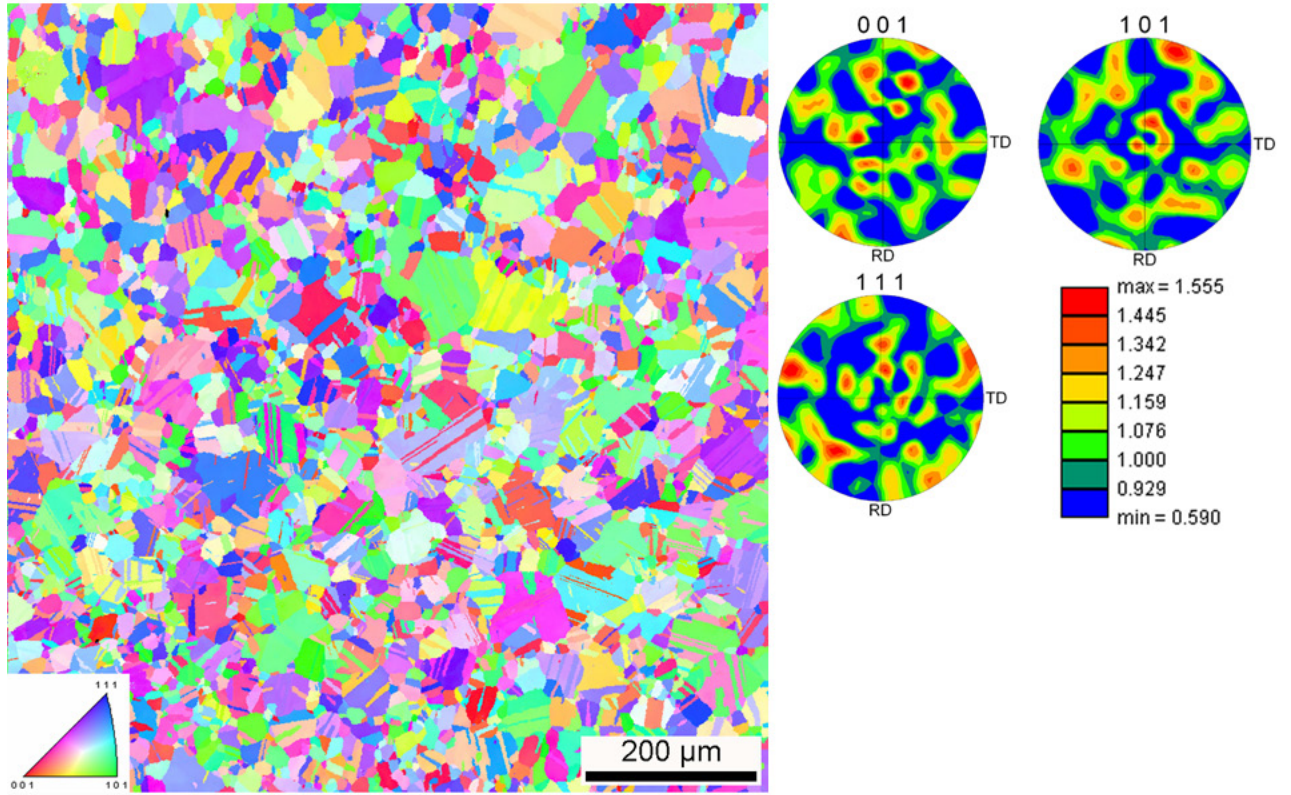
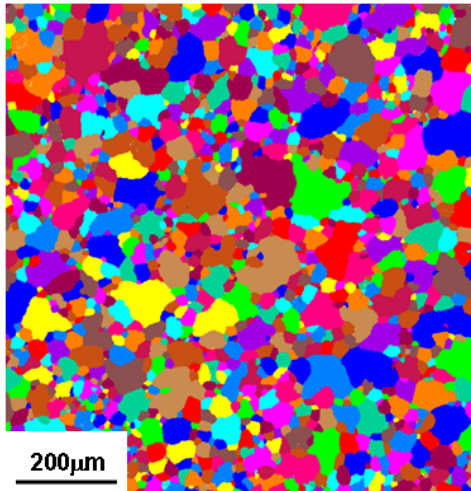


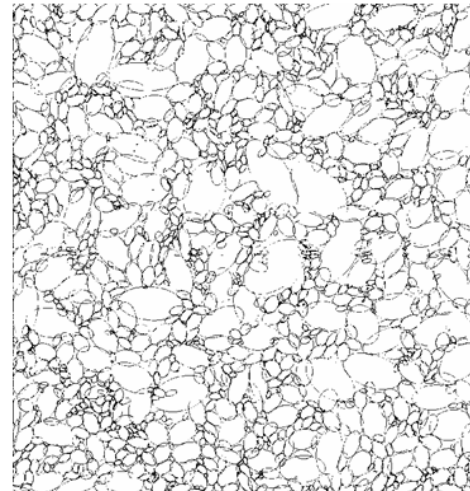
Figure 3.3 Inverse pole figure map of γ grains and corresponding texture pole figure.

The size distribution of the γ grains, excluding twins, was evaluated from the large OIM scan using two methods: equivalent diameter and ellipse fit. Figure 3.4 (a) and (b) show the grain map and corresponding ellipse fit of grains. In the OIM grain size analysis, the minimum grain size was set at 2.4 μm . Therefore, all grains whose sizes are smaller than the minimum size were not considered for grain size distribution analysis. The grain size distribution analyzed used these two methods are shown in Figure 3.4 (c) and (d) respectively. The average grain size of the alloy excluding twins is about 20 μm .

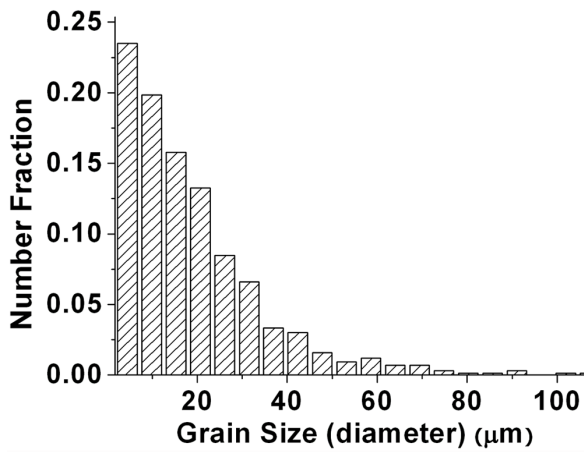
Both methods show that there is a low fraction of large grains on the order of three to five times the average grain size distributed throughout the microstructure.



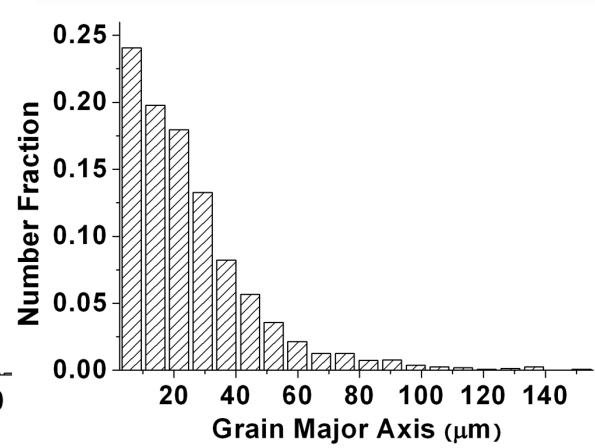
(a)



(b)



(c)



(d)

Figure 3.4 Grain size distribution analysis: (a) grain map; (b) ellipse fit of grains; (c) grain size distribution (equivalent method) and (d) grain size distribution, (ellipse fit method).

Annealing twins are prevalent in the microstructure. Figure 3.5 shows an OIM grain boundary map overlaid by an image quality map. The red lines represent $\Sigma 3$ twin boundaries, while blue lines represents random large angle grain boundaries.

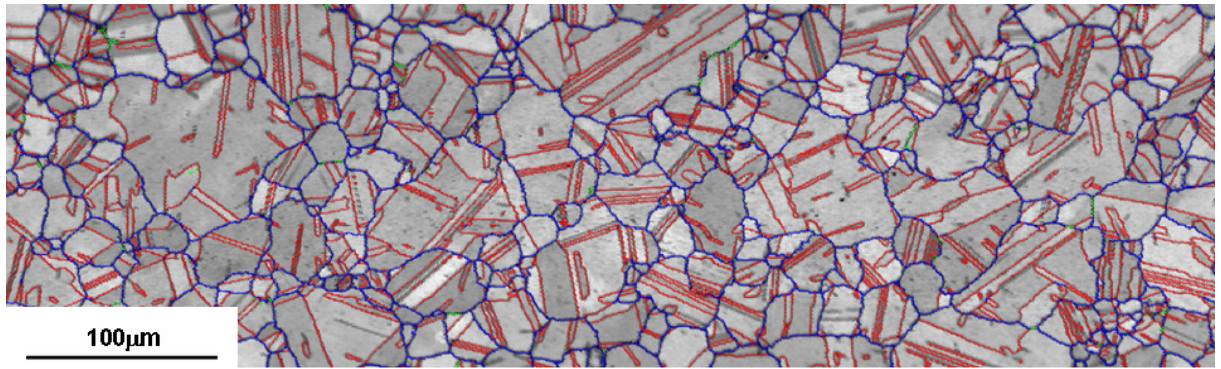


Figure 3.5 Twin boundaries within the microstructure of René 88 DT.

Based on the large OIM scan results shown in Figure 3.3, the grain boundary character distribution in this alloy was analyzed and shown in Figure 3.6. The length fraction of $\Sigma 3$ grain boundary is about 0.58, while the total fraction other Σ grain boundaries in grain interface length is only about 0.08.

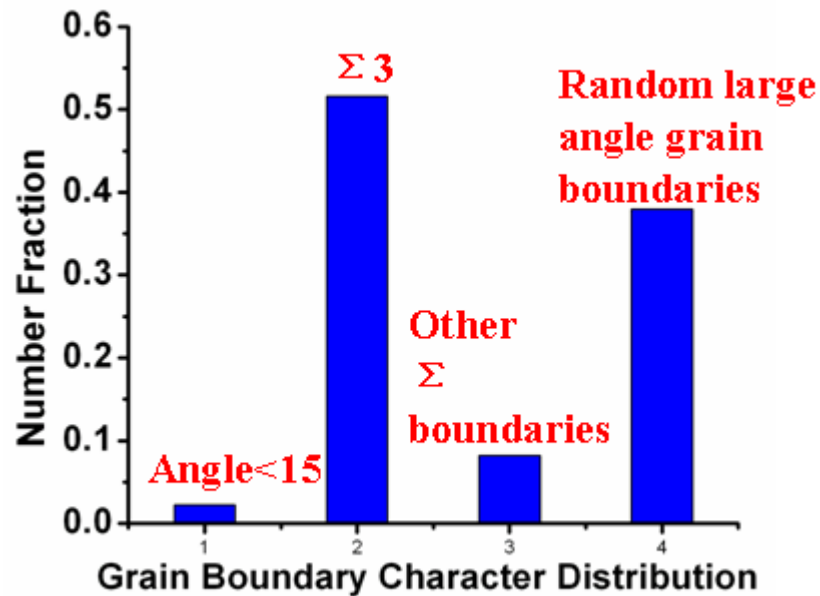


Figure 3.6 Grain boundary character distribution in René 88 DT.

Disc samples for TEM observations were machined from raw material using low speed diamond saw. The samples were mechanically polished to a thickness of approximately 100 μm , and further thinned by twin jet polishing in a solution of 68% methanol, 10% perchloric acid, 9% distilled water and 13% butyl cellosolve under conditions of -35°C , 20 V and 50 mA. TEM studies were conducted using a JEOL 2010F ATEM operated at 200 KeV.

Figure 3.7 is a TEM image showing the typical morphology of secondary and tertiary γ' within a γ grain. There is no primary γ' in the microstructure due to the supersolvus heat treatment. The size of the secondary γ' phase is about 100 -200 nm, while tertiary γ' sizes are about 10~20 nm. Wlodek et al. [8 2] found that René 88 DT contains about 42.5 % γ' phase, distributed between secondary γ' (60%) and tertiary γ' (40%). The mismatch between γ matrix and γ' precipitates was determined to be 0.05% by comparing the lattice parameters of the two phases [82].

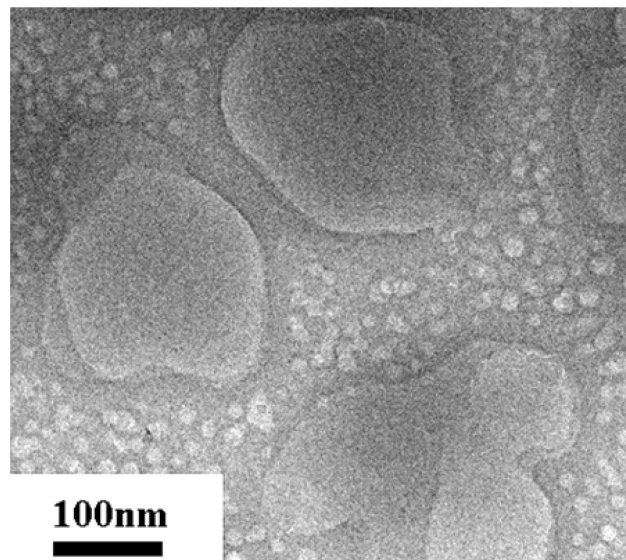


Figure 3.7 TEM image showing the morphology of two types of γ' phase.

TEM EDX mapping in Figure 3.8 shows the distribution of the major alloying elements within γ and γ' phases. There is partitioning of elements to either γ or γ' phases. Cr, Mo and Co are mainly located within the γ matrix, while Al and Ti are primarily partition to the γ' phase. These findings are similar to those obtained using atomic probe techniques [83].

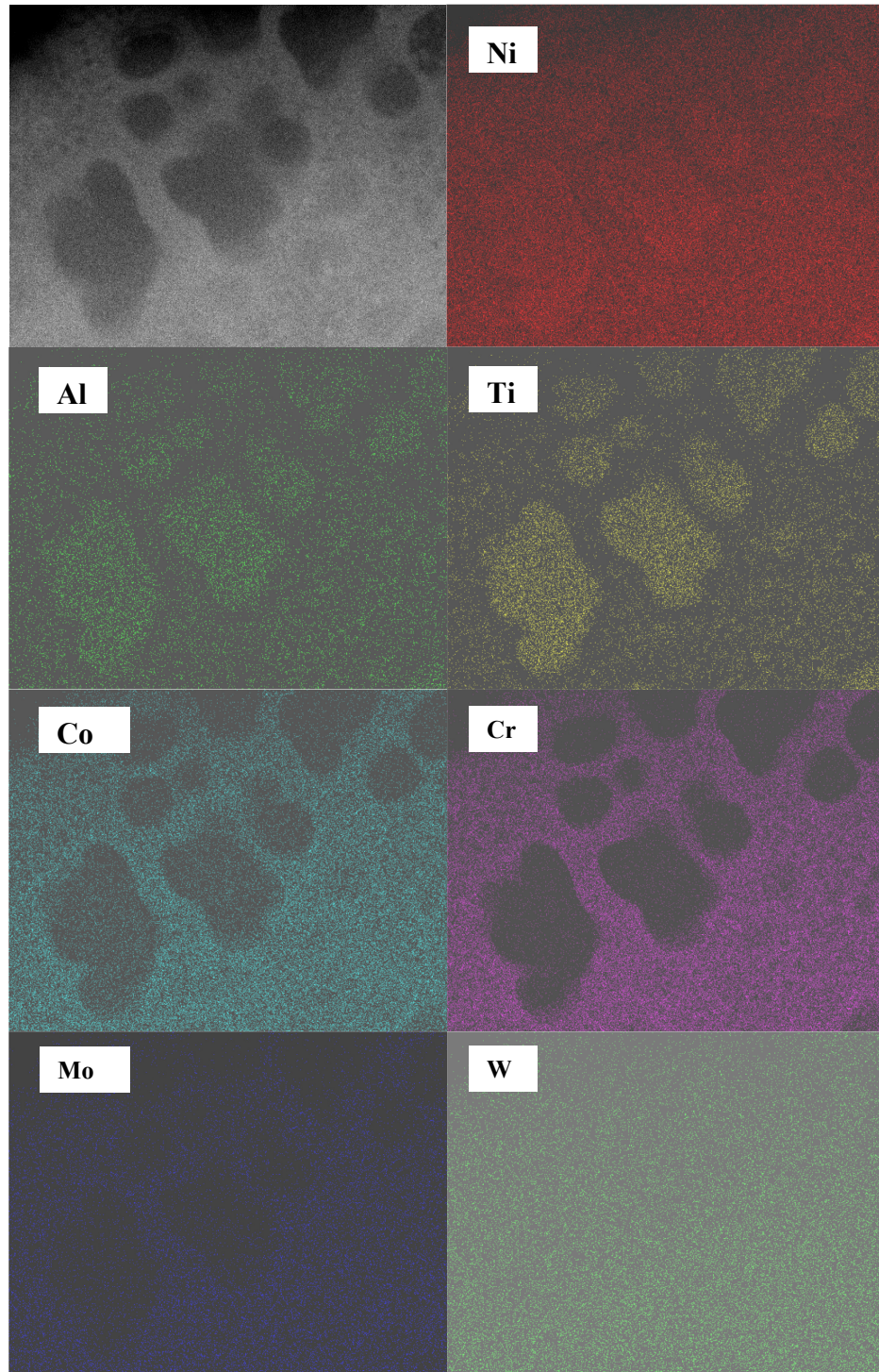


Figure 3.8 EDX mapping showing the distribution of main alloying elements within γ and γ' phases.

3.2 Ultrasonic fatigue testing

3.2.1 Principles of ultrasonic fatigue testing and specimen design

In conventional fatigue testing, test frequency is controlled by servohydraulic, mechanical or electromechanical machines and the test frequency has no relationship to the natural frequencies of fatigue specimens. However, in ultrasonic fatigue testing, fatigue specimens couple in resonance with a load train which is driven by a piezoelectric transducer. Therefore, the geometry of specimens used in ultrasonic fatigue testing needs to be carefully designed to satisfy the resonance requirements of ultrasonic fatigue testing systems.

For experimental convenience, the length of an ultrasonic fatigue specimen is normally designed to be equal to one-half of the wave length of a longitudinal sound wave in the test material for the resonant frequency. Under this condition, the strain or stress maxima occur at the center of specimen gage length, where the displacement is equal to zero. Maximum displacement occurs at each end of the resonating specimen, which corresponds to the node of stress. The length of a resonating cylindrical fatigue specimen can be simply given by [84]

$$L = \frac{1}{2f} \sqrt{\frac{E}{\rho}} \quad (3.1)$$

Where L is the resonance length of the specimen, f is the resonant frequency, E and ρ are the elastic modulus and density of the testing material respectively. From Eq.3.1, it can be seen that the resonant length of a fatigue specimen is inversely proportional to the resonant frequency. Although, high resonance frequency can reduce testing time and improve testing efficiency, the small specimen sizes required for

resonance can cause difficulties in sample machining and in the reduction of the volume of test materials. Therefore, in order to facilitate the preparation of fatigue specimens of structural materials for ultrasonic fatigue, most modern ultrasonic fatigue testing instruments are designed to vibrate with a nominal frequency of 20 KHz.

The wavelength of an elastic wave propagating in an ultrasonic fatigue specimen is much larger than the width of the specimen. Under this circumstance, wave propagation parallel to the specimen axis can be approximately described as a one-dimensional longitudinal elastic wave. The displacement wave within the fatigue specimen can therefore be written as

$$u(x,t) = u(x)e^{i(2\pi f)t} \quad (3.2)$$

and the variation of strain along fatigue specimens can be given by

$$\varepsilon(x,t) = \frac{\partial u(x,t)}{\partial x} \quad (3.3)$$

If the assumption is made that the specimen vibrates within the elastic range, the stress in the specimen can be calculated, if Young's modulus (E) is known, as

$$\sigma(x,t) = E\varepsilon(x,t) \quad (3.4)$$

According to the equation of motion,

$$\rho C(x) \frac{\partial^2 u(x,t)}{\partial t^2} = \frac{\partial F}{\partial x} \quad (3.5)$$

Where ρ is the density of the testing materials, $C(x)$ is the cross section area along the longitudinal direction of the fatigue specimen, $u(x,t)$ is the displacement and F is the loading force, which can be given as:

$$F(x,t) = -E(x)C(x) \frac{\partial u(x,t)}{\partial x} \quad (3.6)$$

Where $E(x)$ is the elastic modulus at different positions along the specimen.

Substituting Eq.6 into the Eq.5, yields

$$\frac{\partial^2 u(x)}{\partial x^2} + \left(\frac{\partial E(x)/\partial x}{E(x)} + \frac{\partial C(x)/\partial x}{C(x)} \right) \frac{\partial u(x)}{\partial x} + k^2 u(x) = 0 \quad (3.7)$$

Here $k=2\pi f/c$.

This equation combined with the boundary conditions for ultrasonic fatigue specimens in resonance can be analytically solved using a fourth-order Runge-Kutta method to obtain the resonance length and the distribution of strain and displacement along the fatigue specimen.

For ultrasonic fatigue testing at room temperature, specimen heating may be induced by the 20 KHz vibration and this can be minimized using compressed cooling air. Under these conditions, elastic modulus variation along the length of the specimen is minimal and can be neglected. However, at high temperature, a large temperature gradient along the length of the specimen and in the lambda rods arises, especially when induction heating is used. The variation of elastic modulus along the specimen length must be taken into account in designing ultrasonic fatigue specimens for high temperature testing.

Ultrasonic fatigue specimens are designed to have a reduced cross section to both minimize power requirements and to localize fatigue damage within a well-defined volume. Two main types of specimen geometry with circular cross section are shown in Figure 3.9. The first type has a cylindrical gage of constant diameter over a prescribed length, as shown in Figure 3.9 (a). The second type sample has an hourglass shape and a

zero gage length as shown in Figure 3.9 (b). Both specimen types have threaded ends for application of mean loads.

Compared to specimens with an hourglass-shape gage section, specimens with a uniform diameter gage section provide a larger volume of material subjected to cyclic loading, which will benefit studying the influence of heterogeneous microstructure or metallurgical defects such as inclusions and pores on fatigue behavior at ultrasonic frequencies. Therefore, the specimen geometry with uniform diameter gage is used in this study.

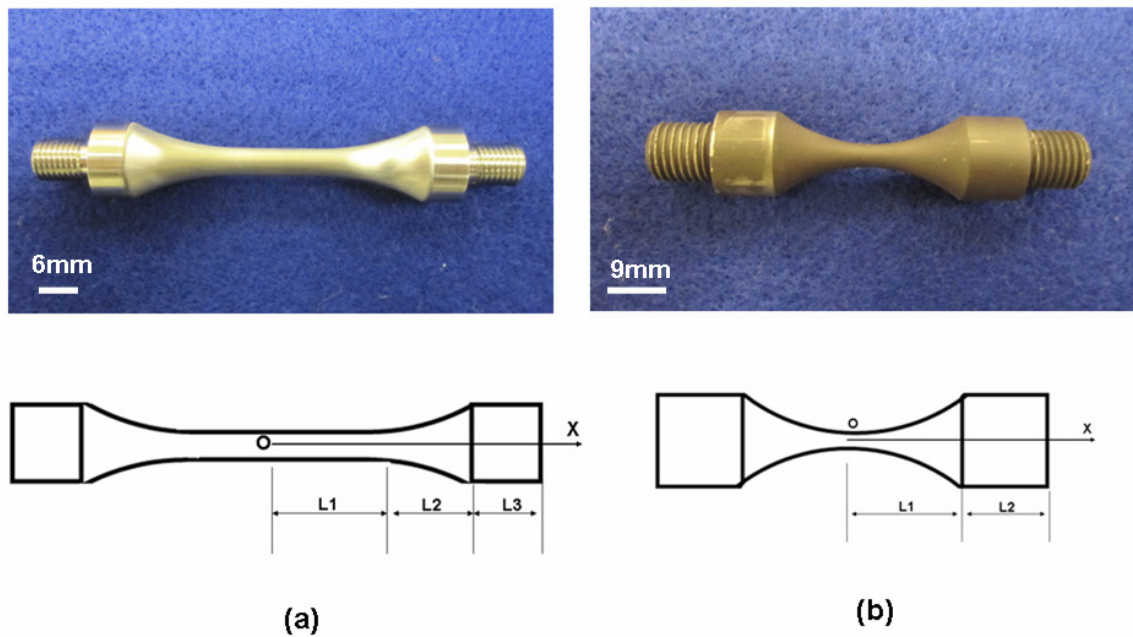


Figure 3.9 Typical ultrasonic fatigue specimen geometries: (a) specimen with uniform cylinder gage section and (b) specimen with hourglass-shaped gage section.

A stress magnification factor is often used to quantify the increase of the maximum stress in the sample due to the design of reduced cross section. This factor is defined as the ratio of the maximum stress in the reduced section specimen to that in constant section specimen with the same material properties and under the same external

excitation condition such as frequency and vibration amplitude. For specimen with circular cross section, the stress magnification factor F can be given by [73]:

$$\begin{aligned}
 F &= \frac{\beta \cos(k \times L_1) \cosh(\alpha \times L_2)}{k \times \sinh(\beta \times L_2)} \\
 k &= 2\pi f \sqrt{\frac{E}{\rho}} \\
 \alpha &= \frac{1}{L_2} \operatorname{arccosh}\left(\frac{R_2}{R_1}\right) \\
 \beta &= \sqrt{\alpha^2 - k^2}
 \end{aligned} \tag{3.8}$$

Where E is the elastic modulus, f is the resonance frequency, L_1 , L_2 , R_1 , and R_2 are the geometry parameters of the specimen with the uniform gage section as indicated in Figure 3.9 (a). From these equations, it can be seen that for specimens made of the same material and vibrating at the same frequency and amplitude, the stress magnification factor for an hourglass specimen ($L_1 = 0$) is always larger than for specimens with a gage length of uniform diameter ($L_1 \neq 0$).

3.2.2 Design of ultrasonic fatigue specimen for nickel-based superalloy René 88 DT

In this section, the details of designing René 88DT specimens for ultrasonic fatigue testing at both room temperature and elevated temperature are given. René 88 DT specimens have a uniform diameter gage. Similar procedures can be used to design ultrasonic fatigue specimen with an hourglass-shaped gage.

The sample geometry for René 88 DT and corresponding one-dimensional coordinate is illustrated in Figure 3.9 (a). Under the condition of free vibration, it is required that displacement reaches a maximum at the end of the specimen and is zero at the midpoint of the gage section. Conversely, the axial strain is maximum at the gage

section of the specimen and is zero at the ends of the specimen. The partial wave equation and corresponding boundary conditions can be written as:

$$\begin{aligned}
 \frac{\partial^2 u(x)}{\partial x^2} + \frac{\partial C(x)/\partial x}{C(x)} \times \frac{\partial u(x)}{\partial x} + k^2 u(x) &= 0 \\
 u(0) &= 0, \\
 \frac{\partial u(x)}{\partial x} \Big|_{x=0} &= A, \\
 \frac{\partial u(x)}{\partial x} \Big|_{x=L_1+L_2+L_3} &= 0, \\
 u(L_1 + L_2 + L_3) &= A_0,
 \end{aligned} \tag{3.9}$$

Where A is the maximum strain in the center of the specimen, A_0 is the maximum displacement at the end of the specimen. By solving the equations using the fourth-order Runge-Kutta method, the resonant length of the René 88 DT sample with a resonant frequency of 20 KHz at room temperature is 64.14mm. The distribution of normalized strain and displacement along the specimen at room temperature is shown in Figure 3.10. It can be seen that the axial strain is essentially constant along the gauge section of the specimen.

The effect of resonant frequency on the resonant length of samples with uniform gage diameter was evaluated analytically. Resonance length at different resonance frequencies was calculated and plotted in Figure 3.11. It can be seen that as the resonance frequency increases, the resonant length of the fatigue specimen decreases.

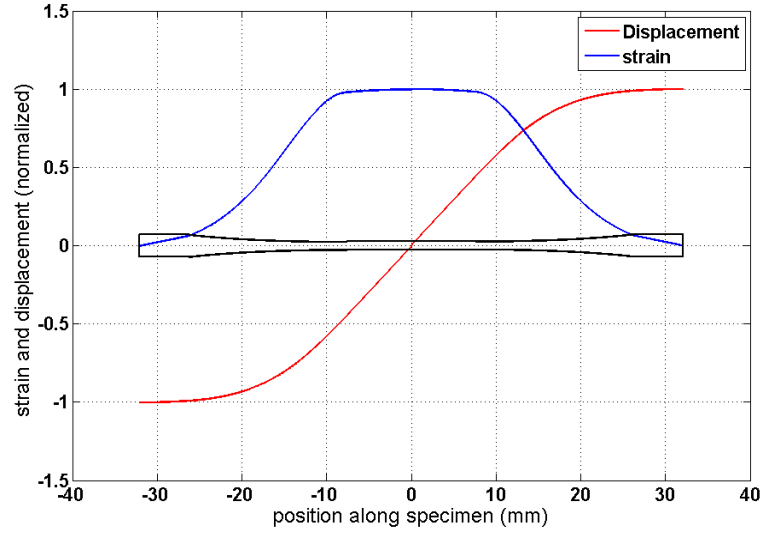


Figure 3.10 The distribution of normalized strain and displacement along the René 88DT specimen at room temperature.

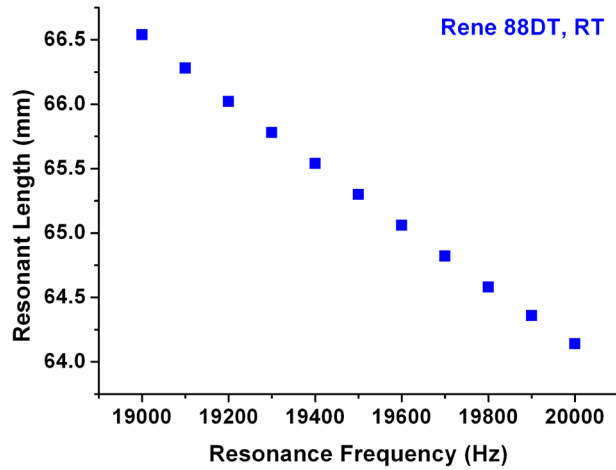


Figure 3.11 The variation of resonance length of René 88 DT sample with resonance frequencies.

The elastic modulus is temperature dependent and in designing ultrasonic fatigue specimens for elevated temperature or high temperature testing, the effects of elastic

modulus variation as a function of position along the resonance length of fatigue specimens and the load train must be considered, as described above. A René 88 DT specimen designed for resonance at room temperature was heated to 593 °C using an induction coil, and the temperature distribution along the specimen was measured. The partial wave equation with corresponding boundary conditions in the elevated temperature case that incorporates a temperature (position) dependent modulus of elasticity is given by

$$\begin{aligned}
 \frac{\partial^2 u(x)}{\partial x^2} + \left(\frac{\partial E(x)/\partial x}{E(x)} + \frac{\partial C(x)/\partial x}{C(x)} \times \frac{\partial u(x)}{\partial x} + k^2 u(x) \right) &= 0 \\
 u(0) &= 0, \\
 \frac{\partial u(x)}{\partial x} \Big|_{x=0} &= A, \\
 \frac{\partial u(x)}{\partial x} \Big|_{x=L_1+L_2+L_3} &= 0, \\
 u(L_1 + L_2 + L_3) &= A_0,
 \end{aligned} \tag{3.10}$$

By solving Eq 3.10, the resonance length for René 88 DT at elevated temperature is determined as 62.2 mm, which is a slightly shorter than the resonance length at room temperature. A similar result has been found in the design of austenitic stainless steel specimens with an hourglass-shaped gage for ultrasonic fatigue testing at high temperature [85]. The distribution of strain and displacement along the sample at elevated temperature is shown in Figure 3.12, and the variation of strain along the gage section is less than 3%.

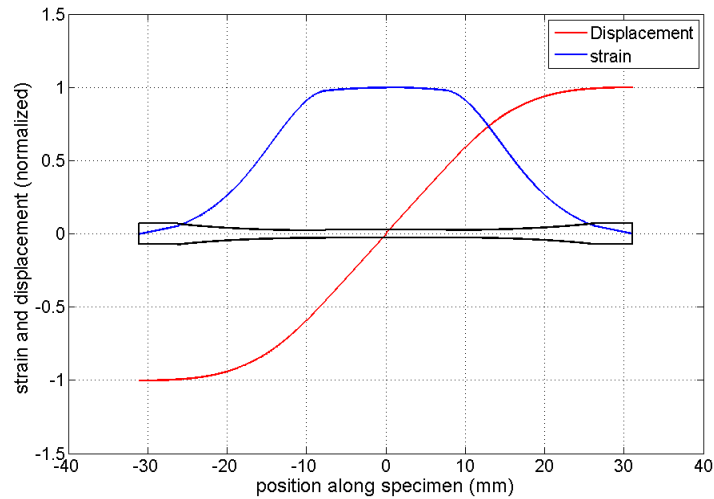


Figure 3.12 The distribution of normalized displacement and strain along the René 88 DT specimen at 593°C.

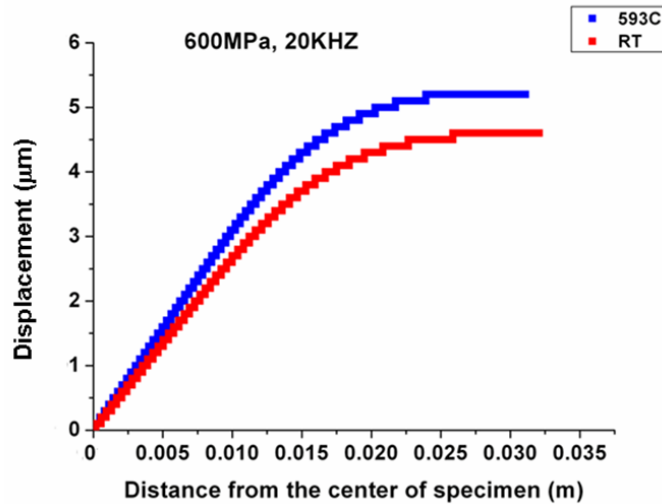


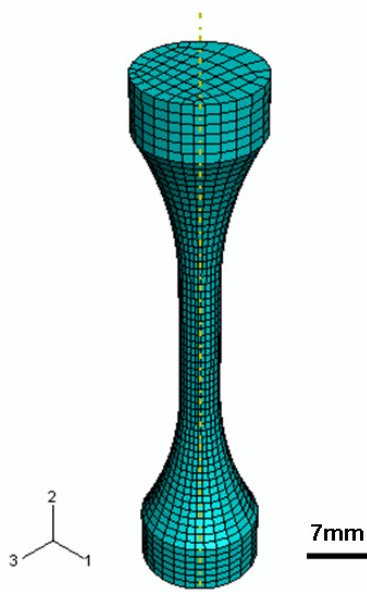
Figure 3.13 Distribution of displacement along half of the ultrasonic fatigue specimen at room temperature and elevated temperature under the same loading ($R = -1$).

Figure 3.13 shows the distribution of displacement along one half of the fatigue specimen at room temperature and elevated temperature. For the same gage section stress, the elevated temperature specimen operating at 593 °C must be driven to a slightly larger maximum displacement than that required at room temperature.

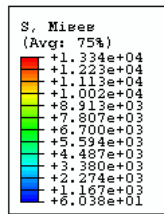
When designing ultrasonic fatigue specimens using the above-described analytical method, the specimens are assumed to vibrate at a frequency of 20 KHz, the nominal resonance frequency of the capacitance transducer. In order to verify these calculations, 3D finite element analysis were developed to study the vibration behavior of ultrasonic fatigue specimens.

The specimen geometry obtained from the analytical calculation was used as input to generate finite element models. The finite element program ABAQUS was used to build the model. Figure 3.14 (a) shows the 3D finite element model for a René 88DT sample at room temperature. Assuming a specimen under the condition of free vibration, a frequency extraction procedure was used to obtain the first 30 natural frequencies of the specimen. Within these 30 vibration modes, the longitudinal vibration mode has a resonance frequency of 18.6 KHz, which is somewhat lower than the frequency used in designing the fatigue specimen. Figure 3.14 (b) and (c) show the distribution of stress and displacement along the fatigue specimen under this vibration mode. Figure 3.15 shows the distribution of stress and normalized displacement along the center line of sample. It can be seen that the maximum stress occurs at the gage section of the specimen. There is a good agreement between the results of the finite element analysis and the analytical solution.

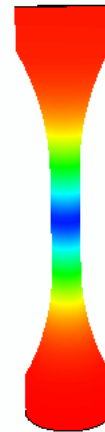
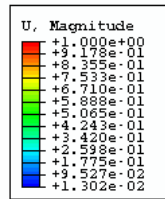
The resonant frequency spectrum of a René 88 DT specimen at room temperature was measured using QUASAR RI-2000 transceiver. The experimental setup for the spectrum measurement is shown in Figure 3.16 (a). The measured spectrum is shown in Figure 3.16 (b). The measured maximum resonant frequency is 18.67 KHz, which is close to the result obtained in the 3D FEM simulation.



(a)

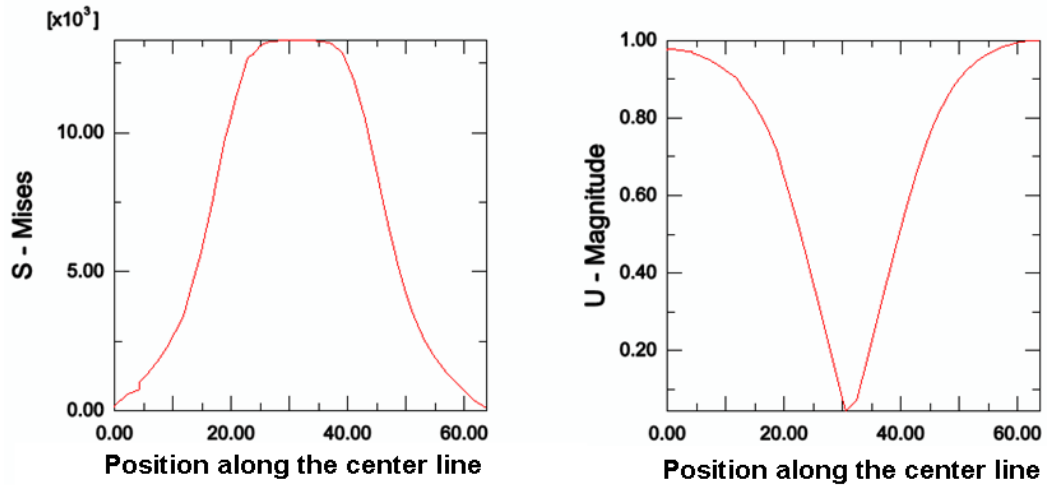


(b)

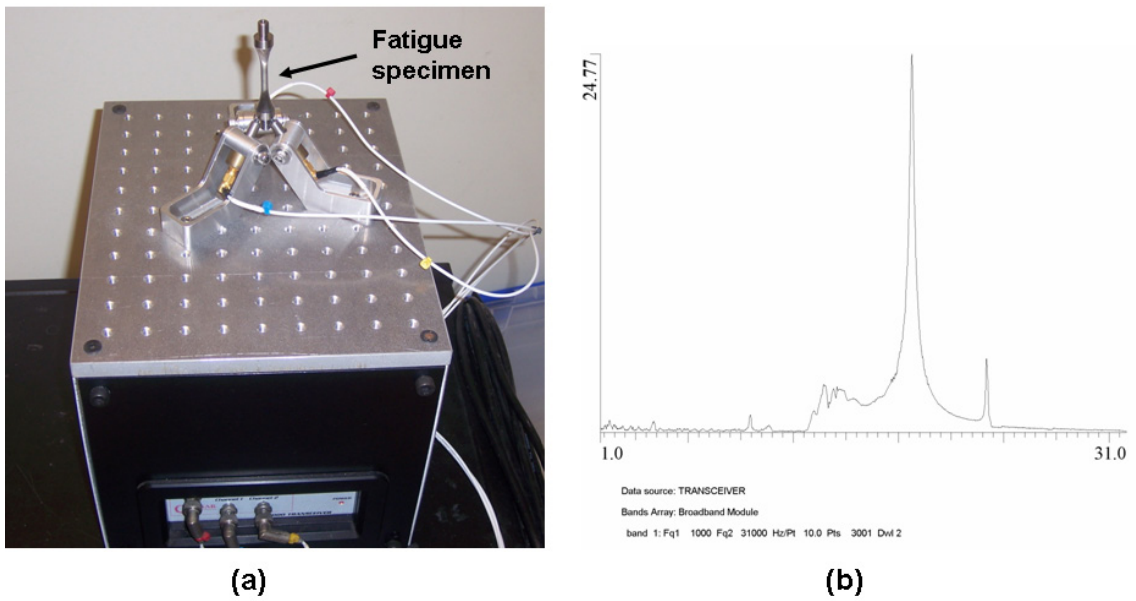


(c)

Figure 3.14 Finite element modeling René 88 DT ultrasonic fatigue sample: (a) 3D FEM Model; (b) distribution of von Mises stress along the specimen and (c) distribution of normalized displacement along the specimen.



(a) (b)
 Figure 3.15 Distribution of stress and displacement along the center line of the ultrasonic fatigue specimen: (a) stress and (b) displacement.



(a) (b)
 Figure 3.16 Determination of resonant frequency spectrum of René 88 DT fatigue specimen at room temperature: (a) experimental setup and (b) resonance frequency spectrum.

3.2.3 Ultrasonic fatigue testing instrumentation and experimental setup

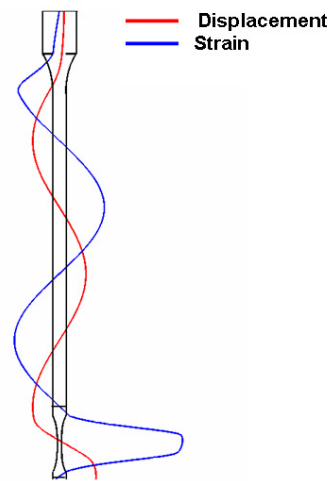
The ultrasonic fatigue testing system used in this study is shown in Figure 3.17 (a). A piezoelectric transducer is driven by ultrasonic amplifier to generate vibration at a resonance frequency close to 20KHz. Figure 3.17 (b) shows the ultrasonic amplifier coupled with a lambda rod and ultrasonic fatigue specimen for testing in a fully reversed loading condition. The distribution of displacement and strain along the load train and ultrasonic fatigue specimen is shown in Figure 3.17 (c). An inductive vibration gage is used to measure the vibration amplitude and frequency. These measurements are used as feedback signal to control the fatigue testing. Depending on specific testing requirements, the vibration of the system can be set in two modes: continuous mode and pause/pulse mode.



(a)



(b)



(c)

Figure 3.17 Ultrasonic fatigue testing system: (a) whole testing system; (b) load train coupling with ultrasonic fatigue sample and (c) strain and displacement distribution along the load train and an ultrasonic fatigue specimen.

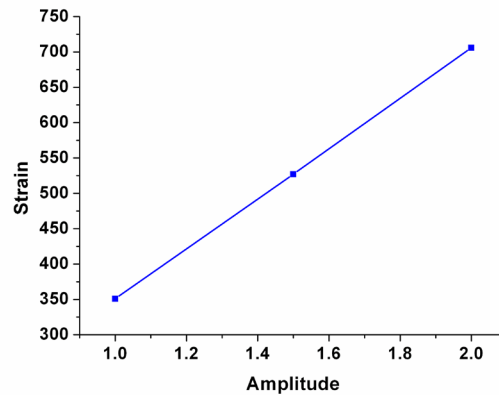
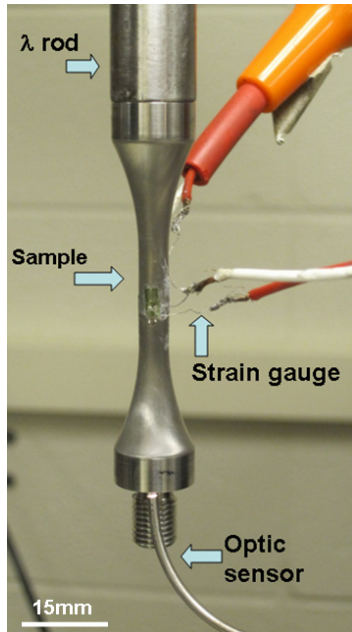
3.2.4 Experimental setup for ultrasonic fatigue testing at room temperature

Ultrasonic fatigue testing is conducted under displacement control within the nominally elastic deformation regime, and the vibration amplitude at the transducer is linearly proportional to the stress in the gauge section. The target cyclic stress for fatigue testing is thus determined by the vibration amplitude according to this linear relationship. Therefore, before each ultrasonic fatigue test is conducted, it is necessary to calibrate the system to obtain this linear relation between vibration amplitude and stress.

The calibration setup for ultrasonic fatigue testing at room temperature under fully reversed loading is shown in Figure 3.18 (a). Two strain gages are mounted on the specimen gauge section to measure the dynamic strain under low amplitude vibration. A MTI-2000 Fotonic sensor, using an optical fiber bundle, is used to measure the axial vibration displacement at the end of the specimen. This displacement measurement can be used as a secondary check on the calibration. The dynamic strain is measured in the gauge section at several input power settings to obtain the relationship between the power input of piezoelectric transducer and strain in fatigue specimens. Calibration amplitudes should be kept small to avoid fatigue damage to specimens during calibration and to assure that only nominally elastic strains are applied. An example of the linear relationship between vibration amplitude and strain is shown in Figure 3.18 (b). The required input power to achieve a specific strain or stress at the gauge section can then be extrapolated.

Alternatively, because the whole load train vibrates in the elastic regime, it is also possible to use strain in the lambda rod as input to calculate the maximum strain on the fatigue sample. In order to verify this, two strain gages were applied at the position of $\frac{1}{4}$ lambda rod to measure the maximum strain on the lambda rod. Using the strain

measurement on the lambda rod, the strain and displacement distribution along the $\frac{1}{4}$ lambda rod and in the fatigue specimen can be calculated. Figure 3.19 shows the distribution of calculated strain and displacement in the one fourth lambda rod for an ultrasonic fatigue specimen under different amplitudes of loading. It can be seen that the maximum strain occurs at the center of the gage section of the fatigue specimen.



(a)

(b)

Figure 3.18 Experimental setup for calibration of ultrasonic fatigue testing under fully reverse loading: (a) experimental setup and (b) linear relationship between vibration amplitude and strain measurement at the gauge section of the ultrasonic fatigue specimen.

The calculated strain on the fatigue specimen is compared with direct measurement using strain gages in Table 3.2. The maximum strains in the gage section predicted using the analytical solution agree very well with the experimental measurements. The maximum strain on the lambda rod is also linear with the strain at the gage section of fatigue sample. Figure 3.20 shows the linear relation between strain

measurement on the lambda rod and strain at the gauge section of fatigue specimen. This linear relationship also can be used to control ultrasonic fatigue testing.

The above method provides a useful tool for calibration for ultrasonic fatigue testing under some critical testing conditions, such as environmental ultrasonic fatigue testing. For these tests, fatigue specimens need to be placed within liquid or gaseous environment, making it is difficult to measure the strain and displacement on specimens using strain gage or optical technique described above. However, strain measurement can be obtained on the lambda rod, which can be used to calibrate the fatigue system.

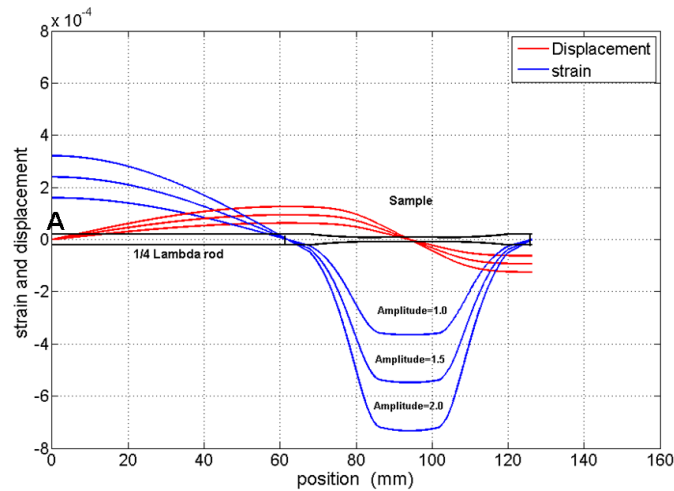


Figure 3.19 Calculated stain and displacement along the specimen and $\frac{1}{4} \lambda$ rod under loading of different amplitudes.

Table 3. 2 Comparison between experimental measurement and analytical calculation.

Amplitude	Strain At position A as indicated in Fig. 3.19	Measured Strain at the center of specimen (micro strain)	Calculated Strain at the center of specimen (micro strain)	Measured Displacement at the end of specimen (μm)	Calculated Displacement At the end of specimen (μm)
1	160	357/365	351	5.5	6
1.5	240	547/533	527	8.2	8
2	321	728/710	706	11	11

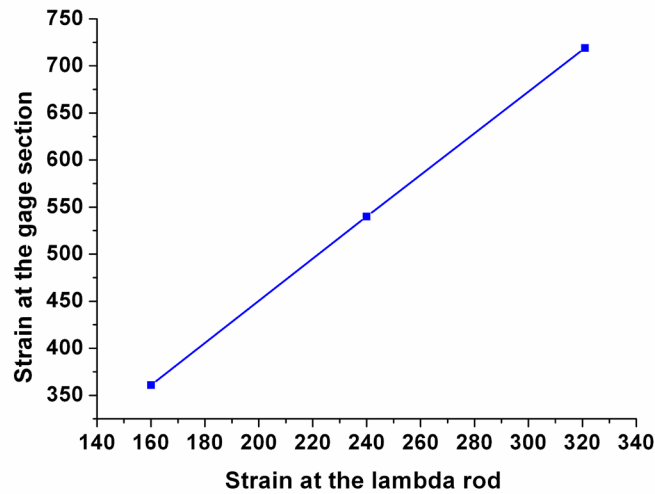


Figure 3.20 Linear relationship between strain at the gage section of ultrasonic fatigue specimen and at the one fourth of lambda rod.

3.2.5 Experimental setup for ultrasonic fatigue testing at high temperature

For ultrasonic fatigue testing with a positive mean stress, the entire ultrasonic fatigue system is housed in an a closed loop servo-hydraulic test system at the

displacement node position of a lambda rod, as indicated in Figure 3.21 (a), thus avoiding the effect on the vibration of the entire system. Ultrasonic fatigue specimens can be heated up to 1000°C by an induction heating system as shown in Figure 3.21 (b). A non-contact infrared pyrometer is used for temperature measurement and control.

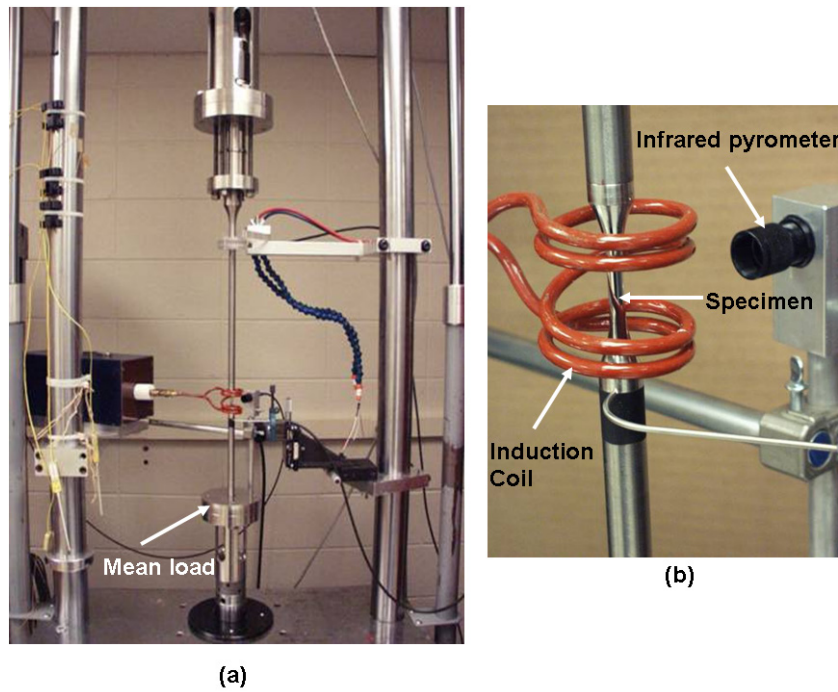


Figure 3.21 Experimental setup for ultrasonic fatigue testing at high temperature under mean load: (a) mean load and (b) induction heating and temperature control.

The main difficulty in conducting ultrasonic fatigue tests at high temperature is to obtain the linear relationship between the maximum strain on fatigue specimen and vibration amplitude. There exists a temperature gradient along the load train and fatigue specimens when the samples are heated to high temperature and conventional strain gage can not be used to measure applied strain at high temperatures.

The linear relationship between input power (vibration amplitude) and dynamic strain at the gage section of René 88 DT specimens at 593°C was verified experimentally using the interferometric strain/displacement gage (ISDG) [86]. The principle of using ISDG for strain measurement is illustrated in Figure 3.22 (a). When an incident laser beam is reflected from two reflective markers on the specimen surface, the interference between two reflective laser beams will generate fringe patterns. Figure 3.22 (b) shows an example of laser fringe patterns. Under high frequency vibration, the position of fringe patterns is changed with the motion of reflective markers on specimens. The displacement and strain of specimens thus can be converted from the motion of fringe patterns [86]. Using this method, the dynamic strain at the gage section of René 88 DT specimens at 593 °C can be measured. Figure 3.22 (c) shows an experimental measurement of dynamic strain vs vibration amplitude for René 88 DT specimen at 593° C, and the strain and input power follow a linear relationship at 593 °C.

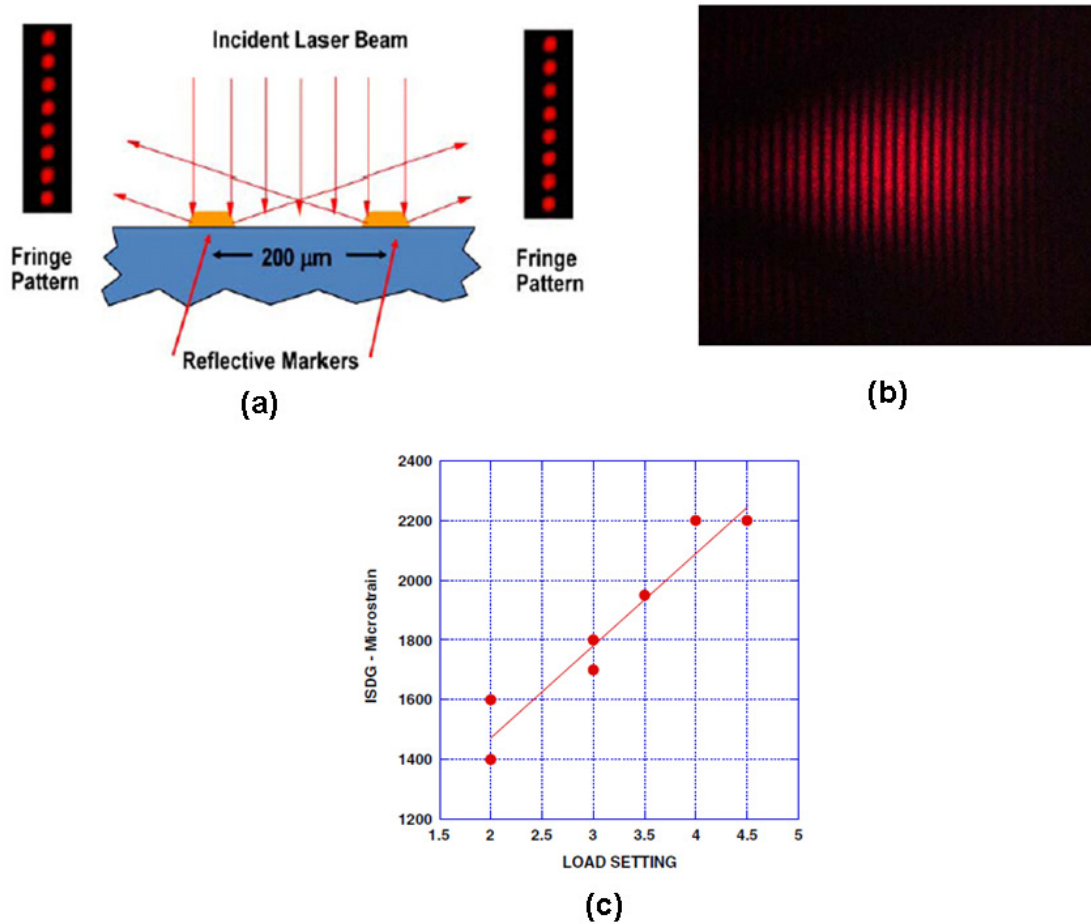


Figure 3.22 Experimental measurement of dynamic strain on René 88 DT fatigue specimen at 593°C: (a) the principle of ISDG; (b) laser fringe pattern and (c) dynamic strain versus vibration amplitude at 593°C [86].

For the calibration of ultrasonic fatigue testing of René 88 DT at elevated temperature, a high temperature strain gage was used to measure the dynamic strain at both 20°C and 593°C. Under the same vibration amplitude (input power of ultrasonic fatigue machine), the strain reading at 593°C increases about 6% as compared with the strain measurement at room temperature [62]. This strain ratio is used to calibrate fatigue testing at elevated temperature. The procedure for the calibration of elevated temperature ultrasonic fatigue testing is as follows: For each elevated temperature test, the specimen is first calibrated at room temperature following the procedures described in the previous

sections. Then the strain readings at room temperature are multiplied 1.06 to obtain the dynamic strain at elevated temperature under the same vibration amplitude. The required input power to achieve a specific strain or stress at the gage section at elevated temperature can then be extrapolated from the linear relation between the calculated dynamic strain at elevated temperature and the vibration amplitude.

3.2.6 Detection of fatigue damage using nonlinear acoustics

Cyclic deformation leads to the accumulation of fatigue damage and this can result in the nonlinearity of material behavior that can be detected and used to track damage. Higher order harmonics will be generated during acoustic wave propagation through materials having nonlinear elastic behavior. The detection and characterization of acoustics nonlinearity is, therefore, a potentially powerful tool to quantify the fatigue damage process in testing materials [87]. A nonlinear parameter β is normally used to evaluate the relative changes in nonlinear acoustic behavior. For the propagation of a one dimensional wave through a nonlinear material, the nonlinear version of Hooke's law is given as

$$\sigma = E\varepsilon(1 + \beta\varepsilon + \dots) \quad (3.11)$$

Where E is the Young's modulus of materials and β is the second order nonlinear elastic coefficient, or nonlinear parameter of materials, σ and ε are stress and strain.

The equation of motion for a one-dimensional longitudinal wave is written as

$$\rho \frac{\partial^2 u}{\partial t^2} = \frac{\partial \sigma}{\partial x} \quad (3.12)$$

Where ρ is the density of the material, U is the displacement, and x is the propagation distance. By combining the equation 3.11 and 3.12 and the strain and displacement relation, the nonlinear wave equation can be rewritten as follows:

$$\rho \frac{\partial^2 u}{\partial t^2} = E \frac{\partial^2 u}{\partial x^2} \left(1 + 2E\beta \frac{\partial u}{\partial x} \right) \quad (3.13)$$

Using perturbation analysis, the solution of above wave equation can be obtained as:

$$\begin{aligned} u &= -\frac{1}{8} \beta k^2 A_1^2 x_1 + A_1 \cos(kx_1 - \omega t) + \frac{1}{8} \beta k^2 A_1^2 x_1 \cos(2(kx_1 - \omega t)) + \dots \\ &= A_0 + A_1 \cos(kx_1 - \omega t) + A_2 \cos(2(kx_1 - \omega t)) + \dots \end{aligned} \quad (3.14)$$

Where, $k=\omega/c$, c is the longitudinal wave velocity and ω is the fundamental frequency of the wave. From this equation, we can get the expression for β using the amplitudes of the first and second harmonics:

$$\beta = \frac{8}{k^2 x} \cdot \frac{A_2}{A_1^2} \quad (3.15)$$

It is noted from the above equation that the nonlinear parameter β is proportional to the magnitude of the second harmonic A_2 . By measuring the magnitude of the first and second harmonic and knowing the wave velocity and fundamental frequency, the nonlinear parameter β can be determined.

The nonlinear parameter can be related to the higher order elastic constant of materials using the following equation [88]:

$$\beta = \frac{\bar{C}_{111111} + 3\bar{C}_{1111}}{\bar{C}_{1111}} \quad (3.16)$$

Where \bar{C}_{1111} and \bar{C}_{111111} are the second order and third order elastic constants of the testing material respectively. From this equation, it can be seen that the nonlinear parameter is an intrinsic property of the material.

In conventional nondestructive ultrasonic methods, the nonlinear behavior of fatigued specimens is examined by transmitting an acoustic wave into samples and detecting the feedback signals. However, during ultrasonic fatigue testing, fatigue specimens are driven by high power ultrasonic waves. It is therefore possible to directly detect the vibration behavior of the ultrasonic specimens to obtain information on nonlinear behavior of fatigue specimens during ultrasonic fatigue testing. Two in-situ techniques have been explored for René 88 DT to acquire nonlinear acoustic information. The first method employs a laser vibrometer to detect the vibration behavior of testing specimens [89]. The second method directly collects this information from the feedback signal used to control the ultrasonic transducer in the load line, which is then analyzed using a Labview program to obtain the frequency spectrum [90]. Figure 3.23 shows the frequency spectra from feedback signals of René 88 DT sample vibrating under different fully reversed cycling at different stress amplitudes.

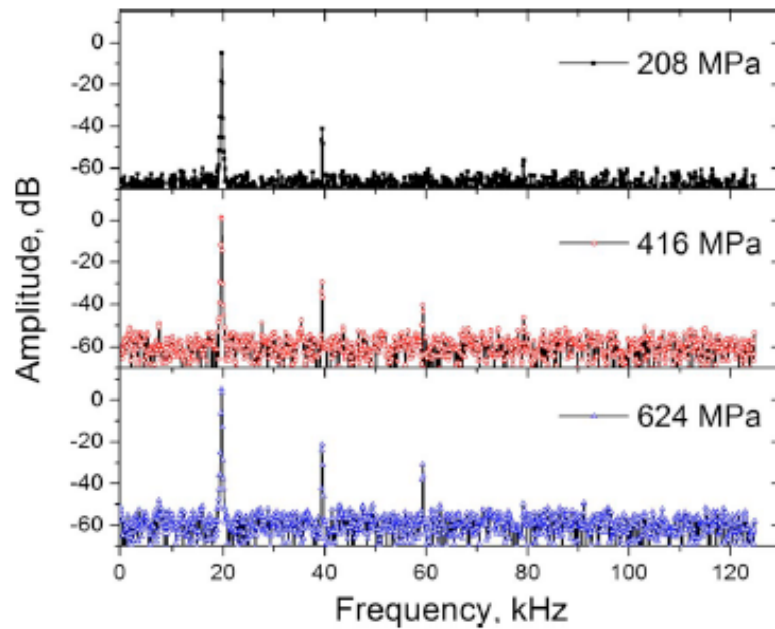


Figure 3.23 Frequency spectra of feedback signals collected on René 88 DT specimens vibrated under fully reversed loading at different cyclic stresses [90].

3.2.7 Ultrasonic fatigue sample preparation

The testing material was cut from a forged René 88 DT pancake and ultrasonic fatigue specimens were machined using low stress grinding of the gage section. The dimensional and geometry of the fatigue specimens used in this study are shown in Figure 3.24. The ultrasonic fatigue specimen drawing for René 88 DT is given in Appendix 1.

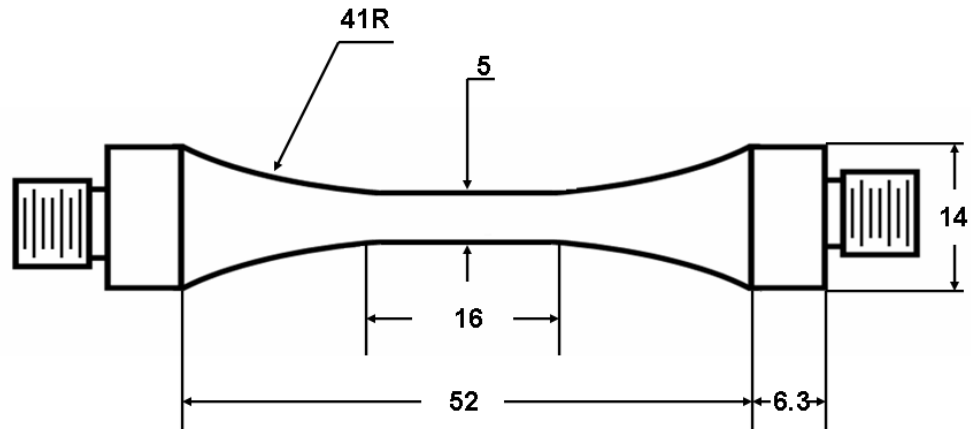


Figure 3.24 Illustration of the geometry and dimensions of René 88 DT ultrasonic fatigue specimens (All dimensions are in mm.).

The diameter of the as-machined specimen was further reduced by approximately 100 μm by electropolishing in order to minimize the effect of surface residual stress produced by machining. Electropolishing was conducted using an electrolyte of 55% ethanol with 35% butyl cellusolve and 10% perchloric acid at 40 V and -30°C .

Chapter 4

Quantitative Characterization of Crack Initiation Sites in René 88 DT Fatigued at 593°C

This chapter covers two topics: the ultrasonic fatigue behavior of René 88 DT at elevated temperature and quantitative characterization of fatigue crack initiation sites. In the first part, the S-N behavior of René 88 DT at 593°C and the general fractographic observations of fatigue failure are presented. In the second part, the crystallographic nature of the fatigue fracture surfaces is described along with the quantitative SEM stereo imaging techniques developed as part of this dissertation research for the determination of the spatial orientation of crystallographic facets. The crystallographic orientation of fatigue fracture facets are quantitative determined by combining SEM stereo image technique with EBSD. In Chapter 5, the results of the characterization described here will be used to develop a more complete understanding of the mechanisms of fatigue crack initiation at elevated temperatures in René 88 DT at very long lifetimes.

4.1 Ultrasonic fatigue behavior of nickel-based superalloy René 88DT at 593°C

4.1.1 S-N data of René 88 DT at 593°C

The fatigue behavior of the nickel-base superalloy René 88 DT was investigated in the lifetime regime of $10^5 \sim 10^9$ cycles at 593°C for a load ratio of 0.05 at a nominal frequency of 20 KHz. The stress-life data (S-N curve) of René 88 DT at 20 KHz are

plotted in blue in Figure 4.1. All test results are also listed in Appendix 2. The fatigue behavior of the same material was also investigated using conventional fatigue testing at 593°C for a load ratio R ($R = \sigma_{\max}/\sigma_{\min}$) of 0.05 at a frequency of 10Hz [61]. The conventional fatigue testing results are also shown in Figure 4.1 for comparison. The control scheme for these two fatigue testing methods is different. As presented in Chapter 3, ultrasonic fatigue testing is conducted under displacement control, while conventional fatigue testing for the data reported here is conducted using load control. As shown in Figure 4.1, the ultrasonic fatigue test results at lower stress levels follow the same trend as the conventional fatigue test results at higher stress levels. Fatigue life and the variability of fatigue life increase with decreasing stress amplitude. Fatigue failures are observed to occur at lifetimes well beyond 10^7 cycles. Furthermore, the variability in fatigue life exceeds two orders of magnitude at $\sigma_{\max} = 600$ MPa in ultrasonic fatigue testing, as shown in Figure 4.1.

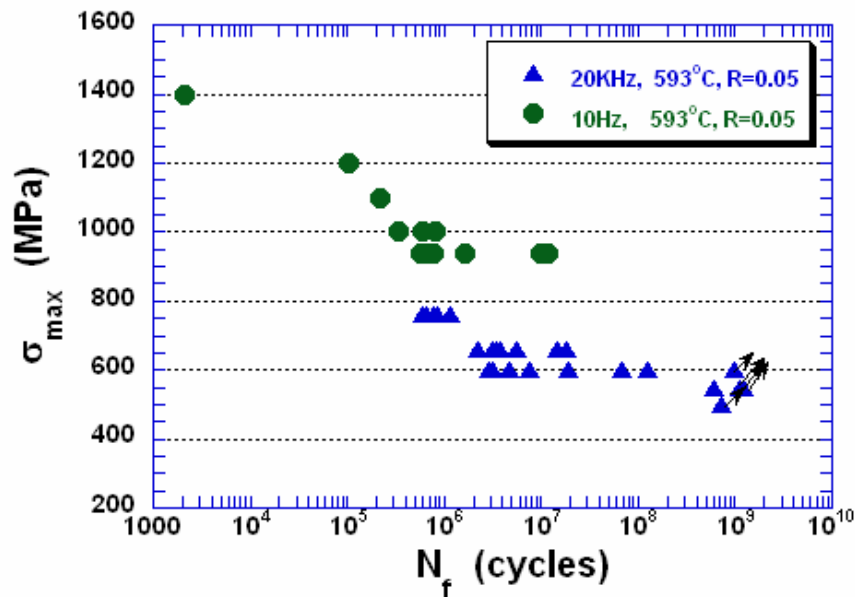
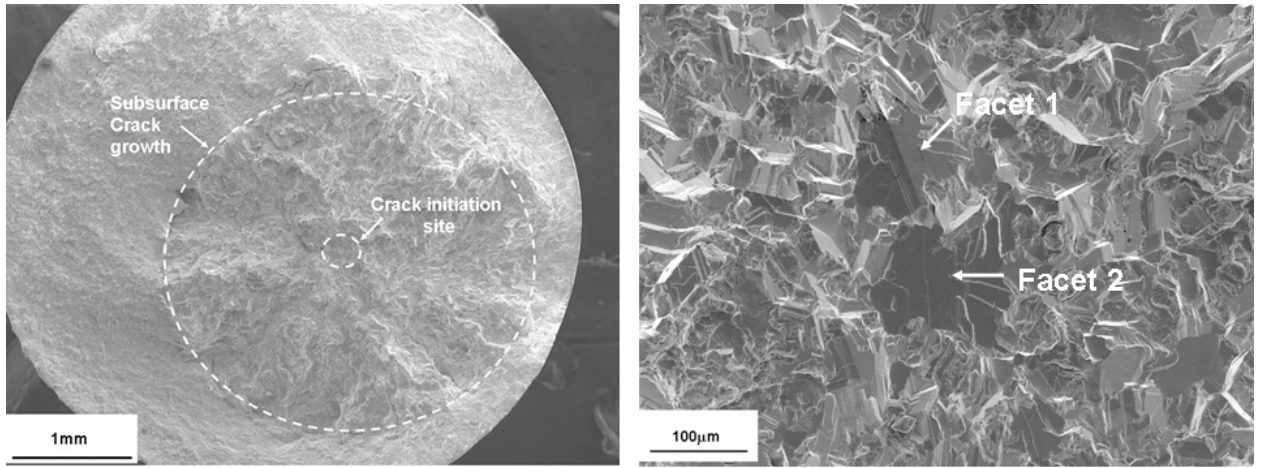


Figure 4.1 S-N data of René 88 DT at 593° C for both ultrasonic fatigue and conventional fatigue [61].

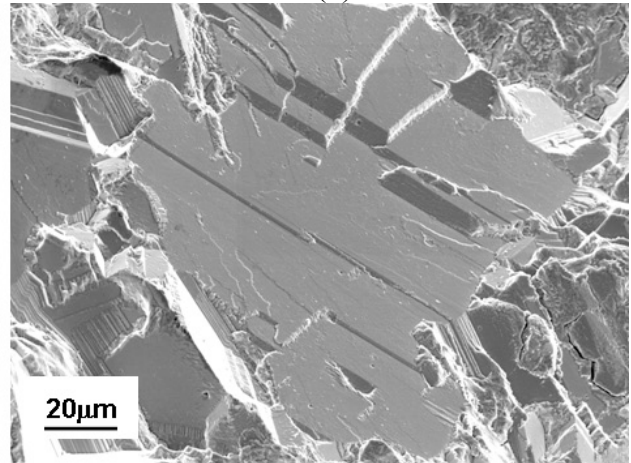
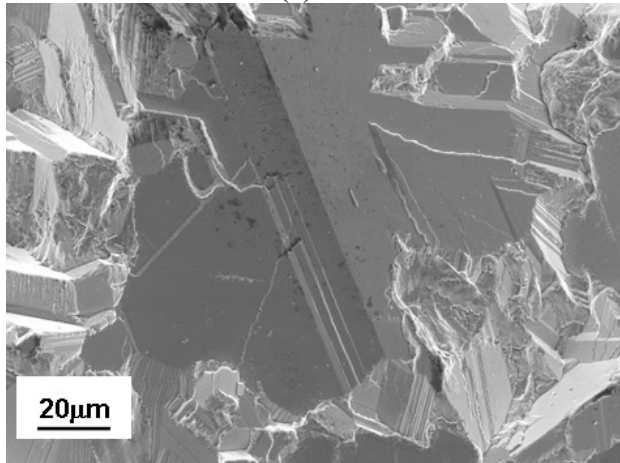
4.1.2 General fractographic observations

The fracture surfaces of 21 failed specimens from ultrasonic fatigue tests were examined using scanning electron microscopy. At 593°C all fatigue failures initiated internally and in 20 specimens, fatigue failure initiated in large grains. Figure 4.2 shows the typical features of subsurface initiation at large grains and subsequent crack propagation. . Among all failed fatigue specimens, one failed from subsurface large inclusion as shown in Figure 4.3



(a)

(b)



(c)

(d)

Figure 4.2 Typical subsurface fatigue fracture surface at elevated temperature: (a) SEM image of fracture surface, (b) large crystallographic facets at crack initiation site, (c) and (d) high magnification SEM images of two large facets at the fatigue crack initiation site as indicated in (b). ($\sigma_{\max} = 660$ MPa, $N_f = 3.44 \times 10^6$ cycles, 593°C).

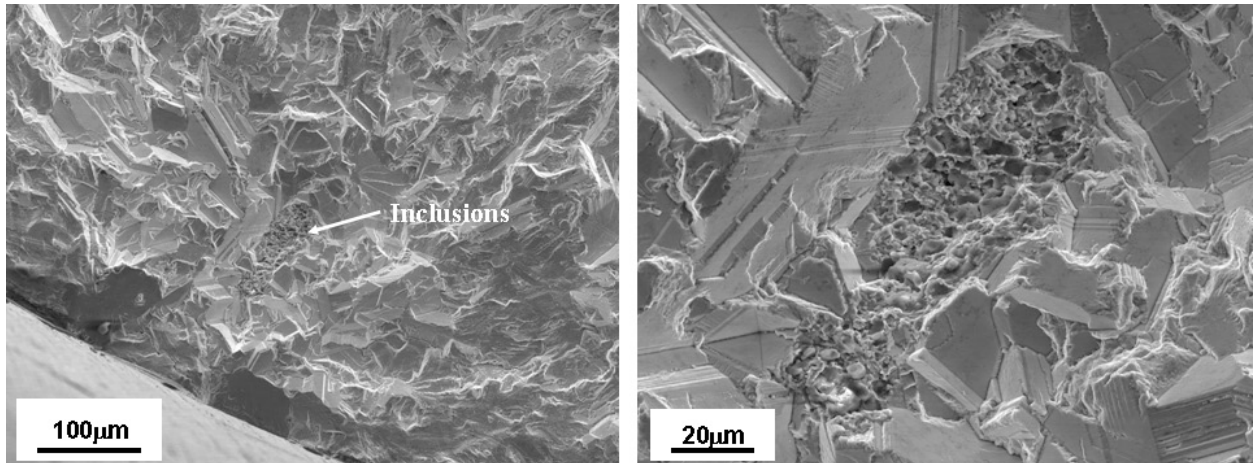


Figure 4.3 Fatigue crack initiation from subsurface large inclusion ($\sigma_{\max} = 600\text{MPa}$, $N_f = 6.64 \times 10^7$ cycles, 593°C).

Fatigue fracture surfaces observed at 593°C can be divided into three regions: 1) crack initiation site, 2) subsurface propagation 3) fatigue crack propagation with exposure to air. The third region occurs if the propagating fatigue crack intersects the specimen surface. The first region is the crystallographic fatigue crack initiation site, consisting of one large facet or a facet cluster that includes several large crystallographic facets. Figure 4.2 (c) and (d) shows the detailed features of two large crystallographic facets in a facet cluster at the crack initiation site indicated in Figure 4.2 (b). It can be seen that the surface of these large crystallographic facets is very smooth and no evidence of initiation from inclusions or pores exists. Figure 4.4 shows another example of a crystallographic crack initiation site. Similarly, there is a facet cluster consisting of two large crystallographic facets at the fatigue crack initiation site. The SEM images from matching halves of large crystallographic facets at crack initiation sites in Figure 4.4 show that these large facets were formed within large grains by transgranular cracking.

The projected size of these large crystallographic facets is about 3~6 times the average grain size of this alloy, which is about 20 μm .

The second region on the fatigue fracture surface is the subsurface fatigue crack propagation area. The environment in which fatigue cracks propagate in subsurface regions is isolated from ambient air and fatigue cracks propagate without interaction with environment. As shown in Figure 4.2 (b), the second region also contains numerous crystallographic facets. These crystallographic facets were formed during fatigue crack propagation period rather than crack initiation. The size of the second region on fracture surface depends on the position of the crack initiation sites. If the crack initiation site is far away from the surface, the size of second region will be very large. Figure 4.2 (a) shows an example of fatigue fracture surface with a very large subsurface crack growth region. Figure 4.5 shows the fracture surface of a specimen whose fatigue crack initiation site is close to the specimen surface. As shown in Figure 4.5 (a), the subsurface crack propagation region is much smaller as compared with that for the specimen shown in Figure 4.2 (a). There is a large crystallographic facet at the fatigue crack initiation site of this specimen as shown in Figure 4.5 (b). When fatigue cracks propagate to the specimen surface, environmental interactions may affect subsequent fatigue crack growth. This fatigue crack growth region corresponds to the third region on fatigue fracture surface.

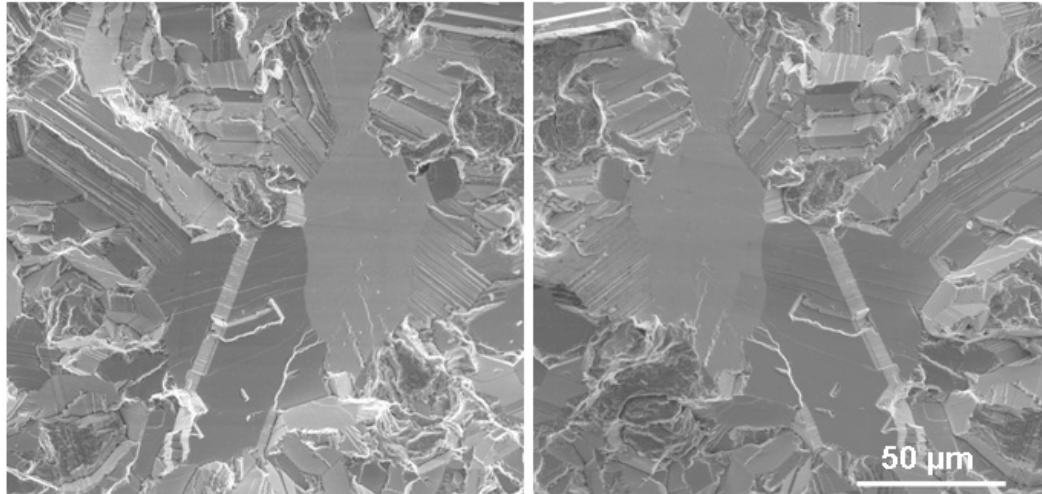


Figure 4.4 SEM matching halves of large crystallographic facets at fatigue crack initiation sites. ($\sigma_{\max} = 600\text{MPa}$, $N_f = 3.16 \times 10^6$ cycles, 593°C).

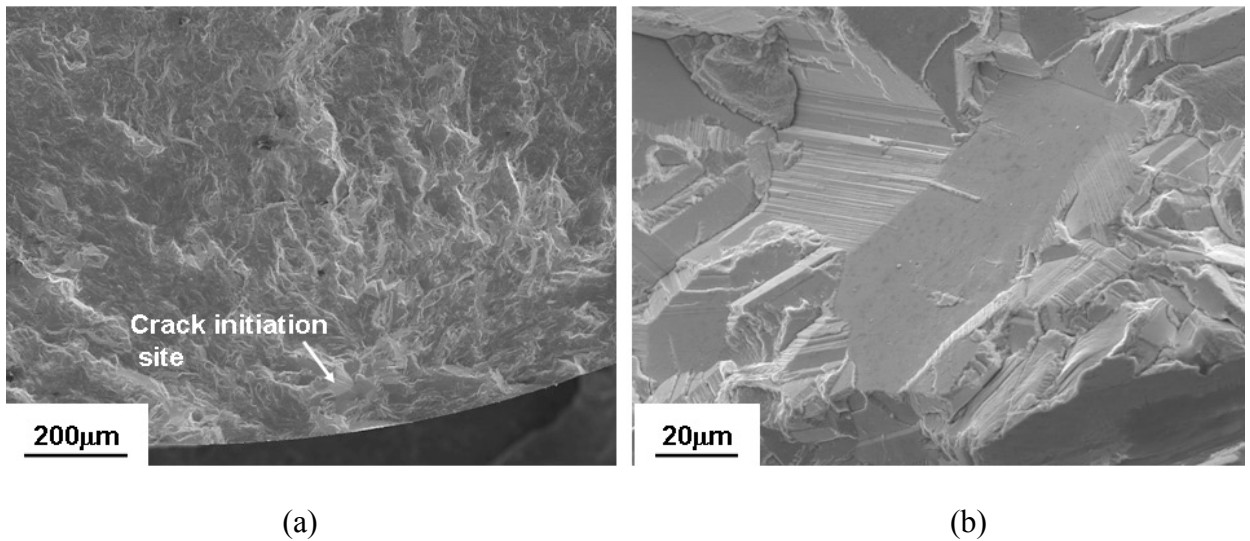


Figure 4.5 Fatigue failure initiated in the region close to specimen surface: (a) fatigue fracture surface and (b) Large crystallographic facet at fatigue crack initiation site. ($\sigma_{\max} = 760\text{MPa}$, $N_f = 6.5 \times 10^5$ cycles, 593°C).

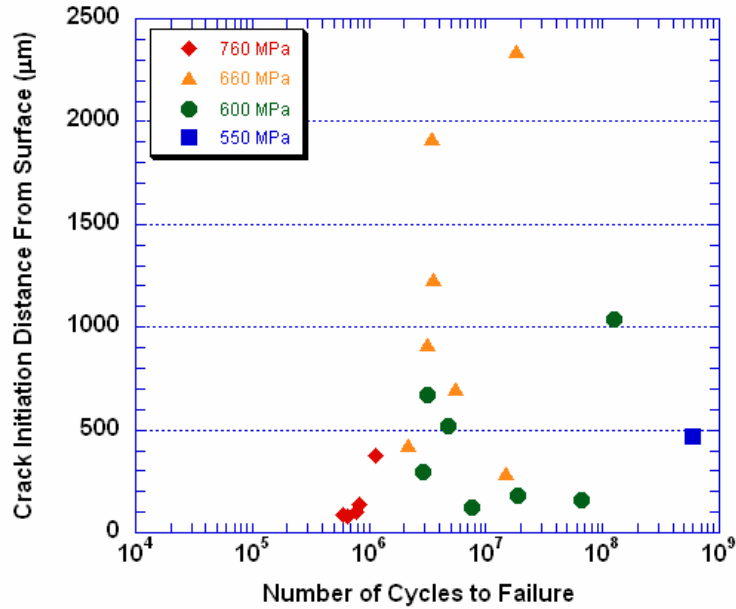


Figure 4.6 The relationship between fatigue life and the distance between fatigue crack initiation sites and specimen surface (The diameter of the gage section is 5 mm).

The distances between fatigue crack initiation sites and the specimen surface for failed specimens are plotted with respect to fatigue life in the Figure 4.6. At higher stress (760MPa) in the shorter lifetime regime, fatigue life increases with the increase of the distance of the initiation site from the surface. However, at lower stresses (600 MPa) in the longer life regime, there is no direct correlation between fatigue life and the distance between fatigue crack initiation sites and specimen surface. The fatigue crack propagation life can be calculated using the results obtained in the previous work on small crack growth behavior in this alloy at 593°C [91]. Figure 4.7 shows the comparison between predicted fatigue crack growth life and the experimental total fatigue life. Two initial small crack sizes for fatigue crack growth life calculation were selected as 60μm and 120 μm which correspond to the observed size of crack initiation grains. As shown in Figure 4.7, at the higher stress (760 MPa) and correspondingly shorter fatigue life (~ 10⁵

cycles), the calculated fatigue crack growth life is close to the measured total fatigue life. The calculation of the fatigue crack growth life is based on surface small crack growth rate, which may be faster than subsurface crack growth rate due to less microstructure constraint and without interaction with environment. It has been reported that the fatigue crack growth rate of this alloy in vacuum is smaller than crack growth rate in air at 593°C [61]. Therefore, it can be expected the actual fatigue crack growth life may be longer than the predicted the crack growth life. Thus, at higher stress level and shorter fatigue lifetime, fatigue crack growth life is likely to be the major portion of the total fatigue life. Moreover, if the fatigue crack initiates at locations far away from the specimen surface, the subsurface crack growth period will be longer, thus the total fatigue life will be longer as compared with the fatigue life of specimens failed at locations close to specimen surface. As shown in Figure 4.7, the scatter of the predicted fatigue crack growth life is also on the same order of the scatter of experimental total fatigue life at 760MPa.

However, at a lower stress level (600MPa) and longer lifetime ($10^6\sim 10^9$ cycles), both the total fatigue life and the variability of fatigue life are much greater than the predicted fatigue crack growth life. Fatigue crack initiation life dominates the total fatigue life. The large variability in fatigue life is due to the variability in fatigue crack initiation. Therefore, the locations of fatigue crack initiation have no large effects on the total fatigue life at lower stress levels. In this circumstance, the study of fatigue crack initiation mechanisms in this alloy is crucial for investigating the large variability in fatigue life in the very high cycle regime.

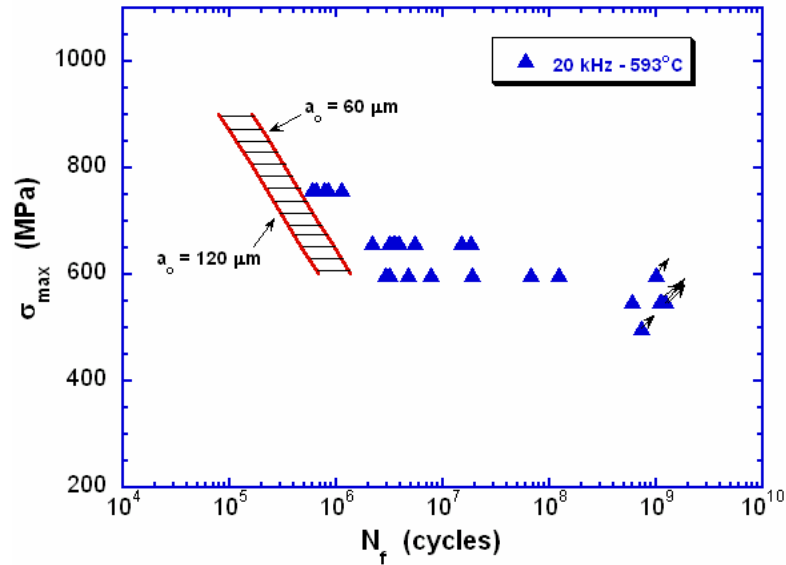


Figure 4.7 Comparison between fatigue growth life and experimental total fatigue life (Fatigue crack growth data are courtesy of Amit Shyam [91]).

4.2 Quantitative characterization of crystallographic fracture surface

The characteristics and features of fatigue fracture surfaces depend on both intrinsic microstructure features and testing conditions such as temperature, environment and fatigue variables (mean stress, frequency and stress amplitude). Facet formation associated with strain localization and subsequent fatigue crack initiation and propagation on specific slip systems has been frequently observed in numerous nickel-based superalloys fatigued under a range of test conditions [61,62,92-95]. The crystallography of fatigue fracture surfaces can therefore provide important information about cyclic deformation processes, fatigue crack initiation and propagation mechanisms and the interaction of fatigue cracks with local microstructure such as grain boundaries. In general, the crystallographic orientation of facets produced by fatigue fracture in nickel-based superalloys can be of $\{111\}$ type or $\{001\}$ type. Gell and Leverant found $\{111\}$

type fracture surfaces in a nickel based alloy fatigued at room temperature [92]. In studying the low cycle fatigue behavior of IN100, Li et al. [93] found fatigue crack growth along $\{001\}$ planes at room temperature, while at elevated temperature, the fatigue crack propagate along $\{111\}$ planes. King [94] observed both $\{001\}$ and $\{111\}$ type facets at room temperature. K. Sadansnda and P. Shahinian reported $\{001\}$ faceted fracture surface in the nickel-base alloy Udimet 720 at both RT and 850 °C [95].

Different techniques, including both qualitative and quantitative methods, have been used to characterize the crystallography of facets in nickel-based superalloys. The shape of γ' precipitates on the crystallographic facet plane has been used to quantitatively determine the crystallography of facets in some nickel-based superalloys [93, 94]. Laue x-ray diffraction method also can be used to identify the orientation of facets in nickel-based superalloy with large grain size [92]. However, these methods are limited by the specific microstructure features of the investigated alloys. In recent years, the electron backscattering diffraction technique has been widely used to characterize the fracture and cracking behavior of engineering materials [96]. The main advantage of using EBSD to determine the crystallography of fatigue fracture surface is that large amount of crystallographic data can be easily collected in a short time, enabling statistical sampling to connect the features observed on fracture surface to the crystallographic orientation of the local microstructure.

Generally, there are two methods available for the determination of the crystallography of fracture surfaces using EBSD: the direct method and the indirect method. In the direct method, electron backscattering diffraction patterns are collected directly from the facet itself [97, 98]. This technique is useful for studying fracture

surface having low roughness. If the fracture surface is very rough, EBSD patterns will be obstructed by the fracture surface. In the indirect method, EBSD patterns are collected from microstructure just beneath the fracture surface. The crystallography of the fracture surface is then determined by combining the spatial orientation of facets and crystallographic orientation of grains where the facets formed. There are two methods available for determining the spatial orientation of crystallographic facets: stereo photogrammetry [97] and quantitative tilt fractography [98-100], both of which are based on the processing of SEM stereo images. In the following sections, the details of the use of these techniques to study the crystallography of fracture surfaces are presented.

4.2.1 Determination of the spatial orientation of crystallographic facets

Figure 4.8 illustrates the definition of spatial orientation of a crystallographic facet on a fatigue fracture surface. An orthogonal coordinate system is chosen such that the Z direction of specimen coordinate coincides with the cyclic loading direction and because the specimen is cylindrical, the X and Y directions of the orthogonal coordinate are arbitrarily selected. The X-Y plane is normal to the Z direction. The spatial orientation of the crystallographic facet is defined as the orientation of the facet normal within the specimen coordinate system. The most important aspect related to the spatial orientation of crystallographic facets is the angle between the facet normal and the Z direction, as indicated in Figure 4.8. Two methods that utilize stereo images can be used to identify the spatial orientation of crystallographic facet: stereo photogrammetry and quantitative tilt fractography. In the stereo photogrammetry method, the determination of spatial orientation of a facet requires three-dimensional reconstruction of the fracture surface, while in the quantitative tilt fractography, this determination process does not

involve a 3D reconstruction process. In the following sections, the application of both methods will be presented. The advantages and disadvantages of using these two methods in studying spatial orientation of crystallographic fracture surfaces will also be described.

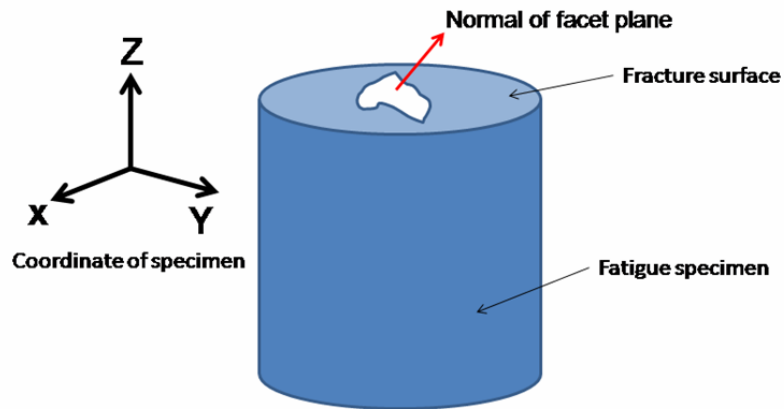


Figure 4.8 Illustration of the definition of spatial orientation of a crystallographic facet.

4.2.1.1 Stereo-photogrammetry

Stereo-photogrammetry is a computer-assisted technique to obtain three dimensional reconstruction of surface morphology using digital image correlation of SEM stereo pairs [97,101]. Figure 4.9 shows a flow chart of the procedures involved in three-dimensional reconstruction. First, SEM stereo images of the target surface are captured by tilting specimens to two different angles, normally within $5\sim 10^\circ$. The tilting angles for capturing an SEM image depend on the surface roughness of specimens. If the surface has small roughness, large tilting angles will be needed for better reconstruction results. The SEM stereo pairs are next preprocessed to remove image noises. Following this step, an automated area searching method is used to find identical points or

homologous points on SEM stereo pair images. Identical points are defined as the image points of the same feature on the specimen surface. After identical points on SEM stereo pairs are found, digital elevation can be calculated using the parallax between two identical points on a SEM stereo pair. These 3D reconstruction surface data can then be used for further analysis.

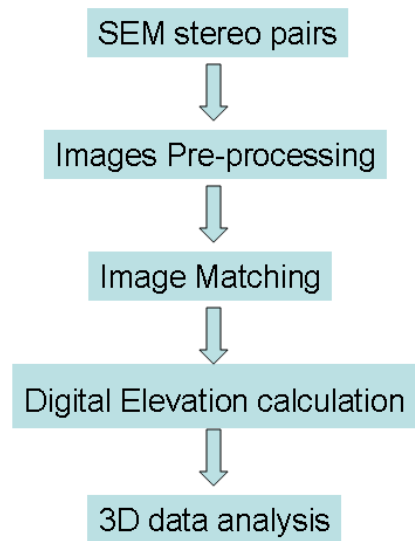


Figure 4.9 Flow chart of three-dimensional reconstruction using SEM stereo pairs.

Figure 4.10 shows an automated searching method used to find identical points on an SEM stereo pairs. As indicated in Figure 4.10, the projected positions of a feature on specimens onto two SEM stereo images are (x_1, y_1) and (x_2, y_2) respectively, which correspond to the two identical points mentioned above. First, two search windows with equal size are defined on two images. Then the search window in the first image is moved within a larger searching area to compute the best matching between two searching windows. This best matching corresponds to the position where the cross

correlation of two search window area reaches a maximum value as indicated in Figure 4.10.

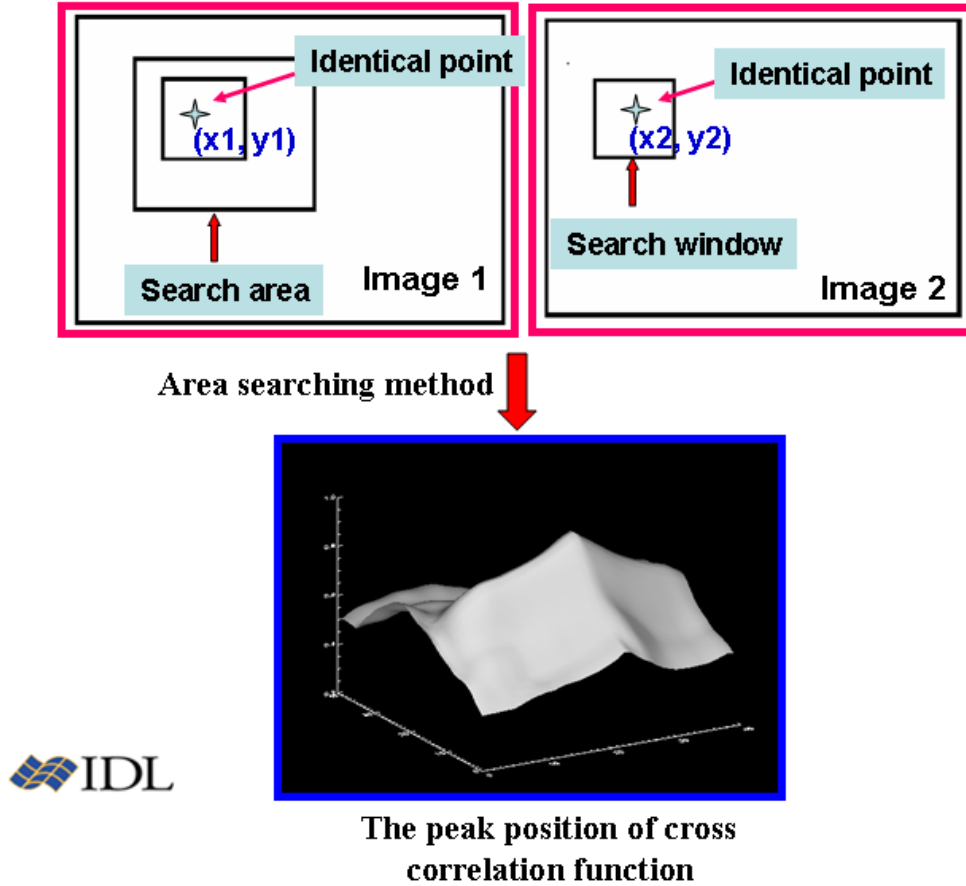


Figure 4.10 Illustration of the automated searching method used for finding identical points on SEM stereo pairs.

After the identical points of a feature are identified, the three dimensional coordinate of this feature can be given as [102]:

$$\begin{aligned}
 X &= \frac{2d - 2Z \cos(\Delta\phi)}{d/x_1 + d/x_2} \\
 Y &= \frac{(Z \cos(\Delta\phi) - d)(2y_1 - \Delta y)}{(\Delta y) \sin \Delta\phi - 2d \cos \Delta\phi} \\
 Z &= \frac{(\Delta y) \cos(\Delta\phi) + (2y_1(y_1 - \Delta y)/d) \sin(\Delta\phi)}{\left(1 + y_1(y_1 - \Delta y)/d^2\right) \sin(2\Delta\phi) + (\Delta y/d) \cos(2\Delta\phi)}
 \end{aligned} \tag{4.1}$$

Here, X, Y, Z are three coordinates of this feature, (x1,y1) and (x2, y2) are the projection coordinates of this feature on two SEM images respectively. The parameter $\Delta\phi$ is the tilting angle used for capturing two stereo images, Δy is the parallax of this feature on two stereo images.

A program was developed using IDL (interactive data language) to accomplish this automated search and reconstruction process. A sample with known geometry can be used to verify the accuracy of the three-dimensional reconstruction program. A Vickers hardness indent was applied on a flat specimen surface for this purpose. Figure 4.11 shows a SEM stereo pair of a Vickers hardness indent. The SEM Stereo pair was captured by tilting the specimen at $\pm 7^\circ$. The SEM stereo pair was input into the program and the three-dimensional shape of the indent was constructed and is shown in Figure 4.12. Figure 4.13 shows a cross section profile of the 3D reconstructed indent. The angle between opposite surface of the indent was calculated as 138° which is close to the standard 136° angle of a Vickers hardness indent.

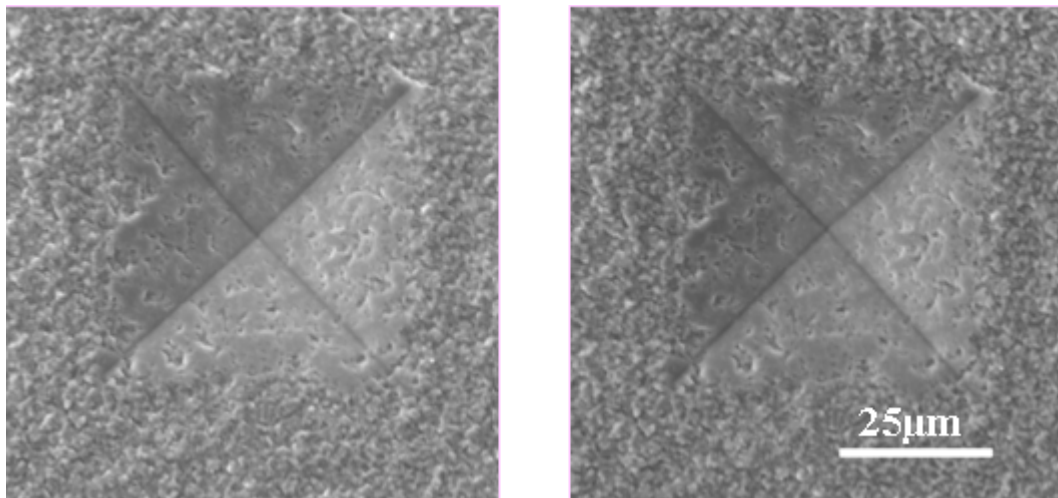


Figure 4.11 SEM stereo pair of a Vickers hardness indent captured by tilting the sample at $\pm 7^\circ$.

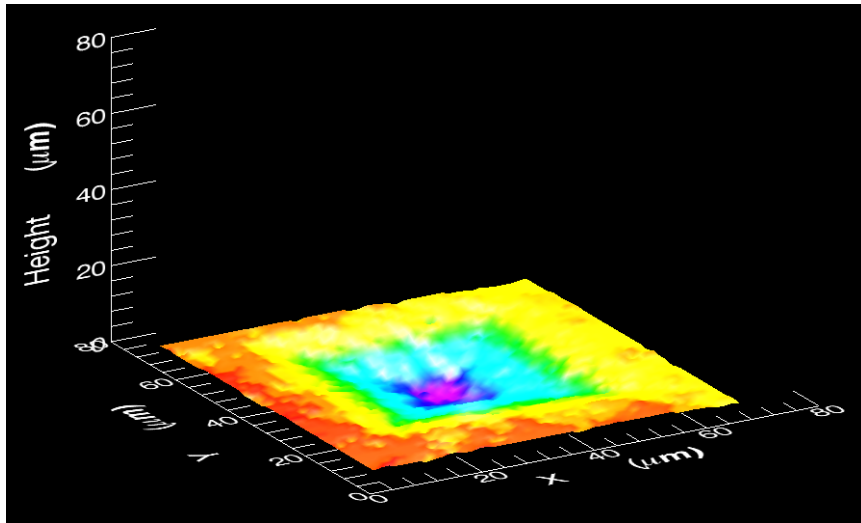


Figure 4.12 3D Reconstruction of the Vickers hardness indent.

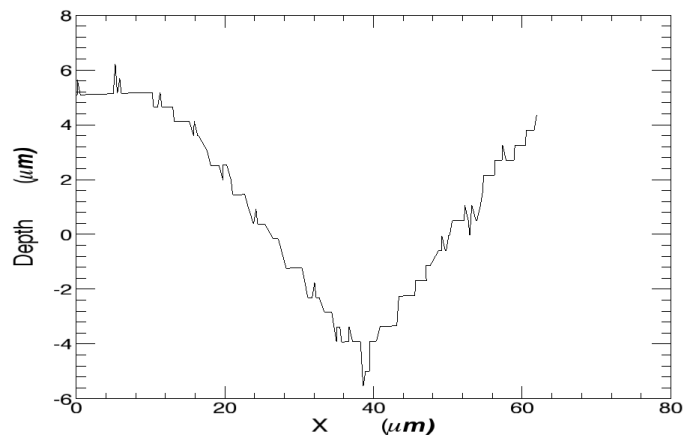


Figure 4.13 Cross-section profile of 3D reconstructed indent.

As compared with other techniques used for the characterization of surface morphology, such as atomic force microscopy, SEM-image-based stereo photogrammetry is more useful for the analysis of surfaces with large elevation change, such as fracture surface, which in most case can not be investigated using atomic force microscopy, as well as more useful for the large areas associated with fracture surfaces.

The facets at fatigue crack initiation sites were quantitatively examined using this SEM stereo image based stereo photogrammetry. Figure 4.14 (a) shows a SEM stereo pair of the initiation site in the subsurface region of a failed fatigue specimen fatigued at $\sigma_{\max} = 660\text{MPa}$ and with a fatigue life of 3.51×10^6 . The SEM stereo pair was captured by titling the sample at $\pm 5^\circ$. As shown in Figure 4.14 (a), there is a cluster of large crystallographic facets consisting of three facets F1, F1 and F3 at the crack initiation site. Figure 4.14 (b) shows the contour line plot of the 3D reconstructed fracture surface and Figure 4.14 (c) shows a 3D view of the reconstruction surface. It can be seen that the large crystallographic facet at the fatigue crack initiation site is inclined to the loading axis, and an inclination angle of 42° was calculated, indicating that the facet plane is oriented close to the maximum resolved shear stress plane.

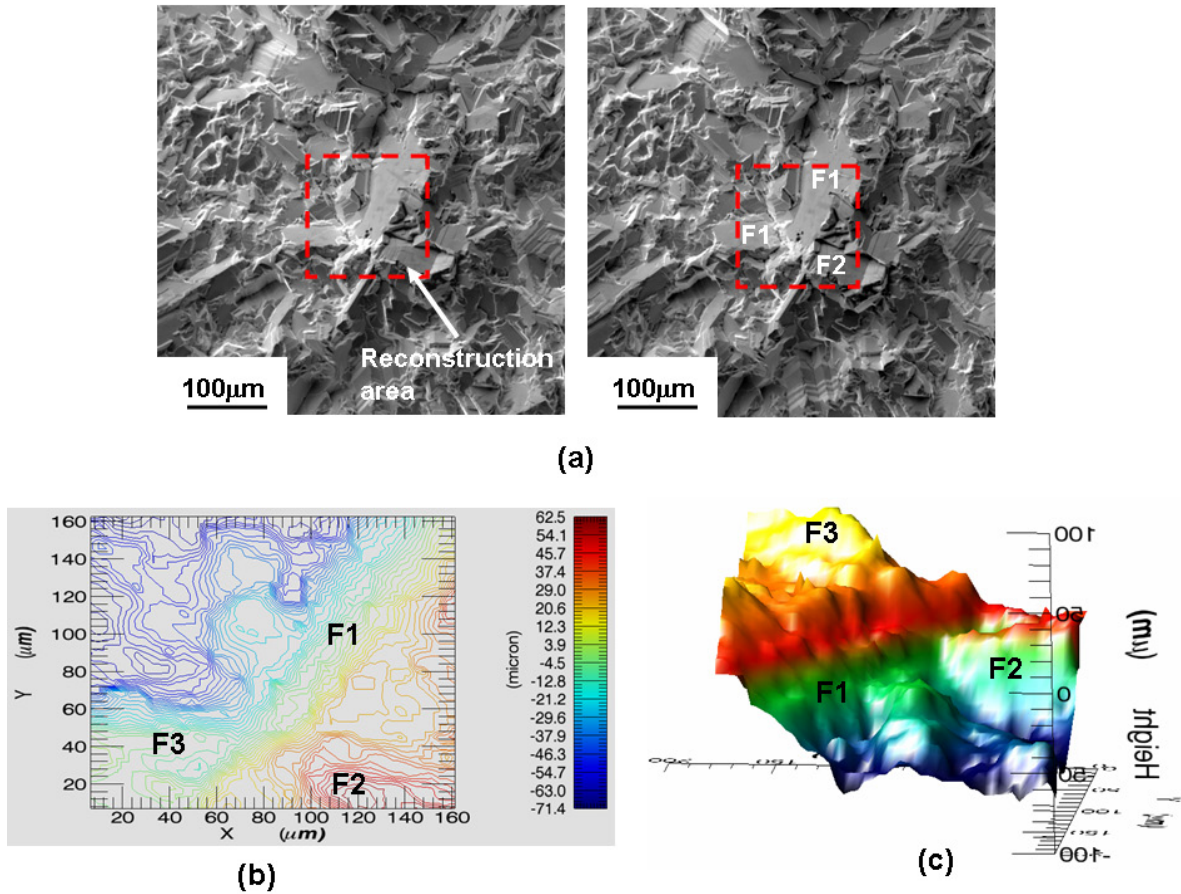


Figure 4.14 3D reconstruction of crystallographic fatigue crack initiation site: (a) SEM stereo image of crystallographic crack initiation site, (b) contour plot of 3D reconstruction fracture surface, (c) 3D view of crystallographic fatigue crack initiation site from different view angles. ($\sigma_{\max} = 660\text{MPa}$, $N_f = 3.51 \times 10^6$ cycles, 593°C).

Two types of crystallographic facets at fatigue crack initiation sites have been identified using this technique: sites with a single plane facet and sites with a chevron facet. The chevron facet is characterized by two intersecting facet planes. Figures 4.15 (a) and (b) show examples of the two types of fatigue crack initiation sites. It is difficult to distinguish differences between these two type facets using SEM imaging alone. Figures 4.15 (c) and (b) show the 3D view of the reconstructed surfaces of these two locations. The crystallographic facet in Figure 4.15 (a) has chevron topography, while the

facet shown in Figure 4.15 (b) is a single facet plane. The detailed microstructure and formation mechanisms for these two types of facets at fatigue crack initiation sites will be presented in Chapter 5.

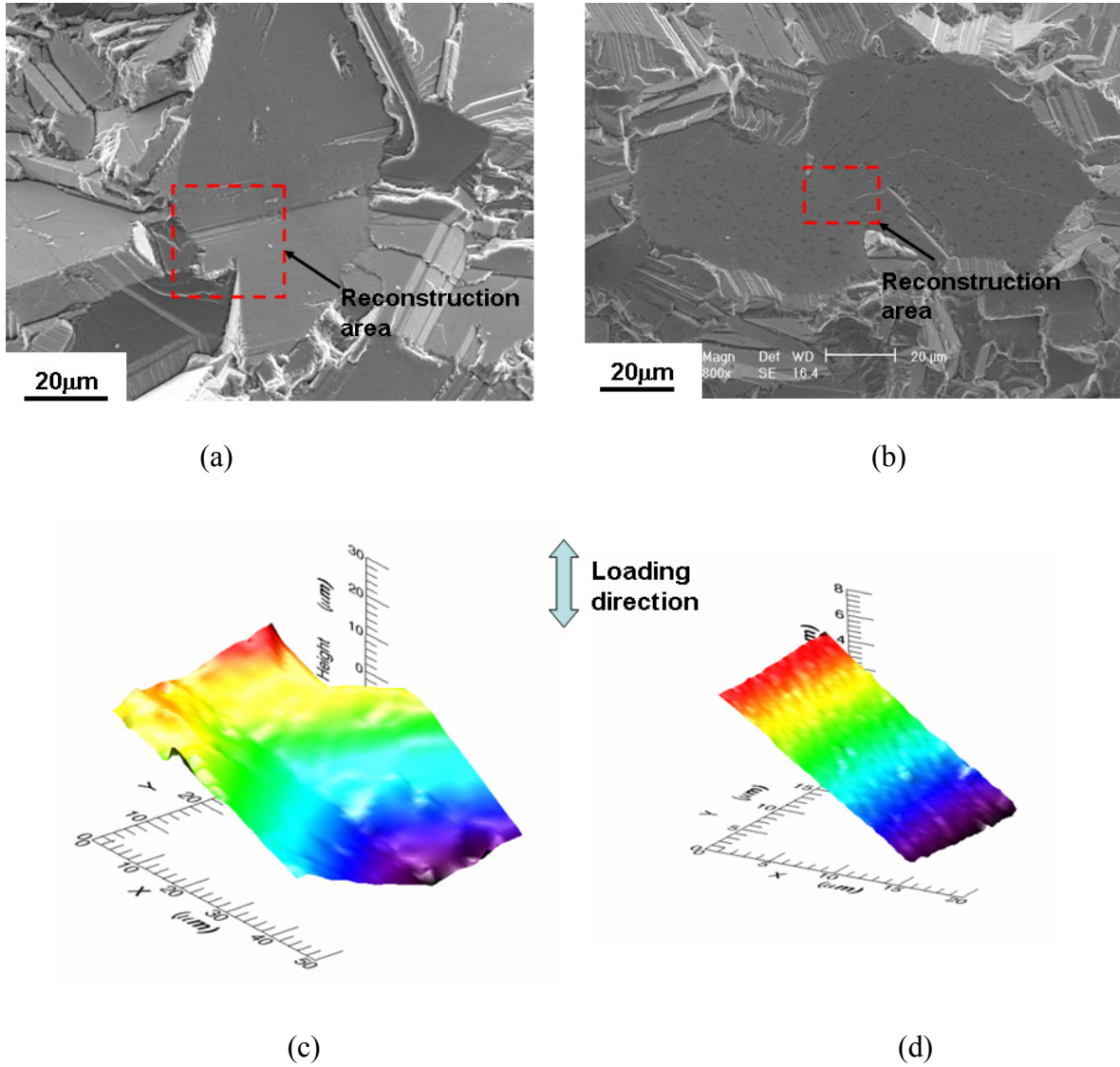


Figure 4.15 Two type crystallographic facet at fatigue crack initiation site: a) SEM images of two types of facet at fatigue crack initiation site, b) 3D view of two types of crystallographic facet at fatigue crack initiation sites. (testing condition for the specimen in image a): $\sigma_{\max} = 600\text{MPa}$, $N_f = 1.89 \times 10^7$ cycles, 593°C , testing condition for the specimen in image b): $\sigma_{\max} = 660\text{MPa}$, $N_f = 5.49 \times 10^6$ cycles, 593°C).

Because the surfaces of facets are very flat, pixel values on SEM images show little variation, resulting in significant difficulty for accurate three dimensional reconstruction by photogrammetry. Another disadvantage of using this method to study the spatial orientation of facets is that the three-dimensional reconstruction process is time consuming and thus is not suitable for generating the large amounts of data required for statistical analysis.

In the next section, the use of quantitative tilt fractography to study the spatial orientation of facets will be described. This technique does not involve 3D reconstruction of full fracture surface feature. Rather, only the coordinates of three different features on facet planes are required. This advantage makes this technology a more powerful tool in the determination of spatial orientation of large numbers of facets.

4.2.1.2 Quantitative tilt fractography

The principle of quantitative tilt fractography involves the determination of 3D coordinates of three different features on SEM stereo pairs. Similar to the stereo photogrammetry method, two SEM stereo images captured at two different tilting angles are required. However, the image quality has a very small effect on the final calculation in the SEM based stereology method, while the stereo photogrammetry method relies heavily on image quality for good reconstruction results. Figure 4.16 shows a SEM stereo pairs captured on the flat surface at $\pm 5^\circ$ tilting angle respectively. The coordinate system for stereo images is indicated in Figure 4.16. The tilt direction is the X direction. Three apparent features (A, B and C) used for determining the spatial orientation of the flat plane are indicated on both images. The coordinates of these three points on the

SEM stereo images are measured and input into Eq.4.2 to obtain the coordinates of the three points in 3D space.

$$\begin{aligned} X &= x_1 = x_2 = \left(\frac{x_1 + x_2}{2} \right) \\ Y &= \left(\frac{y_1 \sin \theta_2 - y_2 \sin \theta_1}{\sin(\theta_2 - \theta_1)} \right) \\ Z &= \left(\frac{-x_1 \cos \theta_2 + x_2 \cos \theta_1}{\sin(\theta_1 - \theta_2)} \right) \end{aligned} \quad (4.2)$$

The normal of a facet plane can be determined by the cross product of two vectors on the facet plane. For example, the three points A, B and C on the image can construct two vectors \overline{BA} and \overline{BC} , and the facet normal n can be given as:

$$n = \overline{BA} \times \overline{BC} \quad (4.3)$$

The accuracy of this method in determination of spatial orientation of crystallographic facets is evaluated using a standard specimen with a spatial orientation of 45° relative to the Z direction. To estimate the effect of magnification on the calculation accuracy, three groups of SEM stereo pair images were captured at magnifications of 500, 2000, and 5000. Each group includes 10 SEM stereo pairs. The average spatial orientations determined using three groups of images are shown in Table 1. It can be seen that within a wide range of magnification this method can provide very high reliability and accuracy in determining the spatial orientation of flat facets. The error using this method for orientation determined is less than one degree.

Table 4. 1 Comparison of experimental measurement of spatial orientation of flat facet using SEM stereo images of different magnifications.

Magnification of SEM stereo images	500	1000	5000
Average measured spatial orientation (degrees)	44.2	45.6	45.4

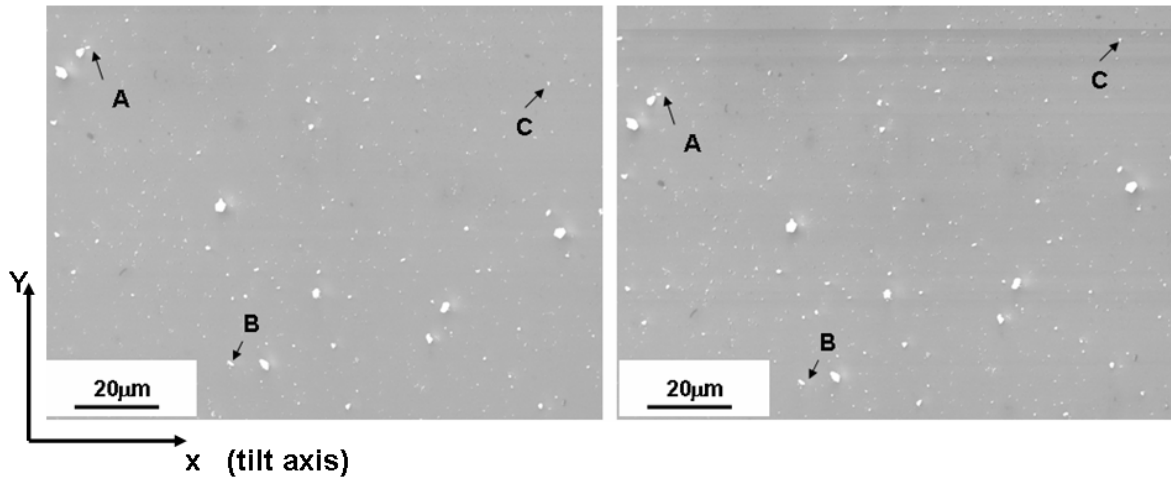


Figure 4.16 SEM stereo pair of a standard sample captured at 1000 X magnification. (A, B and C are three different features on the stereo images).

4.2.2 Determination of crystallographic orientation of crystallographic facets

Here crystallographic orientation is defined as the orientation of the facet normal within the crystal coordinate system. For a cubic crystal, the crystal coordinate system is the $[001]$ - $[010]$ - $[001]$ coordinate frame. At elevated temperature, in René 88 DT, all fatigue failures initiated in subsurface regions and the fracture surface is too rough to directly collect EBSD signals from crystallographic facets. However, using metallographic serial sectioning, the microstructure and grain orientation beneath fracture surface can be determined. The crystallographic information of grains intersecting the fracture surface can thus be obtained from the sectioning planes using EBSD. Therefore, the determination of the crystallographic orientation of facet planes can be achieved by the combination of the spatial orientation of crystallographic facet and crystallographic orientation of grains containing these facets. Two methods used for the determination of spatial orientation of facets were presented in the previous section. The theory for

combining these two methods of spatial orientation determination with EBSD measurement is the same. Because statistical analysis of the crystallographic orientation of facets is needed, only the analysis using the combination of quantitative tilt fractography with EBSD to determine the crystallographic orientation of facets is presented.

The experimental procedures for metallographic sectioning to examine exposing microstructure beneath fatigue fracture surfaces are as follows. Before sectioning, failed specimens are mounted in resin to protect fracture surfaces from damage during sectioning. The mounting materials can be dissolved in acetone after sectioning. Metallographic sectioning planes are parallel to the loading axis. Precise control of sectioning depth is achieved by placing Vickers hardness indents on sectioning surfaces and monitoring their change in size during sectioning. Sectioning is conducted using various grit of SiC grinding paper. After grinding, the sectioning planes are mechanically polishing using 6 μm , and 1 μm diamond suspensions. Final polishing is accomplished with 0.05 μm colloidal silica.

Figure 4.17 shows an example of a sectioned fatigue specimen. The dark regions on the fracture surface are from residual mounting resin. The crystallographic orientation of the grain containing the fracture surface is obtained on the flat sectioning plane just beneath the fatigue fracture surface using EBSD. Figure 4.18 shows an inverse pole figure map collected on the sectioning plane. The map is juxtaposed with a standard SEM image on the metallographic sectioning plane.

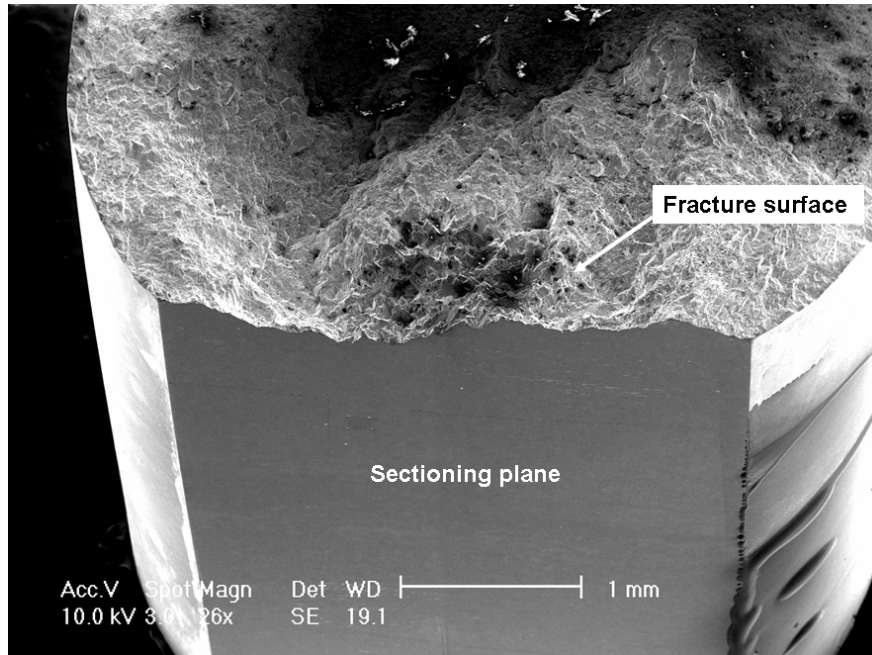


Figure 4.17 Metallographic sectioning of fatigue fracture surface for the determination of the crystallographic orientation of facets.

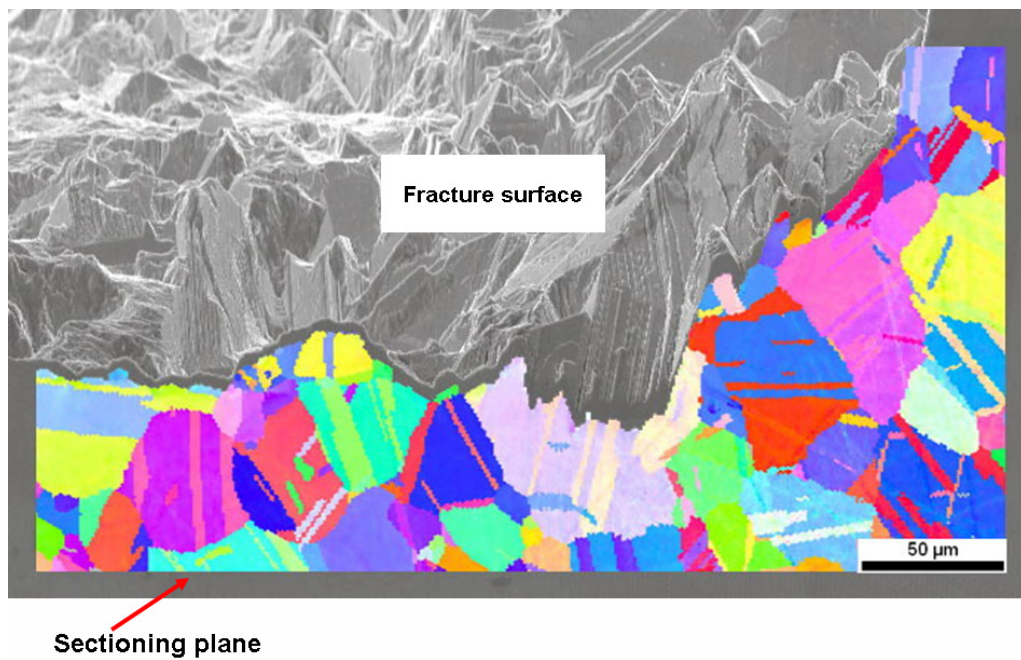


Figure 4.18 Orientation imaging map collected on a metallographically sectioned plane just beneath the fracture surface.

The crystallographic orientations of grains can be described by a transformation matrix \mathbf{g} , which is given as:

$$\mathbf{g} = \begin{pmatrix} \cos \varphi_1 \cos \varphi_2 - \sin \varphi_1 \sin \varphi_2 \cos \varphi & \sin \varphi_1 \cos \varphi_2 + \cos \varphi_1 \sin \varphi_2 \cos \varphi & \sin \varphi_2 \sin \varphi \\ -\cos \varphi_1 \sin \varphi_2 - \sin \varphi_1 \cos \varphi_2 \cos \varphi & -\sin \varphi_1 \sin \varphi_2 + \cos \varphi_1 \cos \varphi_2 \cos \varphi & \cos \varphi_2 \sin \varphi \\ \sin \varphi_1 \sin \varphi & -\cos \varphi_1 \sin \varphi & \cos \varphi \end{pmatrix} \quad (4.4)$$

Where φ_1 , φ and φ_2 are three Euler angles that can be determined using EBSD. These three Euler angles represent three rotations which brings the specimen coordinate system into coincidence with the crystal coordinate system [103]. Figure 4.19 (a) shows the specimen coordinate system (RD-TD-ND) and crystal coordinate system of a crystal within the specimen ([100]-[010]-[001]). The three rotation Euler angles (φ_1 , φ , φ_2) are illustrated in Figure 4.19 (b).

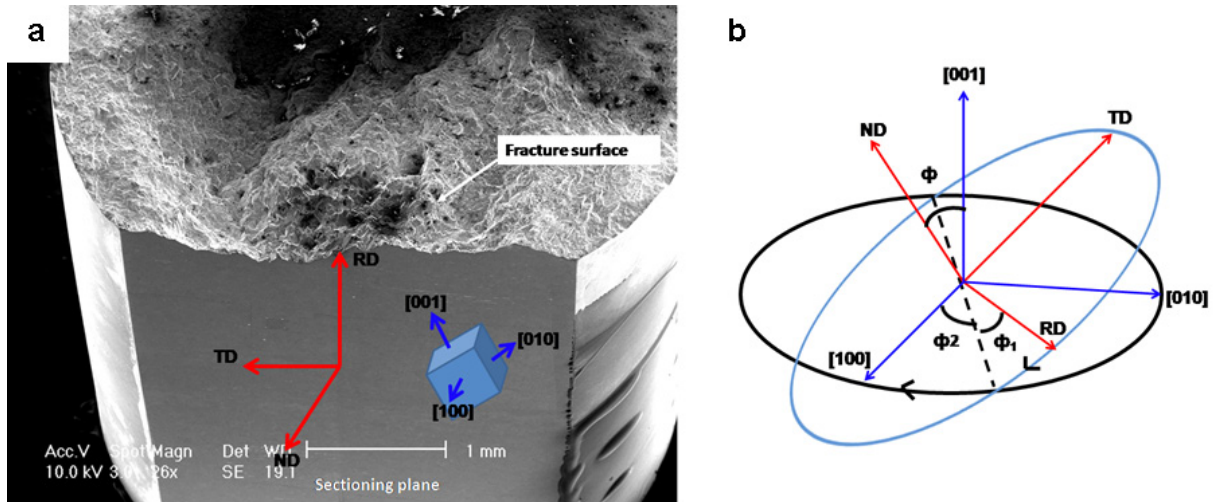


Figure 4. 19 Three Euler angles between specimen coordinate system and crystal coordinate system: (a) specimen coordinates and crystal coordinates and (b) three Euler angles between two coordinate systems.

Figure 4.20 shows a SEM stereo pair of a crystallographic facet. The images were obtained by tilting sample at $+5/-5^\circ$. The metallographic sectioning plane passed

directly through the facet as indicated in Figure 4.20. The spatial orientation of the facet can be determined using quantitative tilt fractography. The crystallographic orientation of the grain can then be obtained using EBSD on the sectioning plane.

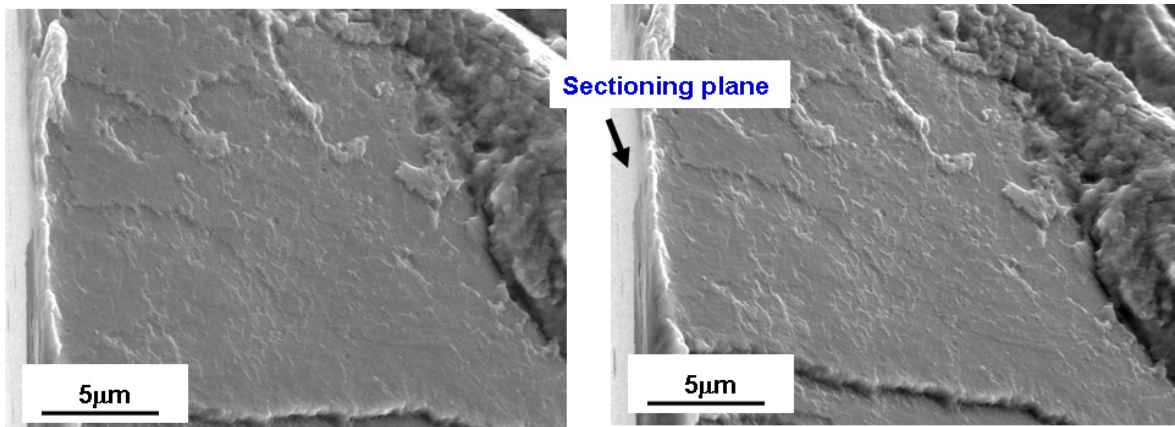


Figure 4.20 SEM stereo pair of a crystallographic facet.

With the knowledge of both the spatial orientation of the crystallographic facet and the crystallographic orientation of the grain where the facet formed, the crystallographic orientation of the facet planes can be determined by transforming the spatial orientation of the facet normal from the specimen coordinate system into the crystal reference frame using

$$n' = \mathbf{g} \bullet n \quad (4.5)$$

Where the n' is the crystallographic orientation of facet normal, n is the spatial orientation of facet plane, \mathbf{g} is the transformation matrix.

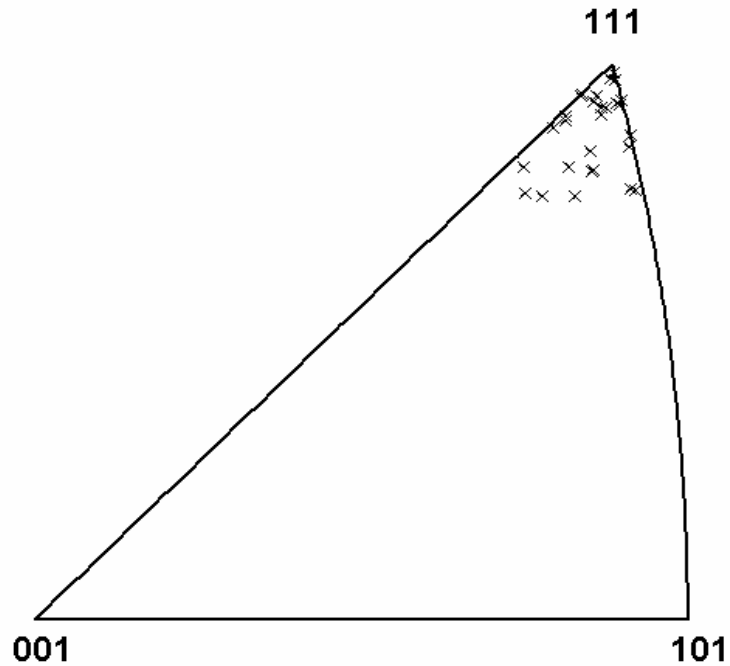


Figure 4.21 Crystallographic orientation of facets on fatigue fracture surface.

The crystallographic orientations of about 20 facets on the fatigue fracture surfaces were collected and determined using the above technique. The angles between the loading direction and the normal of these crystallographic facets vary from 35-65 degrees. The crystallographic orientations of these facets are plot in Figure 4.21, where it can be seen that all facet normal directions are close to the $\langle 111 \rangle$ direction. This result indicates that all these facets were formed on $\{111\}$ slip planes. Therefore, $\{111\}$ slip band cracking is the main subsurface fatigue crack propagation mode in this alloy.

4.3 Summary

The fatigue behavior of nickel-based superalloy René 88 DT was investigated at 593°C in the life time range of $10^5 \sim 10^9$ cycles. Under current testing conditions, all fatigue failures initiated from subsurface regions. Most fatigue crack initiation sites

consist of large crystallographic facets or clusters of large crystallographic facets. The size of large crystallographic facets at crack initiation sites is in the range of 60~120 μm which correspond to the large grains observed in the microstructure. Subsurface fracture surfaces can be divided into three regions corresponding to three periods of fatigue failure stages: fatigue crack initiation and subsurface fatigue crack propagation and surface crack propagation.

At 760MPa, the experimental fatigue life and fatigue life variability is close to the prediction using crack growth data, indicating the fatigue crack growth life is of a large portion of the total fatigue life. However, both fatigue life and the variability of fatigue life at 600MPa is much greater than that predicted fatigue crack propagation alone. Therefore, at lower stresses in longer fatigue life regime, fatigue crack initiation dominates fatigue life and the variation in fatigue crack initiation lifetime is responsible for the large variability in fatigue life that is observed.

In order to quantitatively characterize the spatial orientations of crystallographic facets on fatigue fracture surface at 593°C, two different techniques was explored in this study: SEM-stereo-image based photogrammetry and quantitative tilt fractography. The crystallographic facets at fatigue crack initiation sites were successfully reconstructed using SEM-stereo-image based photogrammetry. Two facets morphologies were found at fatigue crack initiation sites: single plane facet and chevron facet.

By combining quantitative tilt fractography with EBSD and metallographic sectioning, the crystallographic orientations of facets on subsurface fracture surfaces were determined. All facets are of $\{111\}$ type, indicating $\{111\}$ slip band cracking is the first stage of fatigue crack propagation under testing conditions examined in this study.

In Chapter 5, the techniques combining serial sectioning, EBSD and quantitative fractographic analysis described in this chapter will be used to quantitatively characterize critical microstructure features associated with cyclic strain localization and fatigue crack initiation in René 88 DT at elevated temperature.

Chapter 5

Crystallographic Fatigue Crack Initiation in Nickel-based Superalloy René 88 DT at Elevated Temperature

This chapter covers two topics: the mechanism of crystallographic fatigue crack initiation at elevated temperature in René 88 DT and the microstructural neighborhood effects on subsurface fatigue crack initiation and early small crack growth. The environmental influence on the fatigue behavior of René 88 DT at elevated temperature is also discussed.

5.1 Experimental procedures

Metallographic serial sectioning of failed fatigue specimens was used to expose internal crack initiation sites to allow characterization of critical microstructure features controlling fatigue crack initiation and the early stage of small crack growth. The sectioning method is schematically illustrated in Figure 5.1. Before sectioning, failed samples were mounted in resin to protect fracture surfaces from subsequent damage. The mounting materials were dissolved in acetone after sectioning. Metallographic sectioning planes were parallel to the loading axis. Both halves of the failed samples were aligned and sectioned simultaneously to expose the microstructure below both halves of the fracture surface. Precise control of sectioning depth was achieved by placing Vickers hardness indents on sectioning surface and monitoring their change in size during sectioning. Crystallographic information beneath the fracture surface at crack initiation

sites was collected on the sectioning planes using electron backscatter diffraction (EBSD). The EBSD data was collected and analyzed using TSL OIM software version 4.5 installed on a FEG XL-30 SEM.

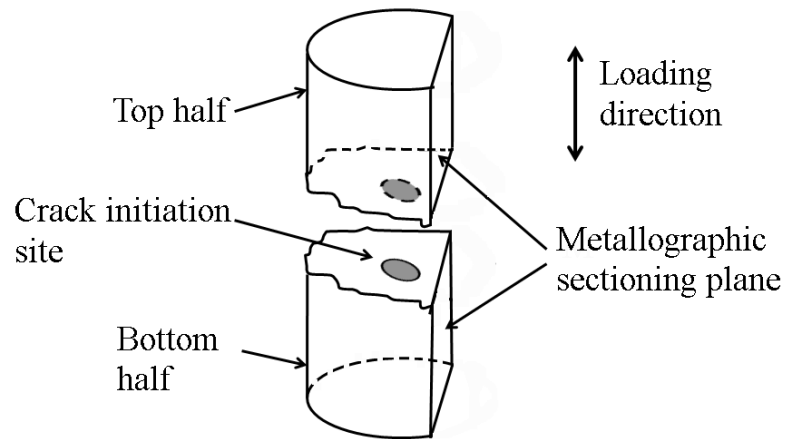


Figure 5.1 Schematic illustration of metallographic sectioning method used in this study.

Disc samples for TEM studies were sectioned perpendicular to the loading axis from the gage section of the failed fatigue specimens. The samples were mechanically polished to a thickness of approximately 100 μm , and further thinned by twin jet polishing in a solution of 68% methanol, 10% perchloric acid, 9% distilled water and 13% butyl cellosolve under conditions of -35°C , 20 V and 50 mA. Observations of the deformation substructures were conducted using a JEOL 2010F ATEM operated at 200 KeV.

5.2 Quantitative characterization of crystallographic fatigue crack initiation sites

5.2.1 Fractography observations of crystallographic crack initiation sites

Fracture surfaces of all failed fatigue samples from the studies described in Chapter 4 were examined using SEM. Fatigue failures initiated from subsurface regions for all failed specimens. Most fatigue cracks originated from microstructural crack initiation sites consisting of large crystallographic facets that can be grouped into two types: those with a single plane facet and those with two intersecting facets, referred to as chevron shape facets [104, 105]. An example of both facet types is shown in Figure 5.2. The projected sizes of the crystallographic facets on which the fatigue cracks initiated are measured using both the equivalent diameter and ellipse fitting method on the SEM images as shown in Figure 5.2 (c) and Figure 5.2 (f). The facets are typically three times larger than the average grain size of this alloy, and are on the order of the largest grain observed in the general microstructure. As shown in Figure 5.2 (c) and Figure 5.2 (f), compared with the equivalent diameter method, the ellipse fit method can better characterize the size and shape of the large crystallographic facets at crack initiation sites.

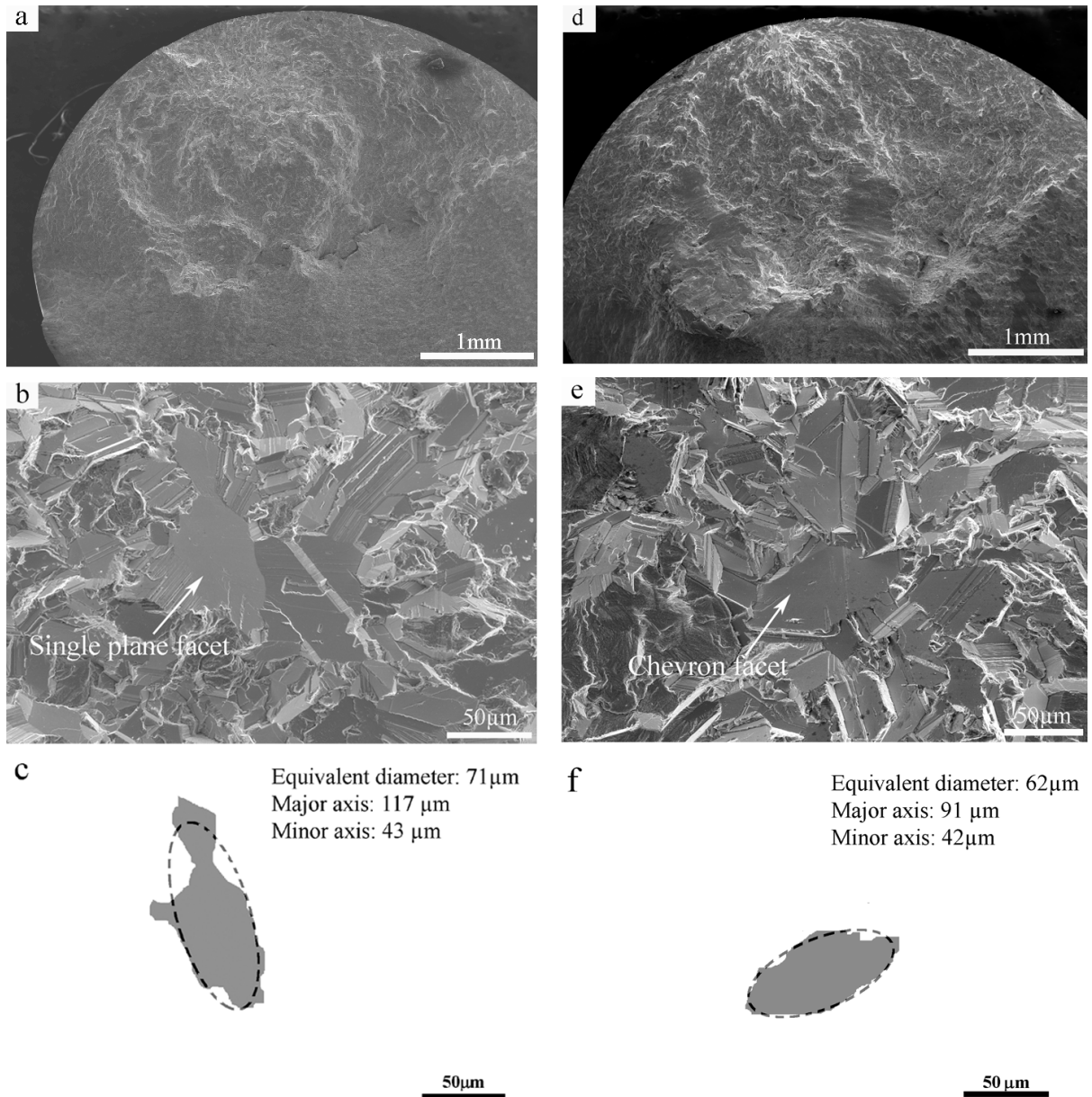


Figure 5.2 Fracture surface of two failed fatigue specimens: (a) fracture surface, (b) crack initiation site and (c) ellipse fit of the single plane facet at crack initiation site for the first specimen ($\sigma_{\max} = 600\text{MPa}$, $N_f = 3.16 \times 10^6$ cycles); (d) fracture surface, (e) crack initiation site and (f) ellipse fit of the chevron facet at crack initiation site for the second specimen ($\sigma_{\max} = 600\text{MPa}$, $N_f = 1.90 \times 10^7$ cycles, 593°C).

5.2.2 Critical microstructure features associated with subsurface crystallographic fatigue crack initiation

The failed specimens shown in Figure 5.2 were sectioned using the method described previously. Figure 5.3 (a) shows that metallographic section that directly cuts through the single plane facet at the crack initiation site shown in Figure 5.2 (b). The microstructure beneath the fracture surface was revealed using EBSD on the sectioning planes on both halves of the sample. Figure 5.3 (b) shows the matched halves of inverse pole figure maps collected on the sectioning planes. Details of the crack initiation grain in which the large single plane facet formed are shown by the inverse pole figure map and the reconstructed grain boundary map in Figure 5.3 (c) and 5.3 (d), respectively. This facet formed within a large grain that contains several parallel twins. The crack initiated near a $\Sigma 3$ twin boundary and intersected the step of the twin boundary as shown in Figure 5.3 (c). Serial sectioning revealed that the facet plane is parallel to the $\Sigma 3$ twin boundary and extended continuously through both the twin and the matrix. Using the crystallographic information determined from OIM, the facet plane was identified as $\{111\}$ type, as indicated in Figure 5.3 (d). The angle between the loading direction and the normal of the facet plane was measured as 53 degrees. Therefore, the facet plane is oriented such that resolved shear stress on the facet plane is near its maximum value. The notation of 12 FCC slip systems [106] is adopted here and is shown in Table 5.1. The Schmid factors for all slip systems in both twin and matrix are calculated and shown in the Figure 5.3 (e). The slip system with the highest resolved shear stress has its slip plane parallel to both the facet plane and the $\Sigma 3$ twin boundary, i.e, the $(1\bar{1}\bar{1})[101]$ slip system with the highest resolved shear stress in twin 1 is parallel to the

corresponding $(\bar{1}\bar{1}1)[011]$ slip system within the matrix 2. This geometrical relationship may provide for a continuous path for crack initiation and extension through the twin and matrix.

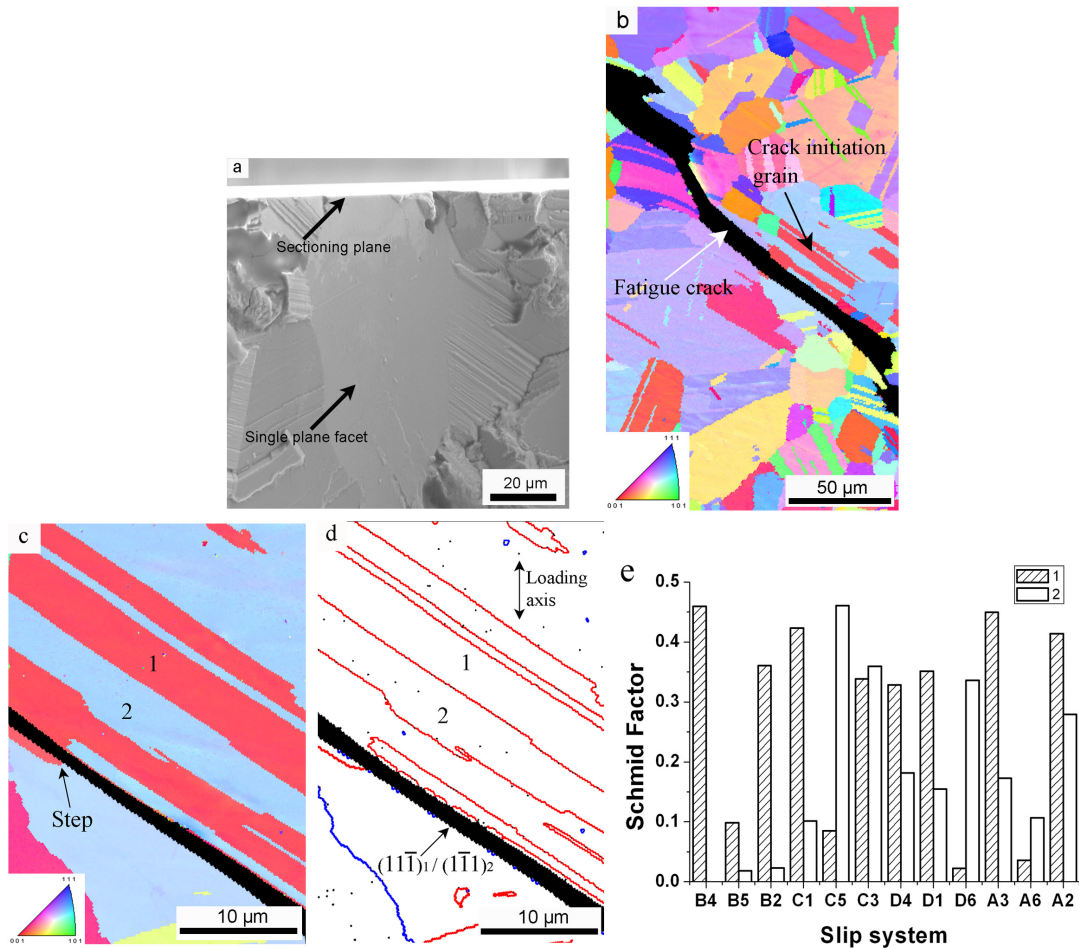


Figure 5.3 Microstructural features of the crack initiation grain: (a) metallographic sectioning through the single plane facet at the crack initiation site; (b) large matching halves of IPF maps (loading direction); (c) IPF map of the crack initiation grain; (d) reconstructed grain boundary map of the crack initiation grain (Blue lines represent random grain boundaries, red lines represent $\Sigma 3$ twin boundaries) and (e) Schmid factors for 12 slip systems within both twin1 and matrix 2 of the crack initiation grain in the first sectioned samples ($\sigma_{\max} = 600\text{MPa}$, $N_f = 3.16 \times 10^6$ cycles, 593°C).

Table 5. 1 Notation for 12 FCC slip systems [106].

Slip system	$(11\bar{1})$			$(1\bar{1}1)$			$(1\bar{1}\bar{1})$			(111)		
	[101]	[011]	$[1\bar{1}0]$	[110]	[011]	$[10\bar{1}]$	[101]	[110]	$[01\bar{1}]$	$[10\bar{1}]$	$[0\bar{1}1]$	$[1\bar{1}0]$
Notation	B4	B5	B2	C1	C5	C3	D4	D1	D6	A3	A6	A2

Figure 5.4 (a) shows the metallographic section intersecting the chevron facet at the crack initiation site shown in Figure 5.2 (e). The microstructure details of the crack initiation grain are revealed by inverse pole figure map of matching halves, Figure 5.4 (b), and the corresponding reconstructed grain boundary map, Figure 5.4 (c), respectively. The fatigue crack initiated within one large grain and formed on the two facet planes “A” and “B” to create the chevron facet within the large grain, as indicated in Figure 5.4 (a). The intersection of two facet planes is a triple junction of $\Sigma 3$ twin boundaries within the large grain, as shown in Figure 5.4 (c). Facet plane A was formed near a $\Sigma 3$ twin boundary and intersected the twin boundary step. The crystallography of both facet planes was identified as $\{111\}$ type, as indicated in Figure 5.4 (c). The angles between the facet plane normal and the loading direction are 49 and 45 degrees for plane A and plane B, respectively. The Schmid factors for 12 FCC slip systems in both the twin 1 and the matrix 2 were calculated and shown in Figure 5.4 (d). Similar to the results found in the single plane facet, the slip plane with the highest resolved shear stresses is parallel to both the facet plane A and the $\Sigma 3$ twin boundary.

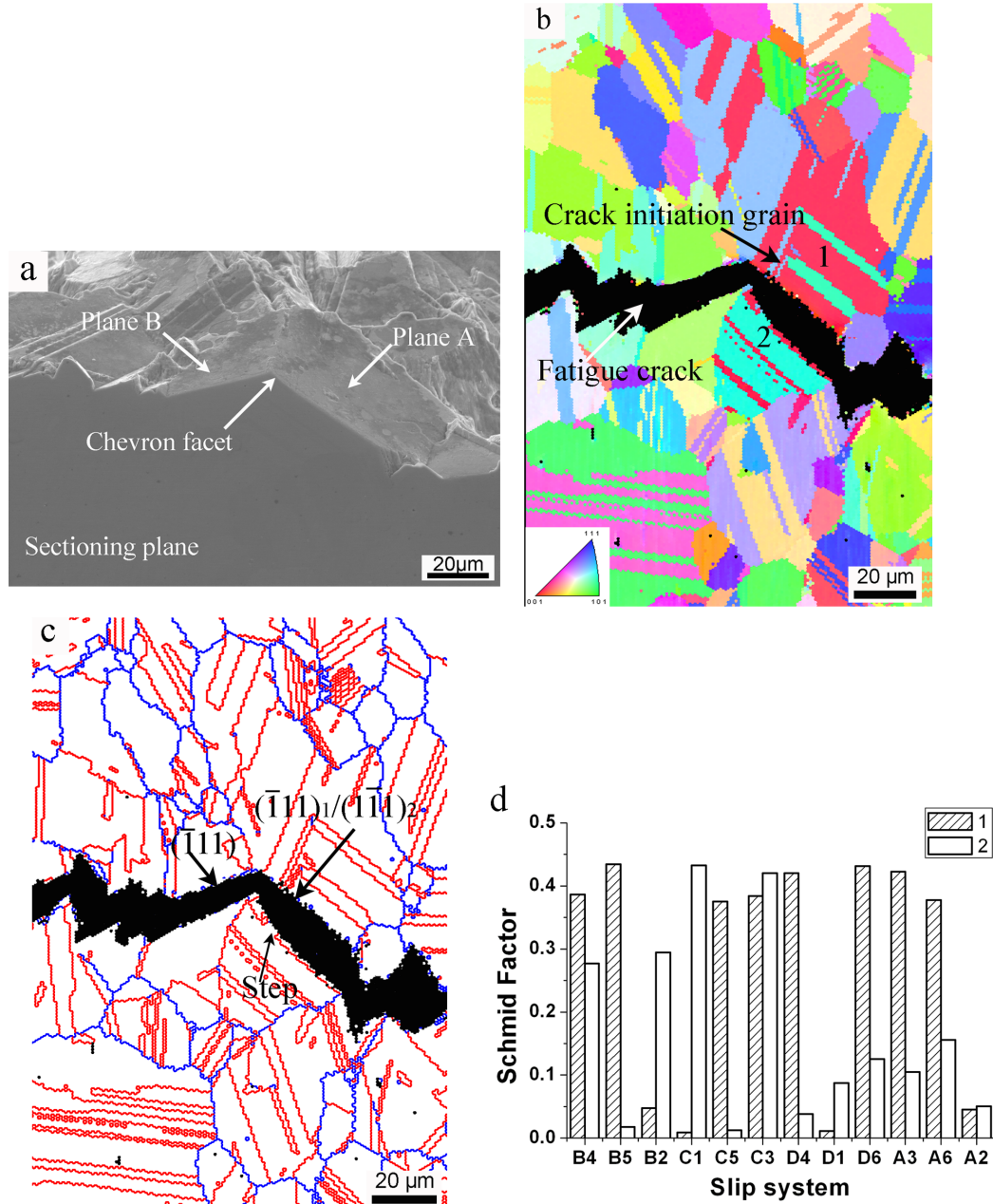


Figure 5.4 Microstructure details of the crack initiation grain in the second sectioned sample: (a) metallographic sectioning through the chevron facet; (b) matching halves of OIM inverse pole figure map (loading direction); (c) matching halves of OIM grain boundary map (red lines represent twin boundaries, blue lines represent random large angle boundaries.) and (d) Schmid factors for 12 slip systems in twin1 and matrix 2 within the crack initiation grain of the second sectioned sample as shown in Figure 5.4 (b). ($\sigma_{\max} = 600\text{MPa}$, $N_f = 1.90 \times 10^7$ cycles, 593°C).

5.2.3 Observations of subsurface non-fatal fatigue crack

Metallographic serial sectioning also exposed subsurface non-fatal fatigue cracks that initiated but did not propagate to failure. An example is shown in Figure 5.5 (a). The detailed structure of the non-fatal fatigue crack is shown in Figure 5.5 (b). EBSD was again used to extract the crystallographic information at the crack initiation site. The crystallography of the fatigue path was identified using EBSD data and illustrated on the Figure 5.5 (b). This subsurface fatigue crack also initiated and propagated along $\{111\}$ slip planes. Cyclic plastic deformation is primarily localized on $\{111\}$ slip planes. An inverse pole figure map collected on the sectioning plane is shown in Figure 5.5 (c). The grain boundary map overlapped by an image quality map in Figure 5.5 (d) showing that the internal fatigue crack initiated in the region close to a $\Sigma 3$ twin boundary which intersected two other $\Sigma 3$ twin boundaries to form a triple junction of $\Sigma 3$ boundaries in the large grain. Serial sectioning indicated that the planar crack that initiated within the large grain formed a chevron shape which has a similar geometry to the one shown in Figure 5.4 (a).

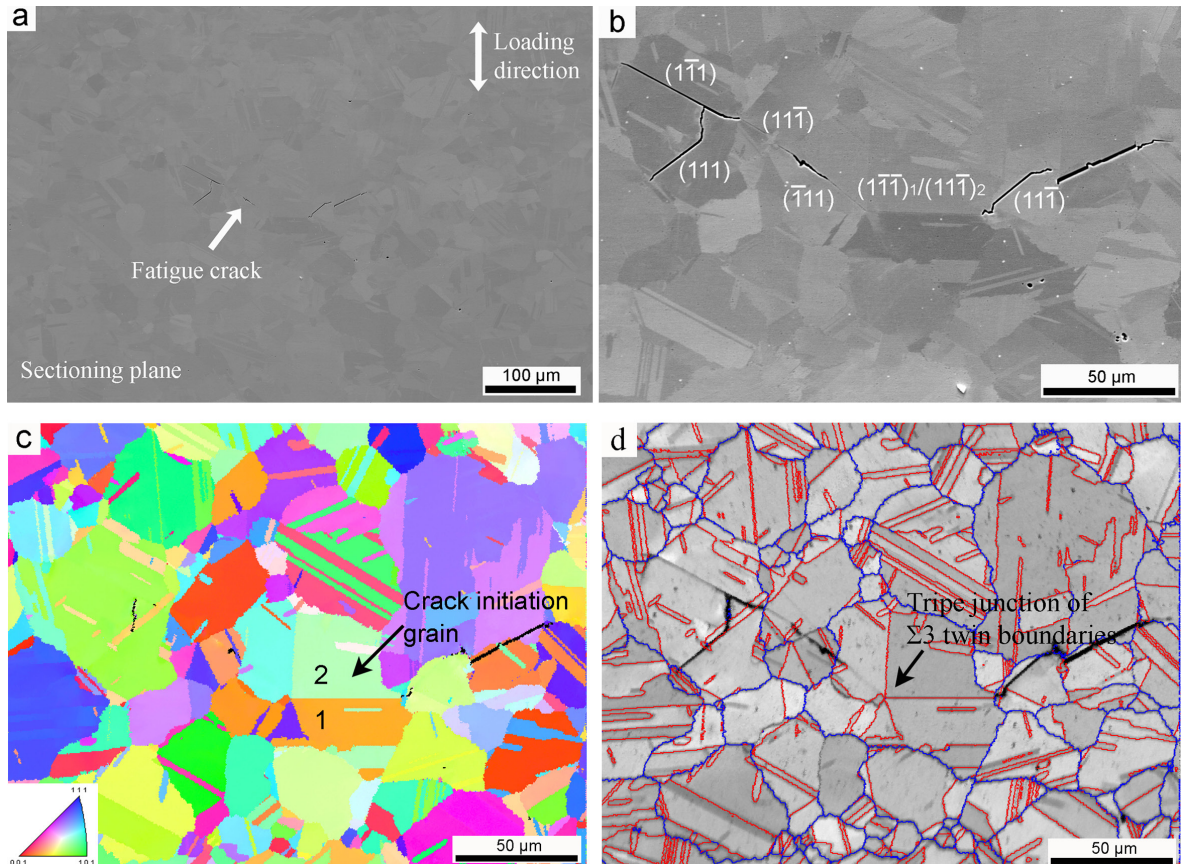


Figure 5.5 Observation of internal non-fatal fatigue crack: (a) the position of internal non-fatal fatigue crack; (b) crystallography of the fatigue crack path; (c) inverse pole figure map (loading direction) and (d) grain boundary map overlapped by image quality map (Blue lines represent random grain boundaries, red lines represent $\Sigma 3$ twin boundaries.) ($\sigma_{\max} = 760$ MPa, $N_f = 5.9 \times 10^5$ cycles, 593°C).

5.2.4 Observations of deformation substructures

To examine the nature of cyclic strain localization and damage accumulation mechanisms under nominally elastic cyclic loading stresses, TEM foils were removed from the gauge section of a failed specimen with fatigue life of 5.85×10^8 cycles at 550 MPa. Overall, the dislocation density was very low, with few grains containing evidence of slip activity. Transmission electron microscopy observations indicate that twin boundaries, discontinuities of twin boundaries such as steps and tips, and intersections of twin boundaries are important sources for cyclic plastic deformation

under such low cyclic loading stresses. Figure 5.6 (a) shows slip bands that formed on the step of twin boundary in a large grain. The dislocation density in the slip band is very high, while the density of dislocations in the surrounding area is very low. This suggests that cyclic plastic deformation was mainly localized within the slip bands. Figure 5.6 (b) shows dislocations and stacking faults observed along twin boundaries near the intersection of two twins. Figure 5.7 shows a slip band formed in the region close to a twin boundary.

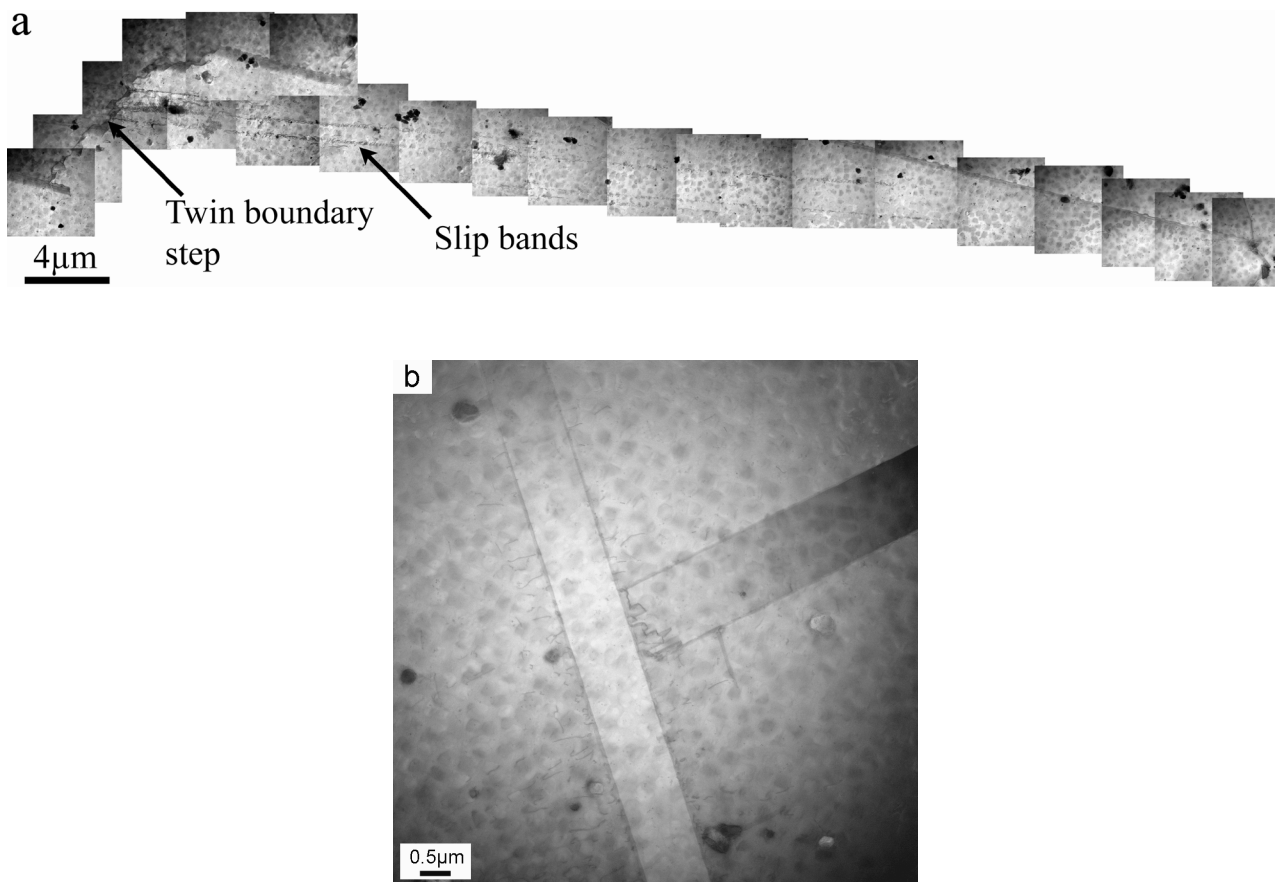


Figure 5.6 Observation of deformation substructure: (a) cyclic strain localization and slip band formation on twin boundary step in a large grain and (b) formation of dislocations and stacking faults at the region close to a twin intersection ($\sigma_{\max} = 550\text{MPa}$, $N_f = 5.85 \times 10^8$ cycles, 593°C).

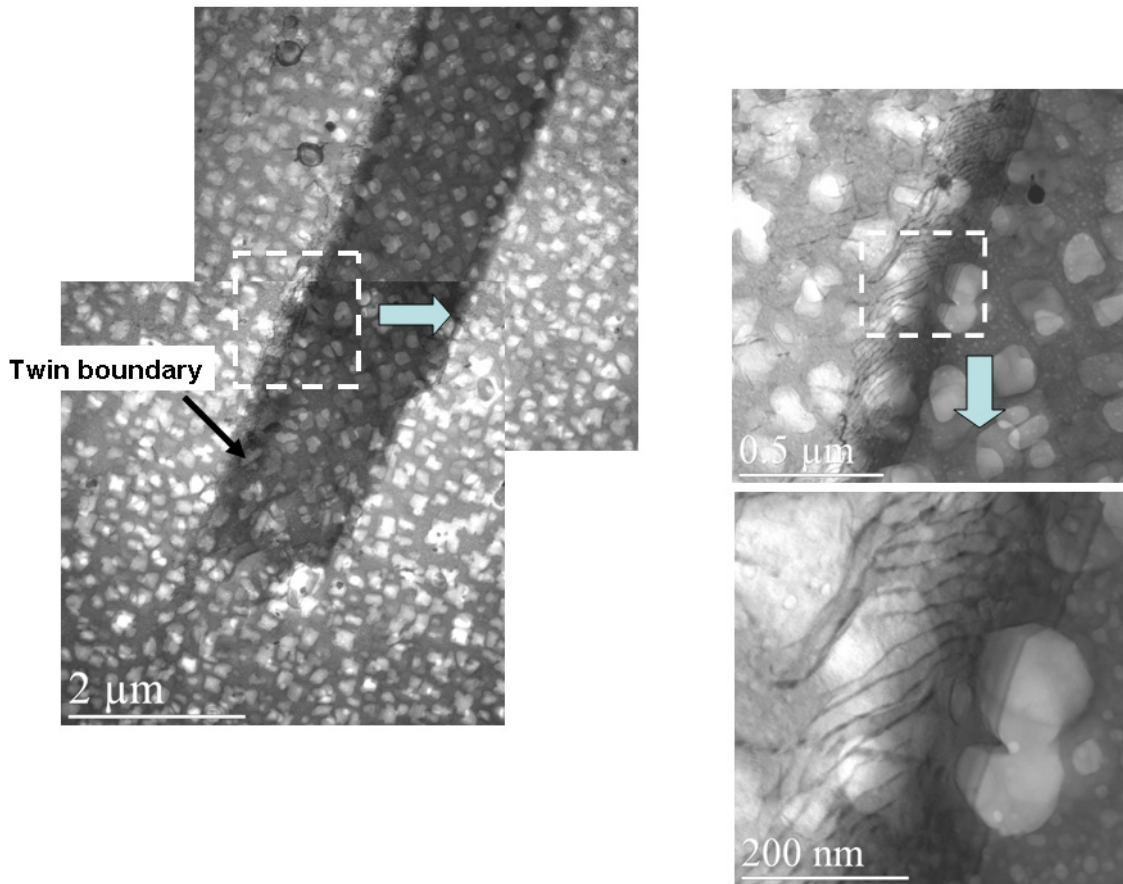


Figure 5.7 TEM image of slip bands formed in the region close to a twin boundary ($\sigma_{\max} = 660$ MPa, $N_f = 3.44 \times 10^6$ cycles, 593°C).

5.2.5 The role of twin boundary in crystallographic fatigue crack initiation

The cyclic loading stresses in this study are in the range of 0.53~0.81 of the yield strength of René 88 DT, and nominally elastic deformation is expected. Thus cyclic plastic deformation and the accumulation of cyclic damage are likely to occur at microstructure heterogeneities with high local stress concentrations. The magnitude of stress concentration and thus cyclic plastic deformation may vary with the type of microstructure heterogeneity, which may include an inhomogenous distribution of grain size, large angle grain boundaries, favorable grain orientations, favorably oriented neighbor grains and synergetic combinations of these features. Based on the analyses of

fatigue crack initiation sites, critical microstructure features associated with fatigue crack initiation grains include large grain size, high Schmid factor and the presence of twin boundaries.

Nickel-based superalloys have relatively high elastic anisotropy and in a polycrystalline nickel-based superalloy, the response of individual grains to cyclic loading varies with grain orientation. In order to maintain compatibility between grains, elastic incompatibility stresses will arise at grain boundaries, especially at high angle grain boundaries. Elastic incompatibility stresses are thought to be one of the important factors resulting in yielding at grain boundaries in polycrystalline materials [107]. Finite element analysis has shown that faceted twin boundaries can induce higher local stresses than are produced at random large angle grain boundaries under normal uniaxial elastic loading in austenitic steel [108].

Fatigue crack initiation in the vicinity of twin boundaries has been frequently observed in other FCC materials such as copper [50, 51] and austenitic steels [52, 53]. The elastic incompatibility stresses between the twin and matrix are thought to be responsible for cyclic strain localization and fatigue crack initiation in these FCC materials [52, 53, 54]. The magnitudes of the incompatibility stresses are orientation dependent [54, 55]. A simple twin/matrix bicrystal model is used here to evaluate the effects of orientation of loading axis on internal incompatibility stress adjacent to a twin boundary in nickel-based superalloys. The bicrystal model and the corresponding twin boundary coordinate system are shown in Figure 5.8. The twin and matrix within the model configuration are designated by superscripts “1” and “2”, respectively. The twin boundary coordinate system in Figure 5.8 (b) is obtained from experimental analysis of

the crack initiation grain in the first sectioned sample, Figure 5.3 (c). Direction 3 is normal to the twin boundary. The incompatibility stresses in the region close to the twin boundary are induced due to the requirement for the continuity of stress and displacement across the twin boundary. The associated stress tensor has three components: σ_{11} , σ_{22} , σ_{12} . Details of the analysis of twin boundary incompatibility stresses are summarized as follows:

Under uniaxial elastic loading and within the twin boundary coordinate as shown in Figure 5.8 (b), the compatibility of twin boundary requires that the stress and strain at the region close to twin boundary to satisfy following requirements [54]:

$$\begin{aligned}\sigma_{31}^1 &= \sigma_{31}^2, & \sigma_{32}^1 &= \sigma_{32}^2, & \sigma_{33}^1 &= \sigma_{33}^2 \\ \varepsilon_{11}^1 &= \varepsilon_{11}^2, & \varepsilon_{12}^1 &= \varepsilon_{12}^2, & \varepsilon_{22}^1 &= \varepsilon_{22}^2\end{aligned}\tag{5.1}$$

Where σ_{ij}^1 and ε_{ij}^1 with superscript “1” represent the stress and strain at the twin side, and σ_{ij}^2 and ε_{ij}^2 with superscript “2” correspond the stress and strain at the matrix side. The total stresses at the region close to twin boundary on both sides are given by

$$\begin{aligned}\sigma_{ij}^1 &= \sigma_{ij}^0 + \Delta\sigma_{ij}^1 \\ \sigma_{ij}^2 &= \sigma_{ij}^0 + \Delta\sigma_{ij}^2\end{aligned}\tag{5.2}$$

where σ_{ij}^0 is the external loading stress and $\Delta\sigma_{ij}^1$ and $\Delta\sigma_{ij}^2$ are the incompatibility stress in the region close to twin boundary on the twin side and matrix side respectively. From equation 5.1, the internal incompatibility stress has three components: $\Delta\sigma_{11}$, $\Delta\sigma_{22}$, and $\Delta\sigma_{12}$. The strain in the region close to the twin boundary for twin side and matrix side is

$$\begin{aligned}\varepsilon_{ij}^1 &= s_{ijkl}^1 (\sigma_{kl}^0 + \Delta\sigma_{kl}^1) \\ \varepsilon_{ij}^2 &= s_{ijkl}^2 (\sigma_{kl}^0 + \Delta\sigma_{kl}^2)\end{aligned}\quad (5.3)$$

Where s_{ijkl}^1 and s_{ijkl}^2 are elastic compliances of the twin and matrix respectively.

Considering that the volume average of the stress in the bicrystal is equal to the external loading stress, and twin and matrix within the model have the same volume, then the volume average of the incompatibility stress is zero [54]. Therefore,

$$\Delta\sigma_{kl}^1 = -\Delta\sigma_{kl}^2 \quad (5.4)$$

Combining equations 5.1 ~ 5.4, three internal incompatibility stress components on the twin side can be given as:

$$\begin{aligned}& \begin{pmatrix} (s_{11kl}^1 - s_{11kl}^2) \sigma_{kl}^0 \\ (s_{22kl}^1 - s_{22kl}^2) \sigma_{kl}^0 \\ 2(s_{12kl}^1 - s_{12kl}^2) \sigma_{kl}^0 \end{pmatrix} + \begin{pmatrix} (s_{1111}^1 + s_{1111}^2) & (s_{1122}^1 + s_{1122}^2) & 2(s_{1112}^1 + s_{1112}^2) \\ (s_{2211}^1 + s_{2211}^2) & (s_{2222}^1 + s_{2222}^2) & 2(s_{2212}^1 + s_{2212}^2) \\ 2(s_{1211}^1 + s_{1211}^2) & 2(s_{1222}^1 + s_{1222}^2) & 4(s_{1212}^1 + s_{1212}^2) \end{pmatrix} \\ & \times \begin{pmatrix} \Delta\sigma_{11}^1 \\ \Delta\sigma_{22}^1 \\ \Delta\sigma_{12}^1 \end{pmatrix} = \begin{pmatrix} 0 \\ 0 \\ 0 \end{pmatrix}\end{aligned}\quad (5.5)$$

By solving this linear equation, three internal incompatibility stress components $\Delta\sigma_{11}$, $\Delta\sigma_{22}$, and $\Delta\sigma_{12}$ can be obtained.

The net effect, including external loading stress and incompatibility stress, can be evaluated using the Von Mises equivalent stress. The equivalent stress on the twin side is given by.

$$\sigma_{eq}^1 = \sqrt{\frac{(\sigma_{11}^1 - \sigma_{22}^1)^2 + (\sigma_{11}^1 - \sigma_{33}^1)^2 + (\sigma_{22}^1 - \sigma_{33}^1)^2 + 6 \times \sigma_{12}^1{}^2 + 6 \times \sigma_{13}^1{}^2 + 6 \times \sigma_{23}^1{}^2}{2}} \quad (5.6)$$

The elastic stiffness of single crystal nickel-based superalloy used in the calculation is

$$C_{11}=210.6 \text{ GPa}, C_{12}=138.6 \text{ GPa}, C_{44}=105.5 \text{ GPa. [109]}$$

In order to study the orientation dependence of incompatibility stresses, the loading direction was rotated in three-dimensional space with respect to the twin boundary coordinates. The three components of the incompatibility stress tensor were calculated and plotted in the stereographic projection within the twin boundary coordinate, Figure 5.9 (a)-(c). The magnitude of incompatibility stresses varies with the orientation of loading axis relative to the twin boundary. When the twin boundary is inclined 45° with respect to the loading axis, the components of incompatibility stress tensor reach a maximum value. When the loading axis is perpendicular to the twin boundary or within the twin boundary plane, there is no incompatibility stress. The Von Mises equivalent stresses at the region close to twin boundary for all possible loading directions were calculated to evaluate the combined effects of external loading and incompatibility stress in the region close to the twin boundary. The results are shown in Figure 5.9 (d). The equivalent stresses reach a maximum value when the angle between the loading direction and the normal to the twin boundary is 55.5° . The incompatibility stress on the matrix side 2 within the crack initiation grains of three sectioned samples is listed in Table 5.2. There is about a 24%~30% increase of equivalent stress at the region close to the twin boundary in the crack initiation grains. This is significant since fatigue experiments are conducted at nominal maximum stresses in the range of 53-81% of yield strength. Therefore, it is reasonable that elastic incompatibility stresses play an important role as local stress raisers in the crystallographic fatigue initiation process.

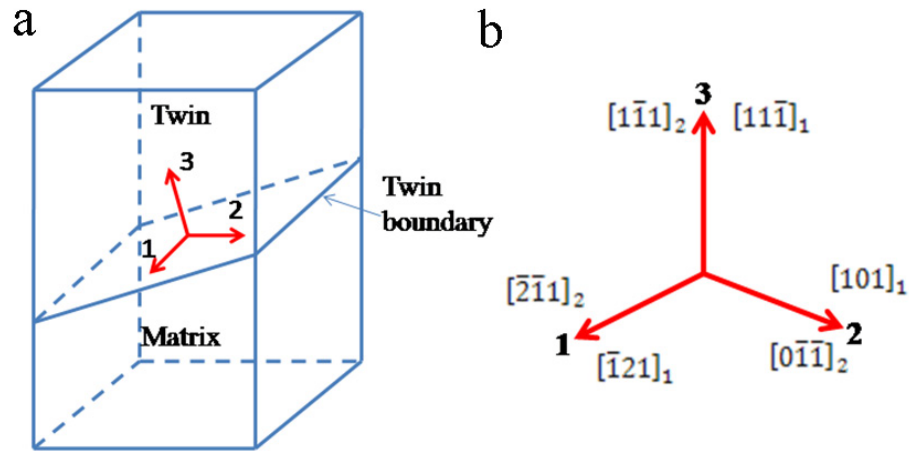


Figure 5.8 Twin/matrix model and twin boundary coordinate for the calculation of internal incompatibility stress at the region close to twin boundary: (a) twin/matrix model, (b) twin boundary coordinate determined by experiment results (superscript 1 represents the twin side, while superscript 2 represents the matrix side).

Previous research [51] on twin boundary cracking in surface grains pointed out that for fatigue crack formation at regions near twin boundaries, slip systems parallel to twin boundary planes need to operate, consistent with the current study. Moreover, the current study shows that the $\{111\}$ slip planes on which internal fatigue cracks formed have the highest resolved shear stresses within both the twin and matrix. Current experiments and calculations show that the orientation of crystallographic fatigue crack initiation grains in the two samples examined in detail satisfy the two criteria for crack formation in the region close to twin boundaries: high resolved shear stress on the slip plane parallel to twin boundaries and high elastic incompatibility stress at the region close to twin boundary, which may also contribute to the operation of secondary slip. It has been reported that the operation of secondary slip system in the region close to twin boundary planes can assist the formation of cyclic strain localization and persistent slip bands [51, 56].

Twin boundaries have both coherent and incoherent regions at steps and tips. TEM observations [51, 56] show that these incoherent regions on twin boundaries are important dislocation sources and stress concentrators. Three-dimensional finite element simulation shows that the highest Von Mises stresses exist at the triple junctions between two $\Sigma 3$ twin boundaries in an austenitic steel under normal uniaxial elastic loading [108]. These twin boundary related microstructure features may also contribute to cyclic plastic strain localization in regions close to twin boundaries.

Table 5. 2 Twin boundary incompatibility stresses on the side 2 near twin boundaries in crack initiation grains.

Samples	$\Delta\sigma_{11}/\sigma_0$	$\Delta\sigma_{12}/\sigma_0$	$\Delta\sigma_{22}/\sigma_0$	σ_{eq}/σ_0
Sample 1 (Fig.3.3)	-0.078	-0.258	0.078	1.265
Sample 2 (Fig.3.4)	-0.132	0.240	0.132	1.303
Sample 3 (Fig.3.5)	-0.192	0.199	0.192	1.243

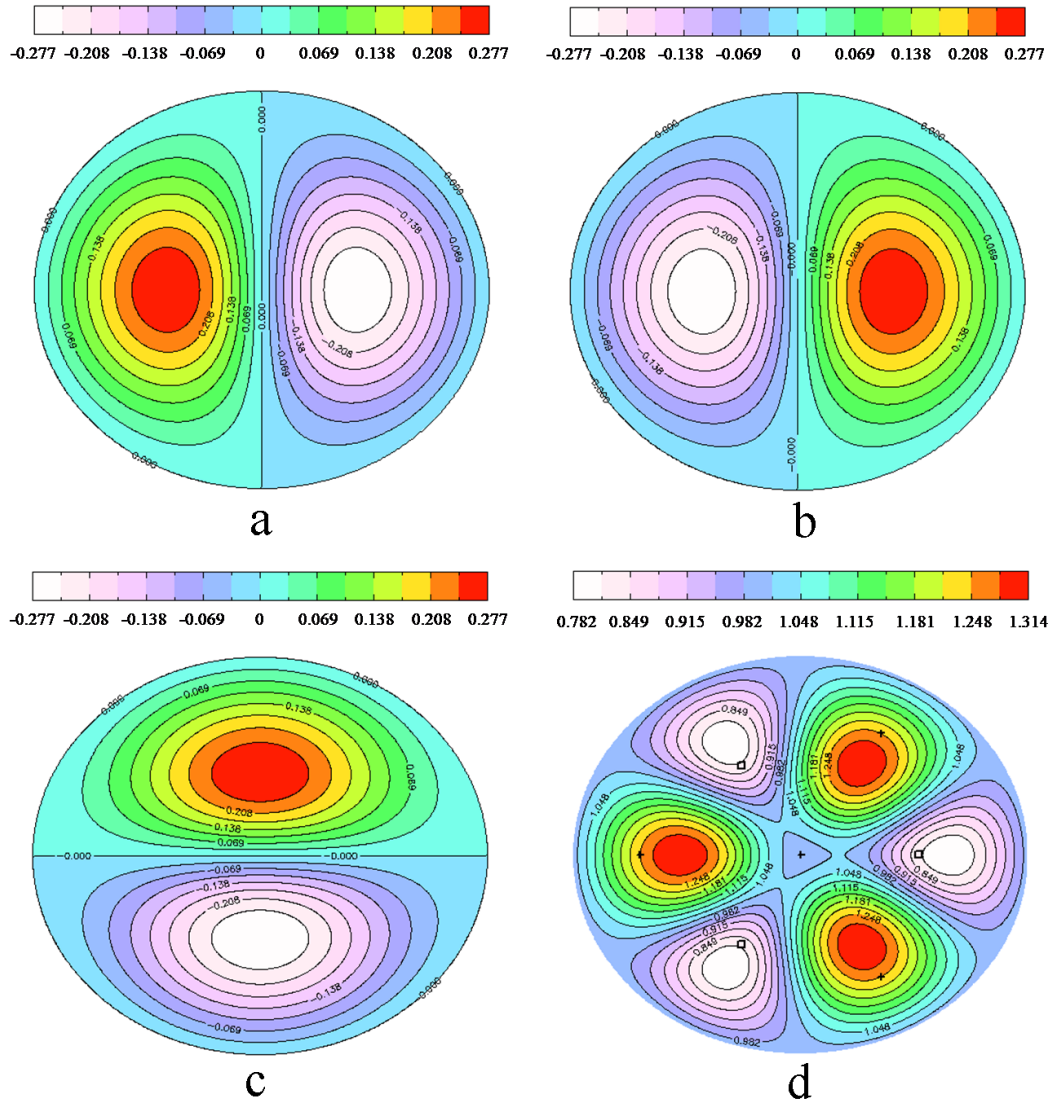


Figure 5.9 The distribution of normalized internal incompatibility stress and Von Mises equivalent stress at the twin side within the bicrystal model as indicated in Fig.5.8 (a): (a) $\Delta\sigma_{11}/\sigma_0$, (σ_0 is the uniaxial external loading stress) (b) $\Delta\sigma_{22}/\sigma_0$, (c) $\Delta\sigma_{12}/\sigma_0$, (d) $\Delta\sigma_{eq}/\sigma_0$ (+ indicates the positions of four $\langle 111 \rangle$ directions, and \square indicates the positions of three $\langle 001 \rangle$ directions).

One important microstructural feature of the nickel-based superalloy studied here is the high fraction of twin boundaries in the microstructure. Under the loading conditions in the current study, twin boundaries alone may not induce enough cyclic strain localization to lead to final failures of fatigue samples. Serial sectioning shows that

another important microstructural feature associated with internal crystallographic fatigue crack initiation is the presence of large grains that are 3-5 times of the average grain size. Large grains can provide a long slip length for cyclic strain localization, resulting in a large initial crack that can more easily propagate to failure. Besides these three major microstructure features, some other microstructure configurations, such as favorably oriented neighbor grains may also contribute to the crystallographic fatigue crack initiation and early small crack growth process [104]. Such variations in microstructure configurations can lead to the large variability of fatigue life especially under low loading stress and high cycle regime. The microstructural neighborhood effects on crystallographic fatigue crack initiation and early small crack growth will be examined in the next section.

5.3 Neighborhood effects on fatigue crack initiation and early small crack growth

Crystallographic orientation associated with the neighborhood of subsurface fatigue crack initiation sites can be collected by combining serial sectioning and EBSD. Figure 5.10 (a) shows the serial sectioning method used for collecting crystallographic orientation of neighborhood. The white dash lines A, B, C, and D represent four different sectioning positions. At each position, the crystallographic orientation of microstructure just beneath fatigue fracture surface was collected using EBSD on the sectioning plane. Figure 5.10 (b) shows an example of sectioning plane at the position C. The sectioning direction was indicated in Figure 5.10 (a).

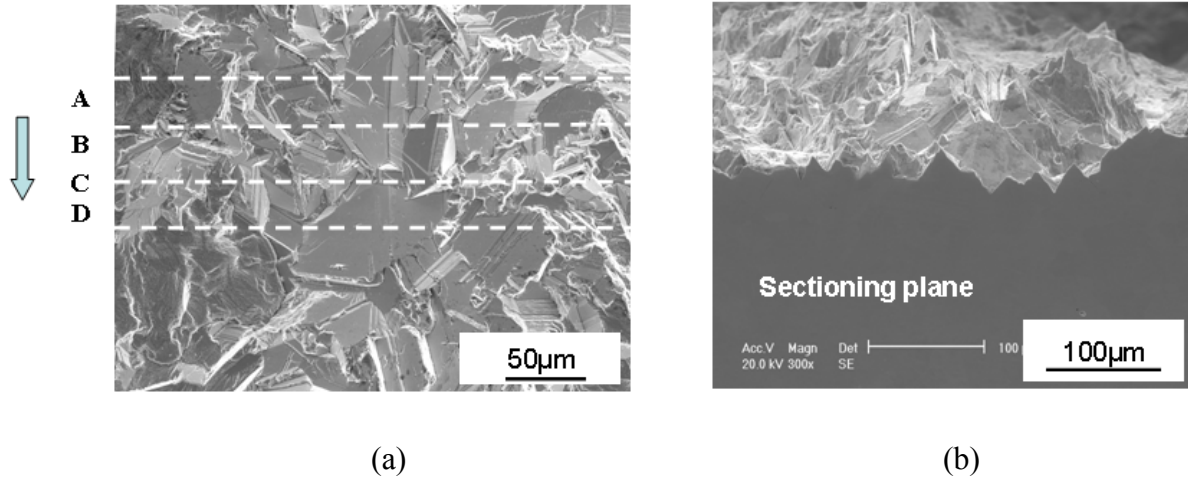


Figure 5.10 Metallographic serial sectioning to collect the crystallographic orientations of neighborhood grains associated with fatigue crack initiation site, (a) Positions of serial sectioning planes, (b) an example of serial sectioning plane ($\sigma_{\max} = 600\text{MPa}$, $N_f = 1.90 \times 10^7$ cycles, 593°C).

Figure 5.11 shows the inverse pole figure maps collected at four sectioning positions described above. The crystallographic orientations of fatigue crack initiation grain (A and G) and its neighbor grains (B, C, D, E and F) as marked in Figure 5.12 (a) were determined and are plotted in Figure 5.12 (b). It can be seen that the orientation of the neighbor grain is close to $\langle 001 \rangle$ direction. The Schmid factor contour plot in Figure 5.12 (b) shows that the orientations of the neighbor grains are favorably oriented for slip. In view of the fact that fatigue crack propagate mainly proceeds by slip band cracking in the early stage of crack growth, these favorably oriented neighbor grains can reduce the resistance to early small crack propagation. Thus, grain size alone cannot explain the likelihood of fatigue crack initiation at a given location.

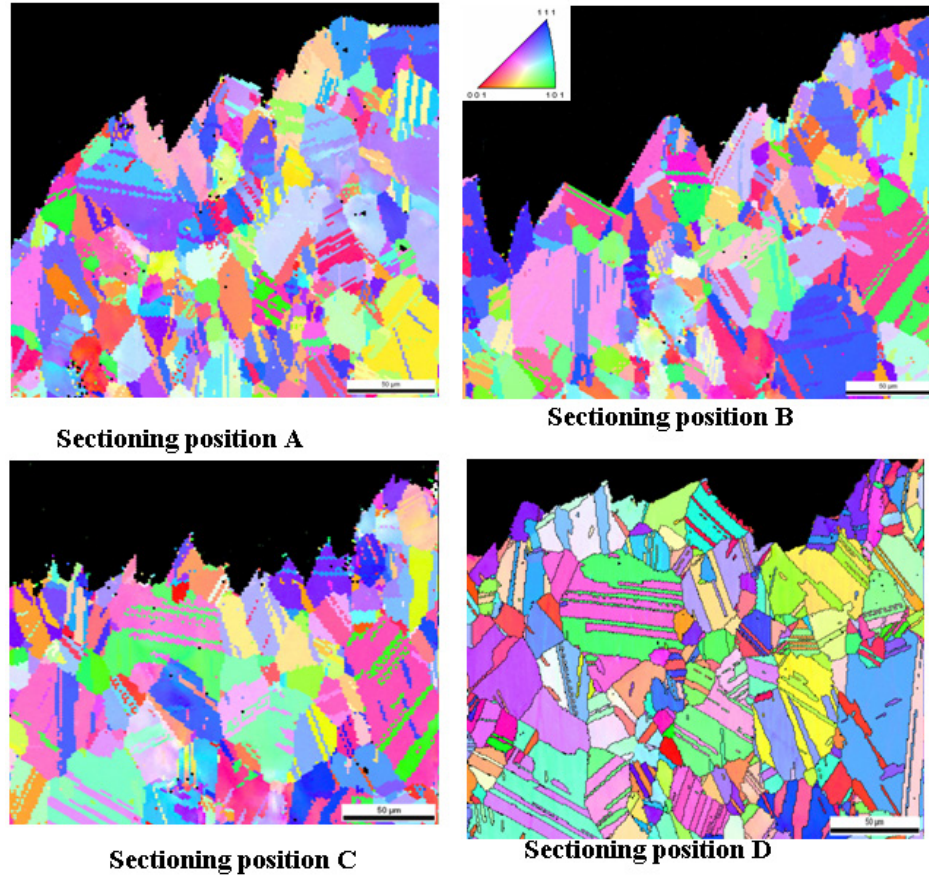
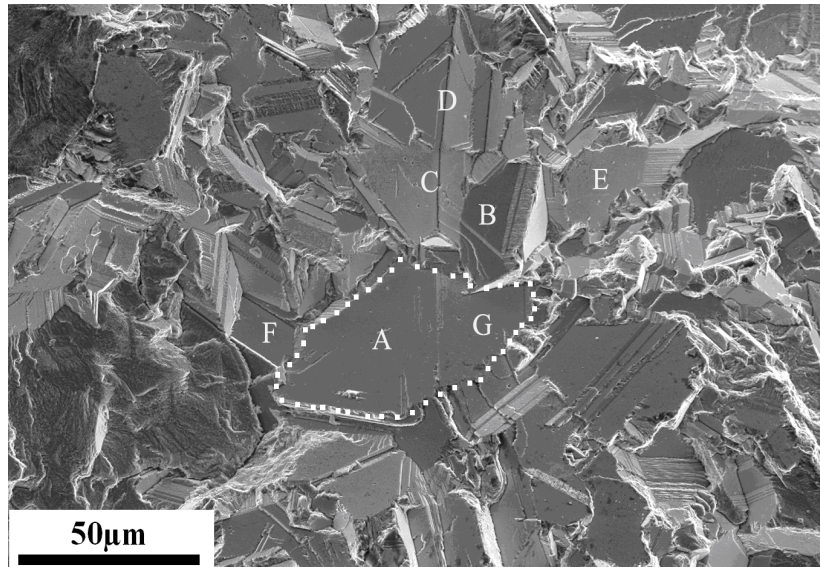
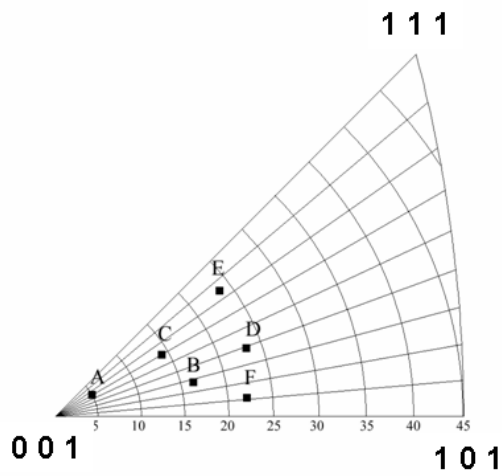


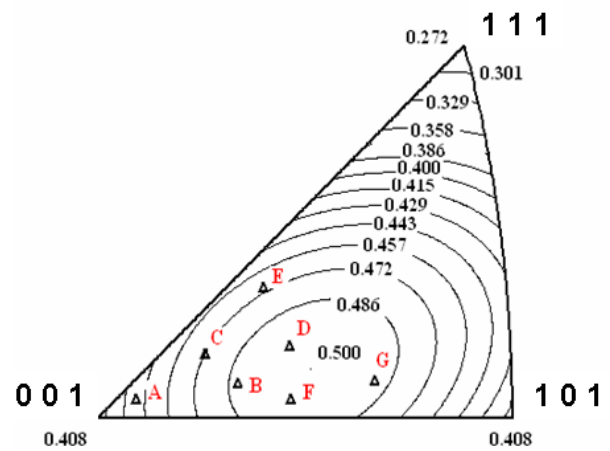
Figure 5.11 Inverse pole figure map collected at four serial sectioning positions.



(a)



(b)



(c)

Figure 5.12 Crystallographic orientation of neighbor grains at the fatigue crack initiation site: (a) SEM image of fatigue crack initiation site, (b) crystallographic orientation of neighbor grain at crack initiation site and (c) contour plot of Schmid factor and crystallographic orientation of neighbor grains ($\sigma_{\max} = 600\text{MPa}$, $N_f = 1.90 \times 10^7$ cycles, 593°C).

As shown in Figure 5.2 (b), there is a second large crystallographic facet near the facet formed in fatigue crack initiation event. This large neighbor facet was also formed by cracking in a large grain. Using serial sectioning, the crystallographic orientation of

this large neighbor grain can also be identified. Figure 5.13 (a) shows a serial sectioning plane that cuts through both the fatigue crack initiation grain and the large neighbor grain. Figure 5.13 (b) shows the side view of sectioning plane, the crystallographic orientation of these two grains was determined by EBSD on the sectioning plane. Figure 5.14 (a) shows the inverse pole figure of these two grains and Figure 5.14 (b) shows the grain boundary map. Red lines represent $\Sigma 3$ twin boundaries. Blue lines represent random large angle grain boundaries. Green lines represent small angle grain boundaries whose misorientation is less than 15 degrees. The orientation relationship between the large crack initiation grain and the neighbor large grain is also shown in pole figure in Figure 5.14 (c). The misorientation relationship between the fatigue crack initiation grain and the neighbor grain is calculated as $14.6\langle 2\ 23\ 5\rangle$. Under cyclic loading, these two large grains can be deformed as one even larger grain making fatigue crack initiation and early crack propagation easier.

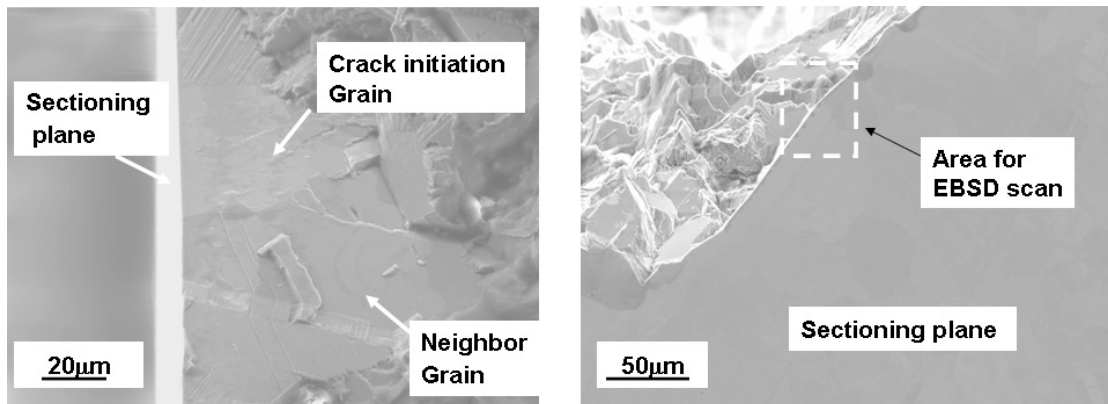


Figure 5.13 Metallographic sectioning through neighbor large grain: (a) top view of fatigue crack initiation site after sectioning and (b) side view of serial sectioning plane ($\sigma_{\max} = 600\text{MPa}$, $N_f = 3.16 \times 10^6$ cycles, 593°C).

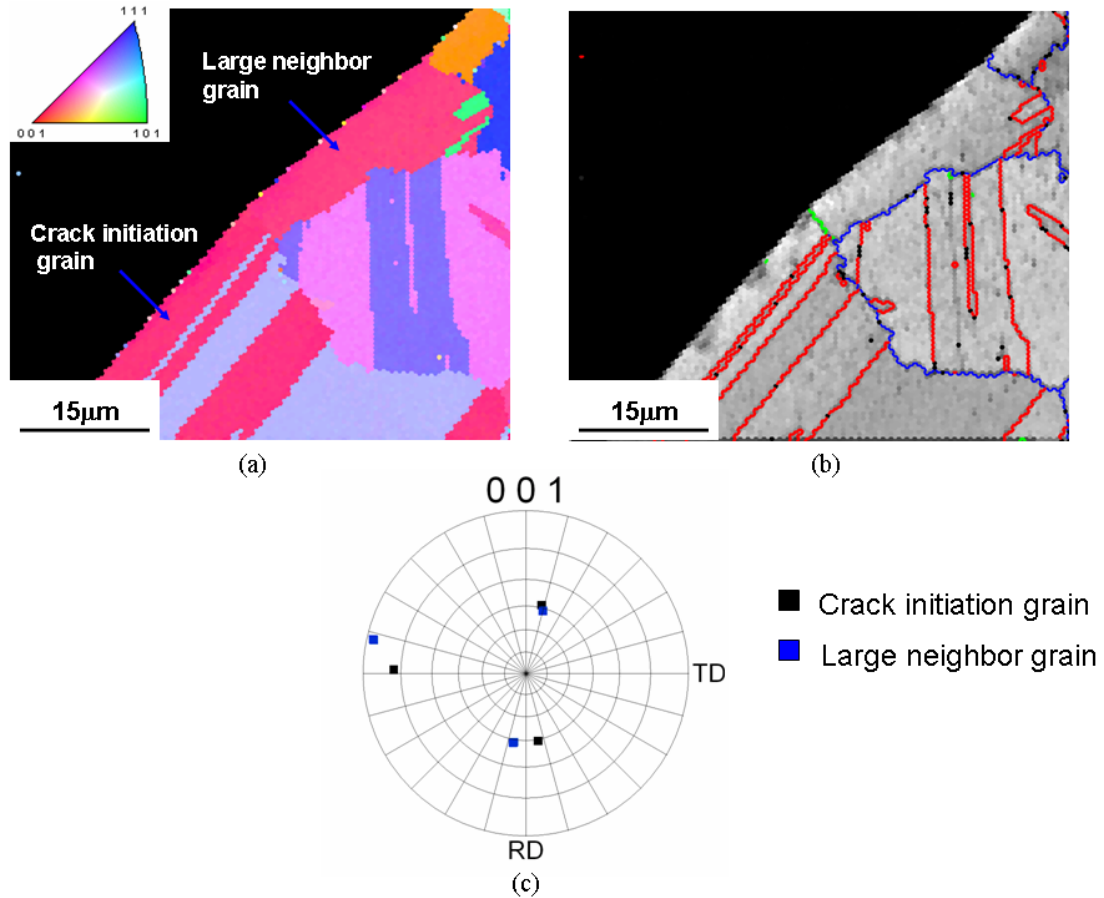


Figure 5.14 Crystallographic orientations of fatigue crack initiation grain and the neighbor large grain: (a) inverse pole figure map; (b) grain boundary map and (c) pole figure showing the orientation relationship between crack initiation grain and neighbor large grain, the grid lines are of 15 degrees ($\sigma_{\max} = 600\text{MPa}$, $N_f = 3.16 \times 10^6$ cycles, 593°C).

5.4 Environmental effects on ultrasonic fatigue behavior at elevated temperature

The surfaces of all specimens were oxidized during ultrasonic fatigue testing at 593°C . Figure 5.15 (a) and (c) show the surface of a failed fatigue specimen and the oxide layer that was formed on the sample surface. Cyclic strain localization in the surface large grain resulted in the formation of slip bands. As indicated in Figure 5.15 (b) and (d), the oxide layers in the vicinity of the slip bands was fractured during cyclic deformation.

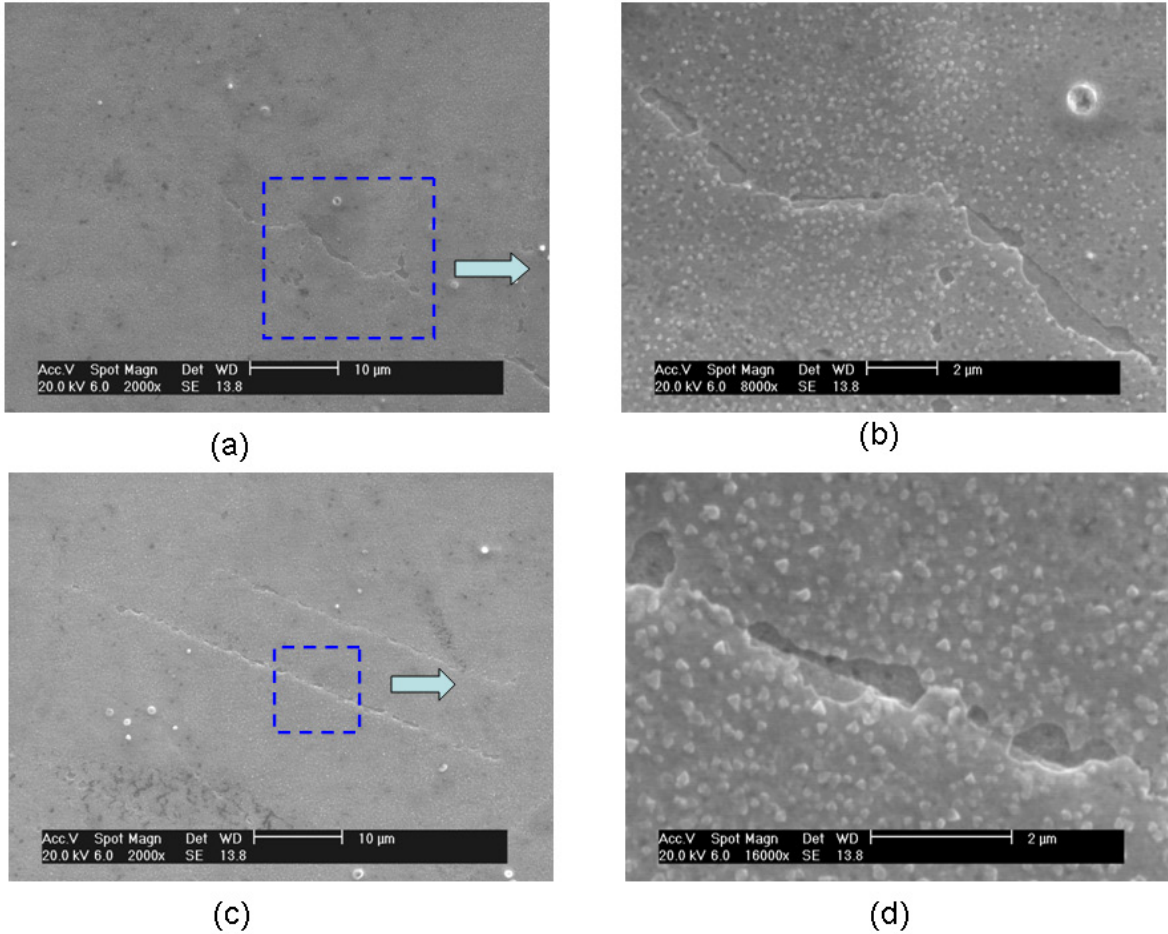


Figure 5.15 Surface oxidation layer formed on fatigue specimens at elevated temperature ($\sigma_{\max} = 660\text{MPa}$, $N_f = 1.48 \times 10^7$ cycles, 593°C).

At 593°C for the stress ranges investigated, all fatigue failures initiated from subsurface regions. One possible reason responsible for subsurface fatigue crack initiation is the interaction between oxygen and the highly localized deformation on the specimen surface. In studying fatigue behavior of single crystal nickel-based superalloy Mar-M200 at the temperature range of $426^\circ\text{C} - 760^\circ\text{C}$, Duquette and Gell [110] found fatigue crack initiated from the subsurface regions in fatigue samples tested in air, while fatigue failures initiated from surface at the same temperature range in vacuum. The inhibition of surface deformation due to the oxidation effect is considered to be

responsible for this transition of fatigue crack initiation site at elevated temperature. Preoxidized specimens were fatigued at elevated temperature in vacuum and surface fatigue crack initiation was observed [110]. This result indicates that the surface oxidation has dynamic, rather than static effects on cyclic deformation on fatigue specimen surface. The spallation of oxide layers as shown in Figure 5.15 may results from in strain localization in the late fatigue process that has not lead to the fatal crack. This also indicates that environmental effects may mainly come from the direct interaction of oxygen with cyclic strain localization rather than from the blocking effect of an oxide layer on slip bands or cyclic strain localization.

5.5 Summary

As shown above, at 593°C, twin boundaries within favorably oriented large grains are important sources for cyclic strain localization and fatigue crack initiation in this alloy. Favorably oriented neighbor grains also contribute to fatigue crack initiation process and especially the easy of early small crack propagation. In Chapter 6, the cyclic deformation behavior of this alloy will be examined at room temperature. Without the effects of environment, direct observation of cyclic deformation and fatigue crack initiation on specimen surfaces can provide important information regarding the role of critical microstructure features on fatigue initiation in this alloy. The findings obtained in room temperature study also can help understand the subsurface fatigue crack initiation process and the environmental effects observed at elevated temperature.

Chapter 6

Cyclic Strain Localization and Fatigue Crack Initiation in Nickel-based Superalloy René 88 DT at Room Temperature

In this chapter, the fatigue behavior of the nickel-based superalloy René 88 DT was examined at room temperature where the propensity for fatigue crack initiation at the specimen surface facilitates the investigation of microstructure effects on damage accumulation and fatigue crack initiation. Using EBSD, a large amount of crystallographic data associated with fatigue crack initiation in large grains and early small crack growth can be quickly obtained. These experimental results can greatly benefit the understanding of the fatigue crack initiation mechanism in René 88 DT and the effects of critical microstructure features on fatigue crack initiation.

6.1 Experimental procedures

Ultrasonic fatigue testing was conducted under fully reversed loading at room temperature ($R = -1$), as described in more detail in Chapter 3. In order to facilitate the crystallographic characterization using EBSD, two parallel flat areas with 2.5 mm in width were machined on the gage section of fatigue specimens originally having a cylindrical gage section. The geometry and dimensions of fatigue specimens with flat areas are illustrated in Figure 6.1. Prior to fatigue testing, the surface of each fatigue specimen was electropolished using the method described in the Chapter 3.

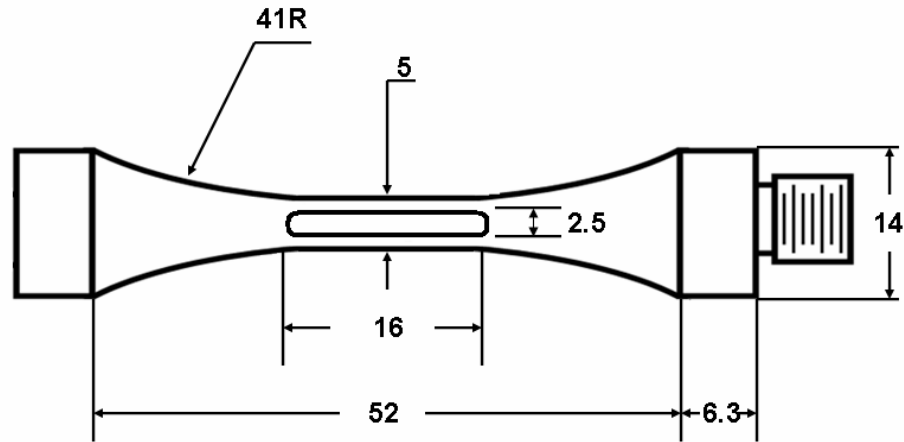


Figure 6.1 Geometry and dimensions of cylindrical ultrasonic fatigue specimens with machined flat areas (all dimensions are in mm).

After fatigue testing, specimen surfaces were examined using SEM to identify regions exhibiting cyclic plastic strain localization and microcracking. Crystallographic information on the fatigue crack initiation sites was collected using electron backscatter diffraction (EBSD) using a TSL OIM system installed in a FEI XL 30 scanning electron microscope.

6.2 Experimental results

6.2.1 S-N data

Fatigue tests were conducted on three fatigue specimens at a stress ratio $R = -1$. One specimen without flat areas was tested at $\sigma_{\max} = 720$ MPa and two other specimens with machined flats were tested at $\sigma_{\max} = 680$ MPa and 640 MPa respectively. All maximum loading stresses were well below the 1200MPa room temperature yield strength. The fatigue life for each specimen is shown in Table 6.1.

Table 6.1 Stress-fatigue life of samples tested at room temperature (R = -1).

σ_{\max} (MPa)	720	680	640
N_f (cycles)	1.92×10^5	1.85×10^5	2.97×10^5

The room temperature S-N data were plotted in Figure 6.2 and compared with elevated temperature testing results. The fatigue lives at room temperature are shorter than those at elevated temperature. The fatigue lives in stresses range of 760 MPa ~ 660 MPa at elevated temperature are about 3~60 times longer than the fatigue lives of three room temperature testing results. The difference in fatigue life may be associated with the shift of subsurface fatigue crack initiation at elevated temperature to surface crack initiation at room temperature, as described later. However, both room temperature and elevated temperature testing were conducted at stress levels well below the yield stress of this alloy, and the observed deformation mode is similar at both temperatures (precipitate shearing and localized planar slip). Thus, these room temperature studies not only can provide information regarding cyclic strain localization and fatigue crack initiation at room temperature, but also can offer useful information regarding the role of critical microstructure features in the fatigue crack initiation process at elevated temperature.

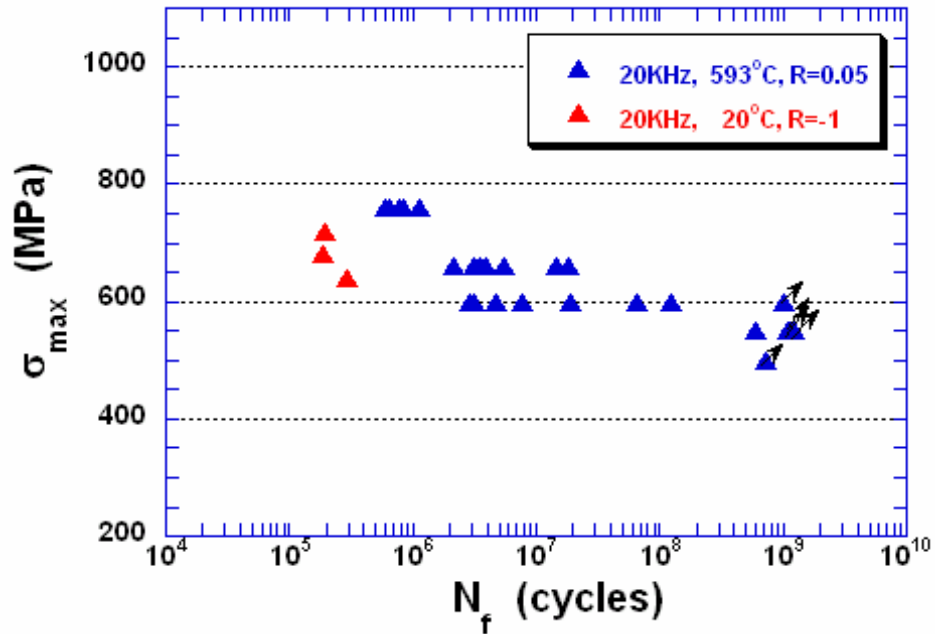


Figure 6.2 S-N data of room-temperature fatigue testing results as compared with elevated temperature testing results.

6.2.2 Observations of the fatal fatigue crack at 720 MPa

Figure 6.3 shows the fatal fatigue crack and the crack initiation site on the surface of the specimen tested at $\sigma_{max} = 720\text{MPa}$. The failed specimen was separated to examine the fracture surface. Figure 6.4 (a) and (b) shows a view of fracture surface normal to the general fracture plane and in a direction parallel to the loading axis. Figure 6.4 (c) and (d) are side views of fracture surface while tilting the specimen at 30° . The crack initiation site is marked in Figure 6.4 (b) and (d).

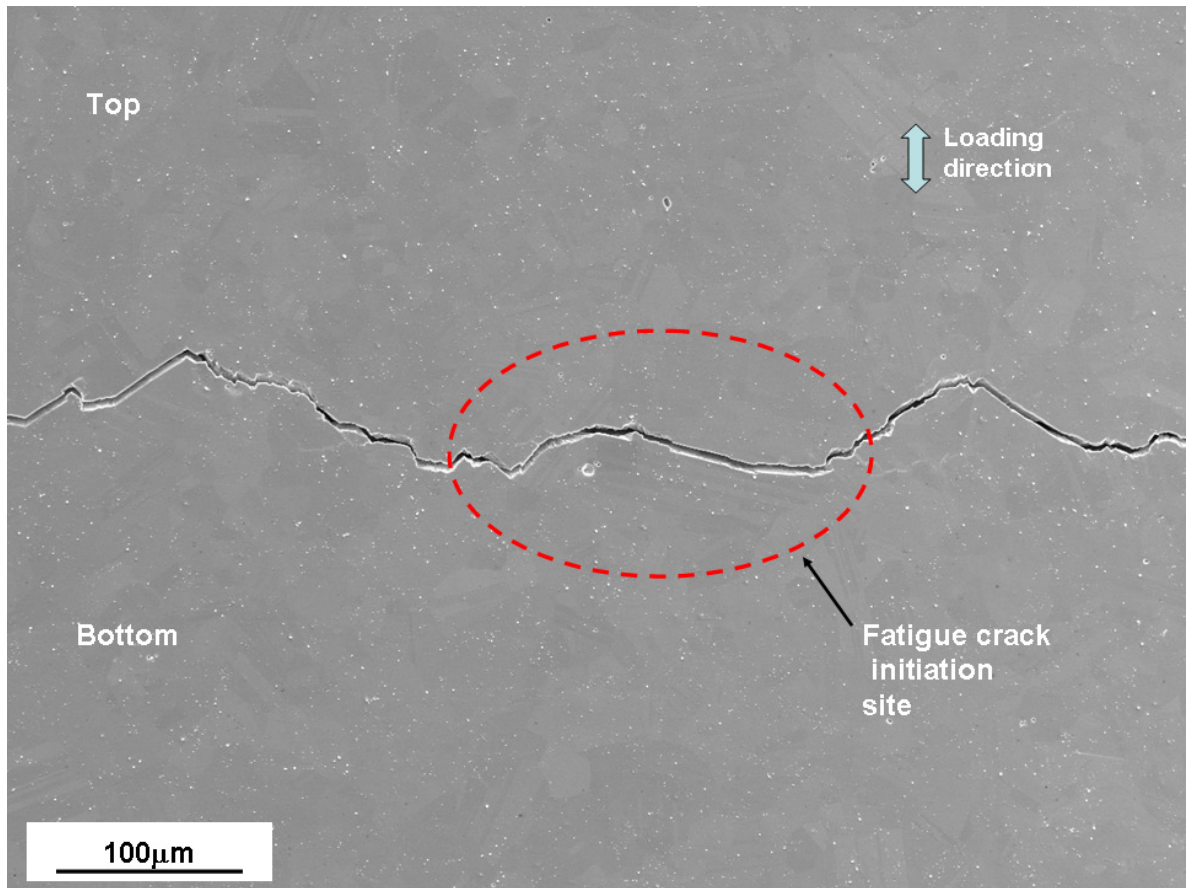


Figure 6. 3 SEM image of the fatal fatigue on the surface of the fatigue specimen tested at $\sigma_{\max} = 720\text{MPa}$.

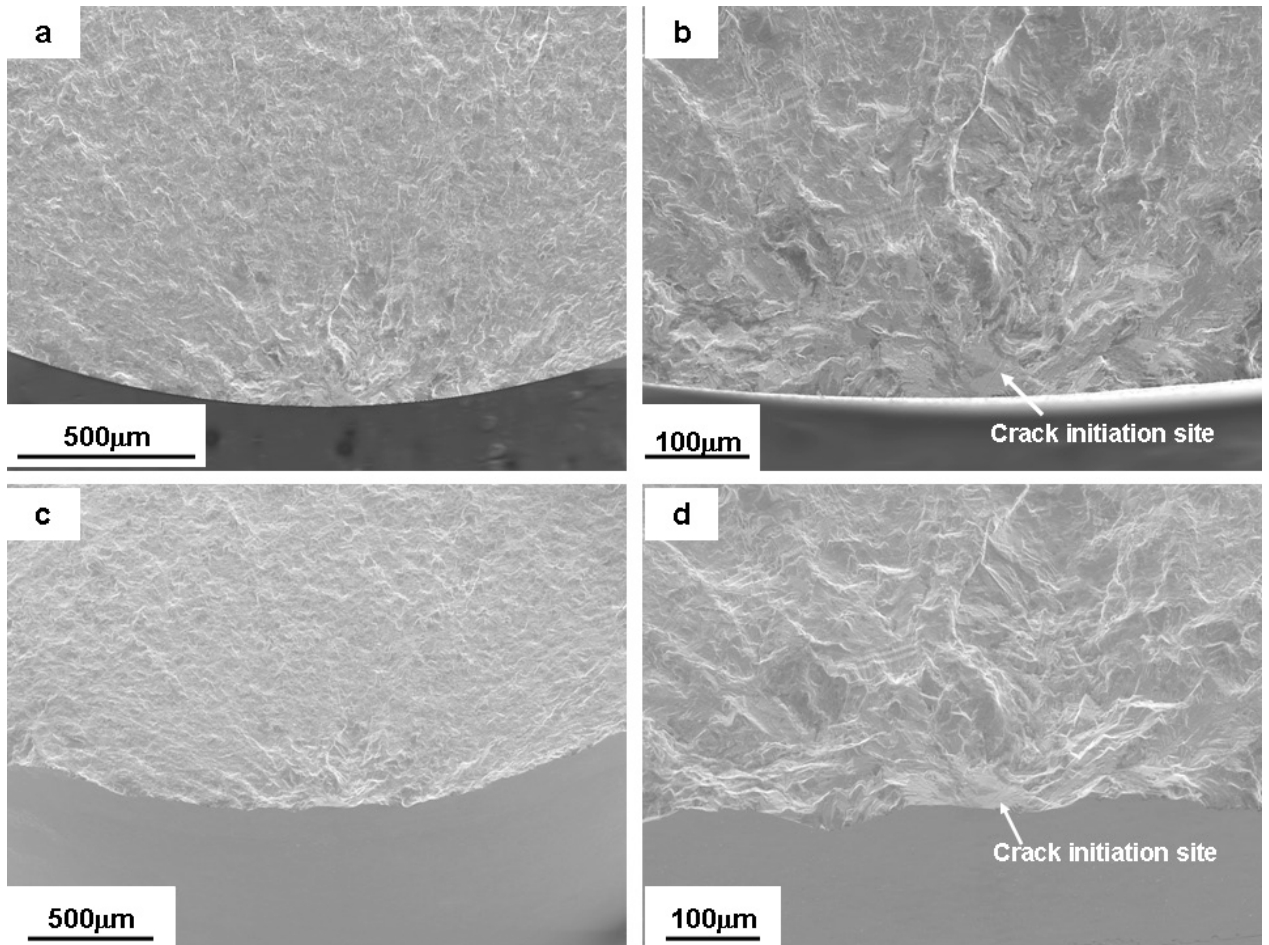


Figure 6. 4 Fracture surface of the failed fatigue specimen: (a) top view of fracture surface (low magnification); (b) top view of the fracture surface (high magnification); (c) side view of the fracture of the tilted specimen, (low magnification) and (d) side view of the fracture surface of the tilted specimen (high magnification). ($\sigma_{\max} = 720\text{MPa}$, $N_f = 1.92 \times 10^5$ cycles, 20°C).

Figure 6.5 (a) shows the fatigue crack initiation site. There is some contamination on the fracture surface as indicated in Figure 6.5 (b). There are steps at the crack initiation site that point to the specimen surface as indicated in Figure 6.5 (a). Very fine striations were observed at the crack initiation site as shown in Figure 6.5 (c). These striations have semi-circular shape as shown in Figure 6.5 (b) and (c). The distance between striations is about 50 nm as indicated in Figure 6.5 (d). The center of these semi-circular striations is the fatigue crack initiation site, which is located at the specimen

surface. This result indicates the fatal fatigue crack initiated at the specimen surface and then grew into the interior of the fatigue crack initiation grain. The crack growth direction is marked on Figure 6.5 (c).

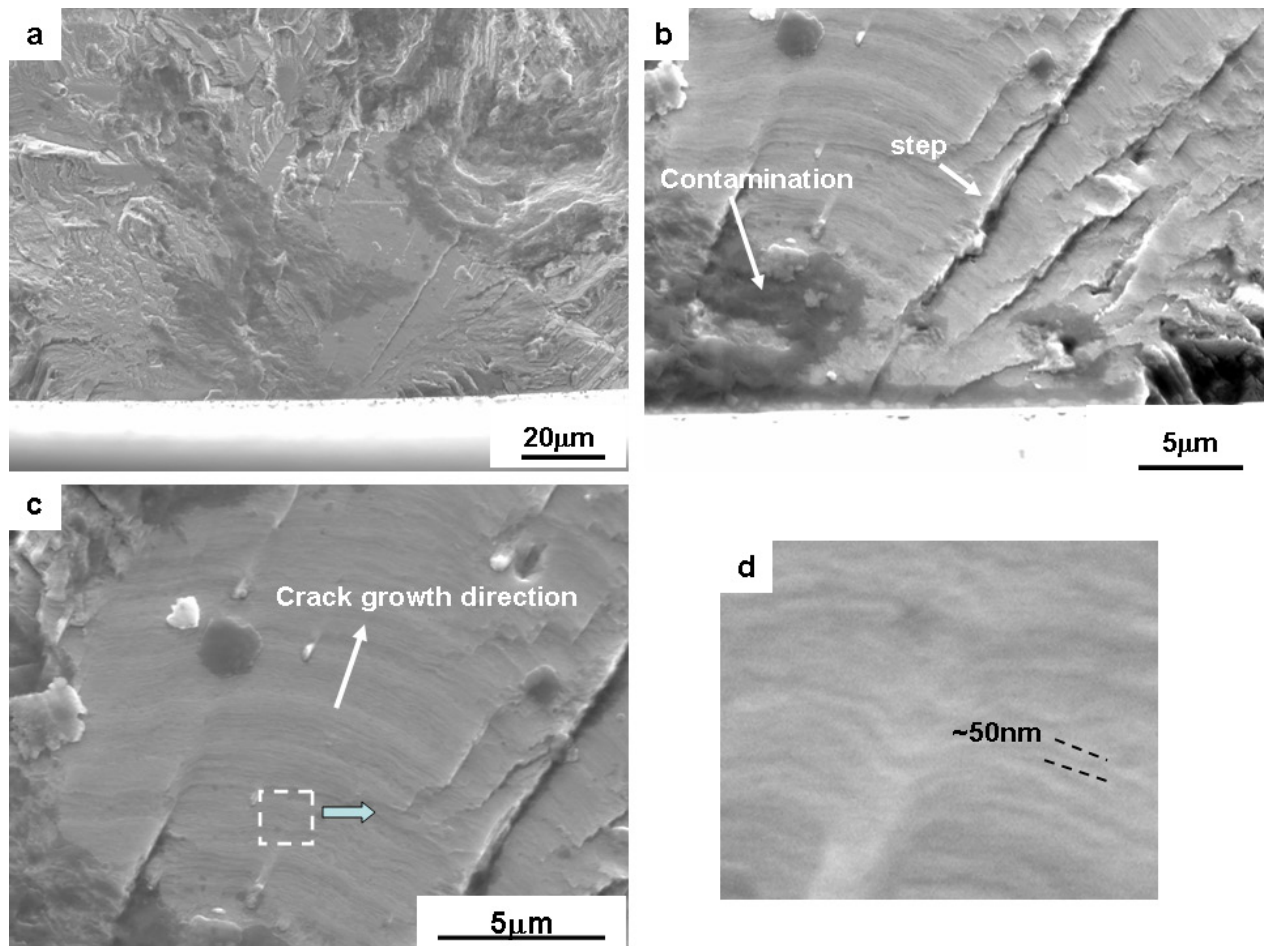


Figure 6.5 Detailed features of the fatigue crack initiation site: (a) low magnification SEM image of the crack initiation site; (b) high magnification SEM image of the crack initiation site; (c) striations at the crack initiation site and (d) enlarged view of the dashed square area in Figure 6.5 (c) ($\sigma_{\max} = 720\text{MPa}$, $N_f = 1.92 \times 10^5$ cycles, 20°C).

Figure 6.6 shows the detailed features of the fatigue crack initiation site on the specimen surface. The position of the fatigue crack initiation site is marked on the figure. Within the fatigue crack initiation grain, besides the fatal fatigue crack, there are several

microcracks or slip bands parallel to the fatal fatigue crack as indicated in Figure 6.6 (c) and (d).

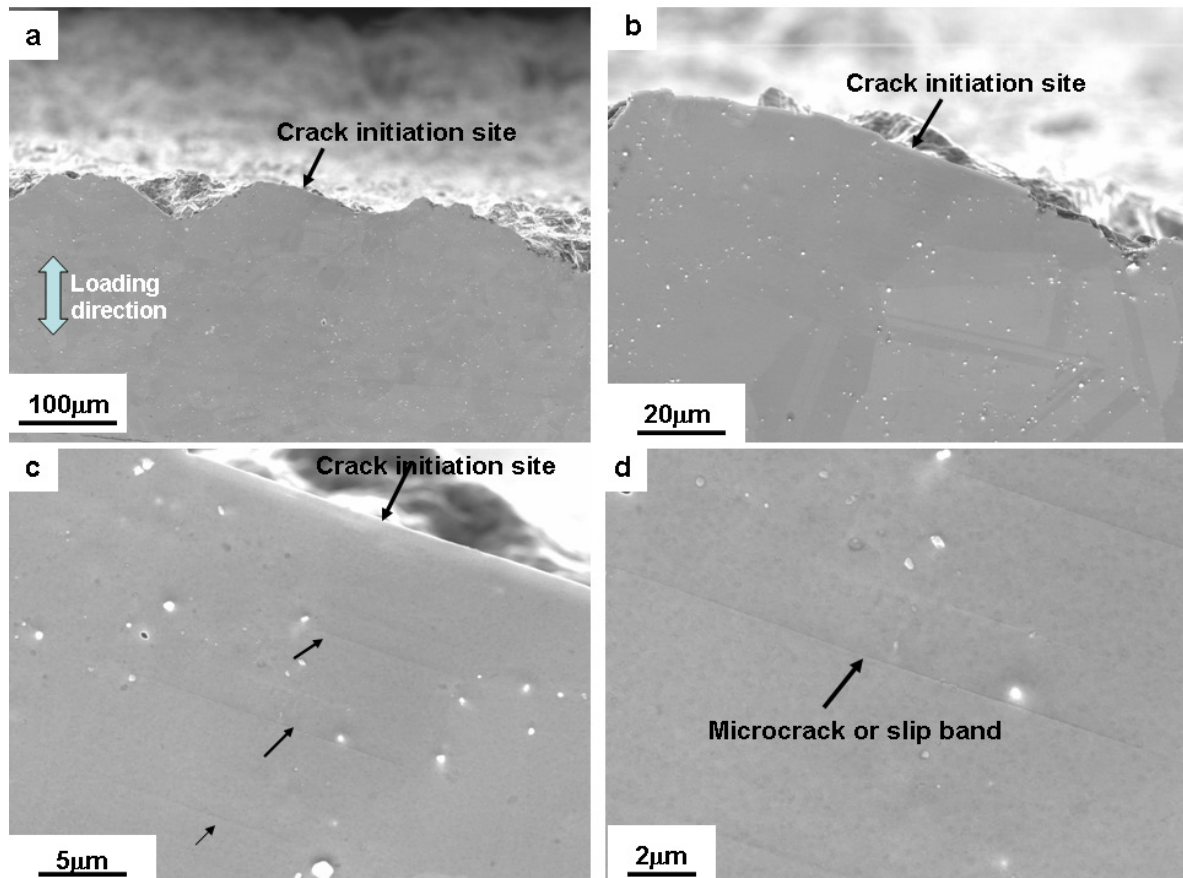


Figure 6.6 Features of the fatigue crack initiation grain on the specimen surface: (a) and (b) low magnification images of the fatigue crack initiation grain, (c) and (d) high magnification images of microcracks or slip bands formed within the fatigue crack initiation grain ($\sigma_{\max} = 720\text{MPa}$, $N_f = 1.92 \times 10^5$ cycles, 20°C).

The fatal fatigue crack initiation site was characterized using EBSD. The cylindrical gage section has no machined flat, thus, the orientations determined may not be accurate because of the difficulty in aligning a curved specimen surface to satisfy the EBSD setup which requires to tilt a flat specimen by 70° with respect to the incident electron beam. However, EBSD results still can offer other microstructural information

such as grain size and the character of grain boundaries at fatigue crack initiation site. Figure 6.7 (a) and (d) shows the inverse pole figure map and grain boundary map of the fatigue crack initiation site respectively. The EBSD results were obtained on the top half of the fatigue specimen as indicated in Figure 6.3. The grain boundary map in Figure 6.7 (b) shows that the fatigue crack initiated in a very large grain close to a $\Sigma 3$ twin boundary as indicated in Figure 6.7 (c).

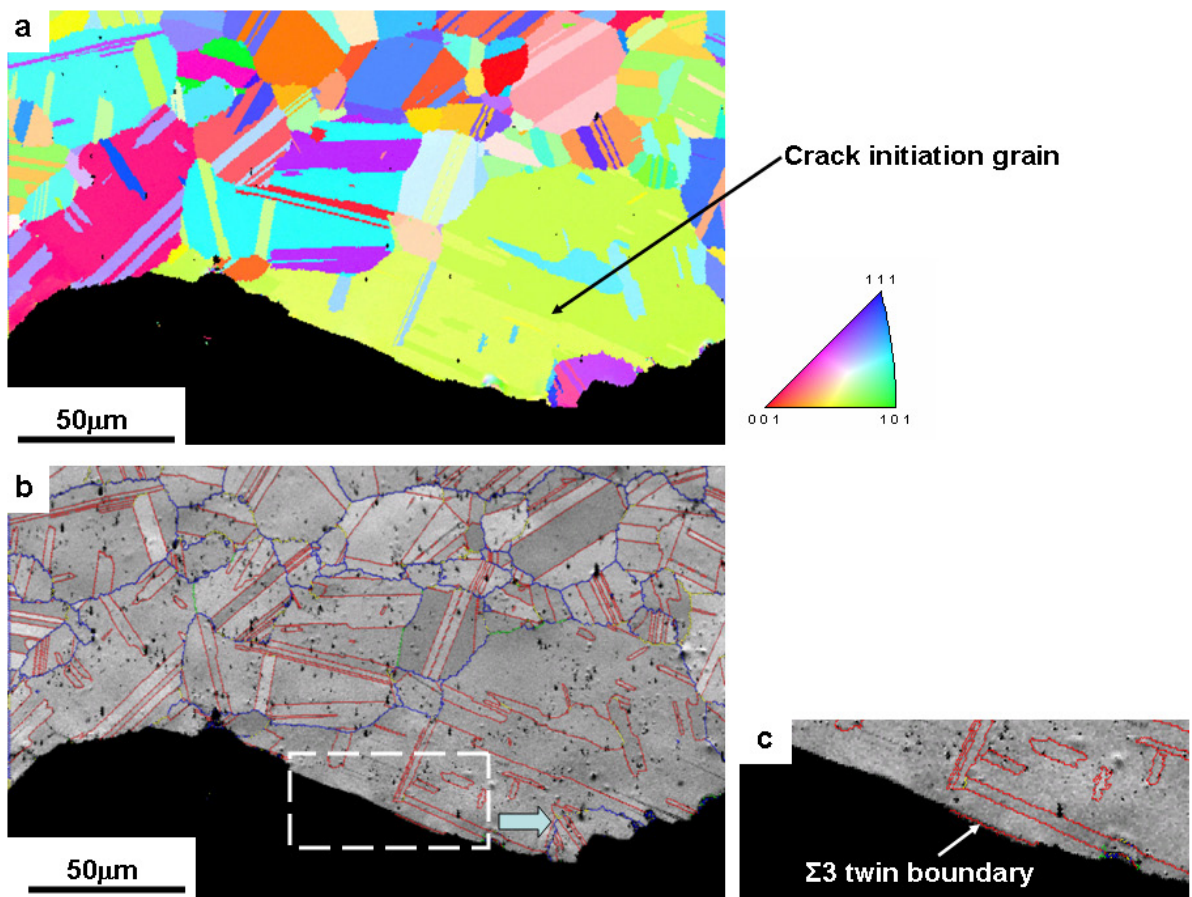


Figure 6.7 EBSD characterization of the fatigue crack initiation grain: (a) inverse pole figure map; (b) grain boundary map (red lines - $\Sigma 3$ twin boundaries, blue lines - random large angle grain boundary, yellow – other Σ grain boundaries and (c) enlarged view of the highlighted area in Figure 6.7 (b) ($\sigma_{\max} = 720\text{MPa}$, $N_f = 1.92 \times 10^5$ cycles, 20°C).

6.2.3 Quantitative characterization of microcracks for specimens with machined flats

Microcracks located on the machined flats and far away from the fatal fatigue cracks were subjected to EBSD examination. Figure 6.8 shows the positions of some of the microcracks on a machined flat subjected to EBSD study on the surface of the fatigue specimen tested at $\sigma_{\max} = 640\text{MPa}$. The image was taken while tilting the specimen at 70° . The tilting axis is indicated on Figure 6.8.

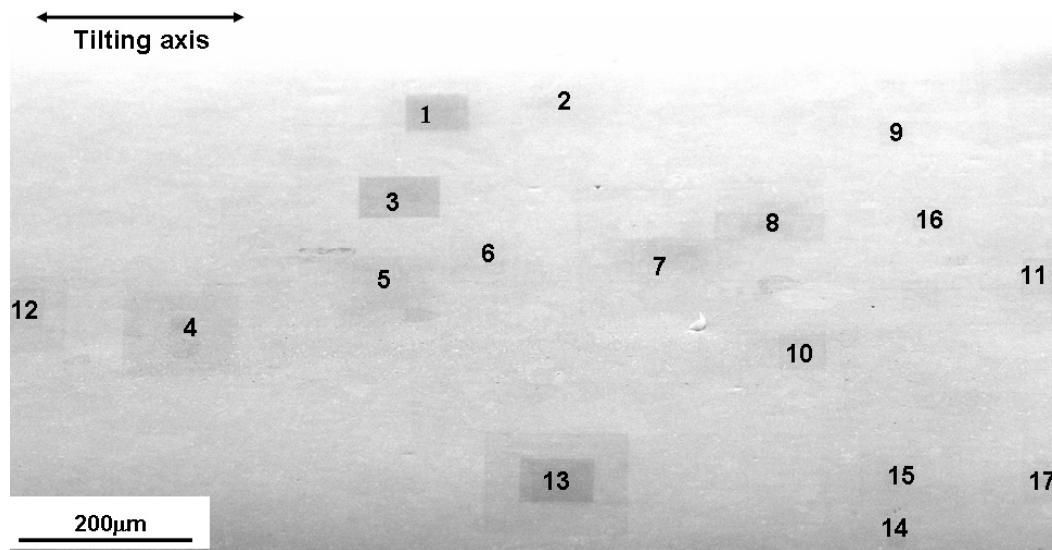


Figure 6.8 The positions of selected microcracks subjected to EBSD investigation ($\sigma_{\max} = 640\text{MPa}$, $N_f = 2.97 \times 10^5$ cycles).

Figure 6.9 shows two microcracks at several magnifications. In Figure 6.9 (a), it can be seen that a microcrack initiated within a large grain and propagated into its neighboring grains. Another small microcrack in the same neighborhood did not propagate beyond the grain in which it initiated. No other slip bands are observed in the surrounding area. The features of the large crack initiation grain are shown in Figure 6.9 (b)-(d). As shown in Figure 6.9 (c), within the initiating grain, there are no other slip

bands. The opening displacement of the microcrack is on the order of several hundreds of nanometers. As indicated in Figure 6.9 (d), there are a very small amount of materials extruded during cyclic plastic deformation at the edge of the microcrack.

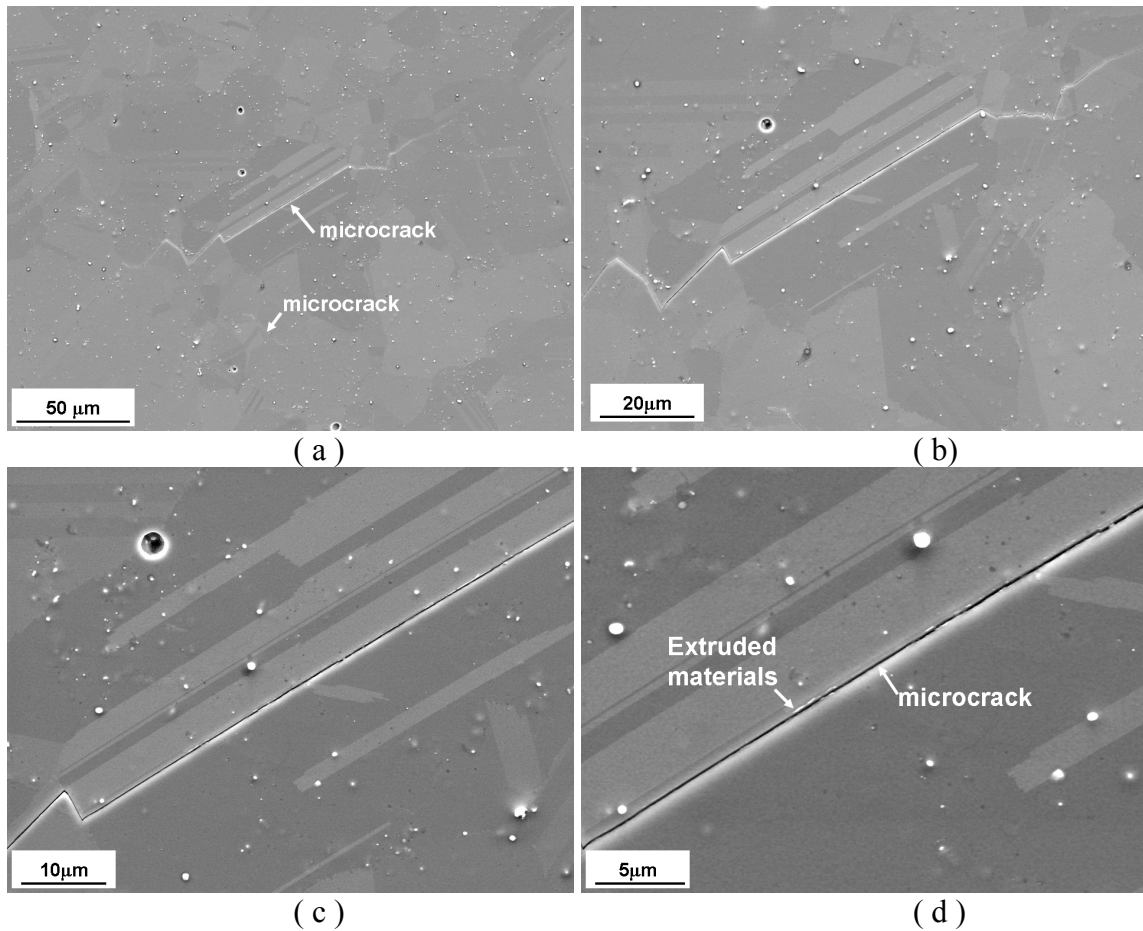


Figure 6.9 SEM images of microcracks: (a) Microcracks and their neighborhood microstructure; (b),(c) and (d) detailed features of microcrack within the fatigue crack initiation grain ($\sigma_{\max} = 640\text{MPa}$, $N_f = 2.97 \times 10^5$ cycles, 20°C).

Of the 30 microcracks and their associated microstructural neighborhood microstructure investigated by EBSD, all initiated in a region near $\Sigma 3$ twin boundaries, $\Sigma 3$ s twin boundaries or at triple junctions of $\Sigma 3$ s twin boundaries. In the following

sections, typical examples of crack initiation sites are presented in term of critical microstructure features.

6.2.3.1 Microcracks initiated at the region close to $\Sigma 3$ coherent twin boundary

Figure 6.10 (a) and (b) show a microcrack with features similar to those for the microcrack shown in Figure 6.9. Figure 6.10 (c) is the inverse pole figure map of the fatigue crack initiation site. The EBSD map was collected at a step size of $0.5 \mu\text{m}$. Figure 6.10 (d) is a grain boundary map superimposed with the SEM image. The red lines represent $\Sigma 3$ twin boundaries. By combining the SEM image with the grain boundary map, it is relatively straightforward to show that the micorcrack was initiated at the region close to the $\Sigma 3$ twin boundary, Figure 6.10 (d). The white lines in Figure 6.10 (e) represent the reconstructed $60^\circ \langle 111 \rangle$ twin boundaries. The coherence of $\Sigma 3$ twin boundary can be determined by comparing the white reconstructed boundary with red $\Sigma 3$ twin boundary line. If the reconstructed $60^\circ \langle 111 \rangle$ twin boundary and the $\Sigma 3$ twin boundary are in alignment with each other, the $\Sigma 3$ twin boundary is a coherent twin boundary and the twin boundary plane is parallel to $\{111\}$ plane. Otherwise, the $\Sigma 3$ twin boundary is incoherent and not parallel to $\{111\}$ slip planes. It can be seen that the $\Sigma 3$ twin boundary close to which the microcarck initiated is a coherent $\Sigma 3$ twin boundary. Variations in local misorientation are a good indicator of cyclic plastic strain localization. The misorientation of a grain can be determined using Kernel method. In this method, misorientations between the grain located at the center of the kernel and all its neighbor grains within the kernel are calculated. The average value of these calculated misorientations is then assigned to the center grain. The Kernel misorientation map was calculated and shown in Figure 6.10 (f). It can be seen in Figure 6.10 (f) that within the

fatigue crack initiation grain, there is at most a very small misorientation along the crack path. However, when the fatigue crack propagated to its neighbor grains, larger misorientation developed along the crack path, arising from the increasing levels of plastic deformation associated with fatigue propagation. This result also shows that within the fatigue crack initiation grain, cyclic plastic deformation is mainly localized within the very small region close to the twin boundary. The Schmid factor on the slip plane parallel to twin boundary and the plane of microcrack was calculated as 0.45.

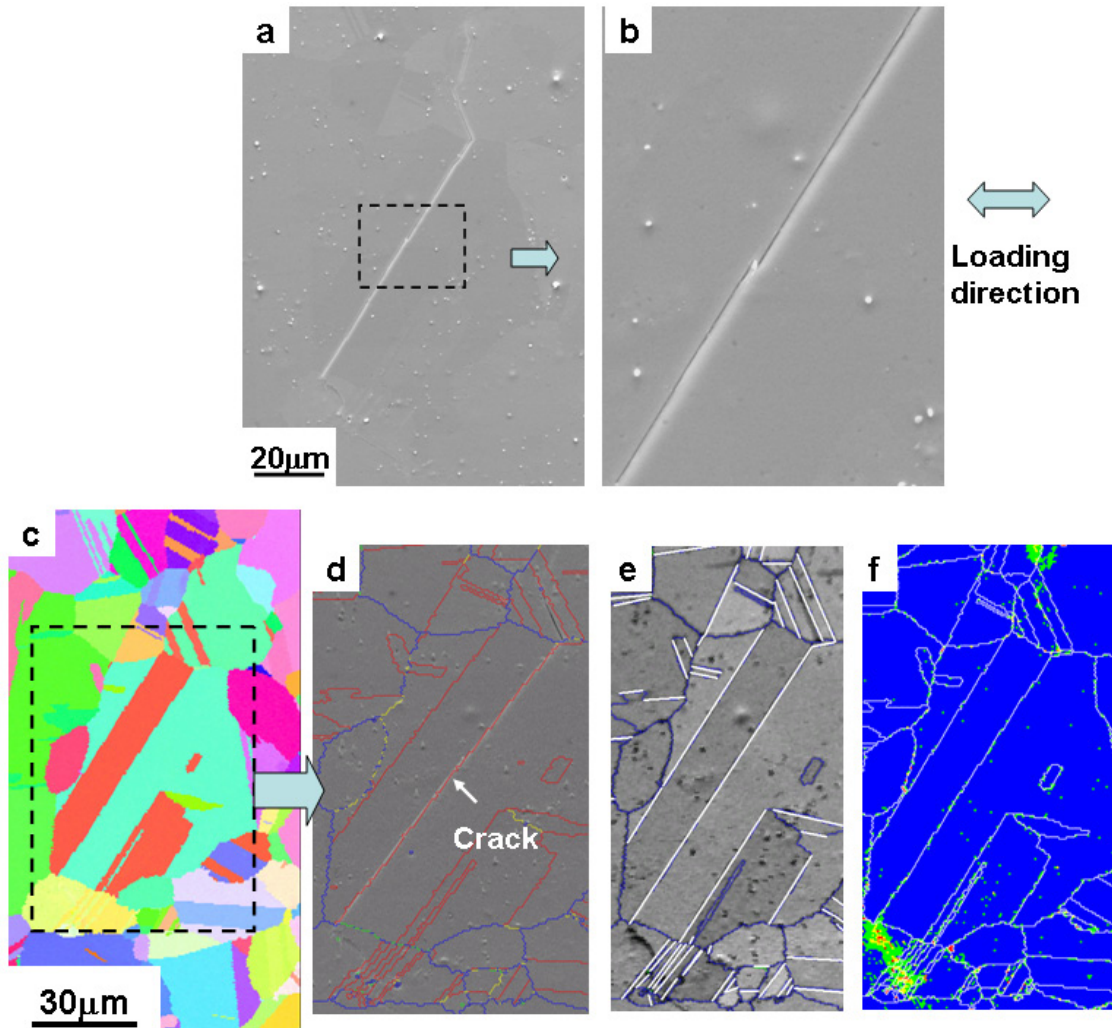


Figure 6.10 Microcrack initiated at the region close to a $\Sigma 3$ coherent twin boundary: (a) SEM image of fatigue crack initiation site; (b) SEM image of region close to the microcrack; (c) Inverse pole figure of fatigue crack initiation site; (d) grain boundary map overlaid by SEM image; (e) reconstructed $\{111\}$ twin plane on grain boundary map over-layed with the image quality map (white lines represent reconstructed $\{111\}$ twin boundaries, blue lines represent large angle grain boundaries, including $\Sigma 3$ twin boundaries) and (f) Kernel misorientation map overlaid by grain boundary map ($\sigma_{\max} = 640\text{MPa}$, $N_f = 2.97 \times 10^5$ cycles, 20°C).

Figure 6.11 (a) shows another microcrack. Similar to the previous results, there are no observations of slip bands in the neighbor grains and there is also very small

amount of extruded materials observed at a small section of the microcrack as indicated in Figure 6.11 (b).

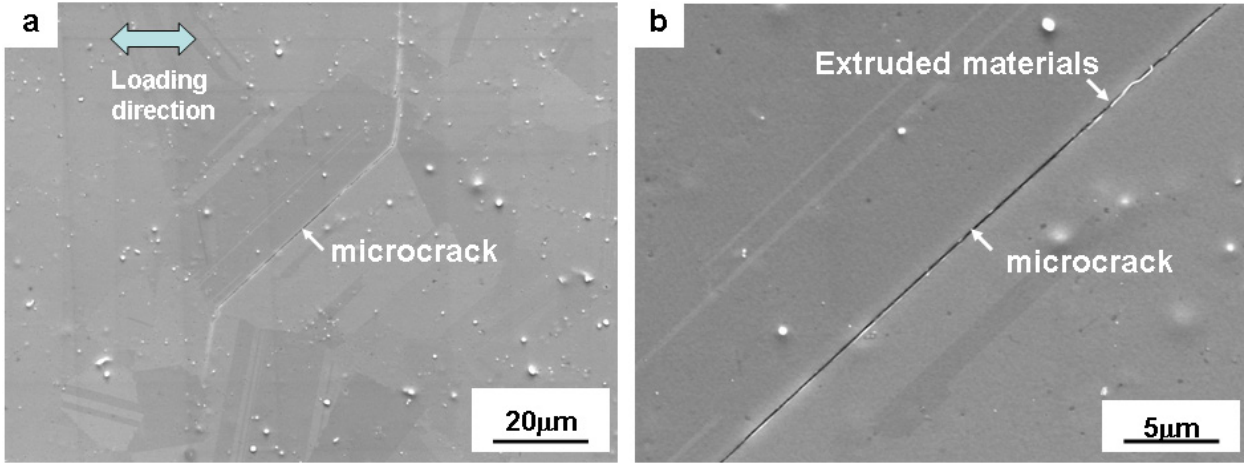


Figure 6.11 SEM image of a microcrack: (a) crack initiation site and (b) detail features of the microcrack. ($\sigma_{\max}=640\text{MPa}$, $N_f=2.97\times 10^5$ cycles, 20°C).

Figure 6.12 (a) shows the inverse pole figure map of the microcrack from Figure 6.11. The position of the microcrack is indicated in the grain boundary map in Figure 6.12 (b). This microcrack also formed near a $\Sigma 3$ twin boundary. The reconstructed $\{111\}$ twin boundary was shown with green lines in Figure 6.12 (d). The $\Sigma 3$ twin boundary where fatigue crack initiated is parallel to the green lines. Thus this $\Sigma 3$ twin boundary is a coherent $\Sigma 3$ twin boundary. The fatigue crack initiated and propagated near and along this $\Sigma 3$ twin boundary. At the position A as indicated in Figure 6.12 (c) and (d), the $\Sigma 3$ twin boundary intersects with another $\Sigma 3$ twin boundary and one $\Sigma 9$ boundary, forming a triple junction of $\Sigma 3$ s twin boundary. The type of Σ twin boundary within a triple junction can be determined by the following rule [111].

$$\begin{aligned} \Sigma A + \Sigma B &= \Sigma A \times B \\ \text{or} & \\ \Sigma A + \Sigma B &= \Sigma A \div B \end{aligned} \tag{6.1}$$

Where A and B are of one of the Σ type of grain boundary in a grain boundary triple junction.

At the triple junction, the microcrack changes direction, following another slip band and continues to grow within the fatigue crack initiation grain. The Schmid factor on the slip plane parallel to the coherent $\Sigma 3$ twin boundary and crack plane was calculated as 0.49. It has the highest Schmid factor within both the twin and matrix. The grain boundary map shows that the fatigue crack initiation grain and one of its neighbor grains has small angle grain boundary as indicated in Figure 6.12 (b).

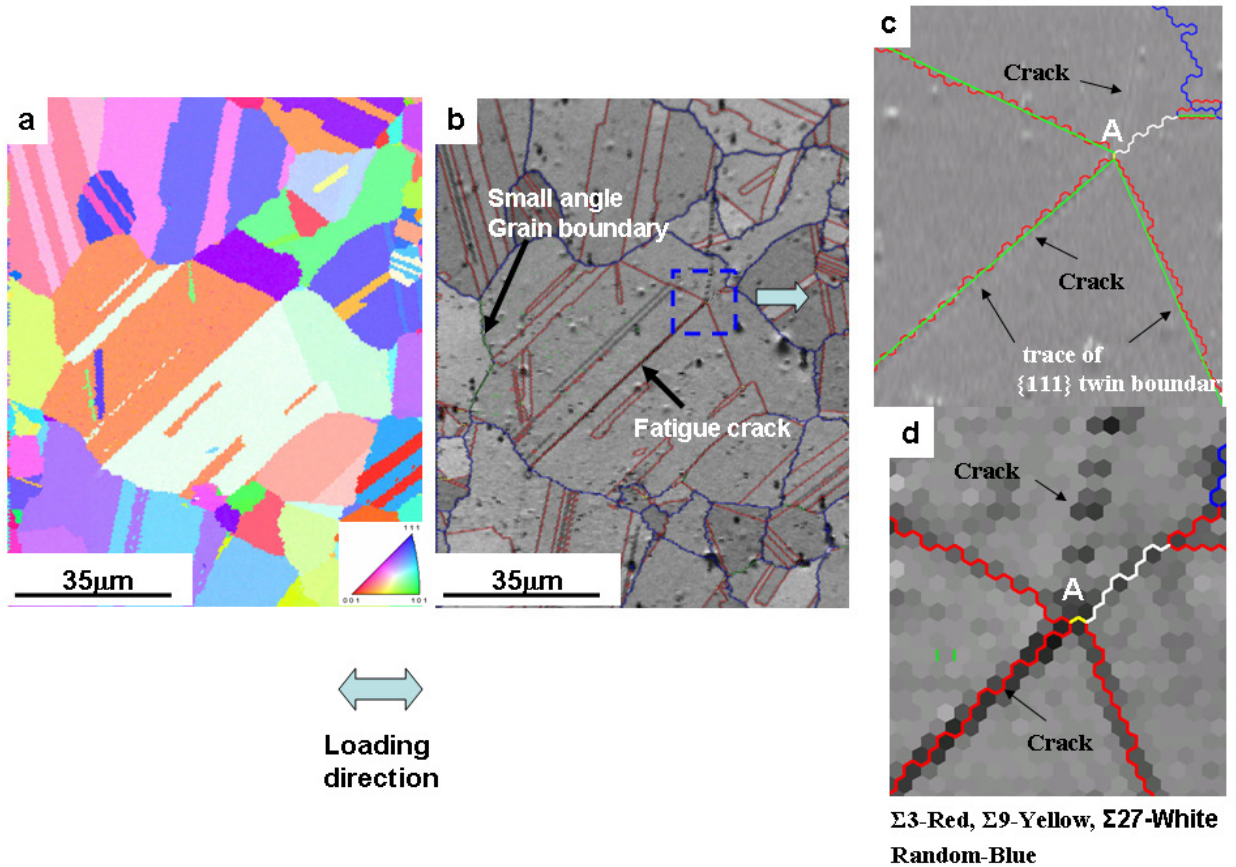


Figure 6.12 EBSD characterization of a microcrack formed at the region close to a $\Sigma 3$ twin boundary: (a) inverse pole figure map of the crack initiation site; (b) grain boundary map; (c) reconstructed $60^\circ \langle 111 \rangle$ twin boundary and grain boundary map overlaid by SEM image, (green lines represent reconstructed $\{111\}$ twin boundaries) and (d) detail structure of the $\Sigma 3$ Triple junction ($\sigma_{\max} = 640 \text{ MPa}$, $N_f = 2.97 \times 10^5$ cycles, 20°C).

6.2.3.2 Fatigue crack formation along both $\Sigma 3$ and $\Sigma 3s$ ($s > 1$) twin boundary

Figure 6.13 (a) shows the inverse pole figure map of a fatigue crack initiation site. Figure 6.13 (b) is the corresponding grain boundary map overlaid with an image quality map showing both the character of grain boundaries and the location of the microcrack. The location of the microcrack is indicated in Figure 6.13 (b). The grain boundary structure within the crack initiation grain is highlighted in Figure 6.13 (c). The red lines represent $\Sigma 3$ twin boundaries and yellow lines represent $\Sigma 9$ twin boundaries. It can be seen that the microcrack was formed along both the $\Sigma 3$ twin boundary and $\Sigma 9$ boundary. The reconstructed $\{111\}$ twin boundary is shown by white lines in Figure 6.13 (d). It can be seen that the $\Sigma 3$ twin boundary near the microcrack is a coherent $\Sigma 3$ twin boundary. The Schmid factor on the slip plane parallel to the $\Sigma 3$ twin boundary and the fatigue crack plane was calculated as 0.5.

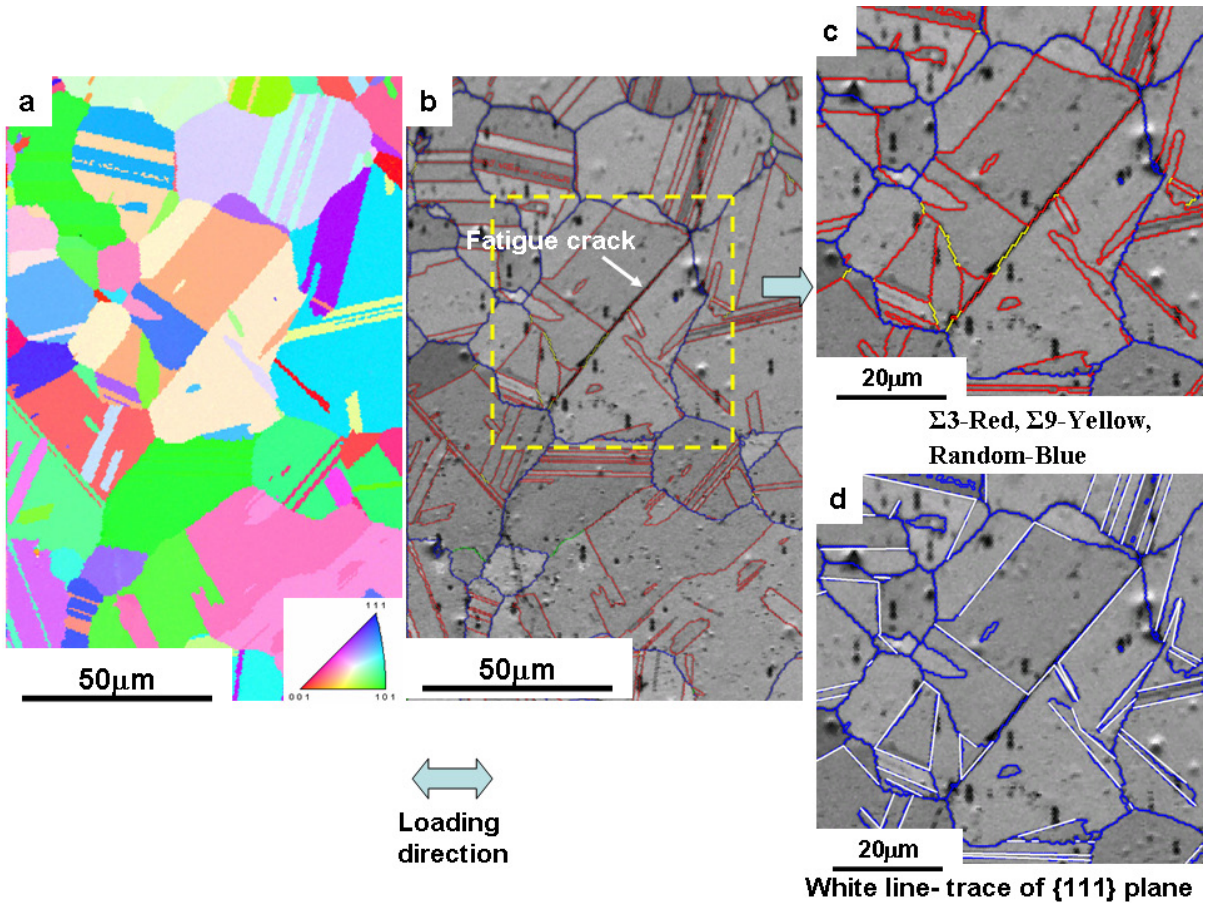


Figure 6.13 Fatigue crack initiated at the region close to Σ_3 s twin boundary: (a) inverse pole figure of the crack initiation site; (b) grain boundary map overlaid by image quality map of the crack initiation site; (c) Σ_3 grain boundaries within the fatigue crack initiation grain (Red lines- Σ_3 boundaries, yellow lines - Σ_9 boundaries, blue lines-random grain boundaries) and (d) reconstructed $\{111\}$ twin boundary and grain boundary map overlaid with the image quality map (white line is the reconstructed $\{111\}$ twin boundary). ($\sigma_{\max} = 640\text{MPa}$, $N_f = 2.97 \times 10^5$ cycles, 20°C).

6.2.3.3 Fatigue crack initiation at Σ_3 twin boundaries with both coherent and incoherent sections

Figure 6.14 (a) shows a region where several microcracks were formed. One of these microcracks grew to several hundred micrometers in length and became a small fatigue crack as indicated in Figure 6.14 (a). The crack initiation grain where this small crack originated is shown in Figure 6.14 (a). The fatigue crack initiated within a very large grain. One interesting observation is that there is a small pore in the region close to

fatigue crack growth path as indicated in Figure 6.14 (a). Figure 6.14 (c) shows that there are no slip bands or microcracks formed at the pore.

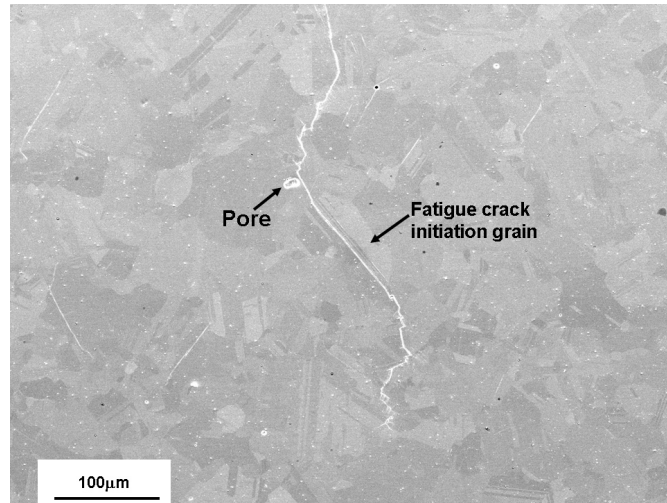
The microstructure along the small crack path was characterized by EBSD and Figure 6.15 (a) shows the inverse pole figure map. The grain boundary map overlaid with an image quality map in Figure 6.15 (b) clearly shows the crack path of the small fatigue crack. The Kernel misorientation map (Figure 6.15 (c)) shows no large misorientation along the fatigue crack in the initiation grain. However, there is an increasing misorientation along the crack path, as the crack grows into other grains, again indicating an increase in crack tip plastic deformation associated with fatigue crack propagation.

Figure 6.16 (a) and (b) shows the detailed structure of fatigue crack initiation grains. As indicated in Figure 6.16 (b), there are several additional individual slip bands formed within the large crack initiation grain that are not associated with a crack. These slip bands are differentiated and marked in Figure 6.16 (b). Figure 6.16 (c) shows a SEM image of the crack initiation grain captured by tilting the sample by 70° relative to the incident electron beam. The grain boundary map overlaid with an image quality map of the crack initiation grain is shown in Figure 6.16 (d). It can be seen that the fatigue crack was formed at the region close to a $\Sigma 3$ twin boundary and also intersects the twin boundary step, as indicated in Figure 6.16 (d). Slip band 1 and slip band 4 are formed in the region close to $\Sigma 3$ twin boundaries. The slip band 2 and 3 are formed at the tip of a $\Sigma 3$ twin boundary as pointed out in Figure 6.16 (d).

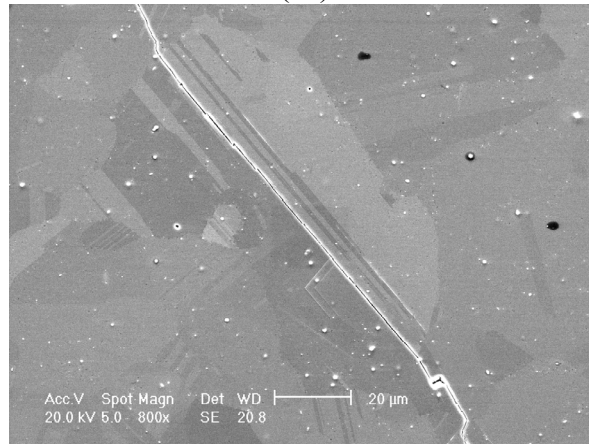
The reconstructed $60^\circ \langle 111 \rangle$ twin boundary is highlighted in blue line in Figure 6.17. It can be seen that part of $\Sigma 3$ twin boundary where the fatigue crack initiated is a

coherent twin boundary. The steps of the $\Sigma 3$ twin boundary are not coherent. The incoherent part of the twin boundary was identified by black arrows in Figure 6.17.

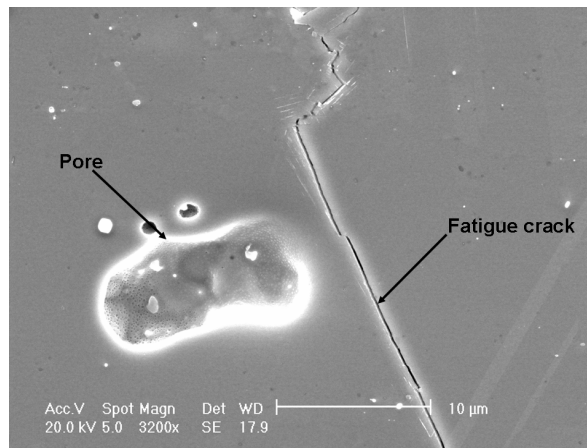
The resolved shear stresses on different slip systems were calculated and the results are shown in Figure 6.16 (c). The slip plane parallel to both the $\Sigma 3$ twin boundary where the small crack was formed and slip band 1 and 4 has a Schmid factor of 0.46. The slip plane which the slip band 3 formed on has a Schmid factor of 0.48. It has the highest Schmid factor among 12 slip systems in the crack initiation grain. This is different from the observation of most other microcracks. Most microcracks formed on slip planes with the highest resolved shear stress in the fatigue crack initiation grains. The possible reason for this difference is that the local stress concentration at the $\Sigma 3$ twin boundary enhances the operation of slip system parallel to twin boundary. The details analysis of the effects of $\Sigma 3$ twin boundaries on slip system parallel to twin boundary are presented in the next section.



(a)



(b)



(c)

Figure 6.14 SEM images of small crack: (a) small crack; (b) crack initiation grain of the small fatigue crack and (c) region close to the small pore ($\sigma_{\max} = 680\text{MPa}$, $N_f = 1.85 \times 10^5$ cycles, 20°C).

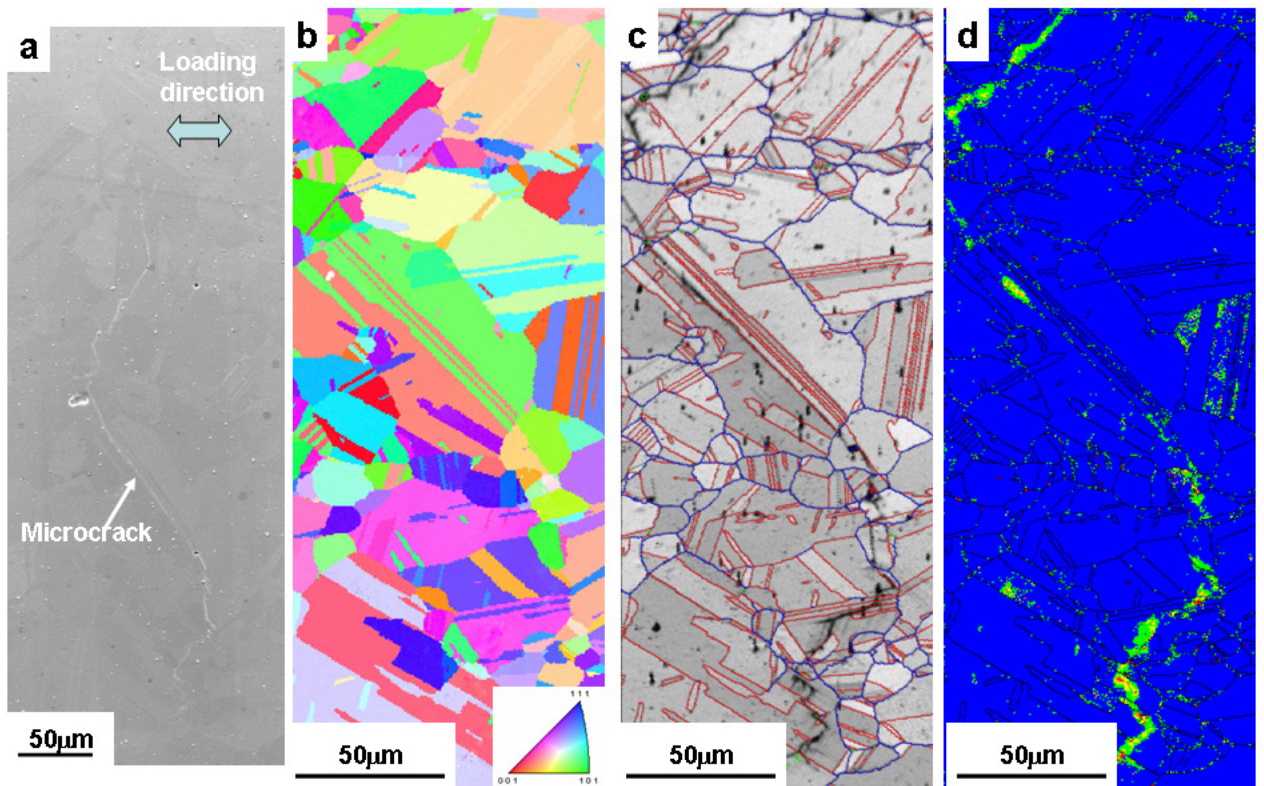


Figure 6.15 EBSD characterization of small crack: (a) SEM image of small crack; (b) inverse pole figure map of small crack; (c) grain boundary map over layered by image quality map; and (d) Kernel misorientation map ($\sigma_{\max} = 680\text{MPa}$, $N_f = 1.85 \times 10^5$ cycles, 20°C).

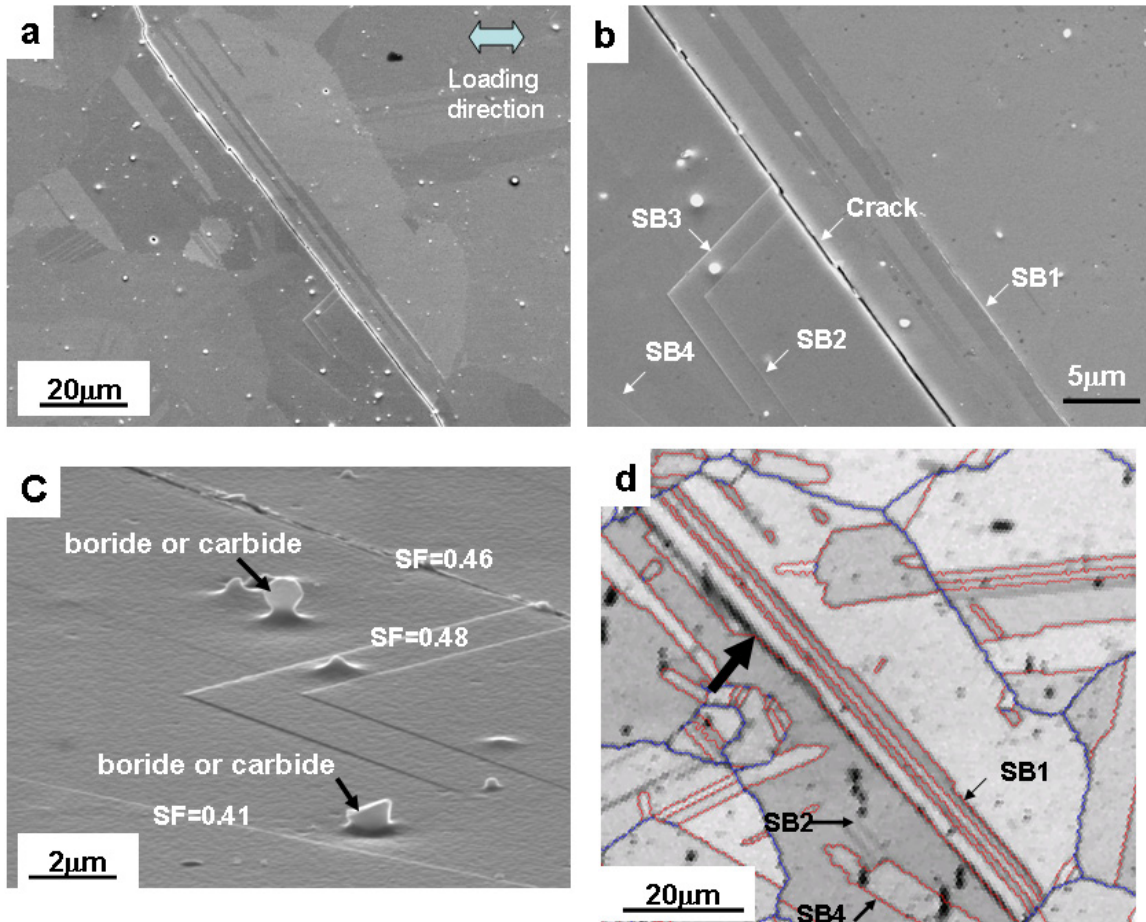


Figure 6.16 Effects of twin boundary step and tips on cyclic strain localization: (a) SEM image of crack initiation grain; (b) SEM images of the micracks and slip bands within the fatigue crack initiation grain (Different slip bands are abbreviated and marked on the figure); (c) SEM image of the crack initiation grain captured at a tilting angle of 70° degrees (The Schmid factor for different slip system abbreviated as SF was shown in the figure) and (d) grain boundary map overlaid with image quality map of the fatigue crack initiation grain (red lines - $\Sigma 3$ twin boundaries, blue lines- random grain boundaries, black arrows indicate the positions of twin boundary step) ($\sigma_{\max} = 680\text{MPa}$, $N_f = 1.85 \times 10^5$ cycles, 20°C).

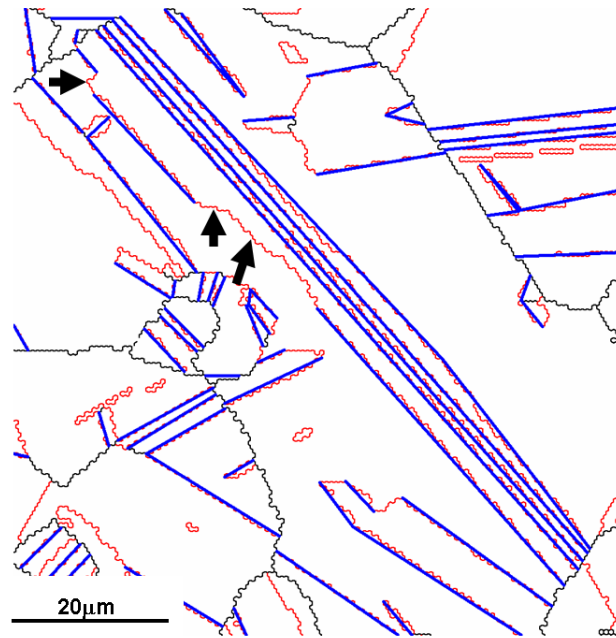


Figure 6.17 The analysis of coherence of $\Sigma 3$ twin boundaries. (red lines - $\Sigma 3$ twin boundaries, blue lines - the reconstructed $60^\circ \langle 111 \rangle$ twin boundaries, the incoherent part on the $\Sigma 3$ twin boundary was pointed out by black arrows). ($\sigma_{\max} = 680\text{MPa}$, $N_f = 1.85 \times 10^5$ cycles, 20°C).

6.2.3.4 Effects of favorably oriented neighbor grains on fatigue crack initiation

Favorably oriented neighbor grains adjacent to the crack-initiation grains can benefit the growth of small cracks. Small angle grain boundaries are one type of favorable orientation relationship that can facilitate slip transmission. A fatigue crack that initiates in a grain that has a favorably oriented grain as its immediate neighbor can more easily propagate into its favorably oriented neighbor grain, than into a grain with a large misorientation. Figure 6.18 (a) and (b) shows the SEM images of a microcrack. The inverse pole figure map and grain boundary map are shown in Figure 6.19 (a) and (b) respectively. The green line indicates a small angle grain boundary between fatigue crack initiation grain and the neighbor grain. The microcrack initiated in the region close to a

$\Sigma 3$ twin boundary in grain1. Due to the small angle grain boundary relationship, it easily propagated into the neighbor grain 2.

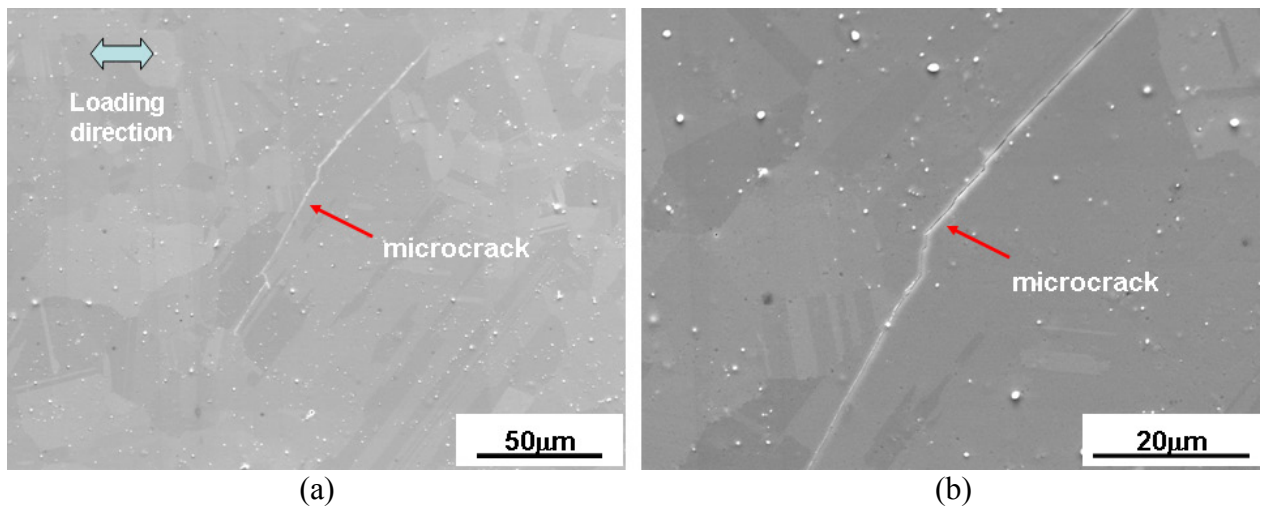


Figure 6.18 SEM image of a microcrack: (a) low magnification and (b) high magnification ($\sigma_{\max} = 680\text{MPa}$, $N_f = 1.85 \times 10^5$ cycles, 20°C).

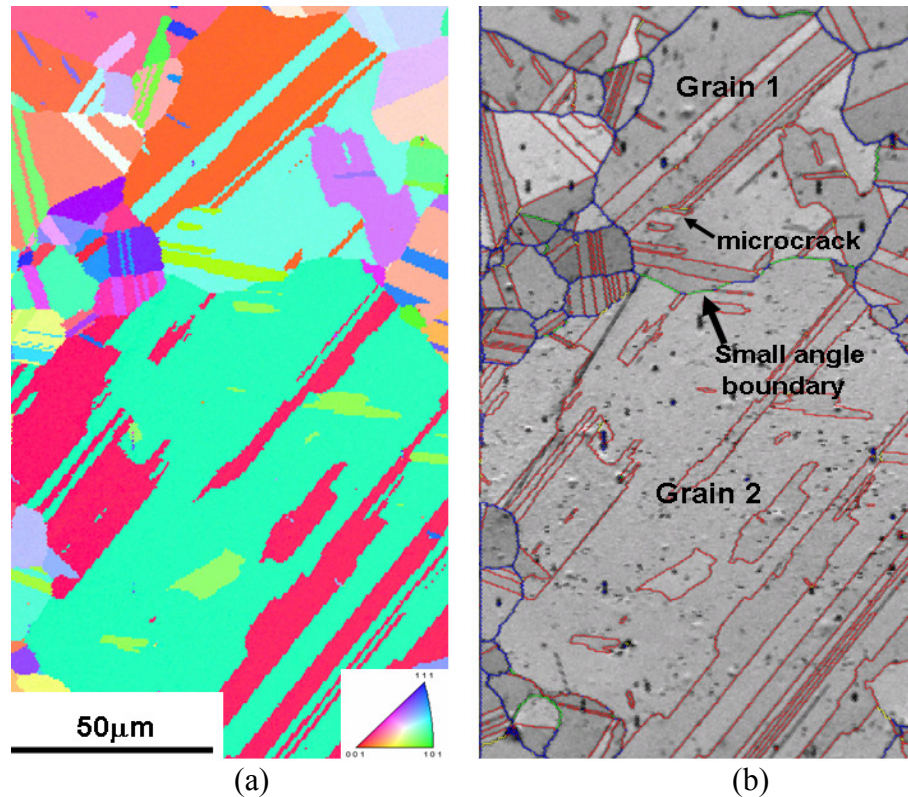


Figure 6.19 Neighborhood effects on fatigue crack initiation and small crack growth: (a) inverse pole figure map of the fatigue crack initiation site and (b) grain boundary map, (blue lines - random large angle grain boundaries, red lines - $\Sigma 3$ twin boundaries, green lines - small angle grain boundaries whose misorientation angles are smaller than 15 degrees.). ($\sigma_{\max} = 680\text{MPa}$, $N_f = 1.85 \times 10^5$ cycles, 20°C).

6.2.3.5 Orientation distribution of fatigue crack initiation grains

Grain orientation relative to the loading direction was determined by EBSD for all grains in which crack initiation was detected and the results are shown in Figure 6.20 (a). Because the twinned part of a grain has a different orientation than the untwinned part, the orientation of either twin or matrix is displayed. The grid in Figure 6.20 (a) was used to measure the deviation of the orientations of grains from one of the low index orientation, in this case, the [001] direction. It can be seen that [001] direction aligns closely with the loading direction in most fatigue crack initiation grains. The orientations of fatigue crack initiation grains are shown in Figure 6.20 (b) superimposed with Schmid

factor contour lines. It can be seen all the grains are favorably oriented for slip with all Schmid factor larger than 0.44. Within most fatigue crack initiation grains, the $\Sigma 3$ twin boundaries near the microcracks are parallel to the slip plane with the highest resolved shear stress. Therefore, Figure 6.20 (b) also indicated that the $\Sigma 3$ twin boundaries near the microcracks are favorably oriented.

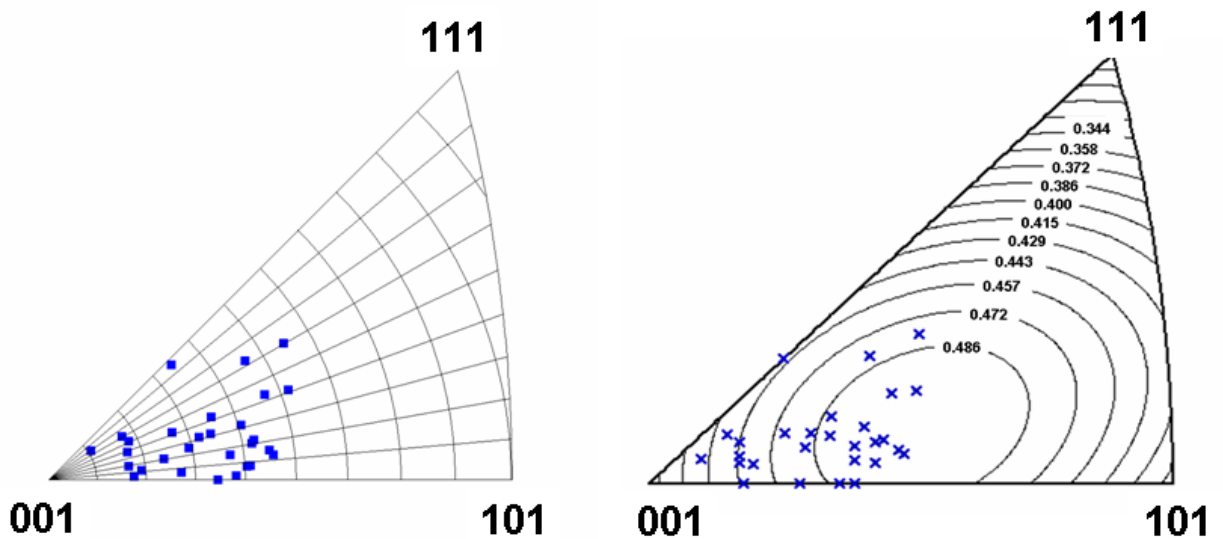


Figure 6.20 Orientation distribution of microcrack initiation grains: (a) orientation distribution and (b) Schmid factor contour plot.

6.3 Discussion

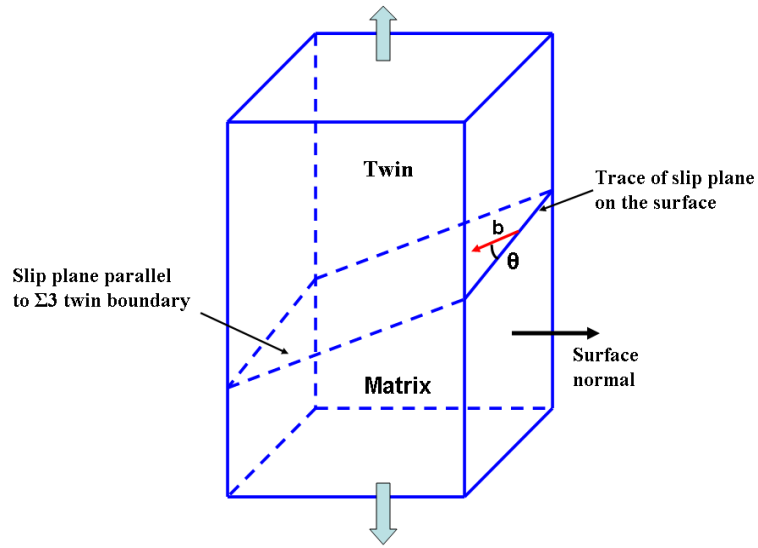
6.3.1 Cyclic strain localization and fatigue crack initiation mechanism at room temperature

The loading stresses in the current study are much lower than the yield stress of this alloy, which is about 1200 MPa at room temperature. As described in the above experimental observations, most of grains within the testing specimens are only subjected to elastic deformation and shows no sign of plastic deformation. All microcracks

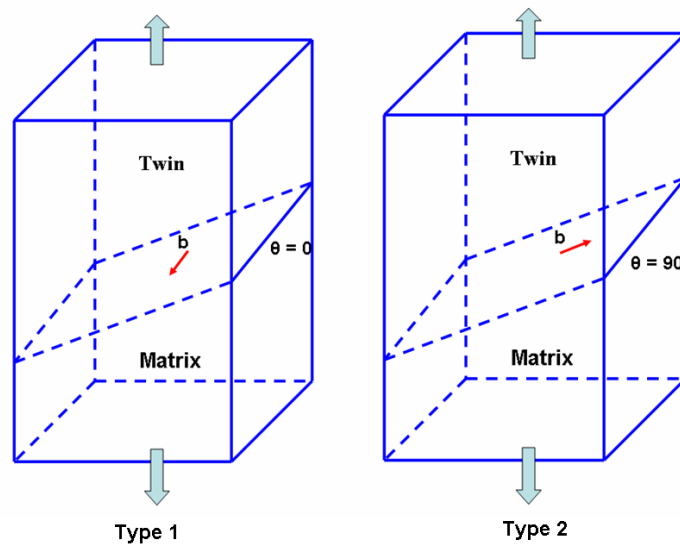
examined by EBSD initiated by cyclic strain localization in the regions close to favorably oriented twin boundaries, especially $\Sigma 3$ twin boundaries and triple junctions of $\Sigma 3$ s boundaries. One important difference between the current study and previous studies of the effects of twin boundaries on fatigue crack initiation [112,113] is that the current study examines crack initiation at much lower stress where cyclic plastic deformation is localized within individual slip bands in favorably oriented large grains.

René 88 DT is mainly strengthened by γ' precipitates. Precipitate shearing is the dominant mode for dislocation slip in nickel-based superalloys at room temperature [29]. The results shown above demonstrate that twin boundaries associated with fatigue cracks initiation are parallel to $\{111\}$ slip planes with highest resolved shear stress. This implies that the slip plane parallel to the twin boundary is favorably oriented for slip.

Figure 6.21 (a) illustrates a geometrical configuration of a $\Sigma 3$ twin boundary with respect to the specimen surface under uniaxial loading conditions. The normal of the specimen surface and the trace of the slip plane parallel to the twin boundary, which is the intersection line of between the slip plane and the specimen surface, is shown in the illustration. The Burgers vector \vec{b} represents the slip direction for dislocations on the slip plane near and parallel to the $\Sigma 3$ twin boundary.



(a)



(b)

Figure 6.21 Geometry of the slip plane parallel to a $\Sigma 3$ twin boundary: (a) illustration of geometry of slip plane and slip direction with respect to specimen surface and (b) two types of shearing deformation in case for the angle relationship between slip direction and the twin boundary trace.

Depending on the geometric relation between slip direction (or Burgers vector of dislocations) and the specimen surface, the shear offsets produced by dislocation slip can be grouped into two types, as shown in Figure 6.21 (b). The angle θ between the Burgers

vector and the trace of the slip plane on the specimen surface can be used to quantify the geometrical relationship between the slip direction and specimen surface. For type 1, the Burgers vector of dislocations is parallel to free surface, and thus parallel to the trace of twin boundary on the specimen surface ($\theta = 0$). In this circumstance, the slip of dislocation along the slip plane will not generate steps on the surface because of the constraint produced by neighboring grains. Under cyclic loading, the slip direction of dislocations switches back and forth with the reversal of the load and the resulting dislocation movement will repeatedly shear γ' precipitates. Due to the irreversible feature of dislocation slip, during the reverse cycle loading, the shear deformation resulting from previous step cannot be completely recovered, leading to accumulation of cyclic strain localization [15]. Because the formation of this kind of cyclic strain localization does not involve the formation extrusions, it can occur in grains in the specimen interior. For type 2 shown in Figure 6.21(b), the Burgers vector is normal to the trace ($\theta = 90^\circ$). When the dislocation with this slip direction slips out the specimen surface, it will leave a step on specimen surface and roughen the specimen surface. If the Burgers vector of dislocations on the slip plane is at certain angle with respect to the trace, because the burgers vector can be dissociated into above two types, both type shearing effects will exist while dislocations slip along the slip plane.

Using the crystallographic information collected from fatigue crack initiation grains, the angles between three $\langle 110 \rangle$ slip directions on the $\{111\}$ slip plane parallel to twin boundary and the trace of twin boundary on specimen surface can be calculated. Because only the slip direction with the largest resolved shear stress is important, the calculated angle between this slip direction and the twin boundary trace is shown in

Figure 6.22. The slip direction with the highest resolved shear stress within most fatigue crack initiation grains are at small angle (less than 20°) with respect to the twin boundary trace. This slip geometry combining the deformation mode of precipitate shearing in nickel-based superalloys offers a possible explanation for the small amount of extruded materials and coverage along the cracks or slip bands observed at crack initiation sites near twin boundaries.

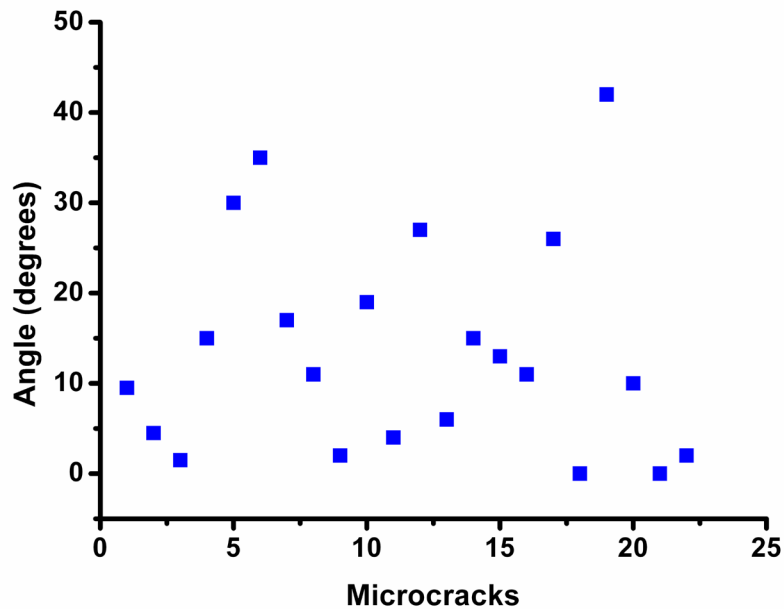


Figure 6.22 The angle between the slip direction (with highest resolved shear stress on the slip plane parallel to twin boundary) and the twin boundary trace.

One remaining question related to surface fatigue crack initiation in the region close to twin boundary concerns the source enhancing the operation of the slip system parallel to twin boundary under such low loading stress. As demonstrated in Chapter 5, twin boundaries are an important source of local stress concentration due to elastic anisotropy. Figure 6.23 illustrates a twin-matrix bicrystal model and twin boundary coordinate system. As shown in Chapter 5, the internal incompatibility stress ($\Delta\sigma_{ij}$) only has three components: $\Delta\sigma_{11}$, $\Delta\sigma_{22}$, and $\Delta\sigma_{12}$:

$$\Delta\sigma_{ij} = \begin{bmatrix} \Delta\sigma_{11} & \Delta\sigma_{12} & 0 \\ \Delta\sigma_{21} & \Delta\sigma_{22} & 0 \\ 0 & 0 & 0 \end{bmatrix} \quad (6.2)$$

This internal incompatibility stress can produce a surface traction t_i on the specimen surface [52].

$$t_i = \Delta\sigma_{ij} \cdot s_j \quad (6.3)$$

Where s_j is the normal of the specimen surface as indicated in Figure 6.23. The surface traction t_i is parallel to the twin boundary plane. Additional shear stresses on the slip systems parallel to the twin boundary plane generated by this surface traction can be given as [52].

$$\tau_{ad} = \beta \cdot b_i \cdot \Delta\sigma_{ij} \cdot s_j \quad (6.4)$$

Where b_i is the slip direction, β is a coefficient which can be obtained from experimental results. Therefore, total shear stress or effective resolved shear stress (τ_{eff}) combining the effects of external loading stress and the additional resolved shear stress on slip systems parallel to the twin boundary on the twin side and the matrix side can be given as:

$$\tau_{eff} = b_i \cdot \sigma_{ij} \cdot n_j \pm \tau_{ad} \quad (6.5)$$

Where σ_{ij} is the uniaxial external loading stress tensor, b_i is the slip direction, n_j is the normal direction of slip plane which is parallel to the twin boundary plane.

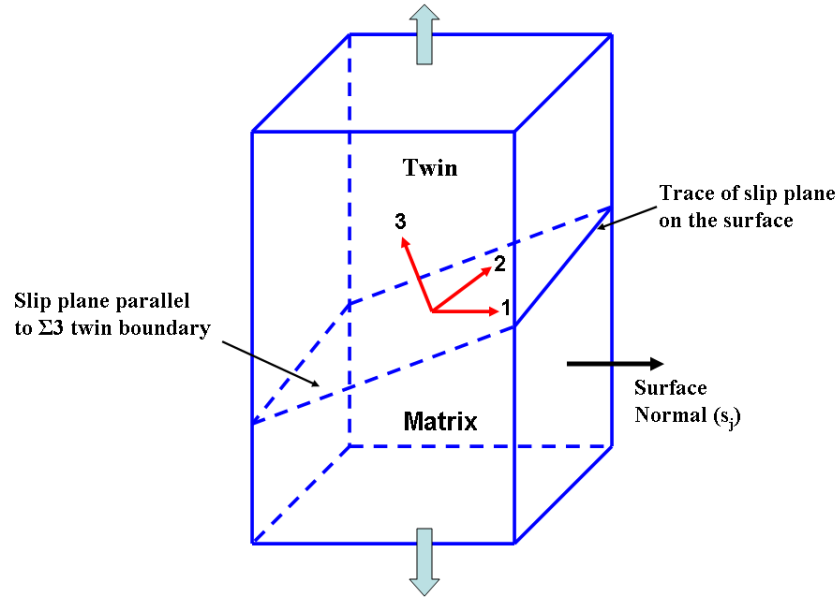
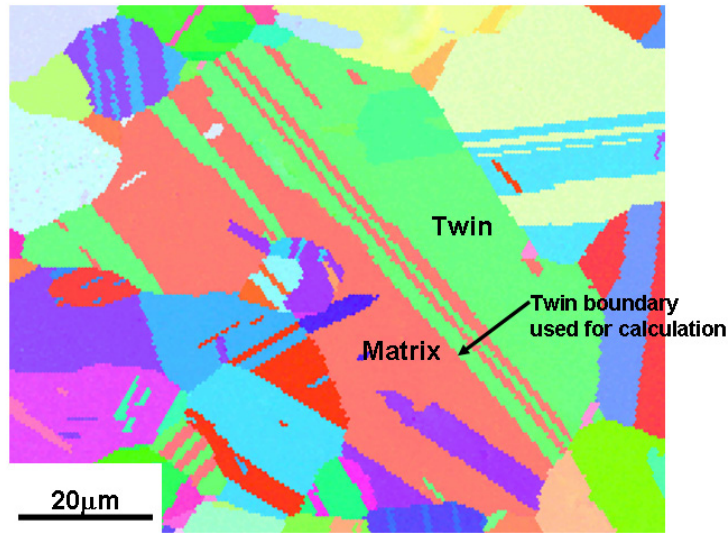


Figure 6. 23 Illustration of twin-matrix model used for calculation additional resolved shear stress on slip plane parallel to twin boundary.

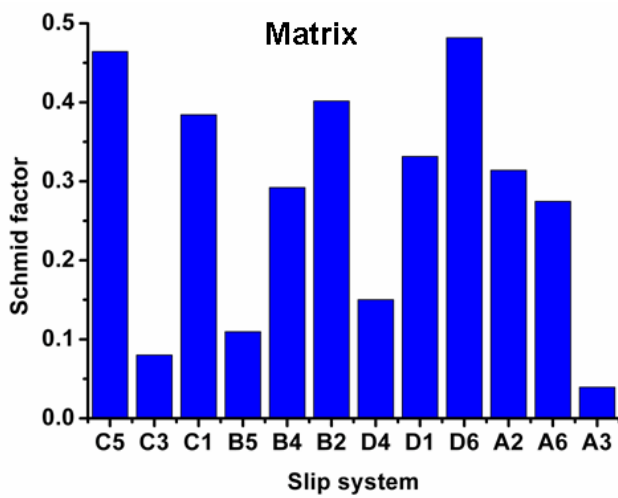
An example of the calculation of effective resolved shear stress is given as follows. The crack initiation grain in Figure 6.16 was used for the analysis. As shown in Figure 6.24 (a), there are several twin variants within the fatigue crack initiation grain. Here, the focus is on the $\Sigma 3$ twin boundary where the fatigue crack initiated as indicated in Figure 6.24 (a). The $\Sigma 3$ twin boundary is parallel to the $(\bar{1}\bar{1}1)$ plane in the matrix side and (111) plane in the twin side. The Schmid factors for the 12 slip systems in the matrix and twin were calculated and plotted in Figure 6.24 (b) and (c). The twin boundary plane is parallel to the slip plane with the highest Schmid factor (0.46) at the twin side and the slip plane with the second largest Schmid factor in the matrix side. By considering the effects of the twin boundary, the effective resolved shear stress on the slip plane parallel to the twin boundary was calculated and the result is shown in Table 6.2. Here, because there are no experimental results for determining the coefficient β , it is assumed to be

unity for the calculation. As shown in the Table 6.2, it can be seen that by taking the effects of twin boundary, the resolved shear stress on the slip system parallel to the twin boundary is enhanced. The largest slip system is C5 on which the ratio between effective resolved shear stress to external loading stress is 0.7. As shown in Table 6.2, the slip direction of the slip system C5 is at a small angle (11°) with respect to the twin boundary trace as indicated in Table 6.2. It is possible that the operation of this slip system led to the initiation of fatigue crack.

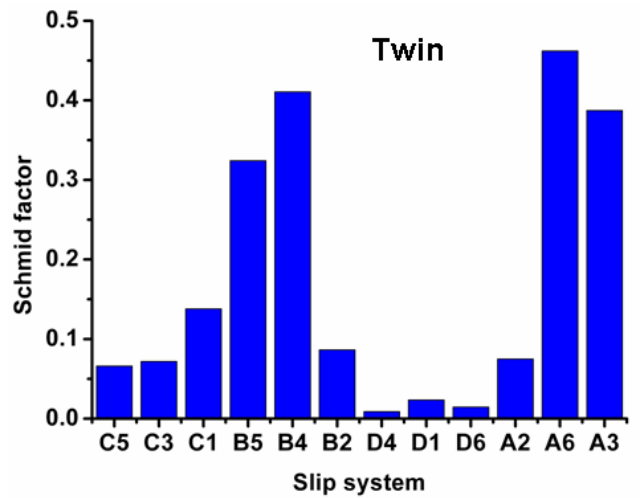
Similarly, the effective resolved shear stress on the slip plane parallel to the twin boundary where the fatigue crack initiated in about 20 fatigue crack initiation grains was calculated and plotted in red in Figure 6.25. The corresponding Schmid factor without considering the effects of twin boundary incompatibility stress was also plotted in the Figure 6.25 for comparison. It can be seen the Schmid factor on the slip plane parallel to twin boundary are in the range of 0.43-0.5, while the ratio between effective resolved shear stress to external loading stress are in the range of 0.55-0.75, and most are above 0.7. Based on this simple analytical analysis, it can be seen that the resolved shear stress on slip planes parallel to the twin boundaries can be greatly enhanced due to the favorably oriented twin boundary, which favors fatigue crack initiation in the region close to Σ 3twin boundary.



(a)



(b)



(c)

Figure 6.24 Schmid factor on slip systems in twin and matrix within a fatigue crack initiation grain: (a) inverse pole figure map of the crack initiation grain; (b) Schmid factor on 12 slip system in the matrix and (c) Schmid factor of the 12 slip systems in the twin side.

Table 6.2 Effects of twin boundary incompatibility stresses on the resolved shear stress on slip system parallel to twin boundary.

	Slip system		
	C5	C3	C1
$\tau_{resolved} / \sigma_{external}$	0.46	0.08	0.38
$\tau_{effective} / \sigma_{external}$	0.7	0.24	0.46
Angle θ (slip direction and twin boundary trace)	11	50	70

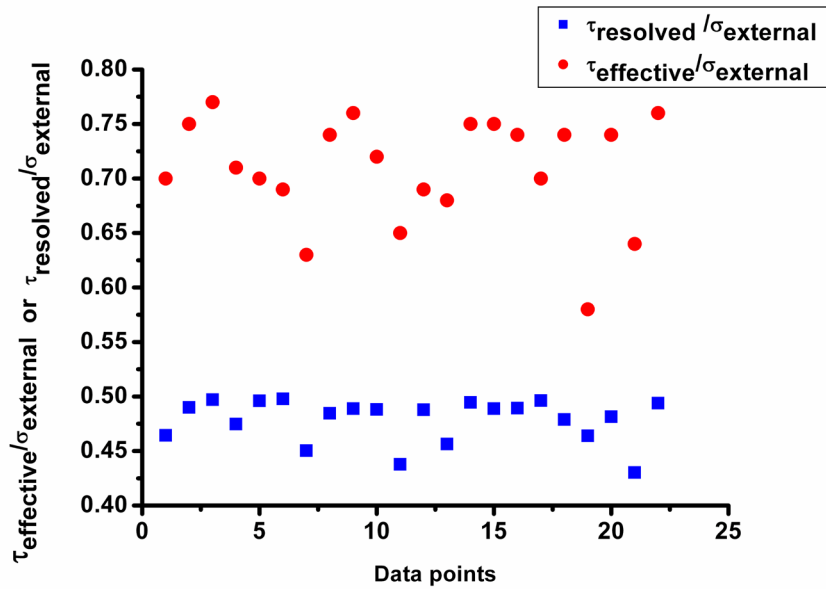


Figure 6.25 The effects of twin boundary on the resolved shear on slip system with the highest Schmid factor on the slip plane parallel to the twin boundary.

6.3.2 Fatigue crack initiation process in René 88 DT at room temperature

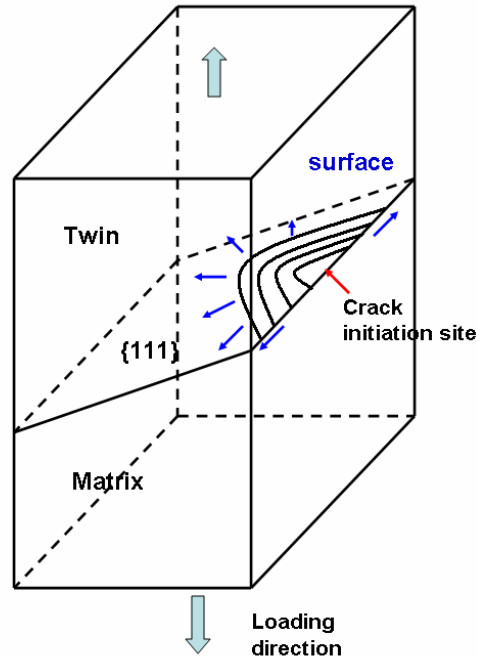


Figure 6.26 Illustration of fatigue crack initiation process at room temperature.

The experimental results shown above indicate that the critical microstructure features associated with fatigue crack initiation at room temperature are similar to those at elevated temperature include: large grain size, twin boundary and favorable orientation. The fatigue crack initiation process at room temperature is illustrated in Figure 6.26. Under cyclic loading, dislocations on $\{111\}$ slip planes near and parallel to favorably oriented twin boundary are activated due to local stress concentration resulted by elastic anisotropy at the twin boundary. Cyclic plastic strain will be localized on the slip plane due to the slip irreversibility. Microcracks will initiate at some portions of the intersection trace of the slip plane and the specimen surface. After the initiation at specimen surface, the fatigue crack will grow both into the interior of the fatigue crack initiation grain and along the specimen surface as indicated in Figure 6.26. Although all

three fatigue specimen failed with shorter life, it can be expected such crack initiation model can operate at even low loading stress level and in very high cycle regime.

These room temperature testing results also provide insights regarding the fatigue crack initiation mechanisms at elevated temperature. As shown in Figure 6.2, although the maximum loading stress levels for room temperature testing and elevated temperature testing are close to each other, fatigue cracks initiate from the specimen surface at room temperature, while at elevated temperature, fatigue cracks initiate from subsurface. This result implies that loading stress itself can not explain the transition of fatigue crack initiation site from surface to subsurface. Thus, environment may play an important role in such transition. The role of environment can be understood in view of the observed dislocation slip behavior. As shown above, the slip direction with the maximum Schmid factor on slip plane near twin boundaries is at small angle with respect to the specimen surface. Due to slip irreversibility, dislocation may only move very small distances during one loading cycle. The main shear offset brought by such dislocation slip is constrained within specimen surface. Therefore, very small amounts of oxide in the front of the motion direction of dislocation slip may reduce the dislocation slip, thus inhibiting surface crack initiation at elevated temperature. However, dislocations on the slip plane within the specimen interior still can move without interaction with environment and may accumulate enough cyclic damage to initiate fatigue crack.

6.4 Summary

In this chapter, the fatigue behavior of nickel-based superalloy René 88 DT was investigated under fully reversed loading at room temperature using ultrasonic fatigue techniques. The testing stresses were in the range of 0.53~0.6 yield stress of René 88 DT at room temperature. All three tested fatigue specimens failed with shorter life in the high cycle regime.

Under current testing conditions, all fatigue failures initiated from specimen surfaces. Critical microstructure features associated with fatigue crack initiation grains include: large grain size, twin boundaries and favorable orientation, similar to the features observed in failed samples after elevated temperature fatigue testing.

All micorcracks initiated near $\Sigma 3$ s ($s \geq 1$) twin boundary, especially $\Sigma 3$ twin boundaries, which are parallel to slip plane with highest Schmid factor in crack initiation grains. The slip directions with highest Schmid factor on these slip planes are at small angles with respect to the free surface (most smaller than 20°), indicating that the main shear offset produced by dislocation slip are constrained within specimen surface rather than perpendicular to specimen surface. Elastic anisotropy at favorably oriented twin boundaries may play an important role in cyclic plastic deformation at room temperature. A simple twin-boundary elastic anisotropy stress model was used to evaluate the effect of $\Sigma 3$ twin boundaries on the operation of slip system parallel to $\Sigma 3$ twin boundaries. Calculations show that the slip system with the highest Schmid factor on the slip plane parallel to $\Sigma 3$ twin boundaries is greatly enhanced.

Chapter 7

Conclusions and Recommendations for Future Work

7.1 Conclusions

7.1.1 Fatigue behavior of René 88 DT at elevated temperature

The fatigue behavior of René 88DT has been investigated in the lifetime range of $10^5 \sim 10^9$ cycles at 593°C using ultrasonic fatigue techniques. Fatigue failures still can occur at fatigue lifetime beyond 10^7 cycles and a conventional fatigue limit does not exist for this alloy. At a lower cyclic stress $\sigma_{\max} = 600\text{MPa}$, the fatigue life variability exceeds two orders of magnitude.

Experimental fatigue life at higher cyclic stress (760MPa) and shorter life range ($\sim 10^5$ cycles) is close to the fatigue life predicted by damage tolerant methods, indicating that fatigue crack growth is the main portion of the total fatigue life at higher loading stresses and correspondingly shorter lifetimes. However at lower loading stresses (600MPa) and in longer life regime ($10^6 \sim 10^9$ cycles), fatigue life and fatigue life variability are much larger than the prediction, indicating fatigue crack initiation is the dominant portion of the total fatigue life at lower cyclic stresses. Therefore the damage tolerant method can not give an accurate prediction of fatigue life in the very high cycle regime in this alloy. The variation in the fatigue crack initiation process is responsible for the large variability in fatigue life.

At 593°C, all fatigue failures initiated from subsurface regions. Most fatigue crack initiation sites consists of a large crystallographic facets or a cluster of large crystallographic facets. The size of large crystallographic facets at crack initiation sites are in the range of 60~120 μm which corresponds to the largest grains observed in the microstructure. Subsurface fatigue fracture surfaces can be divided into three regions corresponding to three stages of fatigue failure: fatigue crack initiation, subsurface fatigue crack propagation and surface crack propagation.

Subsurface fatigue crack initiation makes it is very difficult to directly study critical microstructure features contributing fatigue crack initiation. In this work, a combination of SEM-stereo images based techniques, EBSD and metallographic serial sectioning were explored and successfully used to quantitatively examine subsurface fatigue crack initiation sites.

Two different techniques: SEM-stereo-image based photogrammetry and quantitative tilt fractography, were developed to quantitatively characterize crystallographic fatigue fracture surface. The crystallographic facets at fatigue crack initiation sites were successfully reconstructed using SEM-stereo-image based photogrammetry. Two types of facets were identified at fatigue crack initiation sites: single plane facet and chevron facet. By combining quantitative tilt fractography with EBSD and metallographic sectioning, the crystallographic orientations of facets at subsurface crack initiation sites were determined. All facets are of $\{111\}$ type, indicating $\{111\}$ slip band cracking is the fatigue crack propagation mode under current testing conditions.

By combining metallographic serial sectioning, EBSD and quantitative fractographic analysis, the critical microstructural features associated with subsurface crystallographic fatigue crack initiation were identified as large grain size, twin boundaries and grains with high Schmid factor. Subsurface fatigue cracks are formed by the localization of cyclic plastic deformation on $\{111\}$ slip planes in the region close to and parallel to twin boundaries in favorably oriented large grains. The facet plane in the crack initiation grain is parallel to the slip plane with the highest resolved shear stresses. Elastic incompatibility stresses at regions close to twin boundary in the fatigue crack initiation grains contribute to the onset of cyclic plastic strain localization. Favorably oriented neighbor grains can benefit fatigue crack initiation and especially early small crack growth at elevated temperature. Environmental effects may be responsible for subsurface fatigue crack initiation.

Subsurface fatigue cracks initiate from grains with the combination of critical microstructure features, including large grain size, twin boundary and favorable orientation. A physically-based fatigue life prediction model should incorporate the effects of these critical microstructure features in order to generate valid prediction of fatigue life and the variability of fatigue life. For polycrystalline nickel-based disk alloys, microstructure can be modified through thermal mechanical processing and heat treatment. Among these critical microstructure features, grain size is the one which can be relatively easily controlled. It can be expected that by decreasing the amount of large grain and large grain size, the potential fatigue crack initiation sites in this alloy can be reduced, leading to the increase of fatigue life (or fatigue strength) and the decrease in fatigue life variability.

7.1.2 Fatigue behavior of René 88 DT at room temperature

At room temperature without the effect of environment, cyclic strain localization and critical microstructure features associated with fatigue crack initiation can be directly investigated on specimen surface. This feature can greatly facilitate the study of fatigue crack initiation mechanism in this alloy.

The fatigue behavior of René 88 DT was investigated under fully reversed loading at room temperature using ultrasonic fatigue technique. The testing stresses are in the range of 0.53~0.6 yield stress of René 88 DT at room temperature. Under current testing conditions, all fatigue failures initiated from the specimen surface. Critical microstructure features associated with fatigue crack initiation grains include: large grain size, twin boundaries and favorable orientation, which is similar to those observed at elevated temperature.

All 30 microcracks examined in details initiated near $\Sigma 3$ s ($s \geq 1$) twin boundary, especially $\Sigma 3$ twin boundaries. Most of these $\Sigma 3$ twin boundaries associated with microcrack formation are parallel to slip plane with the highest Schmid factor within crack initiation grains. The slip directions with highest Schmid factor on these slip planes are at small angles with respect to the trace of slip planes on specimen surfaces (most smaller than 20°), indicating that the main shear offset produced by dislocation slip are constrained within specimen surface rather than perpendicular to specimen surface. Elastic anisotropy at favorably oriented twin boundaries may play an important role in cyclic plastic deformation at room temperature. A simple twin-boundary elastic anisotropy stress model was used to evaluate the effect of $\Sigma 3$ twin boundaries on the operation of slip system parallel to $\Sigma 3$ twin boundaries. Calculation results show that the

slip system with the highest Schmid factor on the slip plane parallel to $\Sigma 3$ twin boundaries can be enhanced.

7.2 Recommendations for Future Work

In order to build a physically-based fatigue crack initiation model, following information is needed: 1) the amount shear deformation (or cyclic strain localization) to initiate a fatigue crack, 2) the effects of critical microstructure features on the accumulation of cyclic deformation, 3) deformation substructure at fatigue crack initiation sites. In order to obtain above information, research tasks are recommended as follows. The results of such research would further elucidate the role of critical microstructure features in fatigue crack initiation at elevated temperature and provide critical input to the development of a physically-based fatigue crack initiation life model incorporating these critical microstructure features observed

7.2.1 Quantitative characterization of localized plastic strain

As shown in Chapter 6, the shear offsets produced by dislocation slip on the slip plane near twin boundary at fatigue crack initiation site have two components: one parallel the trace of the slip plane on specimen surface and the other normal to the trace. A combination of EBSD and atomic force microscopy provides a way to quantitatively measure the amount of localized plastic strain associated with fatigue crack initiation process. Atomic force microscopy can measure the shear offset perpendicular to specimen surface and it can not be used to directly measure the shear offset parallel to specimen surface. Using EBSD, the operative slip direction on the slip plane where the fatigue crack initiates can be determined, which can be resolved into the perpendicular

component and parallel component. This information combined with the perpendicular shear offset measured by atomic force microscopy can be used to determine the shear offset parallel to specimen surface. By quantitatively measuring the shear offset of a large amount of microcracks, a statistical energy criterion as to how large shear deformation is needed to initiate fatigue crack can be determined. Because critical microstructure features associated with fatigue crack initiation grains such as grain size and orientation, also can be determined by EBSD, the variation of critical microstructure features on shear offset measurements (the amount of cyclic strain localization) and fatigue crack initiation can be evaluated, which can provide useful insight to the effect of microstructure variation on the variability of fatigue crack initiation life.

As shown in Chapter 6, EBSD kernel misorientation map is a powerful tool to investigate microcracks. Using high resolution kernel misorientation map, it is possible to quantitatively characterize cyclic plastic strain localization at critical microstructure features.

7.2.2 Deformation substructure at fatigue crack initiation site

As shown in Chapter 6, slips systems parallel to favorable oriented $\Sigma 3$ twin boundaries are operative under cyclic loading. However, deformation substructure associated with fatigue crack initiation near twin boundaries is still unknown. Focused ion beam can be used to directly produce TEM thin foils at fatigue crack initiation sites. The deformation substructure at fatigue crack initiation sites can be directly characterized.

7.2.3 Detection of the evolution of fatigue damage using nonlinear ultrasonic signals

The principle of using nonlinear ultrasonic signals to detect fatigue damage was presented in Chapter 3. Figure 7.1 shows the preliminary result of using in-suit ultrasonic signals to investigate fatigue damages. The nonlinear ultrasonic signals were collected on two specimens fatigued at room temperature under fully reversed loading. The fatigue behavior of these two specimens was presented in Chapter 6. It can be seen that the nonlinear parameter increases with the increasing loading cycles, indicating the accumulation of fatigue damage. Using this technique, it is possible to detect fatigue damage and separate fatigue initiation life with fatigue crack growth life. These experimental results can be used to provide direct experimental observation of fatigue crack initiation life and can be use to verify the prediction of fatigue crack initiation life.

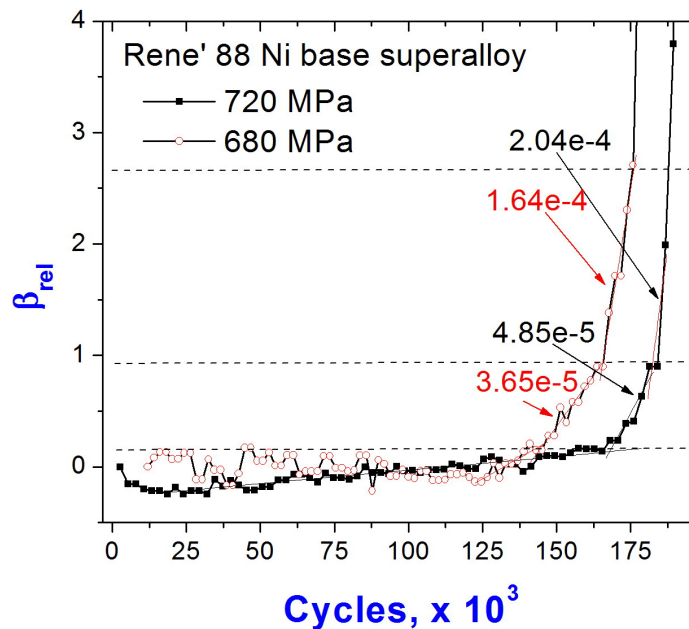
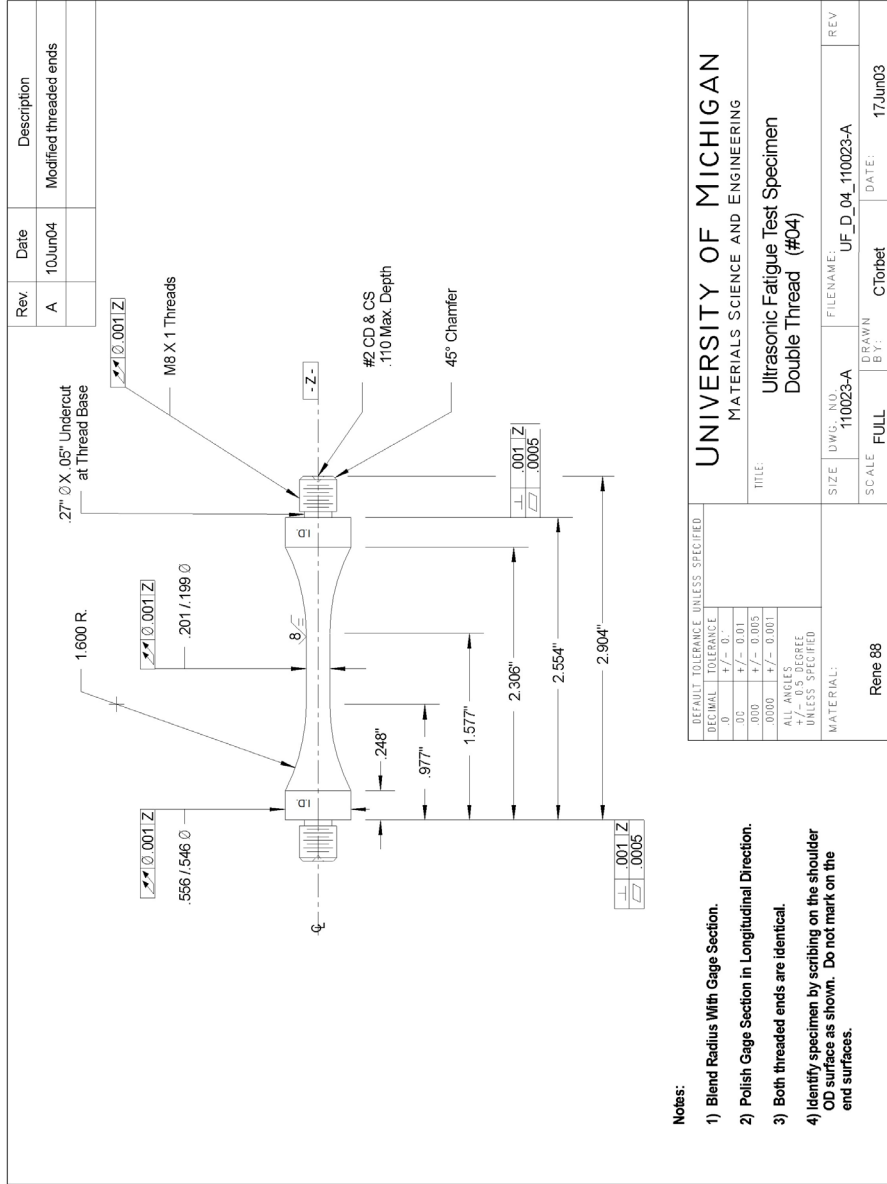


Figure 7.1 The change of nonlinear parameter with fatigue loading cycle in René 88 DT tested at room temperature under fully reversed loading. (Image is courtesy of Dr Anish Kumar).

Appendices

Appendix 1

René 88 DT Ultrasonic Fatigue Specimen Drawing



Appendix 2

S-N Data of René 88 DT at 593°C

σ_{\max} (MPa)	Fatigue life (cycles)	Crack initiation type
760	1.13×10^6	crystallographic
760	7.70×10^5	crystallographic
760	5.93×10^5	crystallographic
760	8.40×10^5	crystallographic
760	6.50×10^5	crystallographic
660	5.49×10^6	crystallographic
660	3.13×10^6	crystallographic
660	2.18×10^6	crystallographic
660	1.85×10^7	crystallographic
660	3.44×10^6	crystallographic
660	1.48×10^7	crystallographic
660	3.51×10^6	crystallographic
660	3.85×10^6	crystallographic
600	6.64×10^7	inclusions
600	2.94×10^6	crystallographic
600	7.67×10^6	crystallographic
600	1.25×10^8	crystallographic
600	4.79×10^6	crystallographic
600	3.16×10^6	crystallographic
600	1.90×10^7	crystallographic

σ_{\max} (MPa)	Fatigue life (cycles)	Crack initiation type
600	1.0×10^9 (runout)	None
550	1.10×10^9 (runout)	None
550	1.21×10^9 (runout)	None
550	1.12×10^9 (runout)	None
550	5.95×10^8	crystallographic
500	7.24×10^8 (runout)	None

References

- [1] Pollock TM, Tin S. Nickel-based superalloys for advanced turbine engines: chemistry, microstructure, and properties. *Journal of Propulsion and Power* 2006; 22 (2): 361-374.
- [2] Christodoulou L, Larsen JM. Using materials prognosis to maximize the utilization potential of complex mechanical systems. *JOM* 2004; 56 (3): 15-19.
- [3] ENSIP, Engine Structural Integrity Program Handbook, <http://engineering.wpafb.af.mil/corpusa/handbook/mh1783/mh1783.pdf>, 2002. 135.
- [4] Mughrabi H. Specific features and mechanisms of fatigue in the ultrahigh-cycle regime. *International Journal of Fatigue* 2006; 28(11):1501-1508.
- [5] Leyens C, Peters M. Titanium and titanium alloys - Fundamentals and applications, Weinheim: Wiley-VCH Verlag GmbH & Co. KGaA; 2005.
- [6] Boston S. Al- Ni (Aluminum-Nickel). *Journal of Phase Equilibria and Diffusion* 2004; 25(4): 394.
- [7] Reed RC, *The superalloys: Fundamentals and Application*, Cambridge: Cambridge University Press; 2006.
- [8] Kozar RW, Suzuki A, Milligan WW, Schirra JJ, Savage MF, Pollock TM. Strengthening mechanisms in polycrystalline multimodal nickel-base superalloys, *Metallurgical and Materials Transactions A* 2009; 40A:1588-1603.
- [9] Tin S, Pollock TM. Stabilization of thermosolutal convective instabilities in Ni-based single-crystal superalloys: Carbide precipitation and rayleigh numbers. *Metallurgical and Materials Transactions A* 2003; 34(9):1953-1967.
- [10] Fecht H, Furrer D. Processing of nickel-base superalloys for turbine engine disc applications. *Advanced Engineering Materials* 2000; 2(12):777-787.
- [11] Davies RG, Stoloff NS. Yield stress of aged Ni-Al alloys. *Transactions of the Metallurgical Society of AIME* 1965; 233(4):714.
- [12] Thornton PH, Davies RG, Johnson TL. The temperature dependence of the flow stress of the γ' phase based upon Ni₃Al. *Metallurgical Transactions* 1970;1:207-218.

- [13] Thornton PH, Davies RG. Temperature dependence of the flow stress of the gamma prime phases having the L12 structure. *Metallurgical Transactions* 1970;1:549-550.
- [14] Kear BH, Wilsdorf HG. Dislocation configurations in plastically deformed polycrystalline Cu₃Au alloys. *Transactions of the Metallurgical Society of AIME* 1962; 224 (2): 382-386.
- [15] Mughrabi H. Cyclic slip irreversibilities and the evolution of fatigue damage. *Metallurgical and Materials Transactions B* 2009; 40: 431-453.
- [16] Gerberich WW, Harvey SE, Kramer DE, Hoehn JW. Low cycle and high cycle fatigue-a continuum supported by AFM observations. *Acta Materialia* 1998; 46(14): 5007-5021.
- [17] Cretegnny L, Saxena A. AFM characterization of the evolution of surface deformation during fatigue in polycrystalline copper. *Acta Materialia* 2001; 49(18):3755-3765.
- [18] Risbet M, Feugas X, Guillemer-Neel C, Clavel M. Use of atomic force microscopy to quantify slip irreversibility in a nickel-base superalloy. *Scripta Materialia* 2003; 49(6): 533-538.
- [19] Shyam A, Milligan WW. A model for slip irreversibility, and its effect on the fatigue crack propagation threshold in a nickel-base superalloy. *Acta Materialia* 2005; 53(3):835-844.
- [20] Laufer EE, Roberts WN. Dislocations and persistent slip bands in fatigued copper. *Philosophic Magazine* 1966; 14(127): 65-78.
- [21] Mughrabi H. Cyclic hardening and saturation behavior of copper single crystals. *Material Science and Engineering* 1978; 33 (2):207-223.
- [22] Essmann U, Gosele U, Mughrabi H. A model of extrusions and intrusions in fatigued metals.1. Point defect production and the growth of extrusions. *Philosophic Magazine* 1981; 44 (2): 405-426.
- [23] Hunsche A, Neumann P. Quantitative measurement of persistent slip band profile and fatigue crack initiation. *Acta Metallurgica* 1986; 34 (2): 207-217.
- [24] Basinski ZS, Basinski SJ. Fundamental aspects of low amplitude cyclic deformation in face-centred cubic crystals. *Progress in Materials Science* 1992; 36: 89-148.
- [25] Kuhlmann-Wilsdorf D, Laird C. Dislocation behavior in fatigue. *Materials Science and Engineering* 1977; 27(2):137-156.

- [26] Lukas P, Kunz L. Role of persistent slip bands in fatigue. *Philosophical Magazine* 2004; 21 (3-5): 317-330.
- [27] Suresh S, *Fatigue of materials*, Cambridge: Cambridge University Press; 1991.
- [28] Mughrabi H. *Dislocations and properties of real Materials*, London: The Institute of Metals; 1984.
- [29] Pineau A, Antolovich SD. High temperature fatigue of nickel-base superalloys – A review with special emphasis on deformation modes and oxidation. *Engineering Failure Analysis* 2009; 16(8): 2668-2697.
- [30] Antolovich SD, Lerch B. Cyclic deformation and fatigue in Ni-base alloys, In: Tien JK, Caufield T (Eds.). *Superalloys, Supercomposites, and Superceramics*, New York: Academic Press; 1989.
- [31] Singh V, Sundararman M, Chen W, Wahi RP. Low-cycle fatigue behavior of nimonic PE16 at room temperature. *Metallurgical Transactions A* 1991; 22(2): 499-506.
- [32] Obrtlík K, Petreňec M, Man J, Polak J, Hrbáček K. Isothermal fatigue behavior of cast superalloy Inconel 792-5A at 23 and 900 °C. *Journal of Materials Science* 2009; 44(12): 3305-3314.
- [33] Lerch B, Gerold V. Room-temperature deformation mechanisms in nimonic 80A, *Acta Metallurgica* 1985; 33(9):1709-1716.
- [34] Lerch BA, Jayaraman N. A study of fatigue damage mechanisms in Waspaloy from 25 to 800° C. *Materials Science and Engineering* 1984; 66: 151-166.
- [35] Organ FE, Gell M. The effect of frequency on the elevated temperature fatigue of a nickel-based superalloy. *Metallurgical Transactions* 1971; 2 (4): 943-952.
- [36] Hyzak JM, Bernstein IM. The effect of defects on the fatigue crack initiation process in two P/M superalloys: part 1. fatigue origins. *Metallurgical Transactions A* 1982; 13: 23-43.
- [37] Hyzak JM, Bernstein IM. The effect of defects on the fatigue crack initiation process in two P/M superalloys: part 2. Surface-subsurface transition. *Metallurgical Transactions A* 1982; 13: 45-52.
- [38] Huron ES, Roth PG. The influence of inclusions on low cycle fatigue life in a P/M nickel-base disk superalloy, in: Rissinger RD, Deye DJ, Anton DD, Getel AD, Nathal MV, Pollock TM, Woodford DA. *Superalloys 1996*. Warrendale; The Minerals, Metals & Materials society: 1996

- [39] Lukas P, Kunz L. Specific features of high-cycle and ultra-high-cycle fatigue. *Fatigue & Fracture of Engineering Materials & Structures* 2002; 25(8-9):747-753.
- [40] Hornbogen E, Verpoort C. Influence of surface treatments on fatigue crack initiation in $\gamma+\gamma'$ precipitation hardening alloys, in: Tien JK, Wlodck ST, Morrow H, Gell M, Maurer GE (Eds.). *Superalloys* 1980. Metals park: ASM; 1980.
- [41] Risbet M, Feaugas X. Some comments about fatigue crack initiation in relation to cyclic slip irreversibility. *Engineering Fracture Mechanics* 2008; 75 (11): 3511-3519.
- [42] Risbet M, Feaugas X, Guillemer-Neel C, Clavel M. Damage in nickel base superalloy: Influence of local parameters measured by electron backscattered diffraction and atomic force microscopy. *Scripta Materialia* 2009; 60 (5): 269-272.
- [43] Healy JC, Grabowski L, Beevers CJ. Monitoring fatigue of a nickel-base superalloy at positive and negative stress ratios using an optical system. *Fatigue & Fracture of Engineering Materials & Structures* 1991; 15 (3):309-321.
- [44] Healy JC, Grabowski L, Beevers CJ. Short-fatigue-crack growth in a nickel-based superalloy at room and elevated temperature. *International Journal of Fatigue* 1991; 13 (2):133-138.
- [45] Boyd-Lee A, King JE. Short fatigue crack path determinants in polycrystalline Ni-base superalloys. *Fatigue & Fracture of Engineering Materials & Structure* 1994; 17 (1): 1-14.
- [46] Alexandre F, Deyber S, Pineau A. Modeling the optimum grain size on the low cycle fatigue behavior of a Ni based superalloy in the presence of two possible crack initiation sites. *Scripta Materialia* 20004; 50: 25-30.
- [47] Davidson DL, Tryon RG, Oja M, Matthews R, Ravi Chandran KS. Fatigue crack initiation in Waspaloy at 20° C. *Metallurgical and Materials Transactions A* 2007, 38: 2214-2225.
- [48] Oja M, Ravi Chandran KS, Tryon RG. Orientation imaging microscopy of fatigue crack formation in Waspaloy: Crystallographic conditions for crack nucleation. *International Journal of Fatigue* 2010; 32 (3): 551-556.
- [49] Chen Q, Kawagoishi N, Wang QY, Yan N, Ono T, Hashiguchi G. Small crack behavior and fracture of nickel-based superalloy under ultrasonic fatigue. *International Journal of Fatigue* 2005; 27(10-12): 1227-1232.
- [50] Thompson N, Wadsworth NJ, Louat N. The origin of fatigue fracture in copper. *Philosophical Magazine* 1956;1(2):113–126.

- [51] Boettner RC, Jr. McEvily JA, Liu YC. On formation of fatigue cracks at twin boundaries. *Philosophical Magazine* 1964; 10: 95-106.
- [52] Heinz A, Neumann P. Crack initiation during high cycle fatigue of a austenitic steel. *Acta Metallurgica et Materialia* 1990; 38(10):1933-1940.
- [53] Blochwitz C, Tirschler W. Twin boundaries as crack nucleation sites. *Crystal Research and Technology* 2005; 40(1-2):32-41.
- [54] Peralta P, Llanes L, Bassani J, Laird C. Deformation from twin-boundary stress and the role of texture - application to fatigue. *Philosophical Magazine A* 1994; 70 (1): 219-232.
- [55] Neumann P. Analytical solution for the incompatibility stresses at twin boundaries in cubic crystals, in: Wu XR, Wang ZG (Eds.). *Fatigue 99, Proceedings of the 7th International Fatigue Congress*. Beijing: Higher Education Press; 1999.
- [56] Llanes L, Laird C. The role of annealing twin boundaries in the cyclic deformation of f.c.c. materials. *Materials Science and Engineering A* 1992; 157 (1): 21-27.
- [57] Kobayashi K, Yamaguchi K, Hayakawa M, Kimura M. High-temperature fatigue properties of austenitic superalloys 718, A286 and 304L. *International Journal of Fatigue* 2008; 30 (10-11): 1978-1984.
- [58] Kobayashi K, Yamaguchi K, Hayakawa M, Kimura M. Grain size effect on high-temperature fatigue properties of alloy 718. *Materials Letters* 2005; 59 (2-3): 383-386.
- [59] Mitchell RJ, Lemsky JA, Ranmanathan R, Li HY, Perkins KM, Connor LD. Process development & microstructure & mechanical property evaluation of a dual microstructure heat treated advanced nickel disc alloy, *Superalloys 2008*, Warrendale: The Minerals, Metals & Materials Society; 2008.
- [60] Brogdon ML, Rosenberger AH. Evaluation of the influence of grain structure of the fatigue variability of Waspaloy, *Superalloys 2008*, Warrendale: The Minerals, Metals & Materials Society; 2008.
- [61] Caton MJ, Jha SK, Rosenberger AH, Larson JM. In: Green KA, Harada H, Howson TE, Pollock TM, Reed RC, Schirra JJ, Walston S (Eds.). *Superalloy 2004*, Warrendale: The Minerals, Metals & Materials Society; 2004.
- [62] Shyam A, Torbet CJ, Jha SK, Larsen JM, Caton MJ, Szczepanski CJ, Pollock TM, Jones JW. In: Green KA, Harada H, Howson TE, Pollock TM, Reed RC, Schirra JJ, Walston S (Eds.). *Superalloy 2004*, Warrendale: The Minerals, Metals & Materials Society; 2004.

- [63] Szczepanski CJ, Jha SK, Larsen JM, Jones JW. Microstructural influences on very-high-cycle fatigue-crack initiation in Ti-6246. *Metallurgical and Materials Transactions A* 2008; 39 (12): 2841-2851.
- [64] Huang J, Spowart JE, Jones JW. Fatigue behavior of SiC_p-reinforced aluminum composites in the very high cycle regime using ultrasonic fatigue. *Fatigue & Fracture of Engineering Materials & Structure* 2006; 29 (7): 507-517.
- [65] Murakami Y, Nomoto T, Ueda T, Murakami Y. On the mechanism of fatigue failure in the superlong life regime ($N > 10^7$ cycles). Part 1: influence of hydrogen trapped by inclusions. *Fatigue & Fracture of Engineering Materials & Structure* 2000; 23 (11): 893-902.
- [66] Murakami Y, Nomoto T, Ueda T. Factors influencing the mechanism of superlong fatigue failure in steels. *Fatigue & Fracture of Engineering Materials & Structure* 1999; 22 (7): 581-590.
- [67] Murakami Y, Nomoto T, Ueda T, Murakami Y. On the mechanism of fatigue failure in the superlong life regime ($N > 10^7$ cycles). Part II: influence of hydrogen trapped by inclusions. *Fatigue & Fracture of Engineering Materials & Structure*; 23 (11): 903-911.
- [68] Weidner A, Amberger D, Pyczak, F, Schönbauer B, Stanzl-Tschegg S, Mughrabi H. Fatigue damage in copper polycrystals subjected to ultrahigh-cycle fatigue below the PSB threshold. *International of Fatigue* 2010; 32: 872-878.
- [69] Bathias C, Paris PC. Gigacycle fatigue of metallic aircraft components. *International Journal of Fatigue* 2009; 32 (6): 894-897.
- [70] Ranc N, Wagner D, Paris PC. Study of thermal effects associated with crack propagation during very high cycle fatigue tests. *Acta Materialia* 2008; 56 (15): 4012-4021.
- [71] Mason WP. Piezoelectric crystal and their application to ultrasonic. Princeton: Van Nostrand; 1950.
- [72] Mayer H. Fatigue crack growth and threshold measurement at very high frequencies. *International Materials Reviews* 1999; 44(1): 1-34.
- [73] Bathias C, Paris PC. Gigacycle fatigue in mechanical practice, New York: Marcel Dekker; 2004.
- [74] Zhu X, Jones JW, Allison JE. Effect of frequency, environment, and temperature on fatigue behavior of E319 cast aluminum alloy: stress-controlled fatigue life response. *Metallurgical and Materials Transactions A* 2008; 39 (11): 2681-2688.

- [75] Paris PC, Gomez MP, Anderson WP. A rational analytic theory of fatigue. *The Trend in Engineering* 1961; 13:9-14.
- [76] Chan KS, Enright MP. Physically-based models for predicting fatigue life variability in Ni-based superalloys. *Proceedings of the TMS Fall Meeting, Columbus: TMS; 2002.*
- [77] Chan KS. A microstructure-based fatigue crack initiation model. *Metallurgical and Materials Transactions A* 2003; 34 (1): 43-58.
- [78] Chan KS, Enright MP. A probabilistic micromechanical code for predicting fatigue life variability: model development and application. *Journal of Engineering Gas Turbines Power* 2006; 128 (4): 889-895.
- [79] Mura T, Nakasone Y. A theory of fatigue crack initiation in solids. *Journal of applied mechanics* 1990; 57 (1): 1-6.
- [80] Mura T. A theory of fatigue crack initiation. *Materials Science and Engineering A* 1994; 176 (1): 61-70.
- [81] Krueger DD, Kissinger RD, Menzies RG. Development and introduction of a damage tolerant high temperature Nickel-Base Disk Alloy René 88 DT, in: Antolovich SD, Stusrud RW, MacKay RA, Anton DL, Khan T, Kissinger RD, Klarstrom DL (Eds.). *Superalloys 1992*. Warrendale: The Minerals, Metals & Materials Society; 1992.
- [82] Wlodek ST, Kelly M, Alden DA. The structure of Rene 88 DT, in: Deye DJ, Anton DL, Nathal MV, Pollock TM (Eds.). *Superalloys 1996*. Warrendale: The Minerals, Metals & Materials Society; 1996.
- [83] Hwang JY, Banerjee R, Tiley J, Srinivasan R, Viswanathan GB, Fraser HL. Nanoscale characterization of elemental partitioning between gamma and gamma prime phases in René 88 DT nickel-base superalloy. *Metallurgical and Materials Transactions A* 2009; 40 (1): 24-35.
- [84] Matikas TE. Specimen design for fatigue testing at very high frequencies. *Journal of Sound and Vibration* 2001; 247: 673-681.
- [85] Cavalieri F, Bathias C, Ranc N, Cardona A, Risso J. Ultrasonic fatigue analysis on an austenitic steel at high temperature, In: Cardona A, Storti M, Zuppa C (Eds.). *Mecánica Computacional Vol XXVII*. AMCA; 2008.
- [86] Sharpe Jr WN. A high-frequency high-temperature optical strain/displacement gage. *Experimental Mechanics* 2010; 50 (2): 227–237.
- [87] Cantrell JH, Yost WT. Nonlinear ultrasonic characterization of fatigue microstructures. *International Journal of Fatigue* 2001; 23: 487-490.

- [88] Kim JY, Jacobs LJ, Qu JM, Little JW. Experimental characterization of fatigue damage in a nickel-based superalloy using nonlinear ultrasonic waves. *Journal of the Acoustic Society of American* 2006; 120 (3): 1266-1273.
- [89] Shiwas M, Furaya Y, Yamawaki H, Ito K, Enoki M, Evaluation of ultrasonic fatigue testing process of high strength steel by non-linear ultrasonic analysis. *Review of Progress in Quantitative Nondestructive Evaluation: Proceedings of the 35th Annual Review of Progress in Quantitative Nondestructive Evaluation* 2009; 1096:1450-1457.
- [90] Kumar A, Torbet CJ, Jones JW, Pollock JW. Nonlinear ultrasonics for in suit damage detection during high frequency fatigue. *Journal of Applied Physics* 2009; 106: 024904 1-9.
- [91] Shyam A, Allison JE, Szczepanski CJ, Pollock TM, Jones JW. Small fatigue crack growth in metallic materials: A model and its application to engineering alloys. *Acta Materailia* 2007. 55 (19): 6606-6616.
- [92] Gell M, Leverant GR. The characteristics of stage I fatigue fracture in a high strength nickel alloy. *Acta Metallurgica* 1968; 16 (4): 553-561.
- [93] Li K, Ashbaugh NE, Rosenberger AH. Crystallographic Initiation of Nickel-based Superalloy IN100 at RT and 538 °C under low cycle fatigue conditions, In: Green KA, Harada H, Howson TE, Pollock TM, Reed RC, Schirra JJ, Walston S (Eds.). *Superalloy 2004*. Warrendale: The Minerals, Metals & Materials Society; 2004.
- [94] King JE. Crystallographic fatigue crack growth in AP1. *Fatigue & Fracture of Engineering Materials & Structure* 1981; 4: 311-320.
- [95] Sadansnda K, Shahinian P. Analysis of crystallographic high temperature fatigue crack growth in a nickel base alloy. *Metallurgical Transactions A* 1981; 12 (2): 343-351.
- [96] Gourgues AF. Electron backscatter diffraction and cracking. *Materials Science and Technology* 2002; 18 (2): 119-133.
- [97] Davies PA, Randle V. Combined application of electron backscatter diffraction and stereo-photogrammetry in fractography studies. *Journal of Microscopy* 2001; 204 (1):29-38.
- [98] Sinha V, Mills MJ, Williams JC. Crystallography of fracture facets in a near-alpha titanium alloy. *Metallurgical and Materials Transactions A* 2006; 37 (6): 2015-2026.
- [99] Slavik DC, Wert JA, Gangloff RP. Determining fracture facet crystallography using electron backscatter patterns and quantitative tilt fractography. *Journal of Materials Research* 1993; 8 (10): 2482-2491.

- [100] Ro YJ, Agnew SR, Gangloff RP. Uncertainty in the determination of fatigue crack facet crystallography. *Scripta Materialia* 2005; 52 (6): 531–536.
- [101] Kuroda T, Ikeuchi K, Nakade K, Inoue K, Kitagawa Y. Three-dimensional reconstruction of cleavage fracture surface for duplex stainless steel. *Vacuum* 2002; 65 (3-4): 541–546.
- [102] Bariani P, De Chiffre L, Hansen HN, Horsewell A. Investigation on the traceability of three dimensional scanning electron microscope measurements based on the stereo-pair technique. *Precision Engineering* 2005; 29 (2): 219-228.
- [103] Randle V, Engler O. Introduction to texture analysis: macrotexture, microtexture and orientation mapping. Gordon and Beach Science Publishers; 2000.
- [104] Miao JS, Pollock TM, Jones JW. Very high cycle fatigue behavior of nickel-based superalloy René 88 DT at 593°C, In: Allison JE, Jones JW, Larson JM, Ritchie RO (Eds.). Fourth international conference on very high cycle fatigue. Warrendale: The Minerals, Metals & Materials Society; 2007.
- [105] Miao JS, Pollock TM, Jones JW. Fatigue crack initiation in nickel-base superalloy René 88 DT at 593°C, in: Reed RC, Green KA, Caron P, Gabb TP, Fahrman MG, Huron ES (Eds.). *Superalloys 2008*, Warrendale: The Minerals, Metals & Materials Society; 2008.
- [106] Basinski SJ, Basinski ZS. Plastic deformation and work hardening, in: Nabarro FRN (Eds.). *Dislocations in solids*, Amsterdam: North Holland; 1997.
- [107] Margolin H. Polycrystalline yielding - perspectives on its onset. *Acta Materialia* 1998; 46 (17):6305-6309.
- [108] Lewis AC, Jordan KA, Geltmacher AB. Determination of critical microstructural features in an austenitic stainless steel using image-based finite element modeling. *Metallurgical and Materials Transactions A* 2008; 39 (5): 1109-1117.
- [109] Pollock TM, Argon AS. Directional coarsening in nickel-based single-crystals with high –volume fractions of coherent precipitates. *Acta Metallurgica et Materialia* 1994; 42 (6):1859-1874.
- [110] Duquette DJ, Gell M. Effects of environment on elevated-temperature fatigue behavior of nickel-based superalloy single-crystals. *Metallurgical Transactions* 1972; 3 (7): 1899-1905.
- [111] Randle V. Twinning-related Grain boundary Engineering. *Acta Materialia* 2004, 52 (14): 4067-4081.

[112] Liu W, Bayerlein M, Mughrabi H, Day A, Quedved PN. Crystallographic features of intergranular crack initiation in fatigued copper polycrystals. *Acta Metallurgica et Materialia* 1992; 40 (7):1763-1771.

[113] Qu S, Zhang P, Wu SD, Zang QS, Zhang ZF. Twin boundaries: strong or weak? *Scripta Materialia* 2008; 59 (10):1131–1134.